



The
University
Of
Sheffield.

An Efficient Numerical Method for Simulating Multiphase Flows with a General Equation of State

Shaban A. Jolgam

A thesis submitted for the degree of Doctor of Philosophy
Department of Mechanical Engineering

Supervisor: Dr Andrew Nowakowski

July 7, 2014

بِسْمِ اللَّهِ الرَّحْمَنِ الرَّحِيمِ

*In the Name of Allah,
the Most Gracious, the Most Merciful*

Dedication

To my beloved Family:

Father, Mother,

Brothers and Sisters

To my lovely wife Nafisa and kids:

Moteaa, Ahmed and Abdalrhman

Acknowledgements

All praises and thanks be to Allah before and after who encourages us to seek for the knowledge for his sake as He says

“and say: Lord! Increase me in knowledge”

(verse 114, Chapter Taha, The Holy Quran)

and who facilitates for us to achieve this work.

Peace and blessings be upon His final messenger **Mohammed** who said:

“One who treads a path in search of knowledge has his path to Paradise made easy by God” (Saheeh Muslim, 4-2072, Hadith)

I would like to convey my gratitude to my supervisor Dr Andrew Nowakowski for providing me an interesting research topic and for his guidance throughout this work. Also my deep thanks and respect are going to Dr Fatma Ghangir for valuable discussions. In addition, I would like to thank Dr Hongwei Zheng and Dr Ali Ibrahim Zein for their helpful information.

I would like to acknowledge J. F. Haas and B. Sturtevant the authors of “Interaction of weak shock waves with cylindrical and spherical gas inhomogeneities ”-(1987) in the Journal of Fluid Mechanics as well as the Cambridge University Press for the permission to reproduce the figures of the authors’ experimental results.

I gratefully acknowledge the Ministry of Higher Education in Libya who supported me financially during my study. The University of Zawiya is also acknowledged for nominating and giving me this opportunity to pursue my study.

I express my thanks and appreciation to my beloved family for their continuous supplication, motivation and patience.

Abstract

An efficient numerical method with a general equation of state has been developed to study multiphase and multi-component flows.

The simulation of multiphase flows, which can be found in a wide range of natural phenomena and engineering applications, is a very challenging task. Such flows are characterised by interfaces that separate the flow materials. A quest to properly resolve these interfaces in a wide range of flow problems has generated an enormous amount of research in recent decades.

This work focuses on compressible flows with interfaces where flow phases or components could be governed by various equations of state. The present research also includes the physical problems characterised by discontinuities between materials under shock waves.

The potential applications of the developed numerical tools may include: simulation of air bubbles in water, cooling systems of nuclear reactors with water under pressure or detonation of high energetic explosive materials. It is critical to handle such flows with the properly chosen equation of state, which will not only account for the physical phenomena under consideration but will also facilitate the usage of the adopted numerical techniques.

To this end a new numerical method has been proposed to enable simulation of a wide range of multiphase problems, that may comprise gases, liquids or solids as flow constituents, with a general equation of state. The developed numerical approach was constructed for a fully non-equilibrium (referred as the seven-equation model in one-dimension) and partially equilibrium (referred as the six-equation model in one-dimension) models. The utilised mathematical models are suitable for fluid mixtures as well as for pure fluids separated by distinct interfaces.

The studied numerical techniques enable the treatment of the governing equations which cannot be written in a conservative form. The capabilities of the numerical algorithms also extend from strictly to non-strictly hyperbolic problems. For the fully non-equilibrium model each phase has its own velocity and pressure. This requires instantaneous velocity and pressure relaxation procedures to be implemented in the numerical solution. In case of the partially equilibrium model the velocity relaxation is not needed.

The developed methodology is described in one and two-dimensions. The specific mathematical model allowing numerical calculations of axisymmetrical multiphase flow is also proposed. The model is equipped with a source term that accounts for area variation allowing an efficient simulation of problems occurring in many practical applications such as for example multiphase flows through convergent-divergent nozzles.

All numerical algorithms are programmed using C++ language in the framework of finite volume methods. Three different approximate Riemann solvers, i.e. the HLL, HLLC and VFRoe, are successively implemented with various equations of state written in the general form of Mie-Grneisen equation of state. The activation of the required equation of state does not affect the model and numerical algorithm. The MUSCL scheme is used to achieve second order accuracy.

The effectiveness and efficiency of the developed numerical code are demonstrated using a selection of flow problems which include the interfaces between fluids (contact discontinuity) and shock waves. The verification checks are performed using exact or fine grid solutions of various shock tube tests with the ideal gas, van der Waals, Tait, stiffened gas, Cochran-Chan and Jones-Wilkins-Lee equations of state that govern gases, liquids and solids. The resolution of the Richtmyer-Meshkov instabilities has demonstrated the capabilities of the numerical tools in two dimensions. The validation tests are conducted using the one-dimensional mixture Hugoniot and two-dimensional experimental data representing the interaction of a planar shock wave with R22 and helium bubbles as well as the underwater explosion near a free surface. Finally the conclusions from the comparison studies between different models and numerical solvers are derived.

Contents

1	Introduction	1
1.1	Background	1
1.2	Aims and objectives	2
1.3	Outline	4
2	Overview of multiphase flows models and numerical methods	6
2.1	Background	6
2.2	Models for compressible multiphase flows	6
2.3	Numerical methods for multiphase compressible flows	7
2.3.1	Sharp Interfaces Methods (SIM)	8
2.3.2	Diffuse Interface Methods (DIM)	10
3	Mathematical and numerical description of the hyperbolic conservation laws	19
3.1	Some mathematical aspects for the hyperbolic conservation laws . . .	19
3.1.1	Hyperbolicity of the conservation laws	19
3.1.2	Weak solution	20
3.1.3	Non-conservative hyperbolic systems	21
3.1.4	The Riemann problem and characteristic fields	23
3.2	Numerical approach to the hyperbolic systems	25
3.2.1	Godunov method	25
3.2.2	The HLL approximate Riemann solver	28
3.2.3	The HLLC approximate Riemann solver	28
3.2.4	The VFRoe approximate Riemann solver	29
3.2.5	Boundary conditions	30
4	The seven-equation compressible multiphase flow model	32
4.1	Mathematical formulation	32
4.1.1	Closure relations	34
4.1.2	Fully non-equilibrium two-phase flow mathematical model . .	37
4.1.3	The model with area variation source term	38
4.2	Equation of state (EOS)	39
4.2.1	Ideal gas (IG) EOS	40
4.2.2	Shock wave (SW) EOS	40
4.2.3	Stiffened gas (SG) EOS	41
4.2.4	Tait's EOS	42
4.2.5	van der Waals gas (vdW) EOS	43
4.2.6	Cochran-Chan (CC) EOS	43
4.2.7	Jones-Wilkins-Lee (JWL) EOS	45
4.3	Mathematical structure of the seven-equation model	46
4.4	Numerical method	48

4.4.1	Numerical solution of the seven-equation model	49
4.4.2	The hyperbolic operator	50
4.4.3	Relaxation and source terms operator	56
4.5	Numerical results - Verification of the methodology	58
4.5.1	Gas-gas test	59
4.5.2	Solid-solid test	62
4.5.3	Interface advection test	63
4.5.4	Copper-explosive impact test	63
4.5.5	Single-phase flow through C-D nozzle	65
4.5.6	Two-phase flows through C-D nozzle	67
4.6	Numerical results - Comparison between solvers	69
4.6.1	Liquid-liquid test	70
4.6.2	Helium-air test	74
4.6.3	Water-air test	78
4.7	Numerical results - Comparison between EOSs	83
4.7.1	Liquid-liquid test	83
4.7.2	Helium-air test	86
4.7.3	Water-air test	89
4.7.4	Water faucet test	92
5	The six-equation compressible two-phase flow model	99
5.1	Partially equilibrium two-phase flow mathematical model	101
5.1.1	Pressure relaxation terms	102
5.1.2	Closure relations	102
5.2	Mathematical structure of the six-equation model	103
5.3	Numerical method	104
5.3.1	Numerical solution of the six-equation model	105
5.3.2	The hyperbolic operator	105
5.3.3	The pressure relaxation operator	109
5.4	Numerical results - Verification of the methodology	110
5.4.1	TNT product gases interaction test	111
5.4.2	Interface advection test	112
5.4.3	Modified Sod test	113
5.4.4	Water-air test	115
5.4.5	Water-air mixture test	115
5.4.6	Molybdenum-MORB interaction test	116
5.5	Numerical results - Validation of the results	118
5.5.1	Mixture Hugoniot test	119
5.6	Numerical results - Comparison between the six and seven-equation models	120
5.6.1	Sod test	122
5.6.2	Detonation products-copper interaction test	125
6	Verification and validation of the two-phase flow models in two dimensions	130
6.1	Extension of the seven-equation compressible multiphase flow model to two dimensions	130
6.1.1	Mathematical structure of the seven-equation model in two dimensions	131

6.2	Extension of the six-equation compressible multiphase flow model to two dimensions	135
6.2.1	Mathematical structure of the six-equation model in two dimensions	136
6.3	Numerical method for the two-dimensional seven-equation model . . .	138
6.3.1	The hyperbolic operator of the two-dimensional seven-equation model	139
6.3.2	The velocity and pressure relaxation operator	140
6.3.3	The MUSCL-Hancock scheme	142
6.4	Numerical method for the two-dimensional six-equation model . . .	145
6.4.1	The hyperbolic operator of the two-dimensional six-equation model	146
6.4.2	The pressure relaxation operator	147
6.5	Numerical results - Verification test problems	148
6.5.1	Air bubble explosion test	149
6.5.2	Interface translation test	152
6.5.3	Gas bubble underwater explosion test	154
6.5.4	Shock-bubble interaction	158
6.5.5	Richtmyer-Meshkov instability	164
6.6	Numerical results - Validation test problems	168
6.6.1	R22 bubble-air shock interaction	170
6.6.2	Helium bubble-air shock interaction	175
6.6.3	Underwater explosion near a free surface test	181
7	Conclusions and future work	191
7.1	Conclusions	191
7.2	Future work	194
	Bibliography	195
	Appendices	204
A	Derivations of speed of sound for various EOSs	205
A.1	Speed of sound for the shock wave EOS	205
A.2	Speed of sound for the van der Waals EOS	206
A.3	Speed of sound for the Cochran-Chan EOS	207
A.4	Speed of sound for the Jones-Wilkins-Lee (JWL) EOS	208
B	Publications	210
B.1	On Equations of State for Simulations of Multiphase Flows	210
B.2	Simulations of Compressible Multiphase Flows Through a Tube of Varying Cross-section	211
B.3	Simulation of Multiphase Flows with Strong Shocks and Density Variations	212
B.4	Capturing of Interface Evolution Using Diffuse Interface Method . . .	213
B.5	The Application of a Multi-component Eulerian Model for the Resolution of Interfaces Interacting with Shock Waves in Two-phase Flows	214

List of Figures

3.1	Initial data for the Riemann problem separated by a discontinuity . . .	23
3.2	Solution of the Riemann problem for the Euler equations	24
4.1	Solution of the Riemann problem for the seven-equation model λ_m are given by (4.44).	49
4.2	Shock tube illustration	59
4.3	Gas-gas test example 4.5.1: Numerical and exact solutions: Current (left) and Kurganov and Tadmor (2000) (right) results are at $t = 0.16$ s for: (a) pressure, (b) velocity and (c) mixture density.	60
4.4	Gas-gas test example 4.5.1: Numerical and exact solutions results are at $t = 0.16$ s for: (d) volume fraction.	61
4.5	Solid-solid test example 4.5.2: Comparison between current numerical solution and fine grid solution at $t = 50 \mu\text{s}$ for: (a) pressure, (b) velocity, (c) mixture density and (d) volume fraction.	62
4.6	Advection test example 4.5.3: VFRoe solver results (circles) com- pared with exact (line) from Petitpas et al. (2007) at $t = 270 \mu\text{s}$ for: (a) pressure, (b) velocity, (c) mixture density and (d) volume fraction.	64
4.7	Copper-explosive test example 4.5.4: Comparison between current numerical results and exact solution from Saurel and Abgrall (1999a) at $t = 85 \mu\text{s}$ for: (a) pressure, (b) velocity, (c) mixture density and (d) temperature.	65
4.8	Normalized nozzle cross-sectional area.	66
4.9	Single-phase flow through a convergent-divergent nozzle at variable exit pressure. Results for: pressure (left) and Mach number (right).	67
4.10	Air-water mixture (50% air) flow through convergent-divergent nozzle at variable exit pressure. Results for: (a) pressure, (b) Mach number, (c) mixture density and (d) velocity.	68
4.11	Air-water mixture flow through convergent-divergent nozzle with vari- able air-water ratios at $p_{exit} = 8.5 \times 10^8$ Pa. Results for: (a) pressure, (b) Mach number, (c) mixture density and (d) velocity.	69
4.12	Liquid-liquid test example 4.6.1: Numerical and exact solutions using SG EOS are at $t = 80 \mu\text{s}$ for: (a) pressure, (b) velocity, (c) mixture density and (d) volume fraction.	71
4.13	Liquid-liquid test example 4.6.1: Scaling order for the HLL, HLLC and VFRoe algorithms.	71
4.14	Liquid-liquid test example 4.6.1: L_2 error norm spatial convergence for: (a) pressure, (b) velocity, (c) mixture density and (d) volume fraction.	72
4.15	Liquid-liquid test example 4.6.1: Temporal convergence for the HLL, HLLC and VFRoe algorithms.	74

4.16	Helium-air test example 4.6.2: Comparion between HLL, HLLC and VFRoe solvers at $t = 0.01$ s for: (a) pressure, (b) velocity, (c) mixture density and (d) volume fraction.	75
4.17	Helium-air test example 4.6.2: Scaling order for the HLL, HLLC and VFRoe algorithms.	76
4.18	Helium-air test example 4.6.2: L_2 error norm spatial convergence for: (a) pressure, (b) velocity, (c) mixture density and (d) volume fraction.	77
4.19	Helium-air test example 4.6.2: Temporal convergence for the HLL, HLLC and VFRoe algorithms.	78
4.20	Water-air test example 4.6.3: Numerical and exact solutions are at $t = 229 \mu\text{s}$ for: (a) pressure, (b) velocity, (c) mixture density and (d) volume fraction.	79
4.21	Water-air test example 4.6.3: Two-dimensional surface plot for time evolution for: (a) pressure, (b) velocity, (c) mixture density and (d) volume fraction.	80
4.22	Water-air test example 4.6.3: Scaling order for the HLL, HLLC and VFRoe algorithms.	81
4.23	Water-air test example 4.6.3: L_2 error norm spatial convergence for: (a) pressure, (b) velocity, (c) mixture density and (d) volume fraction.	81
4.24	Water-air test example 4.6.3: Temporal convergence for the HLL, HLLC and VFRoe algorithms.	82
4.25	Liquid-liquid test example 4.7.1: Comparison between the SG and Tait EOSs using HLLC Riemann solver with 25000 cells at $t = 80 \mu\text{s}$ for: (a) pressure, (b) velocity, (c) mixture density and (d) volume fraction.	84
4.26	Liquid-liquid test example 4.7.1: Scaling order for the HLLC algorithm using the SG and Tait EOSs.	85
4.27	Liquid-liquid test example 4.7.1, L_2 error norm spatial convergence for: (a) pressure, (b) velocity, (c) mixture density and (d) volume fraction.	85
4.28	Liquid-liquid test example 4.7.1: Temporal convergence for the HLLC algorithms using the SG and Tait EOS.	86
4.29	Helium-air test example 4.7.2: Comparison between IG and vdW EOSs at $t = 0.01$ s for: (a) pressure, (b) velocity, (c) mixture density and (d) volume fraction.	87
4.30	Helium-air test example 4.7.2: Scaling order for the VFRoe algorithm using the IG and vdW EOSs.	88
4.31	Helium-air test example 4.7.2: L_2 error norm spatial convergence for: (a) pressure, (b) velocity, (c) mixture density and (d) volume fraction.	89
4.32	Water-air test example 4.7.3: Comparison between IG and vdW EOSs at $t = 229 \mu\text{s}$ for: (a) pressure, (b) velocity, (c) mixture density and (d) volume fraction.	90
4.33	Water-air test example 4.7.3: Scaling order for the VFRoe algorithm using the IG and vdW EOSs.	91
4.34	Water-air test example 4.7.3: L_2 error norm spatial convergence for: (a) pressure, (b) velocity, (c) mixture density and (d) volume fraction.	91
4.35	Water faucet test 4.7.4.	93
4.36	Water faucet test 4.7.4: Results using different mesh resolutions at $t = 0.4$ s. EOSs are for simulation (I) see Table 4.34: (a) air volume fraction and (b) water velocity.	94

4.37	Water faucet test 4.7.4: Comparison between EOSs using 1500 cells for: (a) Air volume fraction (b) Water velocity. Curve (I) water is governed by SG EOS and air is governed by IG EOS. Curve (II) water is governed by SG EOS and air is governed by van der Waals EOS. Curve (III) water is governed by Tait's EOS and air is governed by IG EOS. Curve (IV) water is governed by Tait's EOS and air is governed by van der Waals EOS.	94
4.38	Water faucet test 4.7.4: L_2 error norm spatial convergence for: (a) Air volume fraction (b) Water velocity. Curve (I) water is governed by SG EOS and air is governed by IG EOS. Curve (II) water is governed by SG EOS and air is governed by van der Waals EOS. Curve (III) water is governed by Tait's EOS and air is governed by IG EOS. Curve (IV) water is governed by Tait's EOS and air is governed by van der Waals EOS.	95
4.39	Water faucet test example 4.7.4: Scaling order for the HLL algorithm using the IG and vdW EOSs for air (up) and the SG and Tait EOSs for water (bottom).	97
5.1	Speed of sound of the 5-equation model versus air volume fraction for water-air mixture. The densities and speeds of sound for water and air are: $\rho_{water} = 1000 \text{ kg/m}^3$, $c_{water} = 1568 \text{ m/s}$, $\rho_{air} = 1 \text{ kg/m}^3$ and $c_{air} = 374 \text{ m/s}$	100
5.2	Wave transmission time delay τ through the numerical diffusion zone of an interface (Saurel, Petitpas and Berry, 2009).	100
5.3	Solution of the Riemann problem for the six-equation model λ_m are given by (5.12).	105
5.4	TNT product gases interaction test 5.4.1. Results for: (a) pressure, (b) velocity, (c) mixture density and (d) right component's volume fraction. Numerical solution from 6-eqn. model compared to the fine grid solution at $t = 12 \mu\text{s}$	112
5.5	Interface advection test 5.4.2: Results for: (a) pressure, (b) velocity, (c) mixture density and (d) air volume fraction. Numerical solution (circles) and exact solution (line) Allaire, Clerc and Kokh (2002) at $t = 2.79 \text{ ms}$	113
5.6	Modified Sod test 5.4.3: (a) Pressure. (b) Velocity. (c) Mixture density. (d) Air volume fraction. Numerical solution using the HLLC solver compared to the exact solution at $t = 0.0007 \text{ s}$	114
5.7	Water-air test 5.4.4: Results for: (a) pressure, (b) velocity, (c) mixture density and (d) air volume fraction. Numerical solution (circles) and exact solution (line) at $t = 229 \mu\text{s}$	115
5.8	Water-air mixture test 5.4.5. Numerical solution at $t = 229 \mu\text{s}$ for: (a) pressure, (b) velocity, (c) mixture density, (d) air volume fraction, (e) water density and (f) air density.	117
5.9	Setup and initial conditions for molybdenum-MORB interaction test 5.4.6	117
5.10	Molybdenum-MORB interaction test 5.4.6. Numerical solution at $t = 120 \mu\text{s}$ for: (a) pressure, (b) velocity, (c) mixture density and (d) MORB volume fraction.	118

5.11	Mixture Hugoniot test 5.5.1: Iron-Nickel alloy experimental data (symbols) results from 6 and 7-Eqn. models (lines) obtained using 2000 cells.	120
5.12	Mixture Hugoniot test 5.5.1: Nickel-Copper alloy experimental data (symbols) results from 6 and 7-Eqn. models (lines) obtained using 2000 cells.	121
5.13	Mixture Hugoniot test 5.5.1: Stainless steel alloy experimental data (symbols) results from 6 and 7-Eqn. models (lines) obtained using 2000 cells.	121
5.14	Sod test 5.6.1. Results for: (a) pressure, (b) velocity, (c) mixture density and (d) right component's volume fraction. Numerical solution from 6 and 7-eqn. models using the HLLC 200 cells compared to the exact solution at $t = 0.25$ s.	123
5.15	Sod test 5.6.1. L_2 error norm spatial convergence for: (a) pressure, (b) velocity, (c) mixture density and (d) volume fraction.	123
5.16	Sod test example 5.6.1: Scaling order for the HLLC algorithm for the 6-Eqn. and 7-Eqn. models.	125
5.17	Sod test 5.6.1: Temporal convergence for the HLL algorithm for the 6-Eqn. and 7-Eqn. models.	125
5.18	Detonation products-copper interaction test example 5.6.2. Results for: (a) pressure, (b) velocity, (c) mixture density and (d) temperature. Numerical solution compared to fine grid at $t = 73 \mu\text{s}$	126
5.19	Detonation products-copper interaction test 5.6.2. L_2 error norm spatial convergence for: (a) pressure, (b) velocity, (c) mixture density and (d) temperature.	127
5.20	Detonation products-copper interaction test 5.6.2: Scaling order for the HLL algorithm for the 6-Eqn. and 7-Eqn. models for detonation products-copper interaction test.	129
5.21	Detonation products-copper interaction test 5.6.2: Temporal convergence for the HLL algorithm for the 6-Eqn. and 7-Eqn. models.	129
6.1	Air bubble explosion test 6.5.1: Surface and contour plots for pressure (top) and mixture density (bottom) at $t = 0.25$ s using the seven-equation model.	149
6.2	Air bubble explosion test 6.5.1: Cross-section plot at $y = 1$ m for the pressure (a), mixture density (b) and velocity (c) at $t = 0.25$ s. Comparison between six and seven-equation models with exact from Toro (2009).	150
6.3	Air bubble explosion test 6.5.1: Scaling order for the HLL algorithm.	151
6.4	Air bubble explosion test example: L_2 error norm spatial convergence for: (a) pressure and (b) velocity.	151
6.5	Interface translation test at $t = 0$ s.	153
6.6	Interface translation test 6.5.2: Surface and contour plots for the mixture density distributions at $t = 0$ s (top) and $t = 0.36$ s (bottom) using the six-equation model.	153
6.7	Interface translation test 6.5.2: Cross-section plot of the mixture density results at $y = 0.61$ m and $t = 0.36$ s: a) Different mesh resolutions using the six-equation model. b), c) and d) Comparisons between six and seven-equation models for mixture density, pressure and velocity.	154

6.8	Interface translation test 6.5.2: Cross-section plot (right intrface of the bubble only) of the mixture density results at times 0.09, 0.18, 0.27 and 0.36 s.	155
6.9	Gas bubble underwater explosion test 6.5.3: Surface and contour plots for pressure (top) and mixture density (bottom) at $t = 120 \mu\text{s}$	156
6.10	Gas bubble underwater explosion test 6.5.3: Cross-section plot at $y = 0.5$ m for the pressure (a), mixture density (b) and velocity (c) at $t = 120 \mu\text{s}$. Current results from the six-equation model with different resolutions, exact from Shyue (2001).	156
6.11	Gas bubble underwater explosion test 6.5.3: Scaling order for the HLL algorithm.	157
6.12	Gas bubble underwater explosion test 6.5.3: L_2 error norm spatial convergence for: (a) pressure and (b) mixture density.	158
6.13	Setup for the shock bubble interaction test 6.5.4.	159
6.14	Shock-bubble interaction 6.5.4 results at $t = (1, 2, 3, 4) \times 10^{-4}$ s from top to bottom. Idealised schlieren mixture density current result using the six-equation model (left) and results from Zheng, Shu and Chew (2008) (right).	160
6.15	Shock-bubble interaction 6.5.4 results at $t = (1, 2, 3, 4) \times 10^{-4}$ s from top to bottom. Idealised schlieren volume fraction current result using the six-equation model (left) and results from Zheng, Shu and Chew (2008) (right).	161
6.16	Shock-bubble interaction 6.5.4. Mixture density distribution across line of symmetry at $t = (1, 2, 3, 4) \times 10^{-4}$ s from top to bottom. Current results using the six-equation model (left) and results from Zheng, Shu and Chew (2008) (right).	162
6.17	Shock-bubble interaction 6.5.4. Pressure distribution across line of symmetry at $t = (1, 2, 3, 4) \times 10^{-4}$ s from top to bottom. Current results using the six-equation model (left) and results from Zheng, Shu and Chew (2008) (right).	163
6.18	Richtmyer-Meshkov instability 6.5.5. Results from 7-equation model for (a) mixture density, (b) idealised schlieren mixture density, (c) idealised schlieren pressure, (d) mixture density plot across line of symmetry and (e) pressure plot across line of symmetry at $t = 0$ s (top left column), $t = 0.177$ (top right column), $t = 0.714$ s (bottom left column) and $t = 1.6$ s (bottom right column).	166
6.19	<i>Continued.</i> Richtmyer-Meshkov instability 6.5.5. Results from 7-equation model for (a) mixture density, (b) idealised schlieren mixture density, (c) idealised schlieren pressure, (d) mixture density plot across line of symmetry and (e) pressure plot across line of symmetry at $t = 2.31$ s (top left column), $t = 4.62$ s (top right column), $t = 6.93$ s (bottom left column) and $t = 9.24$ s (bottom right column).	167
6.20	Richtmyer-Meshkov instability 6.5.5. Comparison of spike and bubble positions and mixing zone thickness as functions of time with results of Nourgaliev, Dinh and Theofanous (2006); Terashima and Tryggvason (2009).	168
6.21	Initial configuration for air shock interactions with R22 and Helium bubbles.	169

6.22	Mixture density idealised Schlieren images for R22 bubble-air shock interaction at times: (a) 55 μs , (b)115 μs , (c) 135 μs , (d) 187 μs . Current results (left) and Haas and Sturtevant (1987) results (right).	172
6.23	<i>Continued.</i> Mixture density idealised Schlieren images for R22 bubble-air shock interaction at times: (e) 247 μs , (f) 318 μs , (g) 342 μs , (h) 417 μs and (i) 1020 μs . Current results (left) and Haas and Sturtevant (1987) results (right).	173
6.24	$x-t$ diagram for R22 bubbles (left), key points (right): V_s incident shock; V_R refracted shock; V_T transmitted shock; V_u upstream edge; V_d downstream edge;	174
6.25	Comparison between results of the IG and vdW EOSs for mixture density (left) and pressure (right) plots at axis of symmetry for R22 bubble-air shock interaction at times: (a) 55 μs , (b)115 μs , (d) 187 μs (e) 247 μs , (f) 318 μs , (g) 342 μs , (h) 417 μs and (i) 1020 μs .	176
6.26	Mixture density: Current numerical Schlieren images (left) and experimental (Haas and Sturtevant, 1987) (right) for He + %28 air bubble-air shock interaction at times: (a) 22 μs (32 μs) , (b) 44 μs (52 μs), (c) 56 μs (62 μs) , (d) 72 μs , (e) 82 μs . Times between parentheses are corresponding times in the experiments which are different from numerical times.	178
6.27	<i>Continued:</i> Mixture density: Current numerical Schlieren images (left) and experimental (Haas and Sturtevant, 1987) (right) for He + %28 air bubble-air shock interaction at times: (f) 102 μs , (g) 245 μs , (h) 427 μs (i) 674 μs and (j) 983 μs .	179
6.28	$x-t$ diagram for He + 28% air bubbles (left), key points (right): V_s incident shock; V_R refracted shock; V_T transmitted shock; V_u upstream edge; V_d downstream edge and V_j air jet head.	180
6.29	Comparison between results of the six and seven-equation models for mixture density (left) and pressure (right) plots at axis of symmetry for helium bubble-air shock interaction at times: (a) 28 μs , (b)44 μs , (c) 56 μs , (d) 72 μs , (f) 102 μs , (g) 245 μs , (h) 427 μs and (i) 674 μs (j) 983 μs .	182
6.30	Underwater explosion test 6.6.3.	183
6.31	Underwater explosion near a free surface test 6.6.3. Comparison between the SG and Tait EOSs: Idealised Schlieren images of mixture density (left) and plots of mixture density (kg/m^3) (middle) and pressure (Pa) (right) at line of symmetry at times: (a) 0.0175 ms, (b) 0.035 ms, (c) 0.07 ms.	185
6.32	<i>Continued.</i> Underwater explosion near a free surface test 6.6.3. Comparison between the SG and Tait EOSs: Idealised Schlieren images of mixture density (left) and plots of mixture density (kg/m^3) (middle) and pressure (Pa) (right) at line of symmetry at times: (d) 0.147 ms, (e) 0.225 ms, (f) 0.3 ms.	186
6.33	Underwater explosion near a free surface test 6.6.3. Comparison between the six and seven-equation models: Idealised Schlieren images of mixture density (left) and plots of mixture density (kg/m^3) (middle) and pressure (Pa) (right) at line of symmetry at times: (a) 0.0175 ms, (b) 0.035 ms, (c) 0.07 ms.	187

6.34	<i>Continued.</i> Underwater explosion near a free surface test 6.6.3. Comparison between the six and seven-equation models: Idealised Schlieren images of mixture density (left) and plots of mixture density (kg/m^3) (middle) and pressure (Pa) (right) at line of symmetry at times: (d) 0.147 ms, (e) 0.225 ms, (f) 0.3 ms.	188
6.35	Underwater explosion near a free surface test 6.6.3. Comparison between the SG and Tait EOSs, bottom wall with extrapolation BCs: Idealised Schlieren images of mixture density (left) and plots of mixture density (kg/m^3) (middle) and pressure (Pa) (right) at line of symmetry at time 0.3 ms.	189
6.36	Underwater explosion near a free surface test 6.6.3. Volume fraction and mixture density at times: (a) 0.0175 ms, (b) 0.035 ms, (c) 0.07 ms, (d) 0.147 ms, (e) 0.225 ms, (f) 0.3 ms.	190

List of Tables

4.1	SG EOS parameters for selected materials.	42
4.2	Mie-Grüneisen EOS functions for different EOSs.	44
4.3	Initial data for gas-gas test 4.5.1	60
4.4	Initial data for solid-solid test 4.5.2	62
4.5	Initial data for advection test 4.5.3	63
4.6	Materials properties for the Cochran-Chan EOS.	64
4.7	Initial and boundary conditions for a single-phase flow through the C-D nozzle.	66
4.8	Initial and boundary conditions for mixture flow through the C-D nozzle.	68
4.9	Initial data for liquid-liquid test 4.6.1	70
4.10	The number of time steps and the CPU time for liquid-liquid test using SG EOS	70
4.11	Order of accuracy of the HLL for liquid-liquid test using SG EOS	73
4.12	Order of accuracy of the HLLC for liquid-liquid test using SG EOS	73
4.13	Order of accuracy of the VFRoe for liquid-liquid test using SG EOS	73
4.14	Initial data for helium-air test 4.6.2	74
4.15	The number of time steps and the CPU time for helium-air test using IG EOS	75
4.16	Order of accuracy of the HLL for helium-air test using IG EOS	77
4.17	Order of accuracy of the HLLC for helium-air test using IG EOS	77
4.18	Order of accuracy of the VFRoe for helium-air test using IG EOS	78
4.19	Initial data for water-air test 4.6.3	78
4.20	The number of time steps and CPU time for water-air test using SG EOS	80
4.21	Order of accuracy of the HLL for water-air test using SG EOS	82
4.22	Order of accuracy of the HLLC for water-air test using SG EOS	82
4.23	Order of accuracy of the VFRoe for water-air test using SG EOS	82
4.24	The number of time steps and CPU time for liquid-liquid test using HLLC.	84
4.25	Order of accuracy of the HLLC for liquid-liquid test using SG EOS	86
4.26	Order of accuracy of the HLLC for liquid-liquid test using Tait EOS	86
4.27	The number of time steps and the CPU time for helium-air test using VFRore	88
4.28	Order of accuracy of the VFRoe for helium-air test using IG EOS	88
4.29	Order of accuracy of the VFRoe for helium-air test using vdW EOS	89
4.30	The number of time steps and the CPU time for water-air test using VFRoe.	90
4.31	Order of accuracy of the VFRoe for water-air test using SG EOS	92
4.32	Order of accuracy of the VFRoe for water-air test using vdW EOS	92

4.33	Initial data for water faucet test 4.7.4	93
4.34	EOSs used to govern water and air for water faucet test 4.7.4.	94
4.35	The number of time steps and the CPU run time for water faucet: (I) water is governed by SG EOS and air is governed by IG EOS. (II) water is governed by SG EOS and air is governed by van der Waals EOS.	96
4.36	The number of time steps and the CPU run time for water faucet: (III) water is governed by Tait's EOS and air is governed by IG EOS. (IV) water is governed by Tait's EOS and air is governed by van der Waals EOS.	96
4.37	Order of accuracy of the HLL for water faucet test using IG-SG EOSs	97
4.38	Order of accuracy of the HLL for water faucet test using vdW-SG EOSs	98
4.39	Order of accuracy of the HLL for water faucet test using IG-Tait EOSs	98
4.40	Order of accuracy of the HLL for water faucet test using vdW-Tait EOSs	98
5.1	Initial data for TNT product gases interaction test 5.4.1	111
5.2	Initial data for interface advection test 5.4.2	113
5.3	Initial data for modified Sod test 5.4.3	114
5.4	Initial data for water-air mixture test 5.4.5	116
5.5	Initial data for iron-nickel and nickel-copper mixtures shock impact 5.6.2	119
5.6	Initial data for stainless steel 304 alloy shock impact 5.6.2	119
5.7	Initial data for Sod test 5.6.1	122
5.8	Order of accuracy of the HLLC for the 6-Eqn. model for Sod test using IG EOS	124
5.9	Order of accuracy of the HLLC for the 7-Eqn. model for Sod test using IG EOS	124
5.10	The number of time steps and CPU time for the Sod test	124
5.11	Initial data for detonation products-copper interaction test 5.6.2 . . .	126
5.12	Order of accuracy of the HLLC for the 6-Eqn. model for Sod test using IG EOS	128
5.13	Order of accuracy of the HLLC for the 7-Eqn. model for Sod test using IG EOS	128
5.14	The number of time steps and CPU time for detonation products- copper test	128
6.1	Initial data for air bubble explosion test 6.5.1	149
6.2	The number of time steps and CPU time for air bubble explosion test	151
6.3	Order of accuracy of the HLL for 6-eqn. model for air bubble explo- sion test.	152
6.4	Order of accuracy of the HLL for 7-eqn. model for air bubble explo- sion test.	152
6.5	Initial data for interface translation test 6.5.2	152
6.6	Initial data for gas bubble underwater explosion test 6.5.2	155
6.7	The number of time steps and CPU time for gas bubble underwater explosion test.	157
6.8	Order of accuracy of the HLL for gas bubble underwater explosion test.	157
6.9	Initial data for shock-bubble interaction 6.5.4	159
6.10	Initial data Richtmyer-Meshkov instability 6.5.5	165

6.11	Gases properties used for the shock-bubble interactions.	170
6.12	Initial conditions for the R22 bubble test 6.6.1.	171
6.13	A comparison of the computed velocities for the R22 bubble case with experimental results of (Haas and Sturtevant, 1987) and numerical results of (Quirk and Karni, 1996); for key, see Figure 6.24	171
6.14	Initial conditions for helium bubble-air shock test 6.6.2.	177
6.15	A comparison of the computed velocities for the He+28% air bubble case with experimental results of Haas and Sturtevant (1987), and numerical results of Quirk and Karni (1996) (Numerical (A)) and of Marquina and Mulet (2003) (Numerical (B)); for key, see Figure 6.28	181
6.16	Initial conditions for the underwater explosion near a free surface test 6.6.3.	184

Nomenclature

Latin Symbols

A	Cross-sectional area
$A(W)$	Jacobian matrix
$A(q)$	Jacobian matrix
$B(W)$	Jacobian matrix
C	Continuously differentiable function
c_k	Sound speed of k^{th} phase
c_{ki}	Sound speed of k^{th} phase at the interface
D_p	Pressure relaxation source term
D_s	Area variation source term
D_v	Velocity relaxation source term
E_k	Total energy of k^{th} phase
e_k	Internal energy of k^{th} phase
F_{dk}	Drag force of k^{th} phase
$F(Q)$	Flux vector
$f(q)$	Flux vector
g	Gravitational acceleration
$H(Q)$	Non-conservative vector
i	Node (i)
\mathbf{K}_i	Eigenvector
k	Phase, gas or liquid

M	Mach number
\dot{m}_k	Mass transfer for each phase
m	Degree of freedom
\mathbb{N}	Natural numbers
N	Number of cells
p_{int}	Interfacial pressure
p_k	Pressure of k^{th} phase
Q	Conservative vector
q	Conservative vector
Q_{kint}	Heat transfer for each phase at the interface
\mathbb{R}	Vector of real numbers
S	Wave speed
T	Temperature
t	Time
u_k	Velocity of k^{th} phase(x -component)
u_{int}	Interfacial velocity
v_k	Velocity of k^{th} phase(y -component)
\mathbf{w}	Primitive variables
x, y, z	Cartesian coordinates
\mathbb{Z}	Integer numbers

Subscripts

0	Initial condition
i	Node i
L	Left hand side

m	Dimensions of vector or matrix
R	Right hand side
t	$\frac{\partial}{\partial t}$
x	$\frac{\partial}{\partial x}$
1	The first phase
2	The second phase

Superscripts

m	Dimensions of a vector or matrix
n	Time node
*	Star region or intermediate state
+	Right
–	Left

Greek Symbols

α	Volume or void fraction
Δt	Time increment
Δx	Space increment (x -direction)
Δy	Space increment (y -direction)
Δ	Spatial variation of the void fraction
Γ	Grüneisen coefficient
γ	Specific heat ratio
μ	Pressure relaxation coefficient
λ_i	i^{th} -Eigenvalue
λ	Velocity relaxation coefficient
ϕ	Smooth function

Acronyms

ALEM	Arbitrary Lagrangian-Eulerian Methods
CFL	Courant-Friedrichs-Lewy number
DIM	Diffuse interface method
EOS	Equation of state
EOSs	Equations of state
FTM	Front Tracking Methods
GFM	Ghost Fluid Method
HLL	Harten Lax and van Leer
HLLC	Harten Lax and van Leer with contact
IRM	Interface Reconstruction Methods
JWL	Jones-Wilkins-Lee
LM	Lagrangian Methods
LSM	Level Set Methods
MUSCL	Monotonic Upstream-centered Scheme for Conservation Laws
ODE	Ordinary differential equation
PDE	Partial differential equation
RMI	Richtmyer-Meshkov instabilities
RTI	Rayleigh-Taylor instabilities
SIM	Sharp interface method
SG	Stiffened gas
VOF	Volume Of Fluid

Chapter 1

Introduction

1.1 Background

Fluid flows of more than one phase (solid, liquid or vapour state of matter) or component can be characterised as multiphase flows, in which phases or components are separated by *interfaces*. Such flows occur in our everyday life, for example rain, snow, dust and pollen in air and sediment in water and so on. In addition, biomedical flows can also be considered as multiphase flows such as blood flow, kidney stones flow and nasal cavity flow and so on. Moreover, many engineering processes and systems, in order to be investigated efficiently should be treated as multiphase flows, for example oil and natural gas flows, water used to cool the nuclear reactor core, spray cooling towers and cavitations which may take place on pump impeller or turbine blades or marine propellers, etc.

Multiphase flows can be classified according to either phase materials or interfacial structures of the phases into various types. The first classification is according to phase materials, Brennen (2005) has divided multiphase flows into three types:

1. *Gas-liquid* flows such as separated flows, bubbly flows, gas-droplet flows, etc.
2. *Liquid-solid* flows such as slurry flows, sediment transport, fluidized beds, etc.
3. *Gas-solid* flows such as gas-particle flows, dust collectors, cosmic dust, etc.

The second classification is according to interfacial structures of the phases, Ishii (1975) has divided multiphase flows into the following types:

1. *Separated flows*, in which the two flowing fluids are continuous and separated by an interface.
2. *Dispersed flows*, which occur when the main stream is a liquid or gas phase. In the former case the particulate phase may contain finite solid particles or bubbles. In the latter case the particulate phase may contain finite solid particles or liquid droplets.

3. *Transitional flows*, which are characterised by the presence of both dispersed and separated flows and occur when the interfacial structure changes gradually.

To explore any of the above mentioned types of multiphase flows, this is also true for other phenomena and designs, one may study the case of interest either *experimentally*, *theoretically* or *computationally*. Experimental studies have played a significant role in validating and exploring the limitations of theoretical approximations to the governing equations and their analytical and numerical solutions. Moreover, testing of a prototype presents a cost-effective alternative to full-scale simulations of a real flow. However, in many occasions, where rigorous information are required, experimental studies encounter some difficulties related to inability to test a full-scale system or lack of measurement facilities. Theoretical studies also provide a verification tool to computational simulations. Though, it has to be remembered that in most practical applications an exact or analytical solution is difficult or cannot be obtained.

On the other hand, based on the improvement in computing facilities, computational studies (known as *Computational Fluid Dynamics* CFD) complement experimental and theoretical fluid dynamics by offering an alternative cost-effective way of simulating real flows. Moreover, CFD provides a wide range of flow simulations for conditions unavailable experimentally. In addition, it could provide more comprehensive information about the case study of interest and in a shorter time as compared with a physical experiment (Fletcher, 1991).

Indeed all types of multiphase flows mentioned above are governed by basically the same fundamental conservation flow equations (*mass*, *momentum* and *energy*), including the interaction terms for exchange of mass, momentum and energy between the phases. To solve these equations more information about the nature of the material in question is often needed in the form of an *equation of state* (EOS). Usually, EOS expresses pressure in terms of density and internal energy. In addition, a volume fraction evolution equation is needed to link the phases together. Mathematical and numerical treatments of these equations for multiphase flow are significantly more difficult than those for single-phase flow (Ishii and Hibiki, 2006). These difficulties arise from creation and evolution of the interfaces separating flow components and the discontinuities that may exist in flow properties across these interfaces.

1.2 Aims and objectives

This thesis is concerned with numerical simulations of compressible multiphase flow problems. These problems are described by *hyperbolic non-conservative* flow models. The numerical approximation of these models is realised by means of *finite volume*

methods based on *Godunov-type scheme*. The scheme is implemented with three different *approximate Riemann solvers*.

The study focuses on the seven-equation model which is a *full non-equilibrium* model and its first reduced form (i.e. the six-equation model which is a *partial equilibrium* model). The second reduced form of the seven-equation model (i.e. the five-equation) is not considered owing to the difficulties mentioned in Chapter 5. These difficulties are not present in the seven and six-equation models. Therefore, these models are used as a platform for investigating a wide range of test problems (i.e. which consider non-equilibrium two-phase flows as well as interfaces separating compressible flow components) with a general equation of state EOS. These problems may include: cooling of a nuclear reactor core using water with high pressure, interactions between flow components in supersonic combustions in scramjet engines, interactions between explosion products with solid materials, impact of two solid materials, interactions between two different gases in presence shock waves. Moreover, studying of single and two-phase flows in convergent-divergent nozzles can be addressed using the seven-equation model by including a source term to account for area variations. Several challenges arise in mathematical and numerical treatment of the deforming and moving interfaces separating flow components that coexist in the computational cell.

The task of formulation and consistent numerical implementation of an arbitrary EOS to work with these models has also to be addressed. The numerical implementation usually requires some changes within the numerical application to deal with different EOSs. The thesis will consider this problem to avoid the need to modify the numerical code each time when a different EOS is used. This is in contrast to the work, for example, of Petitpas et al. (2007) who need to make several modifications to their numerical application to account for complex EOSs. Building such application will enable dealing with a wide range of compressible multiphase flows, e.g. gas-gas, gas-liquid, gas-solid, explosives and detonation product interactions, etc.

Therefore, the main aim of the present thesis is to construct a model and numerical application capable of handling interfaces separating various fluids and at the same time having the ability to work with different EOSs.

To achieve the above mentioned aims the specific objectives are identified:

1. Determination of the mathematical structure of the six and seven-equation compressible multiphase flow models in one space dimension.
2. Numerical implementations of both models to be able to deal with the general EOS.
3. Application of a high resolution scheme to solve the above models to obtain a second order accuracy in both space and time.

4. Derivation of the formulae to calculate the speed of sound for various EOSs which are casted in the general form of Mie-Grüneisen EOS.
5. Verification of the numerical results of the six and seven-equation models in one space dimension.
6. Comparison between solvers, EOSs and models in terms of L_2 error norm, number of time steps and CPU run time. The examination of convergence and mesh-sensitivity of solutions of both compressible multiphase flow models is included in this task.
7. Validation of the numerical results of the six and seven-equation models in one space dimension using available experimental results. This requires determination of the stiffened gas EOS parameters for the chosen materials which will be used to validate the results.
8. Verification of the numerical results of the six and seven-equation models in two space dimensions using available exact or published results.
9. Validation of the numerical results of the six and seven-equation models in two space dimensions using available experimental results.

1.3 Outline

The rest of this thesis is organized as follows: Chapter 2 presents an overview of multiphase flow models and numerical methods of previous works depending on the treatment of the interface.

In Chapter 3 some basic facts on the hyperbolic conservation laws are briefly summarised. Hyperbolicity, weak solution and uniqueness of the solution to these laws are discussed. The Riemann problem and characteristic fields are introduced. Non-conservative hyperbolic systems have been defined and their weak solutions are given. A short review of Godunov's method and related approximate Riemann solvers that are implemented in the method is introduced. Then the possible boundary conditions that are imposed to the fictitious cells are explained.

In Chapter 4 the fully non-equilibrium model which is known as the seven-equation model of Saurel and Abgrall (1999a) is described. Closure relations are then discussed. Various EOSs are given and casted in the form of Mie-Grüneisen EOS. The stiffened gas EOS parameters for chosen compressible materials are determined. Then the source term that accounts for area variation is coupled to the multiphase flow model. This is followed by the mathematical structure of this model. The numerical method which is implemented with various Riemann solvers to solve the seven-equation model is presented. Then numerical results are verified using

different EOSs. Then comparisons between solvers and EOSs are carried out in terms of number of time steps, CPU time and the L_2 error norm.

In Chapter 5 the partially equilibrium model which is known as the six-equation model of Kapila, Menikoff and Stewart (2001) is described. The closure relations are given. The mathematical structure of this model is determined. This is followed by the numerical method which is implemented with various Riemann solvers to solve the six-equation model. The numerical results are verified using different EOSs. Then numerical results are verified using different EOSs. Further, the numerical results of both models are validated against experimental results. Finally, comparisons between the results of the six and seven-equation models in terms of number of time steps, CPU time and the L_2 error norm are accomplished.

In Chapter 6 the six and seven-equation models are extended to two space dimensions. The mathematical structures for both models are determined. The numerical method used to solve both models is described. Then numerical results of both models in two space dimensions are verified against exact or available published data. Finally the results are validated against available experimental data.

Finally Chapter 7 is devoted to the conclusions drawn from this work and some suggestions for future work are also outlined.

Chapter 2

Overview of multiphase flows models and numerical methods

2.1 Background

Compressible multiphase flows can be found when flowing fluids have different physical properties. A typical example is the behaviour of the interface separating two gases under a shock wave. Since multiphase flows play an essential role in many industrial processes and other disciplines, their modeling and computing have become a vital research area. Whitaker (1973) presented a derivation of the volume-averaged form of the transport equations for incompressible multiphase flow, and its results have been used to study many processes such as liquid-liquid extraction, gas-liquid mass transfer and dispersion in multiphase systems. Gray (1975) improved the previous derivation done by Whitaker (1973).

Using various averaging techniques the mathematical models of the compressible multiphase flows have been produced from single flow models as described in Ishii (1975); Drew (1983); Stewart and Wendroff (1984); Gray and Hassanizadeh (1989); Drew and Passman (1998). The process of averaging in a control volume which includes the interacting phases leads to non-conservative terms in the flow equations and the introduction of the equation of volume fraction evolution. This process eliminates the interfacial details related to transfer processes and needs introduction of closure relations which are often postulated.

2.2 Models for compressible multiphase flows

Essentially, there are two classes of models based on averaging technique. The first class is known as two-fluid models, which can be divided into three categories. The first is the seven-equation model, which consists of flow equations (mass, momentum and energy) for each phase, complemented by additional equation volume fraction evolution. In this model, each phase has its own different velocity and pressure.

The model first proposed by Baer and Nunziato (1986) to study the combustion and the associated process of the deflagration-to-detonation transition (DDT) in gas-permeable and reactive granular explosives. This model was modified by Saurel and Abgrall (1999a) to study a wide range of applications, which was achieved by including instantaneous relaxation procedures. The second is the six-equation model, which is as the previous model; however, it is without the additional equation for the volume fraction. The system is closed by assuming that the liquid density is constant (incompressible), while gas density is given by EOS. This model is characterised by one pressure and two velocities (Stewart and Wendroff, 1984; Toumi and Raymond, 1995). Another different version of the six-equation model consists of mass and energy equations for each phase and one momentum equation supplemented by an additional equation for the volume fraction equation. This model is derived by Kapila, Menikoff and Stewart (2001), it is characterised by a single velocity and two pressures. The last is the five-equation model, which consists of a mass equation for each phase, and momentum and energy equations for both phases, supplemented by a topological equation. This is characterised by single pressure and single velocity; such models have been proposed by Allaire, Clerc and Kokh (2000); Kapila, Menikoff and Stewart (2001); Murrone and Guillard (2005).

The second class is known as the mixture models, which consist of the Euler equations for the mixture and are supplemented by an additional equation to account for the concentration changes. These concentration changes are traced either by a mass fraction equation or specific heat ratio (γ) of the gas. These models are considered when the relative velocity of the two phases is small. However, such mixture models are inefficient when the kinematic disequilibrium becomes considerable (Cortes, Debussche and Toumi, 1998). Models mentioned above belong to averaging models; a brief description is given in Larreteguy (2002) about other models such as interface tracking models, entity tracking models, and microscopic models.

2.3 Numerical methods for multiphase compressible flows

Many researchers have considered interface problems and compressible multiphase flows using several numerical methods based on the Euler equations, augmented by one or more topological equations. Their main difficulty is the treatment of material interfaces. Some of these methods treat the interface as a sharp discontinuous zone, while others allow it to smear or to diffuse over a narrow band (Hu and Khoo, 2004; Perigaud and Saurel, 2005). At the interfaces, often the equation of state has a limited range of validity, especially for solids and liquids. For example, negative pressure results when the computed thermodynamic variables are slightly outside the range of validity. Therefore, a careful numerical treatment of interfaces is required

when studying fluids separated by interfaces (Saurel and Abgrall, 1999a).

2.3.1 Sharp Interfaces Methods (SIM)

These numerical methods eliminate the numerical diffusion at the interfaces; they consist of five main families:

1. Lagrangian Methods (LM)

In these methods the interfaces are moving with the local flow velocity and they are characterised by specific locations. The interface will be sharp if the artificial viscosity is not used in the method. The mesh moves with the material interface. The large deformation in the interface and the large distortions in the mesh are responsible for errors in the solution. Therefore, periodically updating the mesh is necessary which adds difficulties to these methods. Additional drawbacks are due to sliding lines that causes further complexity (Saurel and Le Métayer, 2001). More details are given in Benson (1992).

2. Arbitrary Lagrangian-Eulerian Methods (ALEM)

The ALEM was originally formulated by Hirt, Amsden and Cook (1974) in which the best features of Lagrangian and Eulerian methods are combined. In Lagrangian methods the mesh moves with the local flow velocity. They preserve good resolution for interfaces separating multiphase flows and during large scale compressions and expansions. However, Lagrangian methods cannot simulate multi-dimensional problems with large deformations due to vorticity and shear. In Eulerian methods such drawback does not exist, but the solutions are subject to be diffusive (Margolin, 1997). These methods use the Lagrangian approach at the interfaces and Eulerian schemes with a moving grid away from the interfaces. They are unlike Lagrangian methods, where larger distortions are allowed; however, their usage is limited. Farhat and Roux (1991) have developed powerful ALE methods using dynamic mesh management which reduces mesh distortions.

3. Front Tracking Methods (FTM)

In these methods the interface is tracked as a moving boundary, in which more than one flow solver are used with fixed mesh. They use Eulerian schemes away from the interface and a specific solver close to the interface. The management of several solvers has been done easily in one dimension by many researchers (Harten and Hyman, 1983; Mao, 1993; LeVeque and Shyue, 1996; Cocchi and Saurel, 1997). Although the methods are difficult in solving hard problems, two-dimensional problems have been carried out by Glimm et al. (1985); Grove (1994). Their results motivated Glimm et al. (1998) to investigate Rayleigh

Taylor instability in three dimensions, the method gave impressive results. The method used by Sousa et al. (2004) to simulate unsteady, incompressible, immiscible, Newtonian and multi-fluid flows with free surfaces in three dimensions. Saurel and Massoni (1998) have proposed a shock tracking method to simulate detonation problems in one dimension with complex EOSs to govern real gases. The method is efficient and robust but difficult to be extended to multi-dimensions.

Terashima and Tryggvason (2009) have combined the FTM with the Ghost Fluid Method (GFM) to study interactions of a planar shock with a helium bubble, the Rayleigh-Taylor instability, the Richtmyer-Meshkov instability, the breakup of a water drop in air and the collapse of an air bubble in water. The same combined method was modified by Bo et al. (2011) who used it to simulate air bubble-shock interaction and Rayleigh instability in two dimensions. Moreover, they simulated a turbulent liquid jet breakup in three dimensions.

4. **Interface Reconstruction Methods (IRM)**

These methods use the concept of a fractional Volume Of Fluid (VOF) (Hirt and Nichols, 1981) and the reconstruction methods (Youngs, 1982). The interfaces are not tracked but reconstructed with the help of phase volume fractions. These methods are not conservative; however, they are efficient and widely used in hydrocodes (Saurel and Le Métayer, 2001).

5. **Level Set Methods (LSM)**

These methods are simpler than front tracking, where the interface is considered as inner boundaries and the level set function is used to capture the front movement. Using the knowledge of the interface location with extrapolation procedures the flow variables are computed at the interface. Despite them not being conservative; their results are efficient in interface simulations. Level set methods have become widely used with the Ghost Fluid Method (GFM) which was originally developed for compressible two-phase flow by Fedkiw et al. (1999). These methods use the concept of a fractional volume of fluid method of Hirt and Nichols (1981) and the reconstruction methods of Youngs (1982). The interfaces are not tracked but reconstructed with the help of phase volume fractions (Saurel and Le Métayer, 2001). Using the GFM, level set methods have been extended to simulate interactions between materials (Hu and Khoo, 2004; Losasso, Shinar and Selle, 2006).

Nourgaliev, Dinh and Theofanous (2006) have used the level set method with an adaptive mesh refinement technique to simulate a wide set of two-dimensional test problems where the fluids are governed by the stiffened gas

(SG) EOS. Adaptive solution techniques are proposed by Kadioglu and Sussman (2008) where an interface solver based on the coupled level set and volume-of-fluid method is used for simulating underwater explosions and implosions. In their work the water is assumed to be compressible and governed by the Tait's EOS and gas governed by the Jones-Wilkins-Lee (JWL) EOS. A semi-implicit time discretisation for the Euler equations is used which removes the constraint on the time step contrary to the explicit discretisation (see for example, Cocchi and Saurel, 1997; Fedkiw et al., 2002).

The main advantages of these methods are that they allow an easy tracking of the interfaces between materials and maintain sharp interface. On the other hand, they possess some drawbacks which include complexity, expensive and they need prior knowledge of the interfaces locations which makes them unable to simulate problems with dynamical creation of interfaces (Saurel, Petitpas and Berry, 2009).

2.3.2 Diffuse Interface Methods (DIM)

These methods allow numerical diffusion at the interfaces, which is necessary for interface capturing and is considered as a drawback; however, its effect can be reduced by grid refinement and using high order methods. They use a single numerical scheme for all computational cells with fixed mesh to study interface problems (Perigaud and Saurel, 2005). Moreover, they have the ability to simulate the dynamical creation and the evolution of interfaces. These methods can also deal with inflow and outflow boundary conditions.

The simplicity of the Diffuse Interface Methods (DIM) to deal with coalescence or breakup among different phases or fluids has led many researchers to consider this approach. In early developments, to simulate material interfaces in compressible multi-fluids the mixture model has been used. This model consists of the Euler equations for a mixture and is complemented with an additional equation for the variable ϕ . Various choices for this variable have been suggested. It was used to represent the mass fraction (see for example, Abgrall, 1988), the specific heat ratio of the fluid γ (see for example, Roe, 1982) and the level set function (see for example, Mulder, Osher and Sethian, 1992).

However, they suffered from unphysical oscillations in the mass fraction and pressure at material interfaces. These oscillations are not present in the solution of the single flow model. In Larrouturou (1991) the mass fraction model was used in which a numerical flux modification was introduced, it guarantees the positivity of mass fraction but produces pressure oscillations. In Karni (1994) the gamma model based on a non-conservative scheme was used to avoid pressure oscillations. This guarantees the mass fraction positivity but it cannot handle strong shock waves.

The scheme was extended using a second-order non-conservative scheme with a sophisticated adaptive mesh refinement technique (Quirk and Karni, 1996). By which they have investigated the interactions of weak planar shock waves in air with different cylindrical gas bubbles. The investigation was carried out in two space dimensions and the results were validated against the experimental results of Haas and Sturtevant (1987). Despite the results were very good, the method is limited to ideal gases and weak shock flows only.

1. Methods based on Euler equations

Using a different approach (Karni, 1996) presented a hybrid scheme to overcome oscillations and inaccuracies near material interfaces separating multi-components. This was the first efficient method based on the mixture Euler equations augmented by the pressure evolution equation. The method was established using a non-conservative formulation of the equations and a level set function to trace the interface location. The pressure at the interface is calculated using the primitive variable formulation (non-conservative) of the Euler equations and away from the interface is calculated using the ideal gas EOS. The method has proven efficiency for capturing strong shock waves and simulating interfaces separating ideal gases. But the simulations of real gases and reacting flows using this method were unclear. The major drawbacks of this method are due to conservation errors, which produce inaccurate internal energy and temperature at the interface. Moreover, they are not easy to be applied with various equations of state (Saurel and Le Métayer, 2001). Furthermore, this method uses the mixture EOS which relies on unphysical assumptions such as density or temperature equilibrium between flow components.

In Abgrall (1996) a quasi-conservative method based on the mass fraction model, i.e. Euler equations for mixture augmented by the mass fraction equation, was used to prevent spurious oscillations in pressure through the contact discontinuities. The conservative equations are solved using the extended Roe scheme for multi-components, to update γ an additional transport equation for $1/(\gamma - 1)$ is used. The method has the ability to handle strong shock waves and can maintain mass fraction positivity. This was achieved by the basic proposed idea that the pressure and velocity of a two-phase flow must remain constant during its time evolution. The method was used to simulate interfaces between two flowing non-reacting gases with different specific heat ratios governed by the ideal gas EOS in one dimension.

Shyue (1998) has derived a γ -based model to extend the work of Abgrall (1996). This enables considering problems with materials, i.e. gases and liquids, that obey the stiffened gas EOS and to simulate problems in multiple

space dimensions. The algorithm is based on a mixture type model which is combined from the Euler equations for mixture and additional two equations for the material-dependent variables for the stiffened gas EOS. The quasi-conservative formulation of the Euler equations presented by Abgrall (1996) was used to ensure an accurate approximation of the energy equation near contact discontinuities. However, the number of equations of this model increases depending on the EOS parameters which complicates the solution method.

Shyue (1999) extended his work (Shyue, 1998) to include real gases using the van der Waals EOS. He proposed the general van der Waals EOS which can be used to consider problems with materials that obey the stiffened gas and van der Waals EOSs. The algorithm is also based on a mixture type model which is combined from the Euler equations for mixture and additional five equations for the material-dependent quantities for the van der Waals EOS. The method used to simulate compressible flows with two different phases, i.e. liquid and gas. The results were verified in one and two space dimensions. However, the number of equations of the model is increased more than when using the stiffened gas EOS which adds further complications to the solution method.

Based on the idea of Abgrall (1996), a simple Godunov-type scheme to solve a set of conservative and non-conservative equations was presented in Saurel and Abgrall (1999b). A second order accuracy was achieved by the MUSCL-Hancock method (Quirk, 1994). In their study the flow governing equations are the Euler equations (conservative) and additional two transport equations (non-conservative) for the stiffened gas EOS parameters γ and π . In their work the Rusanov numerical flux is used and extensions to other schemes are presented for the HLL, Roe and exact Riemann solvers. The method showed its ability to simulate problems with breakup and coalescence. The method is also able to solve problems with very high density ratios and pressures which generate strong shock waves. Many examples of compressible multi-fluid flows have been examined in one, two and three space dimensions. However, the method is restricted to the stiffened gas EOS.

A further extension to a more general case was presented in Shyue (2001), it enables examinations of two-phase flows of real materials modelled by the Mie-Grüneisen EOS. The algorithm is also based on a mixture type model which is combined from the Euler equations for mixture and additional four equations. These additional equations are related to the material-dependent quantities for the Mie-Grüneisen EOS. The Roe Riemann solver was used to solve one and two-dimensional problems and the obtained results demonstrate the efficiency of the algorithm.

A good review of mixture model versions is presented in Abgrall and Karni (2001). They described the numerical difficulties that are encountered in discretisation of such models and different approaches to overcome those difficulties. A simple algorithm was proposed to circumvent those difficulties at the material interface, by considering that the mixture evolves as a single-phase. Two different flux functions are computed across the interface to update the different fluids on both sides.

2. Methods based on multiphase flows equations

This method was proposed by Saurel and Abgrall (1999a), based on the seven-equation model for compressible multiphase flow derived by Baer and Nunziato (1986). The method uses a single algorithm in solving the system at each grid. Moreover, it can handle strong shock waves and it has the ability to deal with the general equations of state (EOS) to simulate real materials interactions test problems. In addition, it gives correct temperatures and internal energies at the interface.

Gonthier and Powers (2000) presented a conservative upwind numerical method based on Godunov's methodology and uses a new approximate solution for the two-phase Riemann problem for arbitrary EOSs. The non-conservative terms have been neglected for two reasons, the system still satisfies the second law of thermodynamics and these terms do not play an important role in the process of deflagration-to-detonation transition (DDT) which was the case study. The method can capture strong shocks with minimal smearing or spurious oscillations. This has been demonstrated by comparing its results with the exact solution of some known tests such as two-phase shock tube and two-phase detonation wave in energetic material results from piston impact.

Allaire, Clerc and Kokh (2000) proposed a compressible two-phase flow model based on assumptions that there is no mass and heat transfer across the interface between flow components, also they assumed that both phases have the same velocity and pressure. Moreover, all diffusive terms and source terms are neglected. The obtained model consists of two mass equations (one equation for each phase), one momentum equation (for mixture), one energy equation (for mixture) and the model is completed by a volume fraction equation. The model is hyperbolic but non-conservative due to the last equation. An isobaric closure is used to close the model with arbitrary EOS.

Saurel and Le Métayer (2001) showed the ability of the seven-equation multiphase model of Saurel and Abgrall (1999a) to solve different applications (interface problems, physics of detonation, shock waves in multiphase, cavitating flows etc.) using the same formulation without the need for mixture

EOS (which relies on unphysical postulations such as equality of temperature and density between phases) at the interfaces. The discretisation method extended to second order in multi-dimensional problems under the assumption of uniformity of pressure and velocity proposed by Abgrall (1996).

Kapila, Menikoff and Stewart (2001) derived two reduced models from the seven-equation (BN) model, one with a single velocity (six-equation) and the other with both a single velocity and a single pressure (five-equation). Both models are hyperbolic and non-conservative; however, they provided ways to fully specify the jump conditions across shock waves.

Allaire, Clerc and Kokh (2002) have proposed a diffuse interface method to solve the model of Allaire, Clerc and Kokh (2000) with a general EOS. This is done to avoid the complexity of the proposed approach of Shyue (1998); Saurel and Abgrall (1999b). The method is based on a Godunov-type scheme with the Roe-type Riemann solver. It is used for simulation of interfaces separating compressible flow components. In this study, they investigated the isobaric and isothermal closures to close the model. The investigation showed that to maintain the stability of the interfaces the isobaric closure is preferable. Numerical results have been presented in one-dimension where the flow components are governed by the Mie-Grüneisen EOS. A simulation of the bubble-shock interaction test is conducted in two space dimensions where the air is governed by the van der Waals EOS and the water is governed by the stiffened EOS.

Andrianov, Saurel and Warnecke (2003) developed a numerical Godunov-type scheme based on a characteristic decomposition for the multiphase model proposed by Baer and Nunziato (1986). The model is non-conservative and non-strictly hyperbolic. The discretisations of the non-conservative terms in one-dimension have been presented at the volume fraction discontinuity in the absence of pressure and velocity jumps. They showed that unphysical solutions may result due to neglecting non-conservative terms when simulating interface problems between pure materials. Moreover, they showed that the existence of the non-conservative terms is essential to preserve the conditions of velocity and pressure uniformity. A good agreement was obtained by the comparison of results with the exact solutions.

Niu (2005) proposed the HLLC Riemann solver based on the two-phase mixture model. The Tammanns (stiffened) EOS was used in the study. An air-liquid shock tube test has been done under very high density ratios up to 10000. The obtained results show the ability of the solver to capture the interface under strong shocks. Moreover, to assess the solver, a two-dimensional

square bubble problem was examined.

Perigaud and Saurel (2005) developed a quasi-conservative formulation based on the five equation model of Kapila, Menikoff and Stewart (2001) to study the effect of surface tension and viscosity on compressible multiphase flows. Various test problems involving break-up and coalescence were considered to ensure that the method was able to deal with dynamic appearance and disappearance of the interfaces.

Murrone and Guillard (2005) proposed an Eulerian diffuse interface model which could be used for simulation of compressible multi-component and two-phase flow problems. The model was derived from the seven-equation model of Baer and Nunziato (1986) using an asymptotic limit of zero pressure and velocity relaxation times. The model is similar to the five equation model of Allaire, Clerc and Kokh (2000); Kapila, Menikoff and Stewart (2001). They studied the mathematical structure of this reduced model and proposed two different approximation schemes for its numerical solution. They examined the model in one and two space dimensional problems with fluids that are governed by the stiffened EOS and the results show that the numerical methods were efficient and robust.

Lallemand, Chinnayya and Le Métayer (2005) have considered the seven-equation model of Saurel and Abgrall (1999a) to simulate compressible multiphase flows. They presented new pressure relaxation procedures for such models which are hyperbolic and compared them with existing ones on the bases of accuracy and performance. An exact procedure was recommended to be used for fluids governed by the stiffened EOS, and other approximate procedures were suggested to be used for fluids governed by the general EOS. These approximate procedures seem to be more suitable for cases with large pressure differences between two phases. The comparison was done using some known test problems.

Schwendeman, Wahle and Kapila (2006) considered the Riemann problem for the Baer and Nunziato (1986) model. The study focused on the effect of non-conservative terms and neglected mass, momentum and energy exchange terms. The solution of the Riemann problem that represents the wave structure and the intermediate states has been obtained by an iterative method. The accuracy of the method was extended to second order using the slope limiter method and the results was compared with different methods available in the literature.

Saurel et al. (2007) proposed a new scheme for the Euler equations to calculate the thermodynamic variables during the computations. This is done

by replacing the conventional Godunov method with a relaxation-projection method. Mechanical relaxation processes were established between different sub-volumes that exist in the computational cell. A new numerical EOS was derived and used to prevent pressure oscillations which occur at the interface for fluids governed by real gas EOS. The method extended to use different EOSs to study interfaces separating liquid and gas. The results show that the method is accurate, free of oscillations and conservative. This method has been extended in Petitpas et al. (2007) to the non-conservative hyperbolic multiphase flow model of Kapila, Menikoff and Stewart (2001). They have proposed two Lagrangian schemes based on internal energy equations and on artificial heat exchanges to circumvent the difficulty of conventional Godunov schemes to converge to the exact solution in presence of strong shocks. However, they need to make several modifications in their algorithm in order to deal with complex EOSs such as the Mie-Grüneisen EOS.

Ghangir et al. (2008) investigated the performance of the HLL and HLLC using the seven-equation model of Saurel and Abgrall (1999a) and the five-equation model of Allaire, Clerc and Kokh (2000) models. In this study they examined only the air-water shock tube test problem in one space dimension. Both flow constituents were governed by the stiffened EOS. According to their investigation they pointed out that the seven-equation model produces better results than the five-equation model. They also concluded that the HLLC solver generates better results than the HLL solver. The seven-equation model again with the stiffened EOS was extended to study two-dimensional problems in Ghangir and Nowakowski (2012). The discretisation of the non-conservative terms in two-dimension was derived for the HLLC scheme using the idea of Abgrall (1996).

Zheng, Shu and Chew (2008) used the five-equation model of Allaire, Clerc and Kokh (2000) with the stiffened gas EOSs to study different compressible two-fluid test problems. In this study an unstructured quadrilateral-mesh based solution adaptive method has been proposed based on the diffuse interface method presented in Shyue (1998); Abgrall and Karni (2001). The HLLC approximate Riemann solver was implemented with second order accuracy which was achieved using the MUSCL scheme. The results were presented for different test problems in one and two space dimensions. No oscillations were observed across the interface in the results of the velocity and pressure distributions.

Saurel, Petitpas and Berry (2009) examined the reduced five-equation model of Kapila, Menikoff and Stewart (2001). The ability of this model for numerical resolution of the interfaces and wave propagation in compressible fluids

and mixtures respectively was considered in Murrone and Guillard (2005); Abgrall and Perrier (2006); Petitpas et al. (2007). However, there are some drawbacks, such as inaccuracy in waves transmission across interfaces, difficulty of maintaining the positivity of the volume fraction in the existence of shocks or strong expansion waves and computations of shock using this non-conservative model. To overcome these drawbacks, they used the six-equation model of Kapila, Menikoff and Stewart (2001) which was the first time this model was used. In this study they validated the model against the experimental results of a planar shock interaction with a helium bubble in air which was conducted by Layes and Le Métayer (2007). The numerical solution was achieved using the same strategy given in Saurel and Abgrall (1999a).

Zein, Hantke and Warnecke (2010) modified the seven-equation model of Saurel and Abgrall (1999a) to include the mass and heat transfer. New terms for thermal relaxation were modeled and the stiffened gas EOS was used to close the model. Mechanical and thermal relaxation processes were performed instantaneously to achieve mechanical and thermal equilibrium. The results were similar to that obtained by Saurel, Petitpas and Berry (2009) using the five-equation model. The same work has been carried out using the six-equation model of Kapila, Menikoff and Stewart (2001) and its results were compared with the results of the seven-equation model in one dimension and it was concluded that they gave almost the same results, but the six-equation model is less expensive.

Banks (2010) investigated the poor behaviour of a classical conservative scheme when applied to a single-phase flow governed by a nonlinear EOS. In such cases, unphysical oscillations arise at the contact discontinuities. Banks included a non-conservative energy correction source term to the quasi-conservative scheme of Banks et al. (2007) and used a switching mechanism to activate the source term whenever the flow field does not have an acoustic characteristic. This modification was used to overcome the unphysical oscillations in a single-phase flow governed by the Jones-Wilkins-Lee (JWL) EOS.

Zheng et al. (2011) extended the study conducted in Zheng, Shu and Chew (2008) to include the general EOS. Various types of EOS were written in a unified form where the so called to-be-determined functions were given for each EOS. In this study, different compressible two-fluid test problems were conducted in one and two space dimensions to examine the performance of the solver. Also no oscillations were observed across the interface in the results of both velocity and pressure.

Dumbser and Toro (2011) proposed a simple extension of Osher and Solomon

(1982) approximate Riemann solver for hyperbolic systems in a non-conservative form. The numerical viscosity is defined in terms of a simple path-integral. The proposed Osher-type scheme is applied to the non-conservative shallow water equations using the first order version and to the non-conservative Baer-Nunziato model of compressible multi-phase flow using the higher-order multi-dimensional version.

Lee et al. (2013) developed an adaptive Osher-type scheme in a primitive-conservative framework for the Euler equations. This scheme was proposed to overcome the numerical difficulties which arose at the contact discontinuities when complex EOSs, usually written in the form of the Mie-Grüneisen EOS, are used. Where spurious solutions are observed when simulating single-phase as well as multiphase flows using conservative schemes with the Euler equations. Using the MUSCL-Hancock method the scheme is extended to obtain the second order accuracy. The results are presented in one and two-dimensional space to demonstrate the verification of the developed scheme.

Chapter 3

Mathematical and numerical description of the hyperbolic conservation laws

In this chapter, some basic facts on the hyperbolic conservation laws are briefly summarised. Hyperbolicity, weak solution and uniqueness of the solution to these laws are discussed. The Riemann problem and characteristic fields are introduced. Non-conservative hyperbolic systems have been defined and their weak solutions are given. A short review of Godunov's method and related approximate Riemann solvers that are implemented in the method is given.

3.1 Some mathematical aspects for the hyperbolic conservation laws

Conservation laws are usually described by a time-dependent system of partial differential equations of mass, momentum and energy written in a divergence form. Wave propagation problems experienced in many areas of physics and engineering are described mathematically by these laws. To solve these laws numerically using conventional methods for solving hyperbolic systems, one has to determine the hyperbolicity of the system being solved.

3.1.1 Hyperbolicity of the conservation laws

Consider the following conservation laws which may be written in one space dimension as follows:

$$\frac{\partial}{\partial t}q(x, t) + \frac{\partial}{\partial x}f(q(x, t)) = 0, \quad (3.1)$$

where $q : \mathbb{R} \times \mathbb{R} \rightarrow \mathbb{R}^m$ is an m -dimensional vector of conserved quantities of the

state variables q_i , i.e., $\int_{-\infty}^{\infty} q_i(x, t) dx$ should remain constant with respect to time t . The spatial distribution of the state variables q_i changes as time evolves. Knowing the value of the state variable $q_i(x, t)$ of the i th component allows to determine the rate of the flux function $f_i(q(x, t))$ at a given point and time.

The equation (3.1) may be written in a compact form as:

$$q_t + f(q)_x = 0. \quad (3.2)$$

This equation with the following initial conditions constitutes an initial value problem known as the Cauchy problem:

$$q(x, 0) = q_0(x). \quad (3.3)$$

The system (3.2) can be written in a *quasi-linear* form as follows:

$$q_t + A(q)q_x = 0, \quad (3.4)$$

where $A(q) = f'(q)$ is the $m \times m$ *Jacobian matrix* of the flux function $f(q)$. The system (3.2) is said to be a *non-strictly hyperbolic* system if the Jacobian matrix $A(q)$ has m real eigenvalues are not distinct:

$$\lambda_1(q) \leq \lambda_2(q) \leq \dots \leq \lambda_m(q),$$

and is said to be *strictly hyperbolic* if the eigenvalues are distinct:

$$\lambda_1(q) < \lambda_2(q) < \dots < \lambda_m(q),$$

with a corresponding set of m *linearly independent* eigenvectors (LeVeque, 1992, 2004; Toro, 2009):

$$\mathbf{K}_1(q), \mathbf{K}_2(q), \dots, \mathbf{K}_m(q).$$

3.1.2 Weak solution

The solution to the Cauchy problem (3.2) may become discontinuous, i.e. containing shocks or contact discontinuity, after some finite time interval even with smooth initial data. Consequently, the differential form equation (3.2) may have a not differentiable solution which poses a mathematical difficulty, this leads to define a weak solution to this form by the appeal to the integral form. Consider the integral form of (3.2) as:

$$\int_0^{\infty} \int_{-\infty}^{\infty} [q_t + f(q)_x] dx dt = 0. \quad (3.5)$$

Multiplying (3.5) by any smooth function $\phi(x, t)$ that vanishes at infinity and integrating one obtains:

$$\int_0^\infty \int_{-\infty}^\infty [q\phi_t + f(q)\phi_x] dx dt + \int_{-\infty}^\infty q(x, 0) \phi(x, 0) dx = 0. \quad (3.6)$$

The advantage of (3.6) is that the derivatives are on ϕ and not on q and $f(q)$. Hence, the equation (3.6) continues to hold even q is discontinuous. Thus, the function $q(x, t)$ is called a weak solution of the Cauchy problem (3.2) if (3.6) continues to hold for all test functions $\phi \in C_0^1(\mathbb{R} \times [0, \infty))^m$, where $C_0^1(\mathbb{R} \times [0, \infty))^m$ is the space of C^1 that are continuously differentiable and have compact support which is identically zero outside of some bounded region of the x - t plane (Smoller, 1983; LeVeque, 1992, 2004).

Another mathematical difficulty is encountered in solving the equation (3.2). This is because the weak solution q to equation (3.2) can have a discontinuity. It is known that not every discontinuity is admissible. Therefore, the following *Rankine-Hugoniot conditions* should be satisfied across the discontinuity:

$$S_i(q_R - q_L) = f(q_R) - f(q_L), \quad (3.7)$$

where S is the propagation speed of the discontinuity, i.e. shock wave or contact discontinuity (see for example, Smoller, 1983).

In addition to that difficulties, the solution to the equation (3.2) and (3.4) can have more than one weak solution even with the same initial data. Only one of these solutions would be physically relevant. LeVeque (1992) provided an example of a non-uniqueness of the weak solution. Therefore, more conditions are required to identify the correct solution among all weak solutions. These conditions are called *entropy conditions*, which state that the entropy of a system increases across a physically admissible shock:

$$\lambda(q_L) > S > \lambda(q_R),$$

where λ is an eigenvalue, q_L and q_R are the states to the left and right of the shock, respectively. More details about admissibility conditions may be found in Lax (1972); Dafermos (1973); Liu (1976); Smoller (1983); LeVeque (1992).

3.1.3 Non-conservative hyperbolic systems

Non-conservative hyperbolic systems have great role in various areas, especially in studying of compressible multi-phase and multi-component flows which may be found in several applications. Non-conservative terms usually appear in a system of equations due to modelling simplification and assumption or a closure hypothesis. The system (3.4) is said to be a conservative system if $A(q)$ is the Jacobian of the

flux function $f(q)$ and can be written (3.4) in the divergence form. But it is called a non-conservative system if it does not have such flux function. Then it is not possible to write the system in the divergence form. Unfortunately, this is the case for most two-phase flow models studied in the literature. Consequently, the above introduced definitions of the weak solution and the Rankine-Hugoniot conditions for the conservation laws cannot be applied to the non-conservative systems. This is one of the major difficulties encountered in dealing with the non-conservative systems. Many authors have considered research on the theory of non-conservative systems (see for example, LeFloch, 1989; Dal Maso, LeFloch and Murat, 1995). Later developments in numerical schemes for non-conservative systems were done by implementing the Dal Maso, LeFloch and Murat (DLM) theory introduced for such systems in Dal Maso, LeFloch and Murat (1995).

A proposed notion of the non-conservative product $A(q)q_x$ is used to define a weak solution to a general non-conservative system which is introduced in Dal Maso, LeFloch and Murat (1995). Also they considered the non-conservative product across a discontinuity to be defined along paths connecting the left and right states. This definition is also applied to the two-phase flow models (Chalmers and Lorin, 2010).

Consider a family of Lipschitz continuous paths, $\varphi : [0, 1] \times \mathbb{R}^m \times \mathbb{R}^m \rightarrow \mathbb{R}^m$ that satisfy the following properties:

1. For any $q_L, q_R \in \mathbb{R}^m$,

$$\varphi(0; q_L, q_R) = q_L, \varphi(1; q_L, q_R) = q_R.$$

2. For any $q \in \mathbb{R}^m$ and every $\tau \in [0, 1]$,

$$\varphi(\tau; q, q) = q.$$

3. For any $q_L, q_R \in \mathbb{R}^m$, for some $k > 0$ and every $\tau \in [0, 1]$,

$$\left| \frac{\partial \varphi}{\partial \tau}(\tau; q_L, q_R) \right| \leq k |q_L - q_R|.$$

4. For any $q_L, q_R, V_L, V_R \in \xi, \tau \in [0, 1]$ and for $k > 0$ such that

$$\left| \frac{\partial \varphi}{\partial \tau}(\tau; q_L, q_R) - \frac{\partial \varphi}{\partial \tau}(\tau; V_L, V_R) \right| \leq k |(q_L - V_L) - (q_R - V_R)|,$$

for every bounded set $\xi \subset \mathbb{R}^m$.

Let the non-conservative product $A(q)q_x$ be defined as a bounded Borel measure $[A(q)q_x]_\varphi$, when q is smooth on a Borel set B . This measure is defined by:

$$[A(q)q_x]_\varphi(B) = \int_B A(q)q_x dx,$$

and when q is piecewise differentiable and contains a jump discontinuity between the left and right states q_L and q_R , respectively. This measure is defined by:

$$[A(q)q_x]_\varphi(x_0, t_0) = \int_0^1 A(\varphi(\tau; q_L, q_R)) \frac{\partial \varphi}{\partial \tau}(\tau; q_L, q_R) d\tau.$$

Employing the above properties and definitions the generalized Rankine-Hugoniot conditions across a discontinuity, which depends on the chosen path φ , is defined as:

$$S(q_L - q_R) = \int_0^1 A(\varphi(\tau; q_L, q_R)) \frac{\partial \varphi}{\partial \tau}(\tau; q_L, q_R) d\tau, \quad (3.8)$$

where S is the speed of the discontinuity. The above relation (3.8) reduces to the classical Rankine-Hugoniot conditions (3.7) when the matrix $A(q)$ is a Jacobian matrix of the flux function $f(q)$, i.e. conservative system. The function q is defined as a weak solution for the non-conservative systems (see for example, Chalmers and Lorin, 2010) if and only if:

$$\int_0^\infty \int_{-\infty}^\infty [q\phi_t + [A(q)q_x]_\varphi\phi] dx dt = 0,$$

for all test functions $\phi \in C_0^1(\mathbb{R} \times [0, \infty))$.

3.1.4 The Riemann problem and characteristic fields

Consider the conservation law:

$$q_t + A(q)q_x = 0, \quad (3.9)$$

together with the left q_L and right q_R piecewise constant initial data having a single jump discontinuity at some point, say $x = 0$:

$$q(x, 0) = q_0(x) = \begin{cases} q_L & \text{if } x \leq 0, \\ q_R & \text{if } x > 0, \end{cases} \quad (3.10)$$

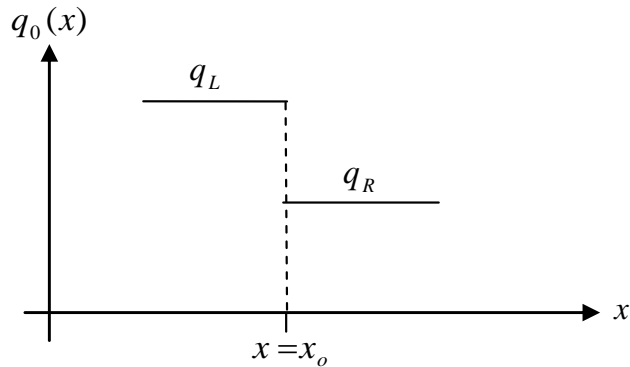


Figure 3.1: Initial data for the Riemann problem separated by a discontinuity is known as the Riemann problem, as shown schematically in Figure 3.1. It is

known as a *shock tube problem* for the Euler equations. The solution of the Riemann problem plays a major role in developing numerical methods for solving hyperbolic problems, in particular the Godunov-type schemes. The solution to the Riemann problem for hyperbolic systems is a self-similar solution that is a function of x/t alone. For a system with $m \times m$ Jacobian matrix $A(q)$ the solution consists of m waves emanate from the origin as shown in Figure 3.2.

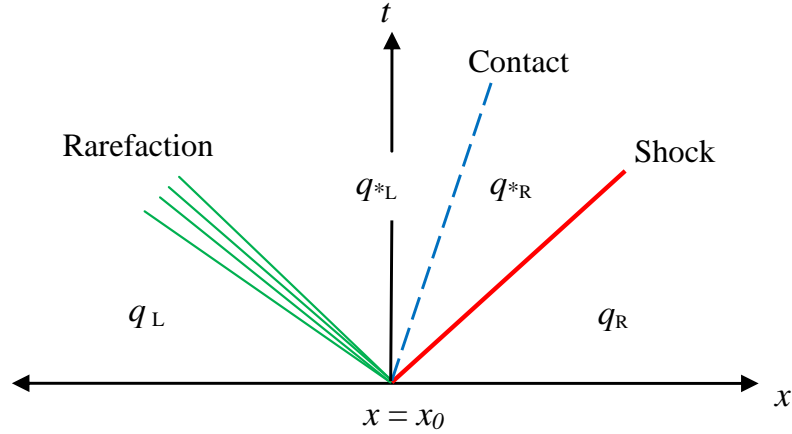


Figure 3.2: Solution of the Riemann problem for the Euler equations

The figure shows the solution to the Riemann problem for Euler equations in the $x-t$ plane. It consists of three different waves corresponding to the eigenvalues or characteristic speeds $\lambda_i(q)$, i.e., shock, contact and rarefaction waves. These waves divide the fields of characteristic into $m + 1$ constant states, the i -th eigenvalue $\lambda_i(q)$ determines the corresponding characteristic field, the λ_i -field. There are two types of characteristic fields as follows:

1. Genuinely nonlinear:

An i -th characteristic field is called a genuinely nonlinear field, if the λ_i -characteristic field satisfies:

$$\nabla \lambda_i(q) \cdot \mathbf{K}_i(q) \neq 0, \quad \text{for all } q \in \mathbb{R}^m, \quad (3.11)$$

where

$$\nabla \lambda_i(q) = \left(\frac{\partial}{\partial q_1} \lambda_i, \frac{\partial}{\partial q_2} \lambda_i, \dots, \frac{\partial}{\partial q_m} \lambda_i \right)^T,$$

is the gradient of $\lambda_i(q)$. In this characteristic field the left and right states are connected by either a single jump discontinuity, i.e., a shock wave in which all flow variables are discontinuous, or a smooth transition, i.e., a rarefaction wave in which all flow variables are continuous. These waves are formed depending on other conditions that must be fulfilled for their formation (for more details see for example Toro, 2009).

2. Linearly degenerate:

An i -th characteristic field is called a Linearly degenerate field, if the λ_i -characteristic field satisfies:

$$\nabla \lambda_i(q) \cdot \mathbf{K}_i(q) = 0, \quad \text{for all } q \in \mathbb{R}^m. \quad (3.12)$$

In this characteristic field the left and right states are connected by a contact discontinuity (density discontinuous, pressure and velocity are constant) that is formed depending on other conditions that must be fulfilled for its formation (for more details see for example Toro, 2009).

3.2 Numerical approach to the hyperbolic systems

In order to solve hyperbolic systems of conservation laws, many numerical efforts have been made. Among them the Godunov method which is proposed in Godunov (1959). The method is basically developed to solve numerically the non-linear Euler equations for compressible flows by utilizing the solution of local Riemann problems on finite volumes. By which the Godunov method gives better results for discontinuous solutions than classical finite difference methods.

3.2.1 Godunov method

Consider the following hyperbolic systems of conservation laws:

$$q_t + f(q)_x = 0, \quad (3.13)$$

with the initial data:

$$q(x, 0) = q_0(x) = \begin{cases} q_i^n & \text{if } x \leq x_{i+1/2}, \\ q_{i+1}^n & \text{if } x > x_{i+1/2}. \end{cases} \quad (3.14)$$

This is a local Riemann problem at intercell boundary $x_{i+1/2}$ with the given initial data at a given time level n . The solution of the global problem is found at a later time level $n + 1$ by solving two local Riemann problems for each cell i . Take an integral average of the combined solutions of these two local problems in this cell and assign the value to u^{n+1} . Assuming that the computational domain is discretised in space and time on the x - t plane using a regular mesh size of Δx and time step of Δt . Consider a numerical solution $Q_i^n \in \mathbb{R}^m$ that is related to the point (x_i, t^n) where:

$$x_i = i\Delta x, \quad i \in \mathbb{Z},$$

$$t^n = n\Delta t, \quad n \in \mathbb{N}_0.$$

The Godunov method assumes a piecewise constant data $\tilde{q}(x_i, t^n)$ to be defined by the approximation Q_i^n as follows:

$$Q_i^n = \frac{1}{\Delta x} \int_{x_{i-1/2}}^{x_{i+1/2}} \tilde{q}(x, t^n) dx, \quad (3.15)$$

which produces the required piecewise constant distribution on the grid cell i at time t^n :

$$Q_i^n = \tilde{q}(x, t^n), \quad x_{i-1/2} \leq x < x_{i+1/2}, \quad (3.16)$$

where $x_{i\pm 1/2} = (i \pm 1/2)\Delta x$. Consider the above initial data (3.16) with the following conservation law:

$$\tilde{q}_t + f(\tilde{q})_x = 0, \quad (3.17)$$

assuming that $\tilde{q}(x, t)$ is an exact solution to (3.17). The integration over the rectangle $[x_{i-1/2}, x_{i+1/2}] \times [t^n, t^{n+1}]$ gives:

$$\begin{aligned} \int_{x_{i-1/2}}^{x_{i+1/2}} \tilde{q}(x, t^{n+1}) dx &= \int_{x_{i-1/2}}^{x_{i+1/2}} \tilde{q}(x, t^n) dx \\ &+ \int_{t^n}^{t^{n+1}} f(\tilde{q}(x_{i-1/2}, t)) dt - \int_{t^n}^{t^{n+1}} f(\tilde{q}(x_{i+1/2}, t)) dt. \end{aligned} \quad (3.18)$$

Dividing by Δx and setting the approximate solution Q_i^{n+1} at time t^{n+1} :

$$Q_i^{n+1} = \frac{1}{\Delta x} \int_{x_{i-1/2}}^{x_{i+1/2}} \tilde{q}(x, t^{n+1}) dx,$$

the left intercell numerical flux function is:

$$F(Q_{i-1}^n, Q_i^n) = \frac{1}{\Delta t} \int_{t^n}^{t^{n+1}} f(\tilde{q}(x_{i-1/2}, t)) dt,$$

and the right intercell numerical flux function is:

$$F(Q_i^n, Q_{i+1}^n) = \frac{1}{\Delta t} \int_{t^n}^{t^{n+1}} f(\tilde{q}(x_{i+1/2}, t)) dt.$$

Then the following scheme is obtained:

$$Q_i^{n+1} = Q_i^n - \frac{\Delta t}{\Delta x} [F(Q_i^n, Q_{i+1}^n) - F(Q_{i-1}^n, Q_i^n)]. \quad (3.19)$$

The right intercell numerical flux $F(Q_i^n, Q_{i+1}^n)$ is computed at the cell boundary $x_{i+1/2}$ by solving the first Riemann problem defined by (3.17) with the following initial data:

$$\tilde{q}(x, t^n) = \begin{cases} Q_i^n & \text{if } x \leq x_{i+1/2}, \\ Q_{i+1}^n & \text{if } x > x_{i+1/2}. \end{cases} \quad (3.20)$$

It is clear that the exact solution of the Riemann problem at this boundary depends only on the data Q_i^n and Q_{i+1}^n . If we refer to this value by $q^*(Q_i^n, Q_{i+1}^n)$, then the right flux may be written as:

$$F(Q_i^n, Q_{i+1}^n) = f(q^*(Q_i^n, Q_{i+1}^n)).$$

Similarly for the left intercell numerical flux $F(Q_{i-1}^n, Q_i^n)$ is computed at the cell boundary $x_{i-1/2}$ by solving the second Riemann problem defined by (3.17) with the following initial data:

$$\tilde{q}(x, t^n) = \begin{cases} Q_{i-1}^n & \text{if } x \leq x_{i-1/2}, \\ Q_i^n & \text{if } x > x_{i-1/2}. \end{cases} \quad (3.21)$$

Then the Godunov scheme may be written in a conservative form as:

$$Q_i^{n+1} = Q_i^n - \frac{\Delta t}{\Delta x} [f(q^*(Q_i^n, Q_{i+1}^n)) - f(q^*(Q_{i-1}^n, Q_i^n))]. \quad (3.22)$$

The solution of the Riemann problem at each cell interface $i \pm 1/2$ is self-similar. In order to insure that the solution preserves the self-similar character, the solution of the first Riemann problem must not be influenced by the solution of the second Riemann problem by satisfying the following condition:

$$\left| \frac{\Delta t}{\Delta x} \lambda_p(Q_i^n) \right| \leq 1, \quad (3.23)$$

where $\lambda_p(Q_i^n) = \mathbf{max}(\lambda_1(Q_i^n), \dots, \lambda_m(Q_i^n))$ are the eigenvalues of the Jacobian matrix of the system (3.17). This condition (3.23) is very important to insure stability of the method and called the Courant number or CFL number.

The original Godunov scheme (3.22) requires only determining the exact solution $f(q^*(Q_L^n, Q_R^n))$ to the Riemann problem at cell boundary based on Riemann data Q_L and Q_R . To find out where q^* lies in state space, the full wave structure and wave speeds must be determined. Computing the exact solution of the Riemann problem is often quite expensive, even though very little information from solving the Riemann problem are used in defining the flux. This has led researchers to develop a wide variety of *approximate Riemann solvers* that can be employed more cheaply than the exact Riemann solver and yet the obtained results in many cases are equally good when implemented in the Godunov-type or high resolution methods (LeVeque, 2004; Toro, 2009). In this work, the HLL, HLLC and VFRoe approximate Riemann solvers have been extended to solve the seven and six equation two-phase flow models.

3.2.2 The HLL approximate Riemann solver

A simple approximate Riemann solver proposed by Harten Lax and van Leer (HLL). This solver which is presented in Harten, Lax and van Leer (1983) is based on a minimum S^- and maximum S^+ wave speeds arising in the Riemann solution. The solver uses a single intermediate state (*) enclosed between these two waves. Hence these waves will divide the characteristic fields into three different states as follows:

$$Q_{i\pm 1/2} = \begin{cases} Q_L & \text{if } 0 \leq S_{i\pm 1/2}^-, \\ Q^{hll} & \text{if } S_{i\pm 1/2}^- \leq 0 \leq S_{i\pm 1/2}^+, \\ Q_R & \text{if } 0 \geq S_{i\pm 1/2}^+. \end{cases} \quad (3.24)$$

where:

$$Q^{hll} = \frac{S_{i\pm 1/2}^+ Q_R - S_{i\pm 1/2}^- Q_L + F_L - F_R}{S_{i\pm 1/2}^+ - S_{i\pm 1/2}^-}, \quad (3.25)$$

and the corresponding HLL fluxes along the cell boundaries are given by:

$$F_{i\pm 1/2}^{hll} = \begin{cases} F_L & \text{if } 0 \leq S_{i\pm 1/2}^-, \\ F^{hll} & \text{if } S_{i\pm 1/2}^- \leq 0 \leq S_{i\pm 1/2}^+, \\ F_R & \text{if } 0 \geq S_{i\pm 1/2}^+. \end{cases} \quad (3.26)$$

where:

$$F^{hll} = \frac{S_{i\pm 1/2}^+ F_L - S_{i\pm 1/2}^- F_R + S_{i\pm 1/2}^- S_{i\pm 1/2}^+ (Q_R - Q_L)}{S_{i\pm 1/2}^+ - S_{i\pm 1/2}^-}. \quad (3.27)$$

The flux of the intermediate state (3.27) is obtained from combining results of applying Rankine-Hugoniot conditions across the left $S_{i\pm 1/2}^-$ and right $S_{i\pm 1/2}^+$ waves, respectively. One can note that, see Figure 3.2 which shows the general case for the Euler equations, the HLL solver ignores all intermediate waves separating other intermediate states and lump them into a single state Q^{hll} known as a *Star Region*. This is considered as a shortcoming of the HLL solver as it ignores contact discontinuities and material interfaces especially when the solution of the Riemann problem contains more than two waves (Toro, 2009).

3.2.3 The HLLC approximate Riemann solver

This solver is introduced by Toro, Spruce and Speares (1994) as an improvement to the HLL approximate Riemann solver to restore the missing waves at the star region. The restored wave is the contact wave which divides the star region into two regions. This solver known as the HLLC approximate Riemann solver where C stands for the restored contact wave. By restoring the missing wave at the star region this solver should be more accurate than the HLL Riemann solver. The HLLC flux along the

cell boundaries are given by:

$$F_{i\pm 1/2}^{hllc} = \begin{cases} F_L & \text{if } 0 \leq S_{i\pm 1/2}^-, \\ F_{*L} = F_L + S_{i\pm 1/2}^-(Q_{*L} - Q_L) & \text{if } S_{i\pm 1/2}^- \leq 0 \leq S^*, \\ F_{*R} = F_R + S_{i\pm 1/2}^+(Q_{*R} - Q_R) & \text{if } S^* \leq 0 \leq S_{i\pm 1/2}^+, \\ F_R & \text{if } 0 \geq S_{i\pm 1/2}^+, \end{cases}, \quad (3.28)$$

where Q_{*R} and Q_{*L} at the star region are obtained as:

$$Q_{*K} = \rho_K \left(\frac{S_K - u_K}{S_K - S^*} \right) \left[\begin{array}{c} 1 \\ S^* \\ \left(\frac{E_K}{\rho_K} + (S^* - u_K) \left[S^* + \frac{p_K}{\rho_K(S_K - u_K)} \right] \right) \end{array} \right], \quad (3.29)$$

where the speed of the middle wave in the star region can be written as:

$$S^* = \frac{p_R - p_L + \rho_L u_L (S^- - u_L) - \rho_R u_R (S^+ - u_R)}{\rho_L (S^- - u_L) - \rho_R (S^+ - u_R)}. \quad (3.30)$$

3.2.4 The VFRoe approximate Riemann solver

This approach was introduced by Gallouët and Masella (1996). Consider the Riemann problem of a hyperbolic system written in terms of primitive variables \mathbf{w} as follows:

$$\frac{\partial \mathbf{w}}{\partial t} + A(\mathbf{w}) \frac{\partial \mathbf{w}}{\partial x} = 0,$$

with the following initial data:

$$\mathbf{w}(x, 0) = \begin{cases} \mathbf{w}_L & x \leq 0, \\ \mathbf{w}_R & x > 0. \end{cases} \quad (3.31)$$

where $A(\mathbf{w})$ is the Jacobian matrix $m \times m$ calculated in the average state:

$$\bar{\mathbf{w}} = \frac{\mathbf{w}_L + \mathbf{w}_R}{2}. \quad (3.32)$$

The intermediate state in the solution of the Riemann problem is:

$$\mathbf{w}^* = \mathbf{w}_L + \sum_{\lambda_i < 0} a_i \mathbf{K}_i, \quad (3.33)$$

where λ_i and \mathbf{K}_i are the eigenvalues and the corresponding eigenvectors of the matrix $A(\bar{\mathbf{w}})$, respectively. The coefficients a_i are the coefficients of eigenvector decomposition of $\mathbf{w}_R - \mathbf{w}_L$ and are determined by:

$$\mathbf{w}_R - \mathbf{w}_L = \sum_{i=1}^m a_i \mathbf{K}_i. \quad (3.34)$$

3.2.5 Boundary conditions

As mentioned earlier, the solutions of the Riemann problem at boundaries of the cell i depend on the neighbouring cell state values \mathbf{w}_{i-1}^n and \mathbf{w}_{i+1}^n , which are required to compute the fluxes $F_{i-1/2}^n$ and $F_{i+1/2}^n$. Consequently, in order to solve the Riemann problem and corresponding fluxes at the left and right boundaries of the computational domain \mathbf{w}_1^n and \mathbf{w}_N^n , respectively, it is required to specify the inflow and outflow boundary conditions at each time step. This is done by adding fictitious cells \mathbf{w}_0^n and \mathbf{w}_{N+1}^n at both boundaries. Various types of boundary conditions are given in LeVeque (2004); Toro (2009). Here, only three types are considered that are the reflective, extrapolated and periodic boundary conditions and they are as follows:

1. Reflective boundary conditions:

This type of boundary conditions is applied when the boundary is a fixed impermeable wall. Consider the boundary at the leftmost of the domain $x = 0$, the fictitious state \mathbf{w}_0^n . The Riemann problem will be solved between \mathbf{w}_0^n and \mathbf{w}_1^n . The state \mathbf{w}_0^n is defined from the known state \mathbf{w}_1^n inside the computational domain as follows:

$$\mathbf{w}_0^n = \mathbf{w}_1^n, \quad (3.35)$$

except for the velocity which is given as $u_0^n = -u_1^n$. For the rightmost boundary of the domain at $x = L$, the fictitious state \mathbf{w}_{N+1}^n is defined as:

$$\mathbf{w}_{N+1}^n = \mathbf{w}_N^n \quad (3.36)$$

except for the velocity which is given as $u_{N+1}^n = -u_N^n$.

2. Extrapolated boundary conditions:

This type of boundary condition is known as transmissive or transparent or far field or non-reflecting boundary condition which can be applied when the boundary of the computational domain is an open end. There are two types of this boundary conditions which can be applied to obtain the state in the fictitious cells:

(a) Zero-order extrapolation:

Consider the leftmost boundary at $x = 0$, the states in the fictitious cell are given by:

$$\mathbf{w}_0^n = \mathbf{w}_1^n, \quad (3.37)$$

and at the rightmost boundary are given by:

$$\mathbf{w}_{N+1}^n = \mathbf{w}_N^n. \quad (3.38)$$

(b) **First-order extrapolation:**

Consider the leftmost boundary at $x = 0$, the states in the fictitious cell are given by:

$$\mathbf{w}_0^n = 2\mathbf{w}_1^n - \mathbf{w}_2^n, \quad (3.39)$$

and at the rightmost boundary are given by:

$$\mathbf{w}_{N+1}^n = 2\mathbf{w}_N^n - \mathbf{w}_{N-1}^n. \quad (3.40)$$

3. **Periodic boundary conditions:**

This type of boundary conditions is applied when it is required to simulate a large system or a system with a repeated manner. A small part of the system is used with imposing these boundary conditions. The states in the fictitious cell at the leftmost boundary $x = 0$ are given by:

$$\mathbf{w}_0^n = \mathbf{w}_N^n, \quad (3.41)$$

and at the rightmost boundary $x = L$ are given by:

$$\mathbf{w}_{N+1}^n = \mathbf{w}_1^n. \quad (3.42)$$

Chapter 4

The seven-equation compressible multiphase flow model

In order to study multiphase or multi-component flows governing mathematical models are needed. Usually, they are in the form of *mass*, *momentum* and *energy* equations. Several approaches and models have been proposed to predict the detailed complex behaviour of such flows. Nevertheless, there are significant differences in the application of these models to various types of multiphase or multi-component flows. In this chapter the seven-equation model of Saurel and Abgrall (1999a) is described, closure relations and various EOSs casted in the form of Mie-Grüneisen EOS are given. The mathematical structure of this model is determined, the numerical method which is implemented with various Riemann solvers to solve the seven-equation model is presented. The numerical results are verified using different EOSs, comparisons between solvers are carried out and finally comparisons between EOSs are accomplished.

4.1 Mathematical formulation

The local instant formulation based on the single-phase equations encounters mathematical and numerical difficulties for most two-phase flow problems with moving interfaces. Therefore, it is not a reasonable or practical approach. This has made it essential to use a macroscopic formulation based on a suitable averaging method which eliminates the interfacial discontinuities and gives a two-phase flow a continuum formulation (Ishii and Hibiki, 2006). There are many types of averaging procedures which can be found in the literature, for example, time averaging, volume averaging and ensemble averaging (Drew and Passman, 1998; Ishii and Hibiki, 2006). The most commonly used procedures among them are the time and volume averaging. In some situations, the above mentioned procedures are special cases of the ensemble average (Drew and Passman, 1998). However, they lead to averaged

equations with essentially the same structure.

Starting from the Navier-Stokes equations for single-phase a compressible two-phase flow model can be obtained by applying the averaging method of Drew (1983) and neglecting all dissipative terms everywhere except at the interfaces. Using this approach Saurel and Abgrall (1999a) developed a two-phase flow model to simulate multiphase mixtures and interface problems between pure fluids. This model was inspired by the model of Baer and Nunziato (1986) which is proposed to investigate the deflagration-to-detonation transition in solid energetic materials. Saurel and Abgrall (1999a) modified the Baer and Nunziato model by introducing a different treatment of interfacial variables and relaxation parameters. These modifications extended the range of applications of the original Baer and Nunziato model. The obtained multiphase flow equations in one dimension have the following compact form:

$$\frac{\partial \alpha_k \rho_k}{\partial t} + \frac{\partial \alpha_k \rho_k u_k}{\partial x} = \pm \dot{m}_k, \quad (4.1a)$$

$$\begin{aligned} \frac{\partial \alpha_k \rho_k u_k}{\partial t} + \frac{\partial (\alpha_k \rho_k u_k^2 + \alpha_k p_k)}{\partial x} = \\ \pm p_{int} \frac{\partial \alpha_k}{\partial x} \pm \dot{m}_k u_{int} \pm F_{dk} \pm \alpha_k \rho_k g, \end{aligned} \quad (4.1b)$$

$$\begin{aligned} \frac{\partial \alpha_k \rho_k E_k}{\partial t} + \frac{\partial (\alpha_k \rho_k E_k u_k + \alpha_k u_k p_k)}{\partial x} = \\ \pm p_{int} u_{int} \frac{\partial \alpha_k}{\partial x} \pm Q_{kint} \pm \dot{m}_k E_{kint} \pm u_{int} F_{dk}, \\ \pm \mu p_{int} (p_k - p_{k'}) \pm \alpha_k \rho_k g u_k. \end{aligned} \quad (4.1c)$$

The average conditions for the interface are:

$$\sum_k \dot{m}_k = 0, \quad (4.2a)$$

$$\sum_k p_{int} \frac{\partial \alpha_k}{\partial x} + \dot{m}_k u_{int} + F_{dk} + \alpha_k \rho_k g = 0, \quad (4.2b)$$

$$\begin{aligned} \sum_k p_{int} u_{int} \frac{\partial \alpha_k}{\partial x} + Q_{kint} + \dot{m}_k E_{kint} + \\ u_{int} F_{dk} + \alpha_k \rho_k g u_k - \mu p_{int} (p_k - p_{k'}) = 0, \end{aligned} \quad (4.2c)$$

where: α_k , ρ_k , u_k , p_k , E_k , are the volume fraction, the density, the velocity, the pressure and the total energy for the phase k , respectively; k' is the other phase; p_{int} , u_{int} are the interfacial pressure and velocity, respectively; g is the gravitational force. The interaction terms are written in the form of mass transfer \dot{m}_k , drag force F_{dk} , heat transfer Q_{kint} and the non-conservative terms $p_{int} \frac{\partial \alpha_k}{\partial x}$ and $p_{int} u_{int} \frac{\partial \alpha_k}{\partial x}$. These are coupling terms and therefore if it has a plus sign, the same term has a minus

sign for the other phase. The total energy E_k is represented by:

$$E_k = e_k + \frac{1}{2}v_k^2, \quad (4.3)$$

where e_k is the specific internal energy of the phase k and:

$$\frac{1}{2}v_k^2 = \frac{1}{2}(u_k^2 + v_k^2 + w_k^2). \quad (4.4)$$

The non-conservative terms which appear on the right hand side of the momentum and energy equations of the model (4.1) result from the averaging process. These terms prevent the model from being written in the divergence form, i.e. conservative form. Consequently, the model (4.1) is a non-conservative model, hence, the weak solution and the Rankine-Hugoniot conditions (3.7) for conservation laws are not applicable (Andrianov, Saurel and Warnecke, 2003).

As a remedy for the non-conservative character of the governing equations it is important to consider the Abgrall's idea (Abgrall, 1996). It states that if the flow is initially uniform in terms of pressure and velocity fields, its time evolution should preserve a contact discontinuity. It was shown by Andrianov, Saurel and Warnecke (2003) that the contact discontinuity is preserved only when the right hand side non-conservative terms are present in the system. These terms may cause some difficulty when dealing with mass transfer problems in the presence of shock waves (Saurel and Le Métayer, 2001).

The last term on the right hand side of the momentum (4.1b) and energy (4.1c) equations is related to the gravitational force. The effect of the gravitational force is not taken into account in the shock tube test but its effect is considered in the water faucet test. These tests are studied in this thesis.

The model (4.1) is not closed. In other words the number of unknowns are more than the number of equations. Therefore, in order to solve the model (4.1) more closure relations or some other assumptions are needed.

4.1.1 Closure relations

Extra terms appear in the model (4.1) due to the averaging process used in its derivation. These terms represent the transfer processes that may take place at the interface and they are unknown. Moreover, new variables which are known as void or volume fraction for each constituent appear in the model (4.1). These variables indicate the presence of each phase within the computational cell. The two-phase flow model (4.1) consists of two mass equations (4.1a), two momentum equations (4.1b) and two energy equations (4.1c). These are six equations which are less than the number of the unknown variables which are twelve. Thus, to close the system (4.1) the following closure relations are considered:

1. Adding an evolutionary equation for the volume fraction for one of the phases which is proposed by Ishii (1975) and considered by other researchers (see for example, Baer and Nunziato, 1986). This equation may be written as:

$$\frac{\partial \alpha_a}{\partial t} + u_a \frac{\partial \alpha_a}{\partial x} = f_a(S_a, S_b) \quad (4.5)$$

where: u_a is the velocity of the phase a (in Baer and Nunziato (1986) phases a, b are considered to be the solid and gas phases, respectively) and $f_a(S_a, S_b)$ is the source term.

2. The volume fraction constraint which indicates the saturation of the phases within the computational cell. It may be written as:

$$\sum_k \alpha_k = 1. \quad (4.6)$$

3. Equations of state are used to couple the thermodynamic variables within each phase. The ability of this model to deal with different EOSs is a great advantage of this model. Various equations of state have been considered in this work and they are given in section 4.2.
4. The interfacial pressure relation. This has been considered in different forms:

- (a) The interfacial pressure (see for example, Stewart and Wendroff, 1984) is assumed to be in equilibrium with the pressure of both phases as follows:

$$p_{int} = p_1 = p_2.$$

This closure leads to an ill-posed model and thus numerical difficulty due to the complex characteristics which results in numerical instabilities in the solution. Moreover, the pressure wave propagation is not described correctly. Many attempts have been made to circumvent numerical instabilities resulting from this approach, either by adding numerical viscosity to reduce instabilities or by adding some correction terms to eliminate the complex characteristics (see for example, Toumi and Raymond, 1995; Tiselj and Petelin, 1997). However, adding large numerical viscosity produces unrealistic solutions (Saurel and Le Métayer, 2001).

- (b) The interfacial pressure (see for example, Baer and Nunziato, 1986) is assumed to be equal to the pressure of the gas phase:

$$p_{int} = p_1.$$

- (c) Another closure for the interfacial pressure is given in Saurel, Gavriluyk and Renaud (2003) and may be written as follows:

$$p_{int} = \frac{Z_1 p_2 + Z_2 p_1}{Z_1 + Z_2} + \frac{Z_1 Z_2}{Z_1 + Z_2} \frac{\nabla \alpha_1}{|\nabla \alpha_1|} \cdot (u_2 - u_1),$$

where Z_k is the acoustic impedance is given by:

$$Z_k = \rho_k c_k, \quad k = 1, 2.$$

where c_k is the speed of sound for the phase k which is defined in Saurel and Abgrall (1999a) as:

$$c_k^2 = \frac{\left. \frac{p_k}{\rho_k^2} - \frac{\partial e_k}{\partial \rho_k} \right|_{p_k}}{\left. \frac{\partial e_k}{\partial p_k} \right|_{\rho_k}}. \quad (4.7)$$

- (d) The interfacial pressure is assumed to be equal to the mixture pressure (Saurel and Abgrall, 1999a). This assumption is adopted in this thesis, as follows:

$$p_{int} = \sum_k p_k \alpha_k. \quad (4.8)$$

5. The interfacial velocity relation. This has been considered in different forms:

- (a) The interfacial velocity is assumed to be equal to the velocity of the solid phase as chosen by Baer and Nunziato (1986):

$$u_{int} = u_1.$$

- (b) The interfacial velocity is also derived by Saurel, Gavriluyk and Renaud (2003) and may be written as follows:

$$u_{int} = \frac{Z_1 u_1 + Z_2 u_2}{Z_1 + Z_2} + \frac{p_2 - p_1}{Z_1 + Z_2} \frac{\nabla \alpha_1}{|\nabla \alpha_1|}.$$

- (c) The mixture velocity at the interface in this thesis is adopted as in Saurel and Abgrall (1999a) which is given by:

$$u_{int} = \frac{\sum_k \alpha_k \rho_k u_k}{\sum_k \alpha_k \rho_k}. \quad (4.9)$$

4.1.2 Fully non-equilibrium two-phase flow mathematical model

The fully non-equilibrium two-phase flow model which is known as the Saurel and Abgrall (1999a) model. The model is obtained by adding the volume fraction evolutionary equation (4.5) to the system (4.1). All dissipative terms, i.e. the viscosity, the surface tension, the heat and mass transfer, etc., are neglected everywhere except at the interfaces. This model, in each pure fluid zone, takes the form of time-dependent Euler equations which are a set of non-linear hyperbolic conservation laws that describe the compressible multiphase flows (Saurel and Abgrall, 1999a). This model, which is considered in this work, for one-dimensional flows with the relaxation and source terms takes the following form:

$$\frac{\partial \alpha_1}{\partial t} + u_{int} \frac{\partial \alpha_1}{\partial x} = \mu(p_1 - p_2), \quad (4.10a)$$

$$\frac{\partial \alpha_1 \rho_1}{\partial t} + \frac{\partial \alpha_1 \rho_1 u_1}{\partial x} = 0, \quad (4.10b)$$

$$\frac{\partial \alpha_1 \rho_1 u_1}{\partial t} + \frac{\partial (\alpha_1 \rho_1 u_1^2 + \alpha_1 p_1)}{\partial x} = p_{int} \frac{\partial \alpha_1}{\partial x} + \lambda(u_2 - u_1) + \alpha_1 \rho_1 g, \quad (4.10c)$$

$$\begin{aligned} \frac{\partial \alpha_1 \rho_1 E_1}{\partial t} + \frac{\partial (\alpha_1 \rho_1 E_1 u_1 + \alpha_1 u_1 p_1)}{\partial x} &= p_{int} u_{int} \frac{\partial \alpha_1}{\partial x} + \\ &u_{int} \lambda(u_2 - u_1) + p_{int} \mu(p_1 - p_2) + \alpha_1 \rho_1 g u_1, \end{aligned} \quad (4.10d)$$

$$\frac{\partial \alpha_2 \rho_2}{\partial t} + \frac{\partial \alpha_2 \rho_2 u_2}{\partial x} = 0, \quad (4.10e)$$

$$\frac{\partial \alpha_2 \rho_2 u_2}{\partial t} + \frac{\partial (\alpha_2 \rho_2 u_2^2 + \alpha_2 p_2)}{\partial x} = -p_{int} \frac{\partial \alpha_1}{\partial x} - \lambda(u_2 - u_1) + \alpha_2 \rho_2 g, \quad (4.10f)$$

$$\begin{aligned} \frac{\partial \alpha_2 \rho_2 E_2}{\partial t} + \frac{\partial (\alpha_2 \rho_2 E_2 u_2 + \alpha_2 u_2 p_2)}{\partial x} &= -p_{int} u_{int} \frac{\partial \alpha_1}{\partial x} - \\ &u_{int} \lambda(u_2 - u_1) - p_{int} \mu(p_1 - p_2) + \alpha_2 \rho_2 g u_2. \end{aligned} \quad (4.10g)$$

In addition to the closure relations mentioned in section 4.1.1. It is necessary to restore the boundary conditions at the interface. To achieve this goal the pressures p_1 and p_2 and velocities v_1 and v_2 are relaxed to the common values at the interface. The relaxation process is restricted to the right hand side terms of the model (4.10). These terms are called pressure relaxation and velocity relaxation terms.

Pressure relaxation terms

Pressure relaxation terms in the volume fraction evolution equation (4.10a) and in the energy equations (4.10d) and (4.10g) in the system (4.10) are given by $\mu(p_1 - p_2)$ and $\mu p_{int}(p_1 - p_2)$, respectively. The former term expresses the expansion rate of the volume fraction which drives the pressure to equilibrium. The latter term expresses the pressure work done by the phases to achieve the pressure equilibrium. This rate

is controlled by the variable μ . This variable depends on the compressibility of each phase, and on the mixture topology. It has finite value in two-phase regions, and grows to be infinite at the interface to enable the pressure relaxation process to take place faster (Saurel and Abgrall, 1999a).

Velocity relaxation terms

The term $\lambda(u_2 - u_1)$ in equations (4.1b) and (4.1c) represents the velocity relaxation term. The velocity relaxation terms are responsible for bringing the relaxed velocity of both fluids to a common value that fulfil the interfacial velocity conditions between fluids. The parameter λ controls the rate at which the velocities of both fluids reach the equilibrium state. More details are given in Saurel and Abgrall (1999a) and Saurel and Le Métayer (2001).

The simultaneous pressure and velocity relaxation processes have made the parent model applicable for a wide range of applications, for instance, simulations of interfaces separating phases, cavitating flows, detonation and so on.

4.1.3 The model with area variation source term

The equations (4.10) only apply to one dimensional problems. This section shows that the present model (4.10) can be easily extended to problems in regular two-dimensional geometries characterised by the symmetry line. These problems can be studied using axisymmetric approach to simplify the problem and to reduce the numerical simulation time. Therefore, the numerical simulations of compressible flow through converging-diverging nozzles with varying cross-sectional area A can be conducted by considering a quasi-linear one-dimensional model. The model

$$\frac{\partial \alpha_1}{\partial t} + u_{int} \frac{\partial \alpha_1}{\partial x} = \mu(p_1 - p_2), \quad (4.11a)$$

$$\frac{\partial \alpha_1 \rho_1}{\partial t} + \frac{\partial \alpha_1 \rho_1 u_1}{\partial x} = -\frac{1}{A} \frac{\partial A}{\partial x} \alpha_1 \rho_1 u_1, \quad (4.11b)$$

$$\frac{\partial \alpha_1 \rho_1 u_1}{\partial t} + \frac{\partial (\alpha_1 \rho_1 u_1^2 + \alpha_1 p_1)}{\partial x} = p_{int} \frac{\partial \alpha_1}{\partial x} + \lambda(u_2 - u_1) - \frac{1}{A} \frac{\partial A}{\partial x} \alpha_1 \rho_1 u_1^2, \quad (4.11c)$$

$$\begin{aligned} \frac{\partial \alpha_1 \rho_1 E_1}{\partial t} + \frac{\partial (\alpha_1 \rho_1 E_1 u_1 + \alpha_1 u_1 p_1)}{\partial x} &= p_{int} u_{int} \frac{\partial \alpha_1}{\partial x} + u_{int} \lambda(u_2 - u_1) + \\ & p_{int} \mu(p_1 - p_2) - \frac{1}{A} \frac{\partial A}{\partial x} \alpha_1 u_1 (\rho_1 E_1 + p_1), \end{aligned} \quad (4.11d)$$

$$\frac{\partial \alpha_2 \rho_2}{\partial t} + \frac{\partial \alpha_2 \rho_2 u_2}{\partial x} = -\frac{1}{A} \frac{\partial A}{\partial x} \alpha_2 \rho_2 u_2, \quad (4.11e)$$

$$\frac{\partial \alpha_2 \rho_2 u_2}{\partial t} + \frac{\partial (\alpha_2 \rho_2 u_2^2 + \alpha_2 p_2)}{\partial x} = -p_{int} \frac{\partial \alpha_1}{\partial x} - \lambda(u_2 - u_1) - \frac{1}{A} \frac{\partial A}{\partial x} \alpha_2 \rho_2 u_2^2, \quad (4.11f)$$

$$\begin{aligned} \frac{\partial \alpha_2 \rho_2 E_2}{\partial t} + \frac{\partial (\alpha_2 \rho_2 E_2 u_2 + \alpha_2 u_2 p_2)}{\partial x} &= -p_{int} u_{int} \frac{\partial \alpha_1}{\partial x} - u_{int} \lambda(u_2 - u_1) - \\ & p_{int} \mu(p_1 - p_2) - \frac{1}{A} \frac{\partial A}{\partial x} \alpha_2 u_2 (\rho_2 E_2 + p_2), \end{aligned} \quad (4.11g)$$

takes a different form from the original one by including an additional source term in the governing equations (4.10) to represent the area variation, which was used in a context of studying a reactor venting problems in Nowakowski, Librovich and Lue (2004). As a result the multiphase flow model with the area variation source and relaxation terms but without mass, heat transfer and gravitational terms takes the above form (4.11).

4.2 Equation of state (EOS)

An equation of state for each phase is needed to relate the pressure with the density and the internal energy i.e. $p = p(\rho, e)$ or $e = e(\rho, p)$. The seven-equation model is flexible and it can deal with different equations of state (EOSs) for each phase. In order to deal with problems with different types of EOSs, various EOSs are written in the general form of the Mie-Grüneisen EOS as follows:

$$p(\rho, e) = \rho \Gamma_{\mathcal{H}}(\rho)[e - e_{\mathcal{H}}(\rho)] + p_{\mathcal{H}}(\rho). \quad (4.12)$$

Where $\Gamma_{\mathcal{H}}(\rho)$ is the Grüneisen function, $e_{\mathcal{H}}(\rho)$ is the reference internal energy and $p_{\mathcal{H}}(\rho)$ is the reference pressure, they are material dependent functions which are obtained at a reference state (Fortov and Lomonosov, 2010). For some materials the Grüneisen function is a power law of density:

$$\Gamma_{\mathcal{H}}(\rho) = \Gamma \left(\frac{\rho_0}{\rho} \right)^{\theta}, \quad (4.13)$$

where Γ is the Grüneisen coefficient at reference density ρ_0 , θ is a coefficient which depends on the material (for most materials $\theta = 0$). The Grüneisen coefficient may be written as $\Gamma = \gamma - 1$, where γ is the adiabatic specific heat ratio depending on the material under consideration, $\gamma = c_p/c_v$. The parameters c_p and c_v are the specific heats at constant pressure and volume, respectively.

The reference curve for $(e_{\mathcal{H}}, p_{\mathcal{H}})$ may be taken along an isentropic locus or a Hugoniot locus. When the flow is considered without presence of viscosity, heat transfer and shock waves the reference curve may be chosen as an isentrope (Menikoff and Plohr, 1989). The reference functions for various EOSs, defined in the following subsections from 4.2.1 to 4.2.7, are listed in Table 4.2. Zheng et al. (2011) attempted to construct a common framework for the general EOS although their approach was different.

Using the reference functions that are listed in Table 4.2 it is now possible to simulate a wide range of applications with various EOSs without the need to modify the algorithm. For example Petitpas et al. (2007) pointed out that in order to deal with complex EOSs they need to make several modifications in their algorithm.

4.2.1 Ideal gas (IG) EOS

In the caloric ideal gas EOS, the pressure has the form:

$$p = (\gamma - 1)\rho e. \quad (4.14)$$

By writing the ideal gas EOS (4.14) in the form of Mie-Grüneisen EOS (4.12), the reference material dependent functions are as given in Table 4.2. The adiabatic specific heat ratio for an ideal gas could also be calculated by the relation:

$$\gamma = \frac{m + 2}{m},$$

where m states the degrees of freedom of a molecule. It takes the value $m = 3$ for monatomic gases and $m = 5$ for diatomic gases.

To derive the local speed of sound for gases governed by the ideal gas EOS (4.14), the derivatives of the internal energy with respect to the density and pressure are obtained and then substituted into (4.7). Finally, the local speed of sound can be written as:

$$c^2 = \sqrt{\frac{\gamma p}{\rho}}. \quad (4.15)$$

These derivatives are also substituted into the following formula (Saurel and Abgrall, 1999a):

$$c_{kint}^2 = \frac{\frac{p_{int}}{\rho_k^2} - \frac{\partial e_k}{\partial \rho_k} \Big|_{p_k}}{\frac{\partial e_k}{\partial p_k} \Big|_{\rho_k}}, \quad (4.16)$$

to obtain the sound speed at the interface which may be written as follows:

$$c_{int}^2 = \frac{p_{int}(\gamma - 1) + p}{\rho}. \quad (4.17)$$

4.2.2 Shock wave (SW) EOS

This equation of state consists of the Mie-Grüneisen EOS (4.12) and:

$$U_s = c_0 + sU_p, \quad (4.18)$$

which is a linear fit for the shock velocity U_s as a function of the particle velocity U_p , c_0 is the speed of sound in the material under consideration at atmospheric conditions and s is a dimensionless parameter. Experimental data for high pressure values are available for many materials in Marsh (1980). Often the reference curve for $(p_{\mathcal{H}}, e_{\mathcal{H}})$ is chosen to fit the experimental data. This curve is a single shock Hugoniot locus and starts from an initial state at standard pressure and temperature or internal energy (p_0, e_0) . Using the Hugoniot jump conditions the shock state can

be determined by calculating $(p_{\mathcal{H}}, e_{\mathcal{H}})$ given in Table 4.2. For the shock wave EOS the local speed of sound is derived, as given in the Appendix A.1, to be as follows:

$$c^2 = \left(\frac{p}{\rho^2} - \frac{-\frac{\rho_o^2 c_o^2}{\rho^2 \eta^2} - \frac{2\rho_o^2 c_o^2 s \psi}{\rho^2 \eta^3}}{\zeta} - \frac{(p - \frac{\rho_o c_o^2 \psi}{\eta^2})\theta}{\zeta \rho} + \frac{p - \frac{\rho_o c_o^2 \psi}{\eta^2}}{\zeta \rho} - \frac{\rho_o c_o^2 \psi}{\eta^2 \rho^2} - \frac{\rho_o c_o^2 s \psi^2}{\eta^3 \rho^2} \right) \zeta, \quad (4.19)$$

where $\eta = 1 - s\psi$, $\psi = 1 - \frac{\rho_o}{\rho}$ and $\zeta = \rho \Gamma \left(\frac{\rho_o}{\rho} \right)^\theta$, and the speed of sound at the interface is found to be:

$$c_{int}^2 = \left(\frac{p_{int}}{\rho^2} - \frac{-\frac{\rho_o^2 c_o^2}{\rho^2 \eta^2} - \frac{2\rho_o^2 c_o^2 s \psi}{\rho^2 \eta^3}}{\zeta} - \frac{(p - \frac{\rho_o c_o^2 \psi}{\eta^2})\theta}{\zeta \rho} + \frac{p - \frac{\rho_o c_o^2 \psi}{\eta^2}}{\zeta \rho} - \frac{\rho_o c_o^2 \psi}{\eta^2 \rho^2} - \frac{\rho_o c_o^2 s \psi^2}{\eta^3 \rho^2} \right) \zeta. \quad (4.20)$$

4.2.3 Stiffened gas (SG) EOS

The stiffened gas EOS (Menikoff and Plohr, 1989) can be used to obtain the behaviour of gases, liquids and compressible solids. The pressure has the form:

$$p = (\gamma - 1)\rho e - \gamma\pi, \quad (4.21)$$

where the parameters γ and π are constants that depend on the particular material under consideration. These parameters can be determined following the procedure given in Cocchi, Saurel and Loraud (1996) for various materials using the experimental data given in Marsh (1980) for example. It can be noticed that if the pressure constant $\pi = 0$, the SG EOS reduces to the ideal gas EOS. By writing the SG EOS (4.21) in the form of the Mie-Grüneisen EOS (4.12), the reference material dependent functions are as given in Table 4.2. The speed of sound in the pure phase and at the interface for materials governed by the SG EOS are obtained as described in subsection 4.2.1. The speed of sound in the pure phase may be written as:

$$c^2 = \frac{\gamma(p + \pi)}{\rho}, \quad (4.22)$$

and at the interface is as follows:

$$c_{int}^2 = \frac{p_{int}(\gamma - 1) + p + \gamma\pi}{\rho}. \quad (4.23)$$

Determination of SG EOS parameter

The SG EOS (4.21) parameters are determined using experimental results. The following relation which relates shock velocity U_s with material velocity U_p is obtained from Hugoniot relations and the SG EOS (Cocchi, Saurel and Loraud, 1996):

$$U_s = \sqrt{c_0^2 + \left(\frac{\gamma+1}{4}U_p\right)^2} + \frac{\gamma+1}{4}U_p, \quad (4.24)$$

where c_0 is the speed of sound in the material under consideration. The above relation is used to determine the parameter γ , the following relation is used to determine the value of π for liquids and solids:

$$\pi = \frac{\rho_0 c_0^2}{\gamma} - p_0, \quad (4.25)$$

where ρ_0 is the material initial density and p_0 is the ambient pressure. The determined SG EOS parameters for some selected materials are given Table 4.1. These values are used to validate the six and seven-equation models in subsection 5.5.1.

Table 4.1: SG EOS parameters for selected materials.

Material	ρ_0 [kg/m ³]	c_0 [m/s]	s	γ	π [Pa]
Iron	7873	3742.4	1.594	3.657	$3.02 \cdot 10^{10}$
Nickel	8875	4590	1.44	3.98	$4.7 \cdot 10^{10}$
Copper	8924	3910	1.51	4.016	$3.4 \cdot 10^{10}$
S. steel 304	7890	4564.6	1.496	4.167	$3.95 \cdot 10^{10}$

4.2.4 Tait's EOS

This EOS is used to govern liquids. It is particularly used for water and it can be written in the following form:

$$p_k = A \left(\frac{\rho}{\rho_o} \right)^\gamma - B, \quad (4.26)$$

where A, B and γ are constant parameters depending on the fluid under consideration. For water these parameters are $A \approx B = 3.31 \times 10^8$ Pa, $\gamma = 7.15$.

Its analogue as given in Ivings, Causon and Toro (1998) and Zheng et al. (2011) is written as follows:

$$p_k = (\gamma - 1)\rho e - \gamma B. \quad (4.27)$$

By writing Tait's EOS (4.27) in the form of the Mie-Grüneisen EOS (4.12) the reference material dependent functions are as given in Table 4.2. The speed of sound in the pure phase and at the interface for materials governed by the Tait EOS are obtained as described in Subsection 4.2.1. The speed of sound at the pure phase may be written as:

$$c^2 = \frac{\gamma(p + B)}{\rho}, \quad (4.28)$$

and at the interface is as follows:

$$c_{int}^2 = \frac{p_{int}(\gamma - 1) + p + \gamma B}{\rho}. \quad (4.29)$$

4.2.5 van der Waals gas (vdW) EOS

The van der Waals gas EOS is used to govern real gases and can be written in the following form:

$$p = \left(\frac{\gamma - 1}{1 - b\rho} \right) (\rho e + a\rho^2) - a\rho^2, \quad (4.30)$$

where γ , a and b are constants that depend on the particular gas under consideration. Van der Waals EOS (4.30) may be rewritten in the form of the Mie-Grüneisen EOS (4.12). The reference material dependent functions are as given in Table 4.2. From (4.30) the internal energy can be written as:

$$e = \left(\frac{p}{\rho} + a\rho \right) \left(\frac{1 - b\rho}{\gamma - 1} \right) - a\rho, \quad (4.31)$$

The local speed of sound is derived, as given in the Appendix A.2, to be as follows:

$$c^2 = \frac{\gamma(p + a\rho^2)}{\rho(1 - b\rho)} - 2a\rho, \quad (4.32)$$

and at the interface is as follows:

$$c_{int}^2 = \frac{p_{int}(\gamma - 1) + p + a\rho^2\gamma}{\rho(1 - b\rho)} - 2a\rho. \quad (4.33)$$

4.2.6 Cochran-Chan (CC) EOS

This EOS is widely used to describe solids under a high-pressure shock wave. It is more accurate than the SG EOS in such conditions (Saurel and Abgrall, 1999a). The Cochran-Chan EOS may be rewritten in the form of the Mie-Grüneisen EOS (4.12) as follows:

$$p = \rho(\gamma - 1) \left\{ e + \frac{A_1}{\rho_o(1 - E_1)} \left[\left(\frac{\rho_o}{\rho} \right)^{1-E_1} - 1 \right] - \frac{A_2}{\rho_o(1 - E_2)} \left[\left(\frac{\rho_o}{\rho} \right)^{1-E_2} - 1 \right] + C_v T_o \right\} + A_1 \left(\frac{\rho_o}{\rho} \right)^{-E_1} - A_2 \left(\frac{\rho_o}{\rho} \right)^{-E_2}, \quad (4.34)$$

where γ , A_1 , E_1 , A_2 , E_2 , ρ_o , C_v and T_o are parameters that depend on the real material under consideration. The reference material dependent functions for the Cochran-Chan EOS are given in Table 4.2. For the Cochran-Chan EOS (4.34) the local speed of sound is derived, as given in the Appendix A.3, to be as follows:

Table 4.2: Mie-Grüneisen EOS functions for different EOSs.

EOS	$\Gamma_{\mathcal{H}}(\rho)$	$e_{\mathcal{H}}(\rho)$	$p_{\mathcal{H}}(\rho)$
Ideal gas	$\gamma - 1$	0	0
Shock wave	$(\gamma - 1) \left(\frac{\rho_0}{\rho}\right)^\theta$	$e_0 + \frac{C_0^2 \left(1 - \frac{\rho_0}{\rho}\right)^2}{2 \left[1 - s \left(1 - \frac{\rho_0}{\rho}\right)\right]^2}$	$p_0 + \frac{\rho_0 C_0^2 \left(1 - \frac{\rho_0}{\rho}\right)}{\left[1 - s \left(1 - \frac{\rho_0}{\rho}\right)\right]^2}$
Stiffened gas	$\gamma - 1$	$\frac{\pi}{\rho}$	$-\pi$
Tait	$\gamma - 1$	$\frac{B}{\rho}$	$-B$
van der Waals	$\frac{\gamma-1}{1-b\rho}$	$-a\rho$	$-a\rho^2$
Cochran-Chan	$\gamma - 1$	$-\frac{A_1}{\rho_0(1-E_1)} \left[\left(\frac{\rho_0}{\rho}\right)^{1-E_1} - 1 \right] + \frac{A_2}{\rho_0(1-E_2)} \left[\left(\frac{\rho_0}{\rho}\right)^{1-E_2} - 1 \right] - C_v T_0$	$A_1 \left(\frac{\rho_0}{\rho}\right)^{-E_1} - A_2 \left(\frac{\rho_0}{\rho}\right)^{-E_2}$
JWL	$\gamma - 1$	$\frac{A_1}{\rho_0 R_1} e^{(-R_1 \frac{\rho_0}{\rho})} - \frac{A_2}{\rho_0 R_2} e^{(-R_2 \frac{\rho_0}{\rho})} - C_{ek}$	$A_1 e^{(-R_1 \frac{\rho_0}{\rho})} + A_2 e^{(-R_2 \frac{\rho_0}{\rho})}$

$$\begin{aligned}
 c^2 = & \frac{p\gamma}{\rho} + \frac{A_1}{\rho} e^{(-R_1 \frac{\rho_o}{\rho})} \left(\frac{R_1 \rho_o}{\rho} - \gamma \right) \\
 & + \frac{A_2}{\rho} e^{(-R_2 \frac{\rho_o}{\rho})} \left(\frac{R_2 \rho_o}{\rho} - \gamma \right),
 \end{aligned} \tag{4.35}$$

and at the interface is as follows:

$$\begin{aligned}
 c_{int}^2 = & \frac{p_{int}}{\rho} (\gamma - 1) + \frac{p}{\rho} + \frac{A_1}{\rho} e^{(-R_1 \frac{\rho_o}{\rho})} \left(\frac{R_1 \rho_o}{\rho} - \gamma \right) \\
 & + \frac{A_2}{\rho} e^{(-R_2 \frac{\rho_o}{\rho})} \left(\frac{R_2 \rho_o}{\rho} - \gamma \right).
 \end{aligned} \tag{4.36}$$

$$\begin{aligned}
 c^2 = & \frac{p\gamma}{\rho} + \frac{A_1}{\rho} \left(\frac{\rho_o}{\rho} \right)^{-E_1} \left[E_1 - \gamma \right] \\
 & - \frac{A_2}{\rho} \left(\frac{\rho_o}{\rho} \right)^{-E_2} \left[E_2 - \gamma \right],
 \end{aligned} \tag{4.37}$$

and at the interface is as follows:

$$\begin{aligned}
 c_{int}^2 = & \frac{p_{int}}{\rho} (\gamma - 1) + \frac{p}{\rho} + \frac{A_1}{\rho} \left(\frac{\rho_o}{\rho} \right)^{-E_1} \left[E_1 - \gamma \right] \\
 & - \frac{A_2}{\rho} \left(\frac{\rho_o}{\rho} \right)^{-E_2} \left[E_2 - \gamma \right].
 \end{aligned} \tag{4.38}$$

4.2.7 Jones-Wilkins-Lee (JWL) EOS

This EOS is used to govern detonation products. The JWL EOS (4.39) may be rewritten in the form of the Mie-Grüneisen EOS (4.12) as follows:

$$\begin{aligned}
 p = & \rho(\gamma - 1) \left(e - \frac{A_1}{\rho_o R_1} e^{(-R_1 \frac{\rho_o}{\rho})} - \frac{A_2}{\rho_o R_2} e^{(-R_2 \frac{\rho_o}{\rho})} - C_{ek} \right) \\
 & + A_1 e^{(-R_1 \frac{\rho_o}{\rho})} + A_2 e^{(-R_2 \frac{\rho_o}{\rho})},
 \end{aligned} \tag{4.39}$$

where γ , A_1 , R_1 , A_2 , R_2 and C_{ek} are constants that depend on the real material under consideration. The reference material dependent functions for the JWL EOS are given in Table 4.2. For the JWL EOS the local speed of sound is derived, as given in the Appendix A.4, to be as follows:

4.3 Mathematical structure of the seven-equation model

Determination of the mathematical structure of a system of PDE is an essential step in order to construct a numerical scheme for its solution. The system (4.10) without relaxation and source terms can be written in a compact form as follows:

$$\frac{\partial \alpha_1}{\partial t} + u_{int} \frac{\partial \alpha_1}{\partial x} = 0, \quad (4.40a)$$

$$\frac{\partial Q}{\partial t} + \frac{\partial F(Q)}{\partial x} = H(Q) \frac{\partial \alpha_1}{\partial x}, \quad (4.40b)$$

where Q , $F(Q)$ and $H(Q)$ are the vectors of conserved variables, fluxes and non-conservative variables, respectively. These vectors are defined as follows:

$$Q = \begin{bmatrix} \alpha_1 \rho_1 \\ \alpha_1 \rho_1 u_1 \\ \alpha_1 \rho_1 E_1 \\ \alpha_2 \rho_2 \\ \alpha_2 \rho_2 u_2 \\ \alpha_2 \rho_2 E_2 \end{bmatrix}, \quad F(Q) = \begin{bmatrix} \alpha_1 \rho_1 u_1 \\ \alpha_1 \rho_1 u_1^2 + \alpha_1 p_1 \\ u_1 (\alpha_1 \rho_1 E_1 + \alpha_1 p_1) \\ \alpha_2 \rho_2 u_2 \\ \alpha_2 \rho_2 u_2^2 + \alpha_2 p_2 \\ u_2 (\alpha_2 \rho_2 E_2 + \alpha_2 p_2) \end{bmatrix}, \quad H(Q) = \begin{bmatrix} 0 \\ p_{int} \\ p_{int} u_{int} \\ 0 \\ -p_{int} \\ -p_{int} u_{int} \end{bmatrix}.$$

The system (4.40) may also be rewritten in a quasi-linear form by applying the chain rule to the flux vector term $F(Q)_x$ of the system (4.40):

$$\frac{\partial F(Q)}{\partial x} = \frac{\partial F}{\partial Q} \frac{\partial Q}{\partial x}.$$

The Jacobian matrix $A(\mathbf{w})$ can be obtained from the flux vector as follows:

$$A(\mathbf{w}) = \frac{\partial F}{\partial Q},$$

thus, the system (4.40) can be written in a quasi-linear form as follows:

$$\frac{\partial \mathbf{w}}{\partial t} + A(\mathbf{w}) \frac{\partial \mathbf{w}}{\partial x} = 0, \quad (4.41)$$

where \mathbf{w} is the vector of primitive variables which is given by:

$$\mathbf{w} = [\alpha_1 \quad \rho_1 \quad u_1 \quad p_1 \quad \rho_2 \quad u_2 \quad p_2]^T, \quad (4.42)$$

and the Jacobian matrix $A(\mathbf{w})$, is given by:

$$A(\mathbf{w}) = \begin{pmatrix} u_{int} & 0 & 0 & 0 & 0 & 0 & 0 \\ \frac{\rho_1(u_1 - u_{int})}{\alpha_1} & u_1 & \rho_1 & 0 & 0 & 0 & 0 \\ \frac{(p_1 - p_{int})}{\alpha_1 \rho_1} & 0 & u_1 & \frac{1}{\rho_1} & 0 & 0 & 0 \\ \frac{\rho_1 c_{1int}^2 (u_1 - u_{int})}{\alpha_1} & 0 & \rho_1 c_1^2 & u_1 & 0 & 0 & 0 \\ -\rho_2 (u_2 - u_{int}) & 0 & 0 & 0 & u_2 & \rho_2 & 0 \\ \frac{\alpha_2}{-(p_2 - p_{int})} & 0 & 0 & 0 & 0 & u_2 & \frac{1}{\rho_2} \\ \frac{\alpha_2 \rho_2}{-\rho_2 c_{2int}^2 (u_2 - u_{int})} & 0 & 0 & 0 & 0 & \rho_2 c_2^2 & u_2, \\ \alpha_2 & & & & & & \end{pmatrix} \quad (4.43)$$

where c_k^2 and c_{kint}^2 are the square local and at the interface speed of sound for phase k , respectively. They are very important to ensure the stability of the numerical solution. The local speed of sound for phase k is given by (4.7) and at the interface is given by (4.16). It is important to emphasise that the choice of the closure relations for the interfacial pressure and velocity will affect the hyperbolicity of the model. The system (4.40) is said to be *strictly hyperbolic* if the Jacobian matrix $A(\mathbf{w})$ has m distinct real eigenvalues:

$$\lambda_1 < \lambda_2 < \dots < \lambda_m.$$

If the eigenvalues are not distinct:

$$\lambda_1 \leq \lambda_2 \leq \dots \leq \lambda_m,$$

then the system is said to be *non-strictly hyperbolic* (LeVeque, 1992; Toro, 2009). For the Jacobian matrix (4.43) there are seven real and distinct eigenvalues:

$$\begin{aligned} \lambda_1 &= u_{int}, \\ \lambda_2 &= u_1 - c_1, \quad \lambda_3 = u_1, \quad \lambda_4 = u_1 + c_1, \\ \lambda_5 &= u_2 - c_2, \quad \lambda_6 = u_2, \quad \lambda_7 = u_2 + c_2. \end{aligned} \quad (4.44)$$

These eigenvalues represent the waves speed that are shown in Figure 4.1 which illustrates the solution of the Riemann problem. The corresponding right eigenvectors

are:

$$\mathbf{K}_1 = \begin{bmatrix} \alpha_1 \alpha_2 \sigma_1 \sigma_2 \\ -\alpha_2 \sigma_2 (\rho_1 (-c_{1int}^2 + \sigma_1) - p_{int} + p_1) \\ \frac{\alpha_2 \sigma_2 (-u_1 + u_{int}) (c_{1int}^2 \rho_1 + p_{int} - p_1)}{\rho_1} \\ \alpha_2 \sigma_2 (c_1^2 (p_{int} - p_1) + c_{1int}^2 \rho_1 (u_1 - u_{int})^2) \\ -\alpha_1 \sigma_1 (\rho_2 (c_{2int}^2 - \sigma_2) + p_{int} - p_2) \\ \frac{\alpha_1 \sigma_1 (u_2 - u_{int}) (c_{2int}^2 \rho_2 + p_{int} - p_2)}{\rho_2} \\ -\alpha_1 \sigma_1 (c_2^2 (p_{int} - p_2) + \rho_2 c_{2int}^2 (u_2 - u_{int})^2) \end{bmatrix},$$

$$\mathbf{K}_2 = \begin{bmatrix} 0 \\ \rho_1 \\ -c_1 \\ \rho_1 c_1^2 \\ 0 \\ 0 \\ 0 \end{bmatrix}, \quad \mathbf{K}_3 = \begin{bmatrix} 0 \\ 1 \\ 0 \\ 0 \\ 0 \\ 0 \\ 0 \end{bmatrix}, \quad \mathbf{K}_4 = \begin{bmatrix} 0 \\ \rho_1 \\ c_1 \\ \rho_1 c_1^2 \\ 0 \\ 0 \\ 0 \end{bmatrix}, \quad (4.45)$$

$$\mathbf{K}_5 = \begin{bmatrix} 0 \\ 0 \\ 0 \\ 0 \\ \rho_2 \\ -c_2 \\ \rho_2 c_2^2 \end{bmatrix}, \quad \mathbf{K}_6 = \begin{bmatrix} 0 \\ 0 \\ 0 \\ 0 \\ 1 \\ 0 \\ 0 \end{bmatrix}, \quad \mathbf{K}_7 = \begin{bmatrix} 0 \\ 0 \\ 0 \\ 0 \\ \rho_2 \\ c_2 \\ \rho_2 c_2^2 \end{bmatrix},$$

where $\sigma_1 = c_1^2 - (u_1 - u_{int})^2$ and $\sigma_2 = c_2^2 - (u_2 - u_{int})^2$.

Thus, the system (4.40) is strictly hyperbolic except when some of the eigenvalues of the phases coincide. If any one of the eigenvectors become linearly dependent the model loses its hyperbolicity which may occur when one of the phases disappears, i.e. α_1 or α_2 , or the value of σ_1 or σ_2 becomes zero. In this work the assumption of existence of both phases holds true everywhere in the domain.

4.4 Numerical method

Numerical methods to solve systems of partial differential equations frequently use finite difference technique in the solution process. A significant drawback of such approach is that they can give acceptable results only when the solution is smooth.

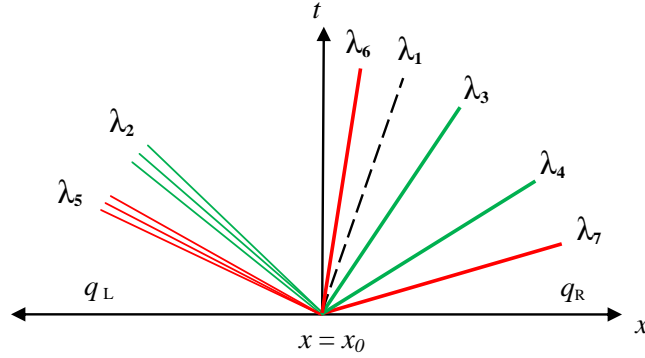


Figure 4.1: Solution of the Riemann problem for the seven-equation model λ_m are given by (4.44).

It is known that in many applications the studied models can admit discontinuous solutions even for smooth initial data. Consequently, the finite volume approach based on Godunov's method is adopted to solve the current system of governing equations. In order to build a numerical scheme to solve such systems it is essential to determine their mathematical structure that is given in the previous section 4.3.

4.4.1 Numerical solution of the seven-equation model

The numerical solution of the two-phase flow model (4.10) is very difficult due to the existence of the non-conservative equation of the volume fraction evolution equation (4.10a) and the non-conservative terms existing on the right hand side of the momentum equations (4.10c, 4.10d) and energy equations (4.10f, 4.10g). Moreover, the existence of the source terms as well as the velocity and pressure relaxation terms that appear on the right hand side of the equations pose some complexity in the solution process. The possible treatment of these equations is to split the model into a hyperbolic part and a source and relaxation part and solving them in succession following the Strang (1968) splitting technique, which can be written as follows:

$$Q_i^{n+1} = L_h^{\Delta t} L_s^{\Delta t} Q_i^n, \quad (4.46)$$

where $L_h^{\Delta t}$ is the hyperbolic part operator including the non-conservative terms, $L_s^{\Delta t}$ represent the relaxation processes and source term operator. The vectors of conserved variables are Q_i^n and Q_i^{n+1} for the node i at times $t = n$ and $t = n + 1$, respectively. The splitting technique has been used by many authors (see for example, (Saurel and Abgrall, 1999a; Lallemand and Saurel, 2000; Lallemand, Chinnayya and Le Métayer, 2005)).

4.4.2 The hyperbolic operator

The solution of the hyperbolic part of the two-phase flow model (4.10) is not direct as for the Euler equations due to the non-conservative equations. Consider the hyperbolic system (4.40). The solution of this system can be obtained by implementing the Godunov-type scheme which takes into account the discretisation of the non-conservative part of the system (4.40). The second equation of the system (4.40) may be discretised as:

$$Q_i^{n+1} = Q_i^n - \frac{\Delta t}{\Delta x} [f(q^*(Q_i^n, Q_{i+1}^n)) - f(q^*(Q_{i-1}^n, Q_i^n))] + \Delta t H(Q_i^n) \Delta_i, \quad (4.47)$$

where Δ_i is the discretisation of the non-conservative term $\frac{\partial \alpha_1}{\partial x}$ in space which depends on the approximate Riemann solver used, $q^*(Q_L^n, Q_R^n)$ represents the exact or approximate solution along the cell boundary $x = x_{i+1/2}$. This is used to compute the intercell flux (by solving the Riemann problem) with the states Q_L^n, Q_R^n and $H(Q_i^n)$ is the vector of non-conservative terms.

The mass, momentum and energy equations of the system (4.47) for phase (1) are written without the subscript (1) for simplicity as follows:

$$(\alpha \rho)_i^{n+1} = (\alpha \rho)_i^n + \frac{\Delta t}{\Delta x} [(\alpha \rho u)_{i+1/2}^* - (\alpha \rho u)_{i-1/2}^*], \quad (4.48a)$$

$$(\alpha \rho u)_i^{n+1} = (\alpha \rho u)_i^n + \frac{\Delta t}{\Delta x} [(\alpha \rho u^2 + \alpha p)_{i+1/2}^* - (\alpha \rho u^2 + \alpha p)_{i-1/2}^*] + \Delta t (p_{int})_i^n \Delta_i, \quad (4.48b)$$

$$(\alpha \rho E)_i^{n+1} = (\alpha \rho E)_i^n + \frac{\Delta t}{\Delta x} [(\alpha \rho u E + \alpha p u)_{i+1/2}^* - (\alpha \rho u E + \alpha p u)_{i-1/2}^*] + \Delta t (p_{int})_i^n (u_{int})_i^n \Delta_i. \quad (4.48c)$$

According to the criterion proposed by Abgrall (1996) that the pressure and velocity of a two-phase flow must remain constant during its time evolution, which enables preservation of a contact discontinuity between the phases, then we have:

$$\begin{aligned} p_i^n &= p_i^{n+1} = (p_{int})_i^n = p_{i\pm 1/2}^* = p, \\ u_i^n &= u_i^{n+1} = (u_{int})_i^n = u_{i\pm 1/2}^* = u. \end{aligned} \quad (4.49)$$

To obtain an expression for Δ_i the equation (4.48a) is multiplied by u , subtracted from (4.48b) and using the pressure uniformity (4.49), then the discretisation for Δ_i may be written as:

$$\Delta_i = \frac{1}{\Delta x} \left(\alpha_{i+\frac{1}{2}}^* - \alpha_{i-\frac{1}{2}}^* \right). \quad (4.50)$$

To obtain a discretisation for the volume fraction equation (4.40a), utilising the definition of E and (4.50) in (4.48c), combining with (4.48a) and using the criteria (4.49), the internal energy equation may be written as:

$$(\alpha \rho e)_i^{n+1} = (\alpha \rho e)_i^n + u \frac{\Delta t}{\Delta x} [(\alpha \rho e)_{i+1/2}^* - (\alpha \rho e)_{i-1/2}^*]. \quad (4.51)$$

The equation of state, which relates the internal energy with pressure, is used with the criterion of pressure uniformity. This implies that $\rho e = \text{constant}$. Finally, one obtains the following equation for the volume fraction:

$$\alpha_i^{n+1} = \alpha_i^n + u \frac{\Delta t}{\Delta x} [(\alpha)_{i+1/2}^* - (\alpha)_{i-1/2}^*]. \quad (4.52)$$

This equation can be used as a discretisation for the first equation of the system (4.40). Then the Godunov-type scheme discretisation for the non-conservative system (4.40) may be written as follows:

$$\alpha_i^{n+1} = \alpha_i^n - u_{int} \frac{\Delta t}{\Delta x} [(\alpha)_{i+1/2}^* - (\alpha)_{i-1/2}^*], \quad (4.53a)$$

$$Q_i^{n+1} = Q_i^n - \frac{\Delta t}{\Delta x} [f(q^*(Q_i^n, Q_{i+1}^n)) - f(q^*(Q_{i-1}^n, Q_i^n))] + \Delta t H(Q_i^n) \Delta_i. \quad (4.53b)$$

Note that the values of α^* and q^* are either exact or approximate solutions obtained by solving the Riemann problem. The computations of the exact Riemann solution are very expensive and in particular for the system (4.53) are complicated. Therefore, approximate Riemann solvers are generally used. A wide variety of approximate Riemann solvers have been developed to obtain the solution of the Riemann problem by computing the intercell fluxes, which require computing the intermediate states (*) in the Riemann solution. These states usually connect Q_L to Q_R by a sequence of shocks or rarefactions. In this work, the HLL, HLLC and VFRoe approximate Riemann solvers have been used to solve the system (4.53).

Extension to the second order accuracy

To achieve a second order accuracy in both time and space for the hyperbolic system (4.53), the MUSCL approach has been used. The name of this approach (MUSCL) stands for Monotone Upstream-centred Scheme for Conservation Laws. In this approach the second order accuracy is obtained by performing the following three steps (Toro, 2009):

1. Extrapolation:

This step is applied using the primitive variables to guarantee that a uniform solution of pressure and velocity is preserved (Saurel and Abgrall, 1999a). This is a reconstruction step where the primitive variables can be obtained at the boundaries by replacing the piecewise constant data \mathbf{w}_i^n by piecewise linear functions as follows:

$$\mathbf{w}_{i-1/2}^+ = \mathbf{w}_i^n - \frac{1}{2} \bar{\Delta}_i, \quad \mathbf{w}_{i+1/2}^- = \mathbf{w}_i^n + \frac{1}{2} \bar{\Delta}_i, \quad (4.54)$$

where $\bar{\Delta}_i$ is the limited slopes, they are defined as:

$$\bar{\Delta}_i = \begin{cases} \max[0, \min(\beta\Delta_{i-1/2}, \Delta_{i+1/2}), \min(\Delta_{i-1/2}, \beta\Delta_{i+1/2})] & \text{if } \Delta_{i+1/2} > 0, \\ \min[0, \max(\beta\Delta_{i-1/2}, \Delta_{i+1/2}), \max(\Delta_{i-1/2}, \beta\Delta_{i+1/2})] & \text{if } \Delta_{i+1/2} < 0, \end{cases}$$

where $\beta = 1$ in the minmod limiter and $\beta = 2$ in the superbee limiter and $\Delta_{i\pm 1/2}$ are defined as follows:

$$\Delta_{i-1/2} = \mathbf{w}_i^n - \mathbf{w}_{i-1}^n, \quad \Delta_{i+1/2} = \mathbf{w}_{i+1}^n - \mathbf{w}_i^n. \quad (4.55)$$

Note that the primitive variables for the seven-equation model are given by the vector (4.42).

2. Evolution:

The values of the boundary extrapolated primitive variables $W_{i\pm 1/2}^\mp$ are evolved by a half time step $t^{n+1/2}$ as follows:

$$\begin{aligned} \bar{\mathbf{w}}_{i-1/2}^+ &= \mathbf{w}_{i-1/2}^+ - \frac{\Delta t}{2\Delta x} A(\mathbf{w}_i)(\mathbf{w}_{i+1/2}^- - \mathbf{w}_{i-1/2}^+), \\ \bar{\mathbf{w}}_{i+1/2}^- &= \mathbf{w}_{i+1/2}^- - \frac{\Delta t}{2\Delta x} A(\mathbf{w}_i)(\mathbf{w}_{i+1/2}^- - \mathbf{w}_{i-1/2}^+). \end{aligned} \quad (4.56)$$

where $A(W)$ is the Jacobian matrix given by (4.43).

3. Solution of Riemann problem:

The computed primitive variables $(\bar{W}_i^n, \bar{W}_{i+1}^n)$ at each cell boundary are used to determine the conservative variables at time $t = n + 1/2$ which are used to solve the Riemann problem with the piecewise constant data $(\bar{Q}_{i+\frac{1}{2}}^-, \bar{Q}_{i+\frac{1}{2}}^+)$ using a suitable Riemann solver. The second order discretisation for the system (4.53) according to the Godunov-type scheme in time and space can be written as:

$$\alpha_i^{n+1} = \alpha_i^n - u_{int} \frac{\Delta t}{\Delta x} \left[\alpha^*(\bar{\alpha}_{i+\frac{1}{2}}^-, \bar{\alpha}_{i+\frac{1}{2}}^+) - \alpha^*(\bar{\alpha}_{i-\frac{1}{2}}^-, \bar{\alpha}_{i-\frac{1}{2}}^+) \right], \quad (4.57a)$$

$$\begin{aligned} Q_i^{n+1} &= Q_i^n - \frac{\Delta t}{\Delta x} \left[f(q^*(\bar{Q}_{i+\frac{1}{2}}^-, \bar{Q}_{i+\frac{1}{2}}^+)) \right. \\ &\quad \left. - f(q^*(\bar{Q}_{i-\frac{1}{2}}^-, \bar{Q}_{i-\frac{1}{2}}^+)) \right] + \Delta t H(Q_i^n) \Delta_i. \end{aligned} \quad (4.57b)$$

where $f(q^*)$ is the numerical flux vector calculated at the intercell boundaries $x_{i\pm 1/2}$ between $\bar{Q}_{i+1/2}^\pm$ and $\bar{Q}_{i-1/2}^\pm$, Δ_i is the discretisation of the volume fraction $\frac{\partial \alpha_g}{\partial x}$ which depends on the approximate Riemann solver and $H(Q_i^n)$ is the vector of non-conservative terms. The time step is calculated from:

$$\Delta t = \frac{\text{CFL } \Delta x}{S_{\max}}, \quad (4.58)$$

where, CFL is the Courant number; for stability it has to be less than one, Δx is the cell size and S_{\max} is the maximum wave speed. The left and right wave speeds at the boundaries $S_{i\pm\frac{1}{2}}^-$ and $S_{i\pm\frac{1}{2}}^+$ can be estimated respectively by:

$$S_{i\pm\frac{1}{2}}^- = \min(u_{k,i\pm\frac{1}{2}}^+ - c_{k,i\pm\frac{1}{2}}^+, u_{k,i\pm\frac{1}{2}}^- - c_{k,i\pm\frac{1}{2}}^-), \quad (4.59a)$$

$$S_{i\pm\frac{1}{2}}^+ = \max(c_{k,i\pm\frac{1}{2}}^+ + u_{k,i\pm\frac{1}{2}}^+, c_{k,i\pm\frac{1}{2}}^- + u_{k,i\pm\frac{1}{2}}^-), \quad (4.59b)$$

where k represents the components or phases 1 and 2.

(a) **The HLL approximate Riemann solver**

This solver is given in subsection 3.2.2 in its simple form for single-phase flows. The discretisation of the volume fraction (4.57a) in time and space according to the HLL is given as follows:

$$\begin{aligned} \alpha_i^{n+1} = \alpha_i^n & - \frac{\Delta t}{\Delta x} \left[\frac{u_i^{n+\frac{1}{2}} \left(S_{i+\frac{1}{2}}^+ \alpha_{i+\frac{1}{2},-}^{n+\frac{1}{2}} - S_{i+\frac{1}{2}}^- \alpha_{i+\frac{1}{2},+}^{n+\frac{1}{2}} \right) + S_{i+\frac{1}{2}}^+ S_{i+\frac{1}{2}}^- \left(\alpha_{i+\frac{1}{2},+}^{n+\frac{1}{2}} - \alpha_{i+\frac{1}{2},-}^{n+\frac{1}{2}} \right)}{S_{i+\frac{1}{2}}^+ - S_{i+\frac{1}{2}}^-} \right. \\ & \left. - \frac{u_i^{n+\frac{1}{2}} \left(S_{i-\frac{1}{2}}^+ \alpha_{i-\frac{1}{2},-}^{n+\frac{1}{2}} - S_{i-\frac{1}{2}}^- \alpha_{i-\frac{1}{2},+}^{n+\frac{1}{2}} \right) - S_{i-\frac{1}{2}}^+ S_{i-\frac{1}{2}}^- \left(\alpha_{i-\frac{1}{2},+}^{n+\frac{1}{2}} - \alpha_{i-\frac{1}{2},-}^{n+\frac{1}{2}} \right)}{S_{i-\frac{1}{2}}^+ - S_{i-\frac{1}{2}}^-} \right]. \end{aligned} \quad (4.60)$$

and in space Δ_i in equation (4.57b) is as follows:

$$\Delta_i = \frac{1}{\Delta x} \left[\frac{S_{i+\frac{1}{2}}^+ \alpha_{i+\frac{1}{2},-}^{n+\frac{1}{2}} - S_{i+\frac{1}{2}}^- \alpha_{i+\frac{1}{2},+}^{n+\frac{1}{2}}}{S_{i+\frac{1}{2}}^+ - S_{i+\frac{1}{2}}^-} - \frac{S_{i-\frac{1}{2}}^+ \alpha_{i-\frac{1}{2},-}^{n+\frac{1}{2}} - S_{i-\frac{1}{2}}^- \alpha_{i-\frac{1}{2},+}^{n+\frac{1}{2}}}{S_{i-\frac{1}{2}}^+ - S_{i-\frac{1}{2}}^-} \right]. \quad (4.61)$$

(b) **The HLLC approximate Riemann solver**

This solver is given in subsection 3.2.3. Here more details are given for computing the star region values for the seven-equation model. The wave speed is computed as follows:

$$S^* = \frac{p^R - p^L + \rho^L u^L (S^- - u^L) - \rho^R u^R (S^+ - u^R)}{\rho^L (S^- - u^L) - \rho^R (S^+ - u^R)}. \quad (4.62)$$

where:

$$\begin{aligned}
 p^K &= \alpha_1^K p_1^K + \alpha_2^K p_2^K, \\
 \rho^K &= \alpha_1^K \rho_1^K + \alpha_2^K \rho_2^K, \\
 u^K &= \frac{\alpha_1^K \rho_1^K u_1^K + \alpha_2^K \rho_2^K u_2^K}{\rho^K}.
 \end{aligned} \tag{4.63}$$

The conservative vector given by equation (4.64) can be written for components 1 and 2 as follows:

$$Q_{*K} = \begin{bmatrix} \alpha_1^K \rho_1^K \left(\frac{S_K - u_1^K}{S_K - S^*} \right) \\ \alpha_1^K \rho_1^K \left(\frac{S_K - u_1^K}{S_K - S^*} \right) S^* \\ \alpha_1^K \rho_1^K \left(\frac{S_K - u_1^K}{S_K - S^*} \right) \left(\frac{E_1^K}{\rho_1^K} + (S^* - u_1^K) \left[S^* + \frac{p_1^K}{\rho_1^K (S_K - u_1^K)} \right] \right) \\ \alpha_2^K \rho_2^K \left(\frac{S_K - u_2^K}{S_K - S^*} \right) \\ \alpha_2^K \rho_2^K \left(\frac{S_K - u_2^K}{S_K - S^*} \right) S^* \\ \alpha_2^K \rho_2^K \left(\frac{S_K - u_2^K}{S_K - S^*} \right) \left(\frac{E_2^K}{\rho_2^K} + (S^* - u_2^K) \left[S^* + \frac{p_2^K}{\rho_2^K (S_K - u_2^K)} \right] \right) \end{bmatrix}, \tag{4.64}$$

where K represents left L or right R values.

The discretisation of the volume fraction in space Δ_i in equation (4.57b) according to the HLLC approximate Riemann solver can be obtained by applying the uniformity of pressure and velocity criterion of Abgrall (1996) as follows:

$$\Delta_i = \frac{1}{\Delta x} \left(\bar{\alpha}_{i+\frac{1}{2}}^* - \bar{\alpha}_{i-\frac{1}{2}}^* \right). \tag{4.65}$$

The values of $\bar{\alpha}^*(\bar{\alpha}_{i\pm\frac{1}{2}}^-, \bar{\alpha}_{i\pm\frac{1}{2}}^+)$ in the discretisation equation of the volume fraction in space and time (4.57a) and in the discretisation in space Δ_i (4.65), which is substituted in (4.57b), according to the HLLC approximate Riemann solver by applying the Abgrall criterion (Ghangir et al., 2008) is as follows:

$$\alpha_{i\pm\frac{1}{2}}^* = \begin{cases} \alpha_{i\pm\frac{1}{2}}^- & \text{if } 0 \leq S_{i\pm\frac{1}{2}}^-, \\ \alpha_{i\pm\frac{1}{2}}^- & \text{if } S_{i\pm\frac{1}{2}}^- \leq 0 \leq S_{i\pm\frac{1}{2}}^*, \\ \alpha_{i\pm\frac{1}{2}}^+ & \text{if } S_{i\pm\frac{1}{2}}^* \leq 0 \leq S_{i\pm\frac{1}{2}}^+, \\ \alpha_{i\pm\frac{1}{2}}^+ & \text{if } 0 \geq S_{i\pm\frac{1}{2}}^+. \end{cases}$$

(c) The VFRoe approximate Riemann solver

This approach was introduced by Gallouët and Masella (1996) and described in detail by Andrianov, Saurel and Warnecke (2003) for the seven-

equation model in one dimension. Consider the Riemann problem of the hyperbolic system (4.57) in terms of primitive variables given by:

$$\frac{\partial \mathbf{w}}{\partial t} + A(\mathbf{w}) \frac{\partial \mathbf{w}}{\partial x} = 0, \quad (4.66)$$

where \mathbf{w} , the vector of primitive variables for the seven-equation model is given by (4.42) and $A(\mathbf{w})$ is the Jacobian matrix given by (4.43). Consider this Riemann problem with the following initial data:

$$\mathbf{w}(x, 0) = \begin{cases} \mathbf{w}_L & x \leq 0, \\ \mathbf{w}_R & x > 0. \end{cases} \quad (4.67)$$

The Jacobian matrix $A(\mathbf{w})$ is computed in the average state using equation (4.67):

$$\bar{\mathbf{w}} = \frac{\mathbf{w}_L + \mathbf{w}_R}{2}. \quad (4.68)$$

The intermediate state in the solution of the Riemann problem (4.67) and (4.66) is given by:

$$\mathbf{w}^* = \mathbf{w}_L + \sum_{\lambda_i < 0} a_i \mathbf{K}_i, \quad (4.69)$$

where the eigenvalues λ_i and the corresponding eigenvectors \mathbf{K}_i of the matrix $A(\bar{\mathbf{w}})$ are given by (4.44) and (4.45) and a_i are the coefficients of eigenvectors decomposition of $\mathbf{w}_R - \mathbf{w}_L$ and are determined by:

$$\mathbf{w}_R - \mathbf{w}_L = \sum_{i=1}^7 a_i \mathbf{K}_i. \quad (4.70)$$

For the Jacobian matrix $A(\bar{\mathbf{w}})$ these coefficients are given by the following expressions:

$$\begin{aligned} a_1 &= \delta_1 / \mathbf{K}_{11}, \\ a_2 &= \frac{\delta_3 \rho_1 c_1 + \delta_4 - a_1 (\mathbf{K}_{13} \rho_1 c_1 + \mathbf{K}_{14})}{2 \rho_1 c_1^2}, \\ a_3 &= \frac{-\delta_3 \rho_1 c_1 + \delta_4 + a_1 (\mathbf{K}_{13} \rho_1 c_1 - \mathbf{K}_{14})}{2 \rho_1 c_1^2}, \\ a_4 &= \delta_2 - a_1 \mathbf{K}_{12} - \rho_1 (a_2 + a_3), \\ a_5 &= \frac{\delta_6 \rho_2 c_2 + \delta_7 - a_1 (\mathbf{K}_{16} \rho_2 c_2 + \mathbf{K}_{17})}{2 \rho_2 c_2^2}, \\ a_6 &= \frac{-\delta_6 \rho_2 c_2 + \delta_7 + a_1 (\mathbf{K}_{16} \rho_2 c_2 - \mathbf{K}_{17})}{2 \rho_2 c_2^2}, \\ a_7 &= \delta_5 - a_1 \mathbf{K}_{15} - \rho_2 (a_5 + a_6). \end{aligned} \quad (4.71)$$

where \mathbf{K}_{11} are the components of \mathbf{K}_1 and δ_k is the k th component of:

$$\mathbf{w}_R - \mathbf{w}_L = (\delta_1, \dots, \delta_7)^T.$$

The discretisation of the volume fraction in time and space for the equation (4.57a) is written as follows:

$$\alpha_i^{n+1} = \alpha_i^n - u_{int} \frac{\Delta t}{\Delta x} \left(\bar{\alpha}_{i+\frac{1}{2}}^* - \bar{\alpha}_{i-\frac{1}{2}}^* \right), \quad (4.72)$$

and in space in the equation (4.57b) according to VFRoe is written as follows:

$$\Delta_i = \frac{1}{\Delta x} \left(\bar{\alpha}_{i+\frac{1}{2}}^* - \bar{\alpha}_{i-\frac{1}{2}}^* \right). \quad (4.73)$$

After solving the hyperbolic part of the model, following the Strang technique (4.46), the solution of the velocity and pressure relaxations is carried out to restore the velocities and pressures at the interface. Finally the source term is solved to consider the area variation.

4.4.3 Relaxation and source terms operator

The second step following the Strang splitting (4.46) is to solve the relaxation and source terms operator (Saurel and Abgrall, 1999a). The velocity and pressure relaxation processes are assumed to be instantaneous. They are important steps in the numerical solution to fulfill the boundary conditions at the interface that separates two fluids. The complete solution is obtained by solving the following ordinary differential equations (ODE):

$$\frac{dQ}{dt} = D_V + D_P + D_S, \quad (4.74)$$

where Q is defined as:

$$Q = [\alpha_1, \alpha_1 \rho_1, \alpha_1 \rho_1 u_1, \alpha_1 \rho_1 E_1, \alpha_2 \rho_2, \alpha_2 \rho_2 u_2, \alpha_2 \rho_2 E_2]^T, \quad (4.75)$$

and D_V , D_P and D_S are the velocity relaxation term, pressure relaxation term and area variation source term, respectively. They are given by:

$$D_V = \begin{bmatrix} 0 \\ 0 \\ \lambda(u_2 - u_1) \\ u_{int} \lambda(u_2 - u_1) \\ 0 \\ -\lambda(u_2 - u_1) \\ -u_{int} \lambda(u_2 - u_1) \end{bmatrix}, \quad D_P = \begin{bmatrix} \mu(p_1 - p_2) \\ 0 \\ 0 \\ p_{int} \mu(p_1 - p_2) \\ 0 \\ 0 \\ -p_{int} \mu(p_1 - p_2) \end{bmatrix}, \quad (4.76)$$

$$\text{and } D_S = \begin{bmatrix} 0 \\ -\frac{1}{A} \frac{\partial A}{\partial x} \alpha_1 \rho_1 u_1 \\ -\frac{1}{A} \frac{\partial A}{\partial x} \alpha_1 \rho_1 u_1^2 \\ -\frac{1}{A} \frac{\partial A}{\partial x} \alpha_1 u_1 (\rho_1 E_1 + p_1) \\ -\frac{1}{A} \frac{\partial A}{\partial x} \alpha_2 \rho_2 u_2 \\ -\frac{1}{A} \frac{\partial A}{\partial x} \alpha_2 \rho_2 u_2^2 \\ -\frac{1}{A} \frac{\partial A}{\partial x} \alpha_2 u_2 (\rho_2 E_2 + p_2) \end{bmatrix}. \quad (4.77)$$

Equation (4.77) is considered in the solution only when area variation is examined.

Solution of the ODE (4.74) is obtained by solving the three integration operators associated with the corresponding vectors (4.76) and (4.77) in succession. Then the solution of (4.74) is given by:

$$Q_i^{n+1} = L_V^{\Delta t} L_P^{\Delta t} L_S^{\Delta t} Q_i^n. \quad (4.78)$$

Velocity relaxation

In order to enable the velocity relaxation process to take place instantaneously, the velocity relaxation parameter λ has to be infinite value. Consider the ODE:

$$\frac{dQ}{dt} = D_V. \quad (4.79)$$

The mass and momentum equations for each phase in the above system (4.79) are combined to give a resultant equation. Integration of the resultant equation yields the following relation for the velocity relaxation:

$$u_1^* = u_2^* = u_{int}^* = \frac{\alpha_1^0 \rho_1^0 u_1^0 + \alpha_2^0 \rho_2^0 u_2^0}{\alpha_1^0 \rho_1^0 + \alpha_2^0 \rho_2^0}, \quad (4.80)$$

where the variables with (*) and (0) represent the states after and before the relaxation process, respectively. Since velocity relaxation terms are present in the energy equation of the system (4.79), update of the internal energy for both phases is necessary after the velocity relaxation process, for more details see (Saurel and Abgrall, 1999a; Saurel and Le Métayer, 2001), using the following relations:

$$e_1^* = e_1^0 + \frac{1}{2} (u_1^* - u_1^0)^2, \quad (4.81a)$$

$$e_2^* = e_2^0 + \frac{1}{2} (u_2^* - u_2^0)^2. \quad (4.81b)$$

Pressure relaxation

The pressure relaxation process has to take place instantaneously as it happens for the velocity relaxation process. Consequently, the pressure relaxation parameter μ has to be infinite. Consider the following ODE for phase 1:

$$\frac{dQ}{dt} = D_P. \quad (4.82)$$

Combining the mass, momentum and energy equations one obtains:

$$\frac{\partial e_1}{\partial t} = -\frac{p_{int}}{\alpha_1 \rho_1} \frac{\partial \alpha_1}{\partial t}. \quad (4.83)$$

Its integration yields:

$$e_1^* = e_1^0 - \frac{p_{int}}{\alpha_1 \rho_1} (\alpha_1^* - \alpha_1^0). \quad (4.84)$$

A similar equation for the second phase can be obtained. The pressures for both phases are obtained from their respective EOS and the iterative procedure (procedure 4) given in Lallemand and Saurel (2000) is used to achieve the equilibrium pressure.

Area variation source term

This source term accounts for variations in flow variables as the cross-section of the tube is changing as a function of its length. The effect of a variable cross-sectional area on the flow variables is determined with the help of the EOS at each time step by solving the following ODE:

$$\frac{dQ}{dt} = D_S. \quad (4.85)$$

This source term is enabled only when considering flows through tubes with varying cross-sectional areas.

4.5 Numerical results - Verification of the methodology

In this section the presented test problems are selected to assess the numerical performance of the developed code dealing with either single or two-phase compressible flow test problems, where the cross-section of the tube is considered either constant or varying. In the first four test cases the cross-section is constant. Among them, the first two cases are single-phase problems, i.e. gas-gas and solid-solid; the third and fourth are two-phase problems. The last two test cases in this section are a single-phase and a two-phase problem through a tube with a varying cross-sectional area, i.e. convergent-divergent nozzle.

In this section various EOSs have been employed in one-dimension to show the generality and the oscillation-free feature of the current method. These EOSs are the ideal gas (4.14), shock wave (4.18), stiffened gas (4.21), Cochran-Chan (4.34) and Jones-Wilkins-Lee (4.39). The code is built to work with three different approximate Riemann solvers, i.e. the HLL, HLLC and VFRoe, with the second order accuracy MUSCL scheme, employing the minmod slope limiter (Toro, 2009).

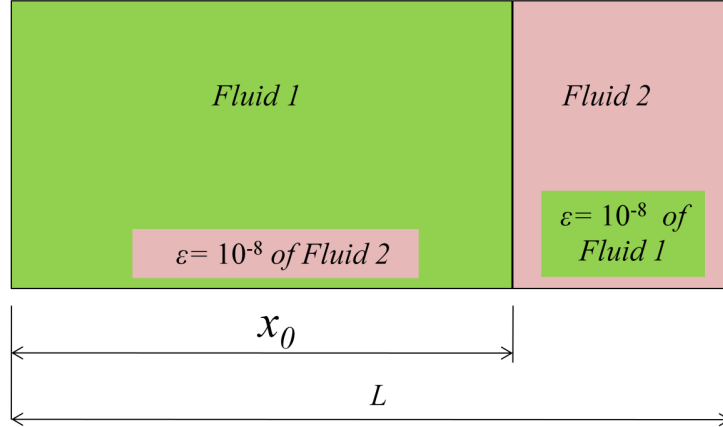


Figure 4.2: Shock tube illustration

The common assumption in all the conducted test problems, which in fact is numerically necessary for all the two-component diffuse interface methods, is the presence of a negligible volume fraction $\epsilon = 10^{-8}$ of the other fluid in the fluid considered as a pure fluid, as shown in Figure 4.2. All test problems are simulated either using the same type of EOS or different type of EOS governing each phase. The simulations have been carried out using the CFL = 0.9 unless otherwise mentioned. For the presented simulations the results were compared with either the exact solution or a fine grid solution, especially for those cases which don't have an exact solution. It can be noticed that no spurious pressure oscillations appeared at the material interface for all the test problems that have been conducted.

4.5.1 Gas-gas test

This test considers a single-phase air-air shock tube which was proposed by Lax (1954). The gas is governed by the ideal gas (IG) EOS (4.14). This test was chosen to check the correctness of the developed two-phase code in a single-phase regime and the outcome of this test will be compared with published single-phase results. Therefore, the left and right sides of the tube are filled with the same constituent: air, $\gamma = 1.4$, at different initial states, which are given in Table 4.3. The separating interface, i.e. the discontinuity, is located at $x = 0.5$ m. The air on the left side is given an initial velocity to the right.

As the interface separating the two parts of the tube is instantaneously removed at $t = 0$ s, three different waves are generated due to the difference in pressure.

Table 4.3: Initial data for gas-gas test 4.5.1

State	ρ_1	u_1	p_1	α_1	ρ_2	u_2	p_2	α_2
	[kg/m ³]	[m/s]	[Pa]		[kg/m ³]	[m/s]	[Pa]	
Left	0.445	0.7	3.53	$1 - \epsilon$	0.5	0.7	3.53	ϵ
Right	0.445	0	0.575	ϵ	0.5	0	0.575	$1 - \epsilon$

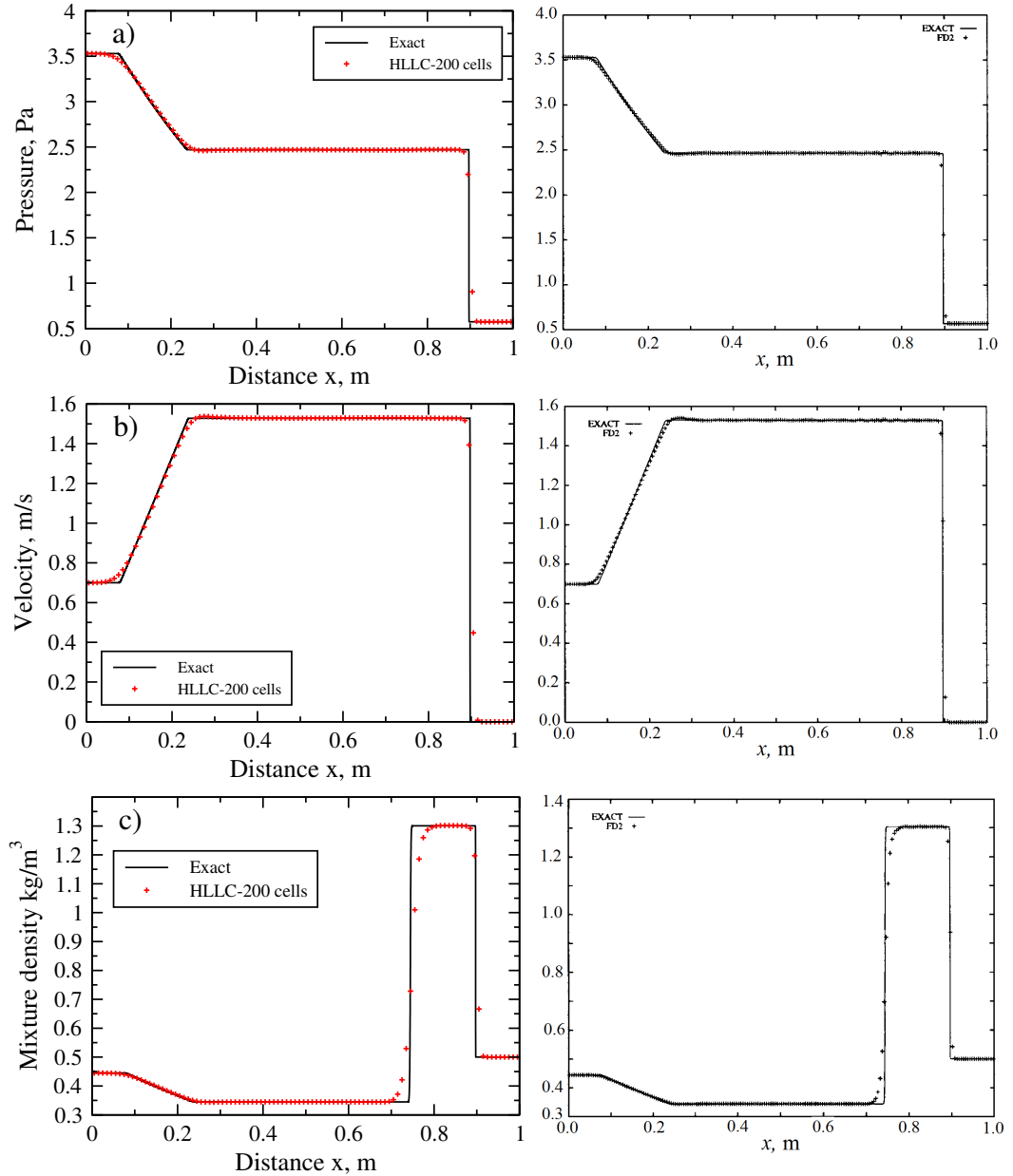


Figure 4.3: Gas-gas test example 4.5.1: Numerical and exact solutions: Current (left) and Kurganov and Tadmor (2000) (right) results are at $t = 0.16$ s for: (a) pressure, (b) velocity and (c) mixture density.

These waves represent the solution of this Riemann problem, two of which are right going, i.e. shock and contact waves, and a left going rarefaction wave. The flow domain is divided into four different state regions by these three waves as shown in Figure 4.3 at $t = 0.16$ s. The first region is on the far left which is enclosed between

the rarefaction wave and the beginning of the tube. In this region the pressure, density and velocity have not changed at this instant (remain at their initial values). The second region is enclosed between the rarefaction wave (across which all flow properties change continuously) and contact discontinuity (across which the pressure and velocity remain constant but the density changes discontinuously). The first region is on the leftmost side which is enclosed between the rarefaction wave and the beginning of the tube. In this region the pressure, density and velocity have not changed at this instant (remaining at their initial values). The second region is enclosed between the rarefaction wave (across which all flow properties change continuously) and contact discontinuity (across which the pressure and velocity remain constant but the density changes discontinuously). In this region the pressure and density have decreased whereas the velocity has increased. The third region is enclosed between the contact discontinuity and shock wave. In this region the pressure and velocity have the same value of the second region whereas the density has decreased. The fourth region which is at the far right of the tube, downstream from the shock wave. In this region the pressure, density and velocity are at their initial values as the flow properties have not changed.

The current results are shown in Figure 4.3 (left column) using the HLLC approximate Riemann solver with $CFL = 0.6$. The current results are in good agreement when compared with the exact solution taken from Kurganov and Tadmor (2000). The results are also in good agreement with the results presented in the same reference, see Figure 4.3 (right column), using a fully discrete central scheme for a single-phase flow with the same mesh, 200 cells.

The developed numerical application is originally constructed to deal with two-phase compressible flows. Here the volume fractions α_1 and α_2 ($\alpha_1 + \alpha_2 = 1$) allow to trace the interface between the zones of different thermodynamic properties as shown in Figure 4.4.

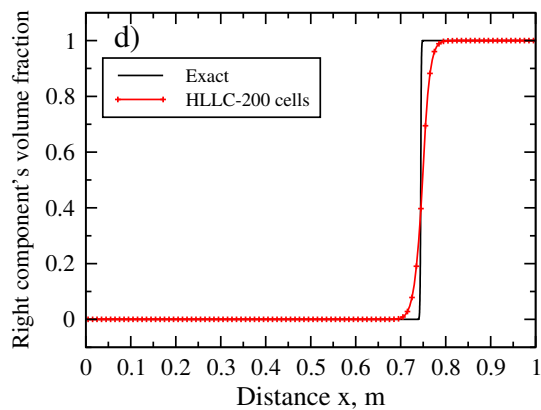


Figure 4.4: Gas-gas test example 4.5.1: Numerical and exact solutions results are at $t = 0.16$ s for: (d) volume fraction.

4.5.2 Solid-solid test

This test is a single-phase solid-solid test problem that is concerned with an impact of an aluminium slab, travelling from right to left with a high speed, with a stationary aluminium slab (Shyue, 2001). This test was conducted here to show that the developed code is able to simulate single solid phase problems governed by the shock wave EOS (4.18). The initial states of the left and right aluminium slabs are given in Table 4.4. The computational domain is 1 m long and the initial interface between them is located at $x = 0.5$ m. The shock wave EOS (4.18) is used to model the thermodynamic behaviour of both slabs. The shock wave EOS parameters for aluminium are $\rho_0 = 2785$ kg/m³, $c_0 = 5328$ m/s, $s = 1.338$, $\gamma = 2$ and $q = 1$.

Table 4.4: Initial data for solid-solid test 4.5.2

State	ρ_1 [kg/m ³]	u_1 [m/s]	p_1 [Pa]	α_1	ρ_2 [kg/m ³]	u_2 [m/s]	p_2 [Pa]	α_2
Left	4000	0	7.93×10^9	$1 - \epsilon$	2785	0	7.93×10^9	ϵ
Right	4000	-2000	1×10^5	ϵ	2785	-2000	1×10^5	$1 - \epsilon$

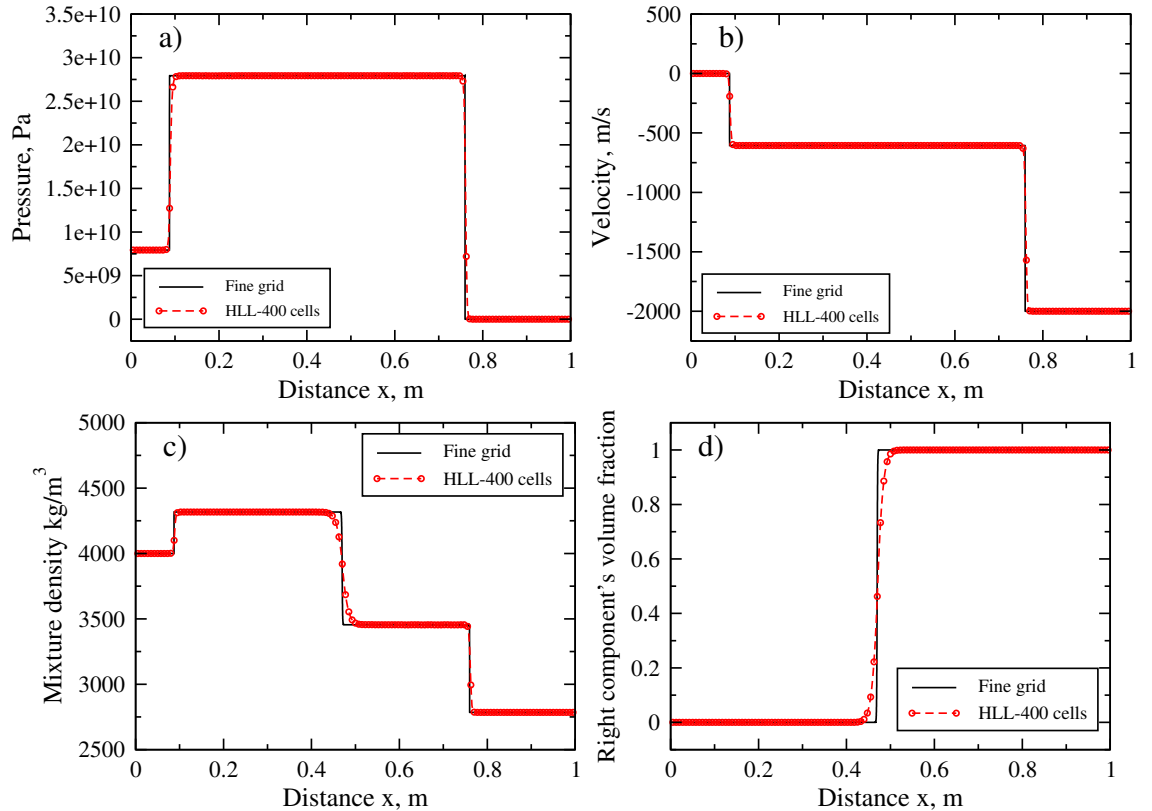


Figure 4.5: Solid-solid test example 4.5.2: Comparison between current numerical solution and fine grid solution at $t = 50 \mu\text{s}$ for: (a) pressure, (b) velocity, (c) mixture density and (d) volume fraction.

The solution of this Riemann problem consists of a left going shock wave propagating through the stationary slab, another right going shock wave propagating through

the moving slab and a contact wave moving to the left. The results of the numerical solution using the HLL approximate Riemann solver are obtained at $t = 50 \mu\text{s}$. The results of the pressure (a), velocity (b), mixture density (c) and the volume fraction of the right moving slab (d) are shown in Figure 4.5, these results are computed using 400 cells. As the test does not have an exact solution, the results are compared with a fine grid solution. The results are in good agreement with the reference results.

4.5.3 Interface advection test

This is a multiphase test problem presented in Petitpas et al. (2007), where two different gases are considered. It is examined to demonstrate the capability of the code to preserve a contact discontinuity moving with uniform velocity and pressure profiles. The ability to deal with various EOSs, written in the general form of the Mie-Grüneisen EOS (4.12), is also examined. The initial conditions are given in Table 4.5. The test is conducted in a computational domain of 1 m long. This

Table 4.5: Initial data for advection test 4.5.3

State	ρ_1 [kg/m ³]	u_1 [m/s]	p_1 [GPa]	α_1	ρ_2 [kg/m ³]	u_2 [m/s]	p_2 [GPa]	α_2
Left	2182	1000	20	$1 - \epsilon$	100	1000	20	ϵ
Right	2182	1000	20	ϵ	100	1000	20	$1 - \epsilon$

domain is divided into two equal chambers, the left chamber is filled with a real gas governed by the JWL EOS (4.39) and the right chamber is filled with air governed by the SG EOS (4.21). The JWL EOS parameters for the real gas are as follows: $\rho_o = 1590 \text{ kg/m}^3$, $A_1 = 353.91 \times 10^9 \text{ Pa}$, $R_1 = 4.15$, $A_2 = 3.45 \times 10^9 \text{ Pa}$, $R_2 = 0.9$, $C_v = 815 \text{ J/(kg} \cdot \text{K)}$, $\gamma = 1.35$ and $C_{ek} = 0$ and the air is considered as an ideal gas whose $\gamma = 1.4$ and $\pi = 0$.

The results for the advection test representing pressure (a), velocity (b) and mixture density (c) are shown in Figure 4.6. They are obtained at time $t = 270 \mu\text{s}$ using the VFRoe Riemann solver. The results show that the method preserves the contact discontinuity (interface) between two different gases, each of them is governed with a different EOS, as the flow evolves at a uniform velocity and pressure. A good agreement is achieved compared to the exact solution taken from Petitpas et al. (2007). The test is also conducted by employing other EOSs and no pressure and velocity oscillations are noticed in the results of all EOSs.

4.5.4 Copper-explosive impact test

This test problem considers an impact of a copper plate with a solid inert explosive. This test has been examined by many researchers (see for example, Saurel and Abgrall, 1999a; Shyue, 2001). In this test both materials are governed by the

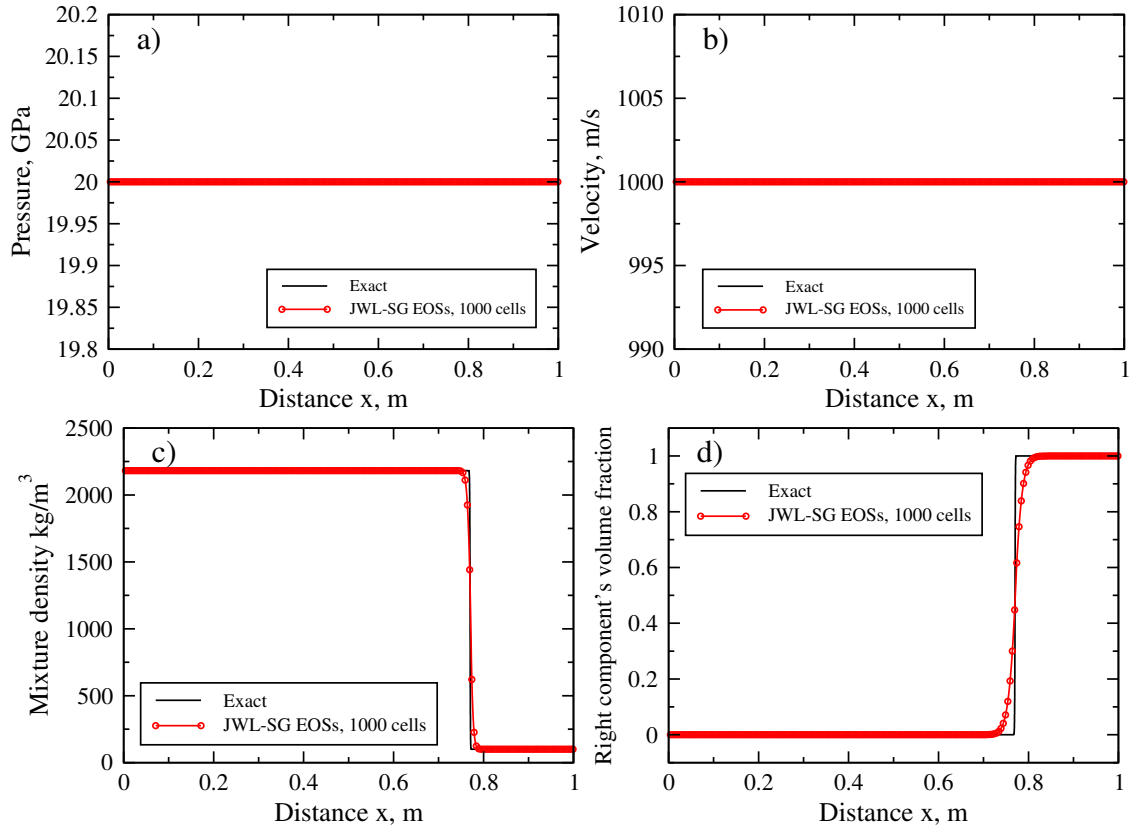


Figure 4.6: Advection test example 4.5.3: VFRoe solver results (circles) compared with exact (line) from Petitpas et al. (2007) at $t = 270 \mu\text{s}$ for: (a) pressure, (b) velocity, (c) mixture density and (d) volume fraction.

Cochran-Chan (CC) EOS (4.34). Both materials are at atmospheric pressure with the initial densities and EOS parameters given in Table 4.6. The problem is conducted in a computational domain of 1 m length and the material interface initially is located at $x = 0.5$ m. The copper plate which has an initial velocity of 1500 m/s to the right is put on the left hand side and the explosive material which is at rest is put on the right hand side of the computational domain.

Table 4.6: Materials properties for the Cochran-Chan EOS.

parameter	Copper	Explosive
ρ_0 , [kg/m ³]	8900	1840
C_v , [J/kg·K]	393	1087
A_1 , [Pa]	1.45667×10^{11}	1.2871×10^{10}
A_2 , [Pa]	1.47751×10^{11}	1.34253×10^{10}
E_1	2.994	4.1
E_2	1.994	3.1
T_0	300	300
γ	3	1.93

The solution of this problem comprises of two shock waves and a contact discon-

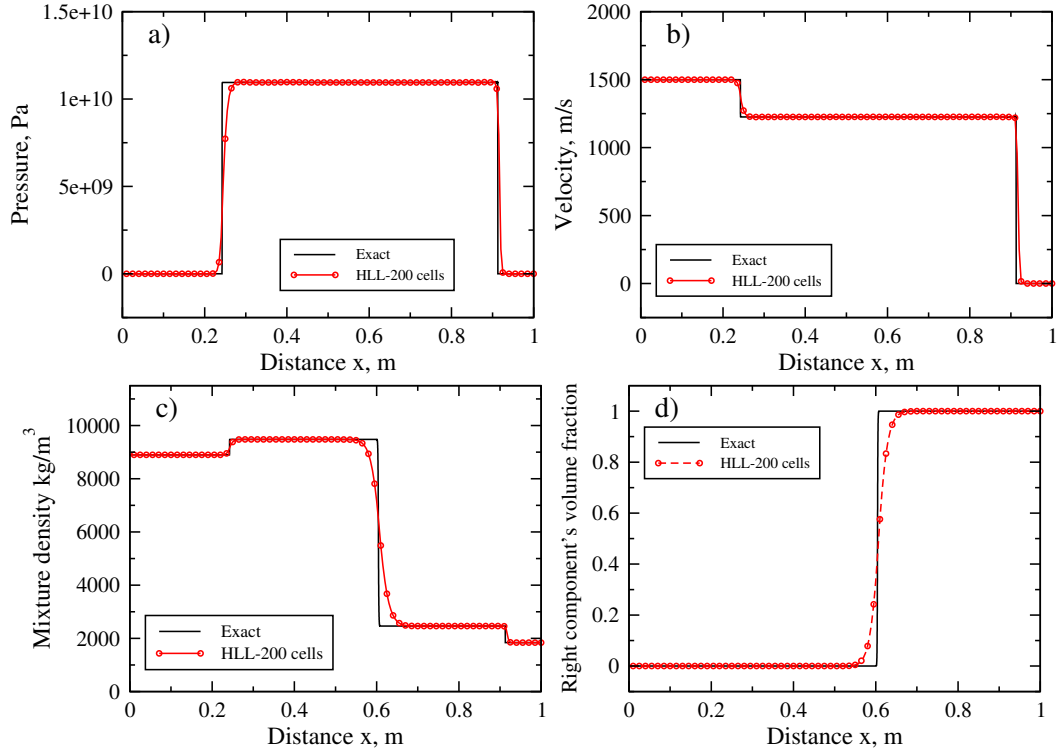


Figure 4.7: Copper-explosive test example 4.5.4: Comparison between current numerical results and exact solution from Saurel and Abgrall (1999a) at $t = 85 \mu\text{s}$ for: (a) pressure, (b) velocity, (c) mixture density and (d) temperature.

tinuity wave. The first shock wave is propagating to the right in the inert explosive, and the second is propagating to the left in the copper as shown in Figure 4.7. It can be observed, from the same figure, that the contact discontinuity moves to the right. Figure 4.7 shows the results of the HLL solver for pressure (a), velocity (b) and mixture density (c) using 200 cells. The results are compared with the exact solution at time $t = 85 \mu\text{s}$. A good agreement was achieved compared with the results of Saurel and Abgrall (1999a) and Shyue (2001).

4.5.5 Single-phase flow through C-D nozzle

All previous test problems were concerned with flows through a tube of a constant cross-sectional area. In this test problem a compressible flow of a single-phase through a convergent-divergent nozzle is considered, such a flow has a well know behaviour of flow properties. This test is conducted here as a verification test to assess the model (4.11) which is equipped with the source term that accounts for area variation. It is expected that using the two-phase flow model with the additional relaxation and source terms in the case of the same constituents, should produce exactly the same behaviour for flow parameters as a single-phase flow model does. This test considers a flow of pure air as a working fluid, the air is governed by the IG EOS (4.14). The air enters the nozzle shown in Figure 4.8 at a pressure of a fixed value (upstream reservoir pressure) and exits with different values of pressure

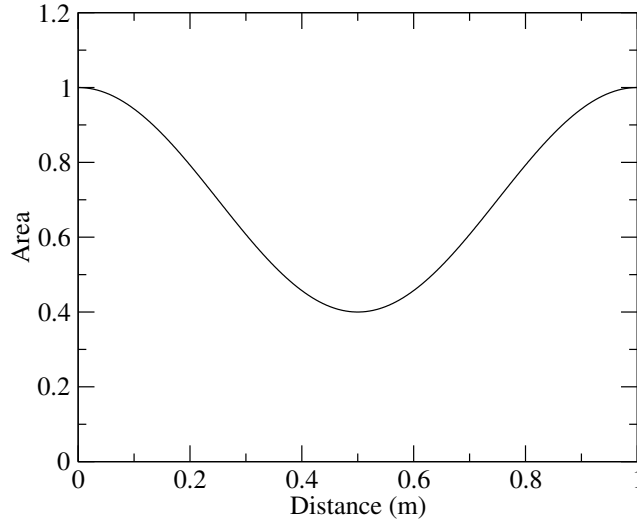


Figure 4.8: Normalized nozzle cross-sectional area.

(back pressure) at each run. The test is performed to compare the distribution of pressure and Mach number along the nozzle with theoretical data for such flows (see for example, Anderson, 1990). The nozzle area profile is governed by the following equation:

$$y = 0.7 + 0.3 \cos(2\pi x). \quad (4.86)$$

Where the throat is designed to be at $x = 0.5$ m as shown in Figure 4.8.

The initial data for the air entering and exiting the nozzle are presented in Table 4.7. The selection of variable exit pressures: 1×10^9 , 9.995×10^8 , 8.5×10^8 and 4×10^7 Pa have been considered in the computations.

Table 4.7: Initial and boundary conditions for a single-phase flow through the C-D nozzle.

Physical properties	Air in	Air out
Density, [kg/m ³]	50	50
Velocity, [m/s]	0.0	0.0
Pressure, [Pa]	10^9	<i>variable</i>

The results of the VFRoe Riemann solver for both pressure and Mach number distributions through the convergent-divergent nozzle using 1000 cells are presented in Figure 4.9. It is observed that when the exit (back) pressure is set equal to 1×10^9 Pa, which is equal to the reservoir pressure, the values for pressure and velocity remain unchanged; no flow through the nozzle. By reducing the back pressure to 9.995×10^8 Pa the air starts to flow downstream, the flow in this condition is a subsonic flow ($M < 1$) as shown in the right hand side of Figure 4.9. It is observed that the minimum pressure at the throat is above the critical pressure value (0.528) which is indicated by the horizontal green dashed line on the left hand side of Figure 4.9. When the back pressure is reduced further, for example 9.5×10^8 Pa,

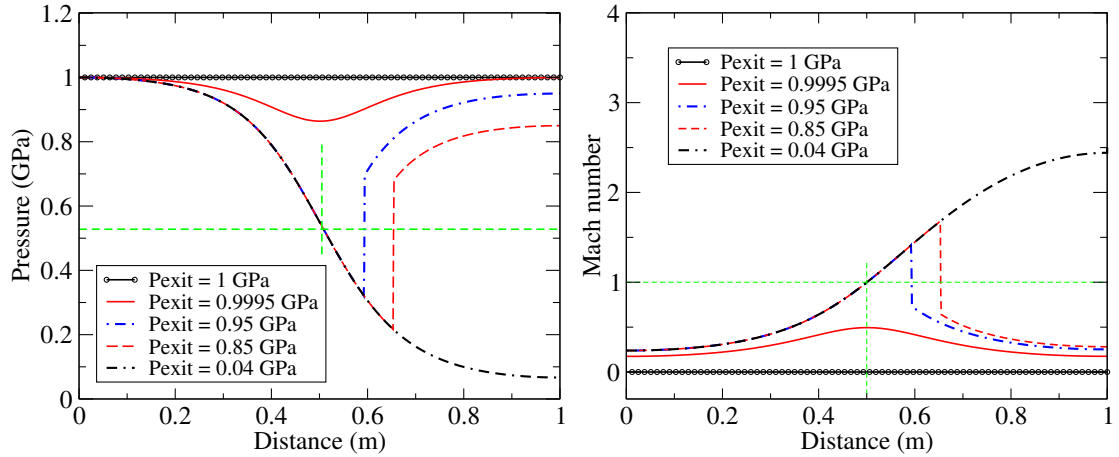


Figure 4.9: Single-phase flow through a convergent-divergent nozzle at variable exit pressure. Results for: pressure (left) and Mach number (right).

the flow at the throat becomes sonic ($M = 1$) with the critical pressure value. The flow downstream the throat becomes supersonic ($M > 1$) and the pressure falls below the critical value where a shock wave is formed at about $x = 0.593$ m. The flow downstream the shock returns to the subsonic flow where the pressure builds up to the exit pressure value. The position of the shock moves downstream as the back pressure is reduced further. For example, when the back pressure is reduced to 8.5×10^8 Pa the position of the shock moves to $x = 0.654$ m. This movement of the shock position continues downstream as the back pressure is reduced continuously. When exit pressure is equal to 4×10^7 Pa the shock formed outside the exit plane of the nozzle and any further reduction of the exit pressure will have no effect on the flow through the nozzle.

The results shown in Figure 4.9 are in good agreement with the reference data. It can be noticed that the values of Mach number equal unity at the throat $x = 0.5$ m for all supersonic flows and the corresponding values for the pressure equal to the critical value 0.528, which are exactly the same as the theoretical values reported in many gasdynamics textbooks.

4.5.6 Two-phase flows through C-D nozzle

This is a two-component flow problem that considers flows of an air-water mixture through the convergent-divergent nozzle shown in Figure 4.8 with various air-water ratios. While the air is governed by the IG EOS (4.14) the water is governed by the SG EOS (4.21) and is treated as a compressible fluid at high pressure; the SG EOS parameters for water are $\gamma = 4.4$ and $\pi = 6 \times 10^8$ Pa. This test is designed to investigate the behaviour of the two-component flow parameters through the C-D nozzle. Two numerical experiments have been performed using the same Riemann solver and number of cells as in the previous test with a reservoir pressure of 10^9 Pa:

The first experiment considers a flow of air-water mixture with fixed ratio of

50% air and 50% water. The initial data are given in Table 4.8. The selection of variable back pressures: 1×10^9 , 8.5×10^8 and 1×10^8 Pa have been examined in the computations. The steady state results for pressure, Mach number, mixture density and velocity for this test are presented in Figure 4.10. It is known that for the case of isentropic compressible gas flow through a convergent-divergent nozzle, the sonic flow occurs at the minimum cross-sectional area, i.e. the throat. As shown in the Figure 4.10, the two-component flow behaves qualitatively like the single-phase flow as described in the previous test, however, larger quantitative differences appear for the air-water mixture of 50% air with respect to the sonic flow parameters, i.e. critical pressure and Mach number. The position of the sonic flow moved downstream from the throat into the divergent part of the nozzle.

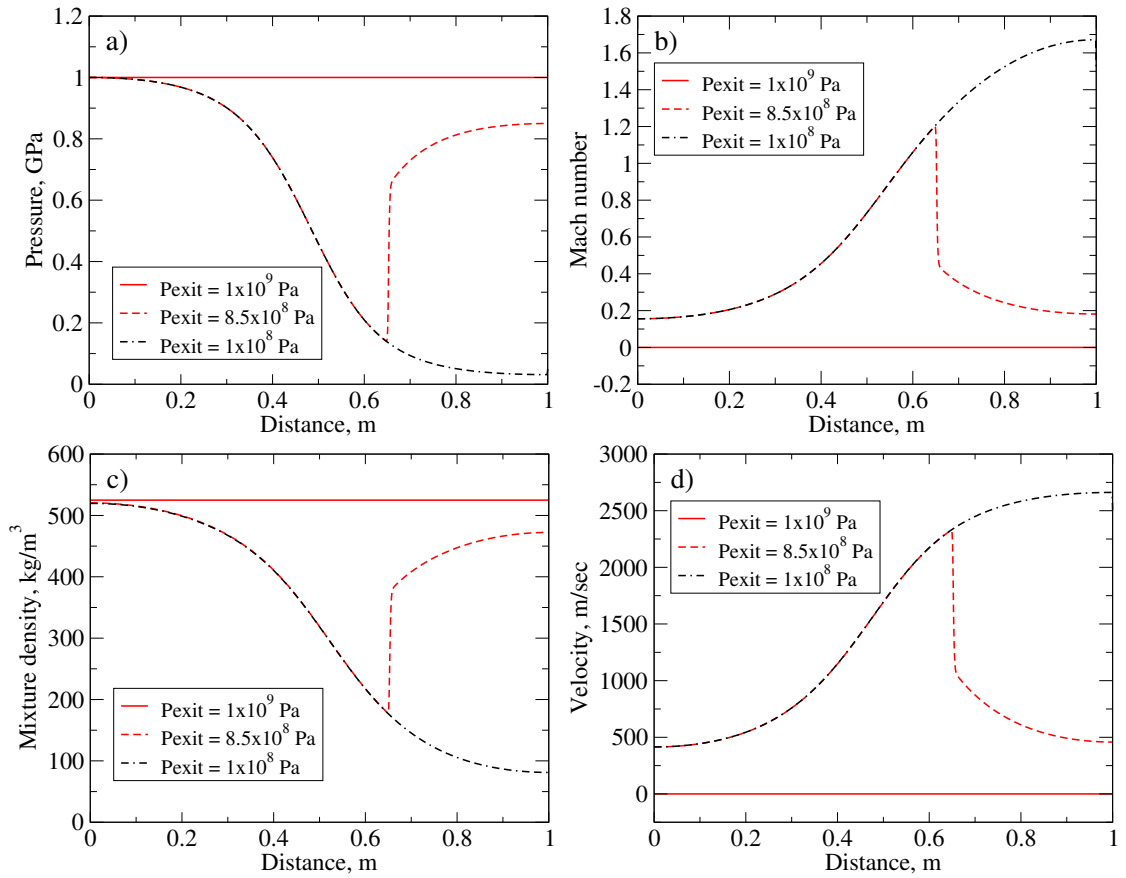


Figure 4.10: Air-water mixture (50% air) flow through convergent-divergent nozzle at variable exit pressure. Results for: (a) pressure, (b) Mach number, (c) mixture density and (d) velocity.

Table 4.8: Initial and boundary conditions for mixture flow through the C-D nozzle.

Physical properties	Water	Air
Density, [kg/m ³]	1000	50
Velocity, [m/s]	0.0	0.0
Pressure, [Pa]	10^9	<i>variable</i>

The second experiment involves a flow of air-water mixture with various air ratios of 25%, 50% and 75% at a fixed exit pressure of 8.5×10^8 Pa. The results for the distribution of pressure, Mach number, mixture density and velocity along the nozzle are presented in Figure 4.11. It can be observed that the distribution of the flow parameters is again qualitatively like the single-phase flow for all investigated air-water ratios. However, a quantitative variation can be noticed in the values of the flow parameters. Moreover, the location of the sonic flow moved downstream from the throat as the liquid content is increased.

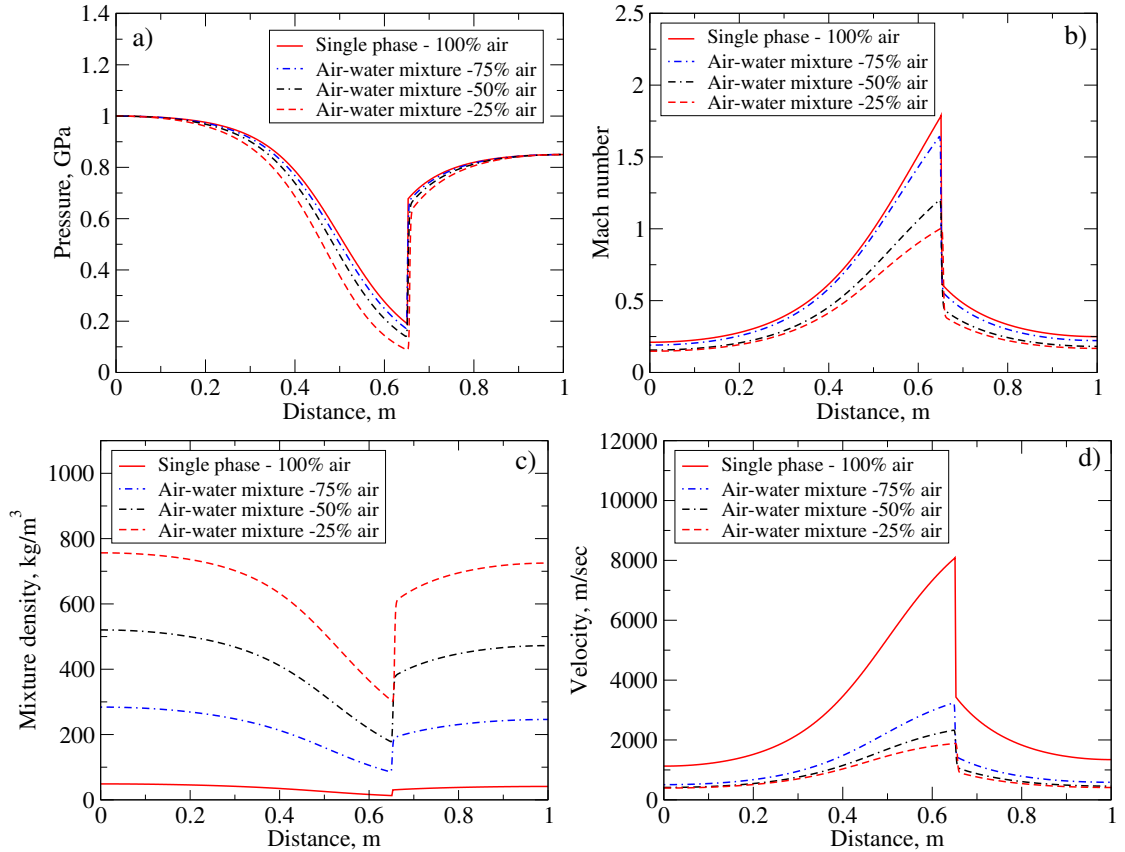


Figure 4.11: Air-water mixture flow through convergent-divergent nozzle with variable air-water ratios at $p_{exit} = 8.5 \times 10^8$ Pa. Results for: (a) pressure, (b) Mach number, (c) mixture density and (d) velocity.

4.6 Numerical results - Comparison between solvers

In this section comparisons between the HLL, HLLC and VFRoe approximate Riemann solvers have been investigated using various test problems. The first test is a single-phase liquid-liquid test where the SG EOS is employed to govern water. The second test is a two-phase helium-air test where the IG EOS is employed to govern both phases. The last test in this section is a standard water-air test problem where water is governed by the SG EOS and air is governed by the IG EOS. The comparisons are done in terms of L_2 error norm, time steps and CPU time required

to obtain the solution.

4.6.1 Liquid-liquid test

This test is a single-phase water-water shock tube problem considered in Gallouët, Hérard and Seguin (2002). This test was chosen to assess the developed code when dealing with single-phase problems governed by SG EOS (4.21). The test consists of a tube 1 m long divided into two parts separated by an interface located at $x = 0.5$ m. The initial conditions, i.e. density, velocity, pressure and volume fraction, of the left and right states are given in Table 4.9. The only difference between the left and right states was, that the left hand side had a higher pressure. The SG EOS parameters for water are $\gamma = 4.4$ and $\pi = 6 \times 10^8$ Pa.

Table 4.9: Initial data for liquid-liquid test 4.6.1

State	ρ_1 [kg/m ³]	u_1 [m/s]	p_1 [Pa]	α_1	ρ_2 [kg/m ³]	u_2 [m/s]	p_2 [Pa]	α_2
Left	1×10^3	2000	5×10^8	$1 - \epsilon$	1×10^3	2000	5×10^8	ϵ
Right	1×10^3	2000	1×10^6	ϵ	1×10^3	2000	1×10^6	$1 - \epsilon$

As the interface separating the two parts of the tube is instantaneously removed at $t = 0$ s, three different waves are generated due to the high difference in pressure. These waves represent the solution of this Riemann problem, two of which are right going, i.e. shock and contact waves, and a left going rarefaction wave. The flow domain is divided into four different state regions by these three waves as shown in Figure 4.12 at $t = 80 \mu\text{s}$. These regions are as described in the gas-gas test, subsection 4.5.1.

Table 4.10: The number of time steps and the CPU time for liquid-liquid test using SG EOS

Mesh cells	HLL		HLLC		VFRoe	
	Time step	CPU (s)	Time step	CPU (s)	Time step	CPU (s)
100	42	0.01	42	0.01	42	0.02
1000	378	0.94	378	1.10	378	1.65
5000	1871	23.20	1871	27.41	1871	40.76
10000	3738	92.25	3738	108.61	3738	162.30
25000	9338	623.95	9338	719.24	9338	1064.85
50000	18671	2637.61	18671	3172.63	18671	4514.25

The results for this test are obtained using the HLL, HLLC and VFRoe approximate Riemann solvers with the SG EOS. Figure 4.12 shows the results at the instant $t = 80 \mu\text{s}$ for pressure (a), velocity (b), mixture density (c) and volume fraction (d)

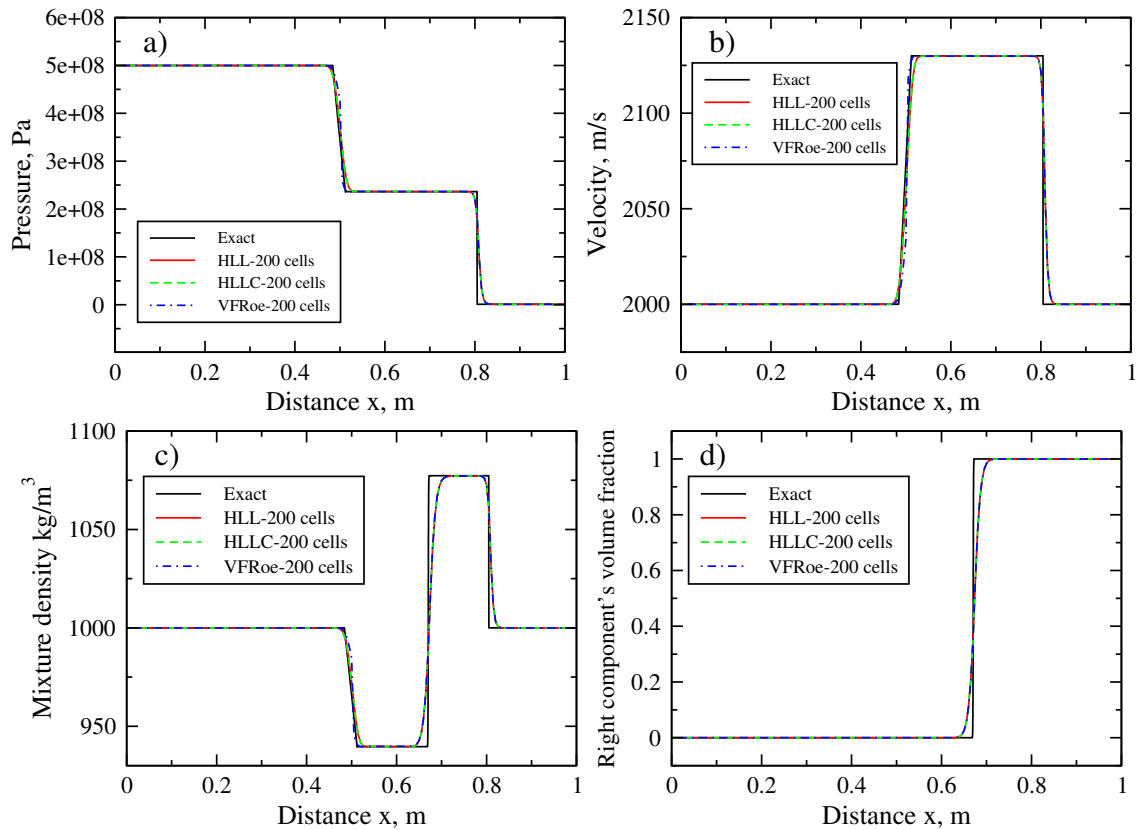


Figure 4.12: Liquid-liquid test example 4.6.1: Numerical and exact solutions using SG EOS are at $t = 80 \mu\text{s}$ for: (a) pressure, (b) velocity, (c) mixture density and (d) volume fraction.

using the three solvers. It can be seen that all three solvers gave almost the same results which are in good agreement with the exact solution using a relatively low resolution of 200 cells.

The number of time steps (n) and the CPU time needed by the code to obtain

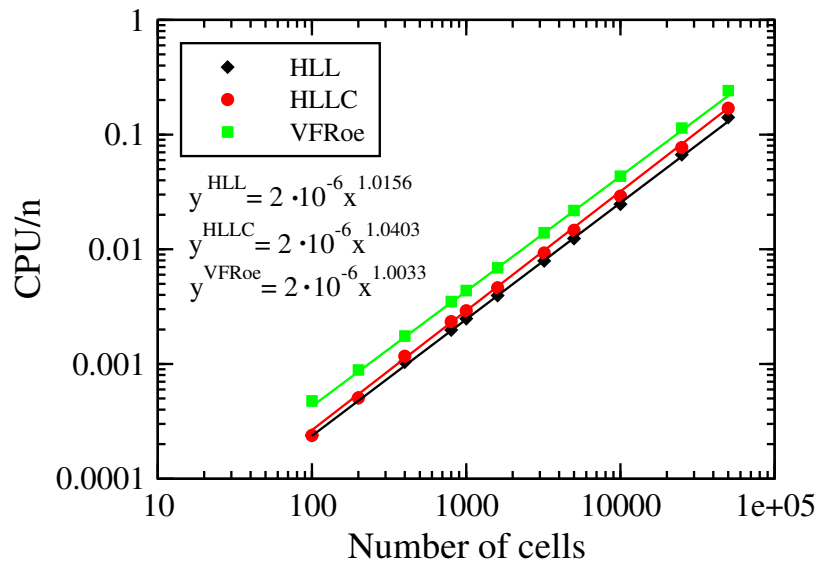


Figure 4.13: Liquid-liquid test example 4.6.1: Scaling order for the HLL, HLLC and VFRoe algorithms.

the solution for different mesh resolutions are given in Table 4.10. All solvers with the SG EOS need the same number of time steps to obtain the solution for this test problem. However, it can be observed that the cheapest solver is the HLL solver, whereas the most expensive solver is the VFRoe for all mesh resolutions, where the HLLC needs 14.74 % more CPU time than the HLL solver and the VFRoe needs 78.16 % more CPU time than the HLL solver. The scaling order for the HLL, HLLC and VFRoe algorithms for this test are 1.0156, 1.0403 and 1.0033, respectively, as shown in Figure 4.13.

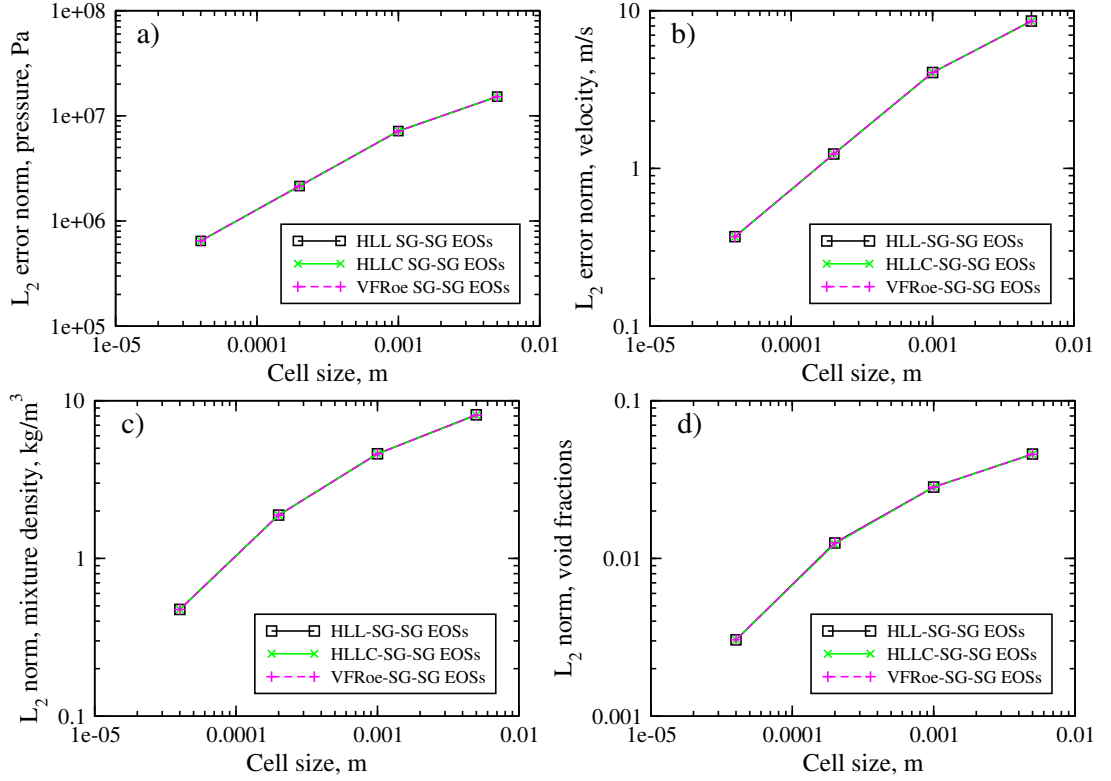


Figure 4.14: Liquid-liquid test example 4.6.1: L_2 error norm spatial convergence for: (a) pressure, (b) velocity, (c) mixture density and (d) volume fraction.

The results have been used to calculate and to compare the accuracy of the three solvers by calculating the error norm (L_2) for these solvers using the following formula:

$$L_2 = \sqrt{\frac{\sum_i^N (x_{i,ex} - x_{i,num})^2}{N}}. \quad (4.87)$$

Where N is the number of cells used in the computations, the subscript ex represents the values of the exact solution of the property x (could be pressure, velocity, etc.) and num represents the values of the same property obtained from the numerical solution. The error norm L_2 is drawn against the cell size for the HLL, HLLC and VFRoe solvers using the SG EOS. The results of spatial convergence are obtained using a very small time step of 2.38×10^{-8} s for various cell sizes with the grid refinement factor ($r=5$) ($r = \Delta x_{k+1}/\Delta x_k = \Delta x_{k+2}/\Delta x_{k+1} = \Delta x_{k+3}/\Delta x_{k+2} = \dots$).

The spatial convergence for this test is shown in Figure 4.14 for the pressure, velocity, mixture density and volume fraction. The precision of these solvers increases when the number of mesh cells increases.

The order of accuracy can be calculated using the following equation (de Vahl Davis, 1983):

$$P = \frac{\ln\left(\frac{L_{2(k+1)}}{L_{2(k)}}\right)}{\ln(r)} \quad (4.88)$$

The order of accuracy of the HLL, HLLC and VFRoe algorithms for the results of the liquid-liquid test using the SG EOS are given in Tables 4.11-4.13. It can be observed that the order of accuracy is less than 2 due to the presence of the discontinuities in the solution. The algorithms used in this work are second order accurate in smooth solutions as pointed in LeVeque (1992, 2004).

Table 4.11: Order of accuracy of the HLL for liquid-liquid test using SG EOS

Mesh cells	L_2		Order	
	p	ρ	p	ρ
200	15243362.84	8.139966		
1000	7159231.25	4.607308	0.46957	0.35363
5000	2148989.67	1.88168	0.74772	0.55639
25000	646537.29	0.474995	0.74630	0.85534

Table 4.12: Order of accuracy of the HLLC for liquid-liquid test using SG EOS

Mesh cells	L_2		Order	
	p	ρ	p	ρ
200	15222668.74	8.100902		
1000	7154702.837	4.600686	0.46912	0.35153
5000	2147424.75	1.88054	0.74778	0.55588
25000	646095.74	0.474834	0.74627	0.85517

Table 4.13: Order of accuracy of the VFRoe for liquid-liquid test using SG EOS

Mesh cells	L_2		Order	
	p	ρ	p	ρ
200	15222666.60	8.10102		
1000	7154702.14	4.6007	0.46912	0.35154
5000	2147423.85	1.88047	0.74778	0.55590
25000	646096.00	0.47481	0.74627	0.85518

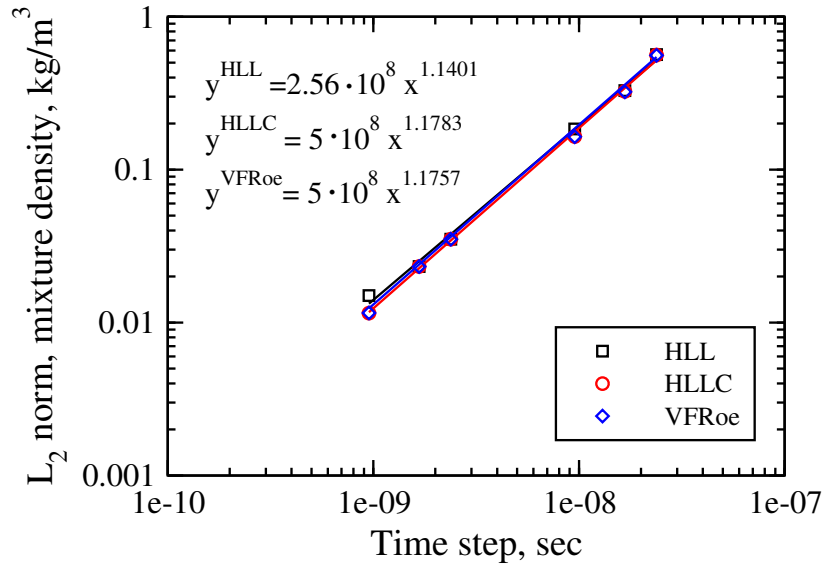


Figure 4.15: Liquid-liquid test example 4.6.1: Temporal convergence for the HLL, HLLC and VFRoe algorithms.

The temporal convergence is obtained using a fine mesh resolution of 12800 cells and various time steps. The order of temporal convergence for the HLL, HLLC and VFRoe solvers are 1.1401, 1.1783 and 1.1757 as shown in Figure 4.15, respectively.

4.6.2 Helium-air test

This is a two-phase test problem, where two different gases are considered. Helium is filled in the left chamber at a higher pressure than the air, which occupies the right chamber. Both gases are separated by an interface located at $x = 0.2$ m. In this test the SG EOS (4.21) is employed to govern air. This EOS reduces to the IG EOS (4.14) when the parameter π equals to zero. The EOS parameters for helium $\gamma = 1.667, \pi = 0$ Pa and for air $\gamma = 1.4, \pi = 0$ Pa. The initial conditions are given in Table 4.14.

Table 4.14: Initial data for helium-air test 4.6.2

State	ρ_1 [kg/m ³]	u_1 [m/s]	p_1 [Pa]	α_1	ρ_2 [kg/m ³]	u_2 [m/s]	p_2 [Pa]	α_2
Left	3.984	27.355	1000	$1 - \epsilon$	0.01	27.355	1000	ϵ
Right	3.984	0	1	ϵ	0.01	0	1	$1 - \epsilon$

At the instant $t = 0$ s the helium was given an initial velocity to the right, this velocity is increased due to the high pressure and density difference and at the mean time the pressure and mixture density are decreased as shown in Figure 4.16. Three waves are generated during the time of evolution. These waves which represent the solution of the Riemann problem are right going shock and contact discontinuity waves and a left going rarefaction wave.

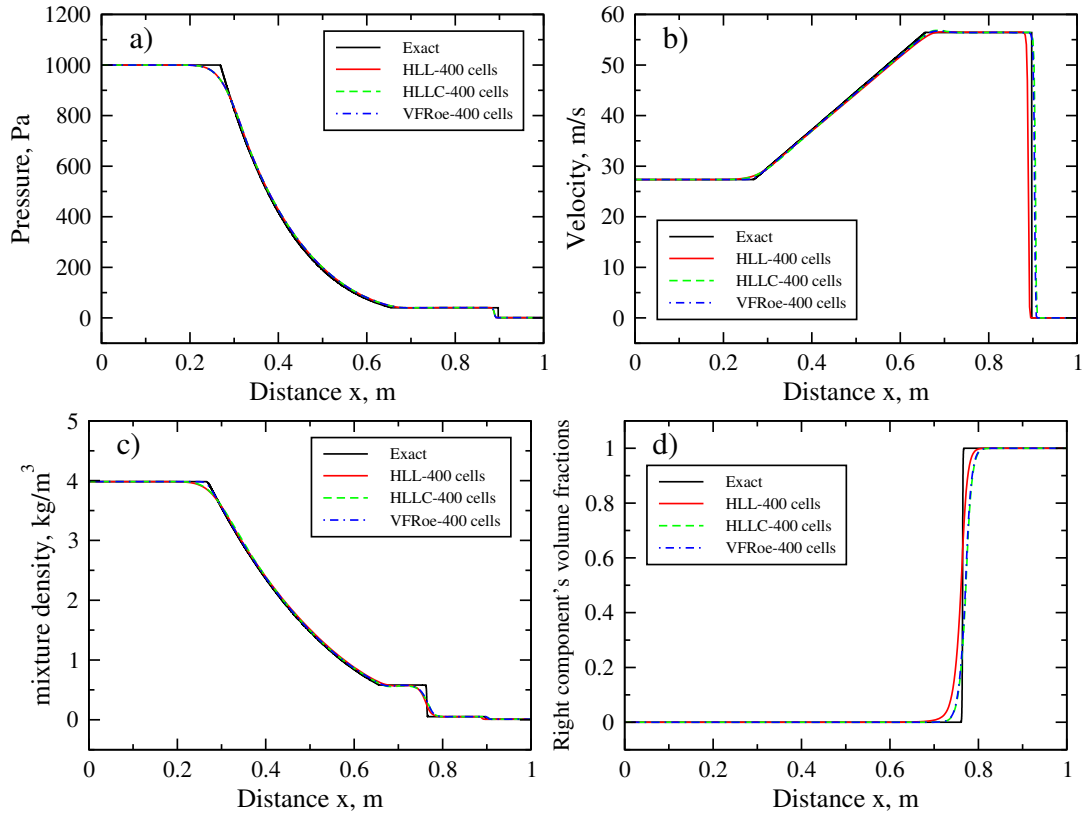


Figure 4.16: Helium-air test example 4.6.2: Comparison between HLL, HLLC and VFRoe solvers at $t = 0.01$ s for: (a) pressure, (b) velocity, (c) mixture density and (d) volume fraction.

The results for the helium-air test at time $t = 0.01$ s using the HLL, HLLC and VFRoe approximate Riemann solvers are shown in Figure 4.16. The figure shows a comparison between these solvers using 400 cells. It can be noted in Figure 4.16(b) and (c) that the positions of the shock and that of the contact discontinuity predicted by the HLLC and VFRoe are identical and are slightly different from that predicted by the HLL solver. But they have almost the same offset, using 400 cells, from those positions obtained from the exact solution. This offset is diminished as the mesh is refined.

Table 4.15: The number of time steps and the CPU time for helium-air test using IG EOS

Mesh cells	HLL		HLLC		VFRoe	
	Time step	CPU (s)	Time step	CPU (s)	Time step	CPU (s)
100	445	0.13	453	0.16	453	0.23
200	897	0.51	899	0.61	900	0.92
1000	4466	12.85	4468	15.46	4470	22.7
5000	22311	346.33	22313	417.02	22315	856.82
10000	44618	1442.83	44620	1705.5	44622	2410.92
25000	111538	9058.37	111540	10717.54	111542	15032.27

The number of time steps and the CPU time needed by the code to obtain the solution for the helium-air test using the SG EOS with different mesh resolutions are given in Table 4.15. The number of time steps required for all solvers are almost the same for all mesh resolutions. However, it can be seen that the cheapest solver is the HLL solver. In order to obtain the solution the HLLC Riemann solver needs 20.06 % more CPU time than the HLL solver, whereas the VFRoe solver needs 71.21 % more CPU time than the HLL solver.

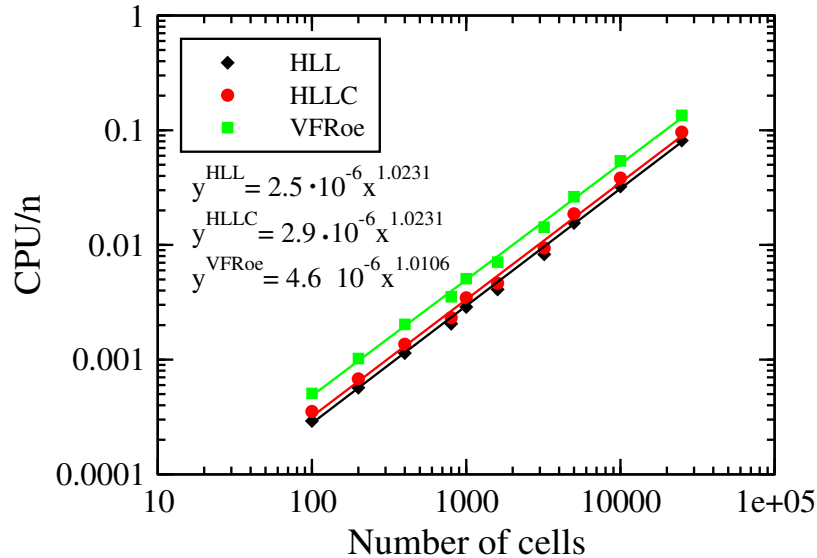


Figure 4.17: Helium-air test example 4.6.2: Scaling order for the HLL, HLLC and VFRoe algorithms.

The scaling order for the HLL, HLLC and VFRoe solvers for this test are 1.0231, 1.0231 and 1.0106, respectively, as shown Figure 4.17

A comparison of the L_2 error norm is carried out for the three solvers for the helium-air test. The results of the spatial convergence of the three solvers are shown in Figure 4.18 for the pressure (a), velocity (b), mixture density (c) and volume fraction (d). It can be observed that the VFRoe solver produced results with lower error than the HLL and HLLC solvers which gave almost the same error for pressure and mixture density fields as shown in Figure 4.18(a) and (c), respectively. The HLL solver generates a higher error than the HLLC and VFRoe solvers at a mesh with less than 300 cells for velocity as shown in Figure 4.18(b). The accuracy of the HLL solver becomes almost as precise as that of the HLLC solver at about 200 mesh cells for pressure and mixture density results. The HLL solver produced results with lower values of L^2 error norm for the volume fraction than that predicted by the HLLC and VFRoe solvers as can be seen in Figure 4.18(d).

The order of accuracy of the HLL, HLLC and VFRoe algorithms for the results of the helium-air test using the IG EOS are given in Tables 4.16-4.18. It can also be observed that the order of accuracy is less than 2 due to the presence of the discontinuities in the solution as mentioned in the previous test.

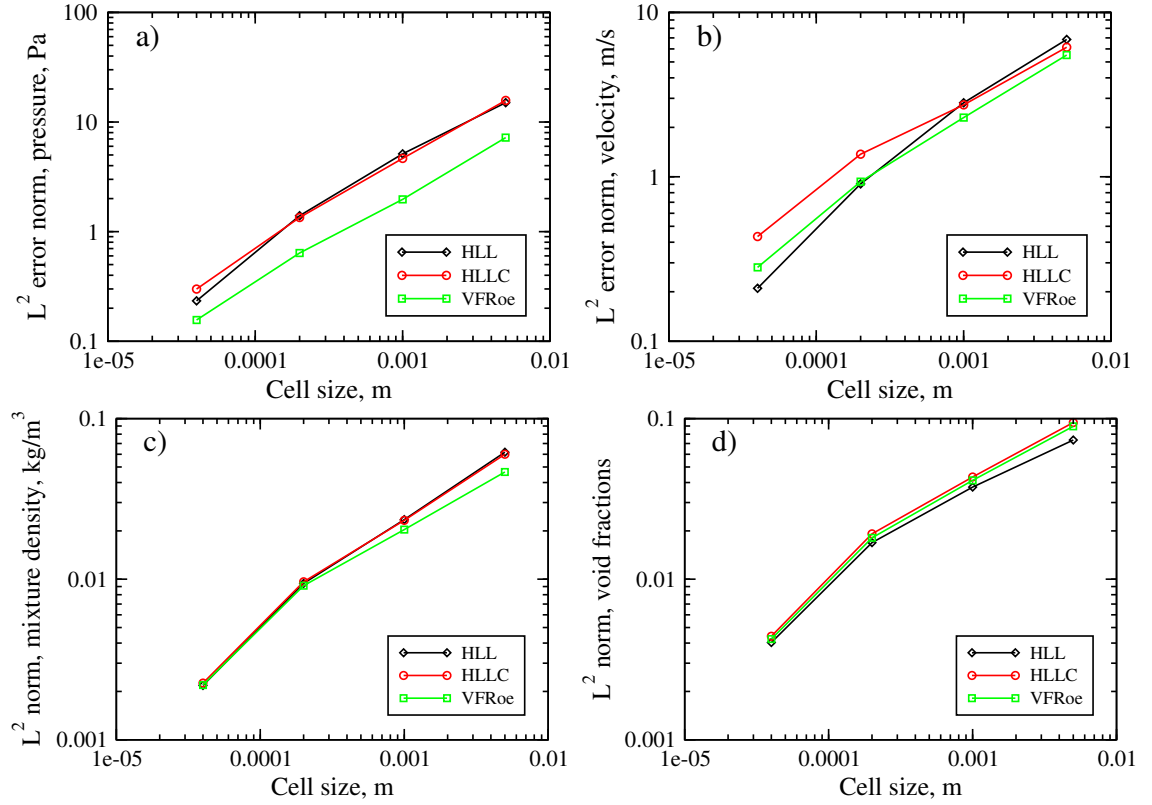


Figure 4.18: Helium-air test example 4.6.2: L_2 error norm spatial convergence for: (a) pressure, (b) velocity, (c) mixture density and (d) volume fraction.

Table 4.16: Order of accuracy of the HLL for helium-air test using IG EOS

Mesh cells	L_2		Order	
	u	ρ	u	ρ
200	6.84593	0.061796		
1000	2.820868	0.023489	0.55088	0.60102
5000	0.906073	0.009419	0.70564	0.56778
25000	0.20995	0.002178	0.90855	0.90983

Table 4.17: Order of accuracy of the HLLC for helium-air test using IG EOS

Mesh cells	L_2		Order	
	u	ρ	u	ρ
200	6.136048	0.060009		
1000	2.739687	0.023251	0.50101	0.58912
5000	1.37312	0.009634	0.42919	0.54743
25000	0.433457	0.002256	0.71643	0.90200

The temporal convergence is obtained using a fine mesh resolution of 12800 cells and various time steps. The order of temporal convergence for the HLL, HLLC and VFRoe solvers are 0.9991, 1.104 and 1.3662, respectively, as shown in Figure 4.19.

Table 4.18: Order of accuracy of the VFRoe for helium-air test using IG EOS

Mesh cells	L_2		Order	
	u	ρ	u	ρ
200	5.503139	0.046535		
1000	2.292497	0.02037	0.54409	0.51331
5000	0.933792	0.009108	0.55805	0.50012
25000	0.281199	0.002191	0.74572	0.88528

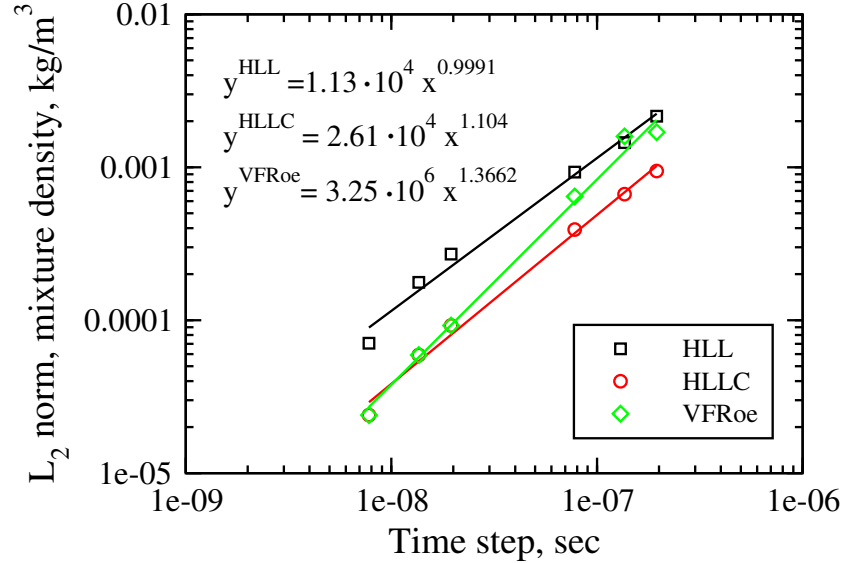


Figure 4.19: Helium-air test example 4.6.2: Temporal convergence for the HLL, HLLC and VFRoe algorithms.

4.6.3 Water-air test

This is a standard water-air shock tube which has been considered by many researchers (see for example, Saurel and Abgrall, 1999a; Saurel and Le Métayer, 2001). In this test the tube is 1 m long and is divided into two chambers. Liquid water is filled in the left hand chamber at a higher pressure and air is filled in the right hand chamber at atmospheric pressure. The interface separating water and air is located at $x = 0.7$ m. Air is governed by the IG EOS (4.14), $\gamma = 1.4$ and water is governed by the SG EOS (4.21), $\gamma = 4.4$ and $\pi = 6 \times 10^8$. The initial data are provided in Table 4.19.

Initially both fluids are at rest, however, as soon as the membrane separating

Table 4.19: Initial data for water-air test 4.6.3

State	ρ_1 [kg/m ³]	u_1 [m/s]	p_1 [Pa]	α_1	ρ_2 [kg/m ³]	u_2 [m/s]	p_2 [Pa]	α_2
Left	1000	0	10^9	$1 - \epsilon$	50	0	10^9	ϵ
Right	1000	0	10^5	ϵ	50	0	10^5	$1 - \epsilon$

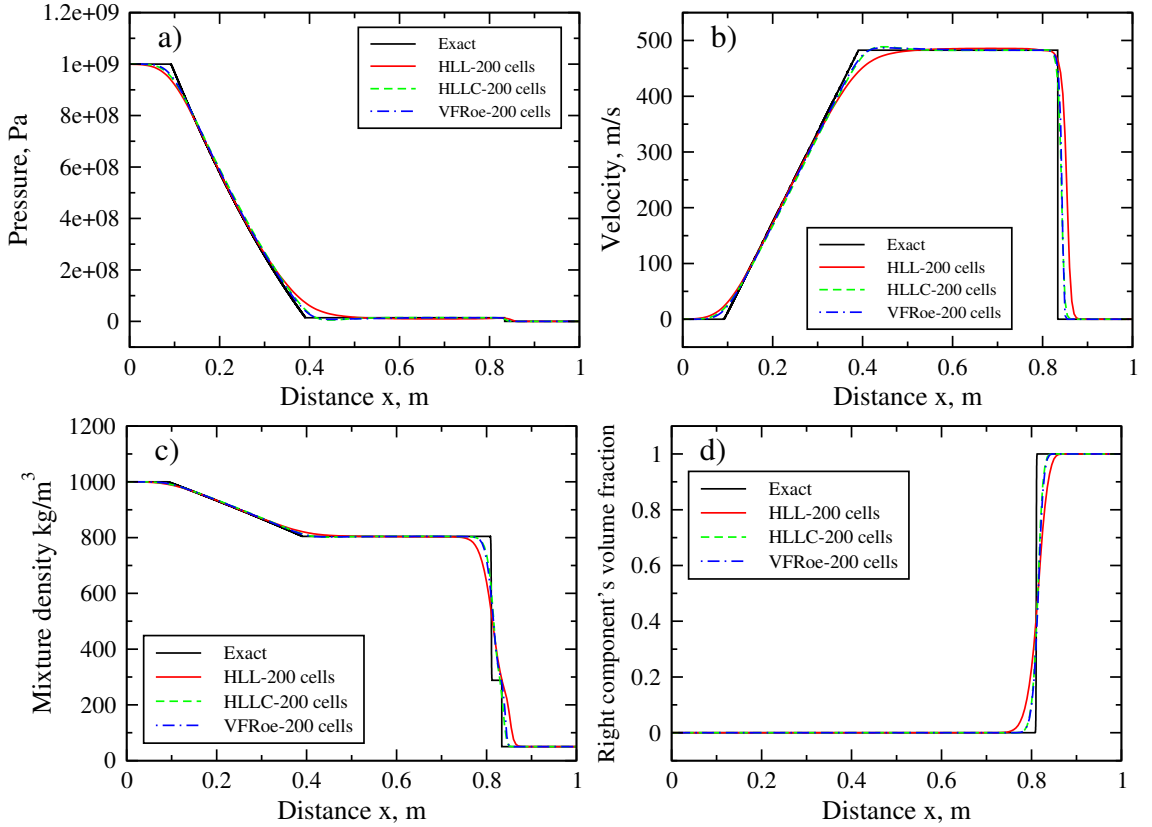


Figure 4.20: Water-air test example 4.6.3: Numerical and exact solutions are at $t = 229 \mu\text{s}$ for: (a) pressure, (b) velocity, (c) mixture density and (d) volume fraction.

the two fluids is removed, the water starts to move to the right due to the high pressure and density differences. Consequently, right going strong shock and contact discontinuity waves and a left going rarefaction wave are generated. The results for the water-air shock tube test problem at time $t = 229 \mu\text{s}$ are obtained from the HLL, HLLC and VFRoe approximate Riemann solvers with 200 cells. It can be noted from Figure 4.20 that the HLLC and VFRoe solvers gave almost the same results which are better than that obtained from the HLL solver. At this resolution the position for waves, i.e. shock and contact discontinuity, are away from the exact position, these positions become closer as the mesh is refined. Figure 4.21 shows the surface plots for the results of evolution of pressure (a), velocity (b), mixture density (c) and volume fraction (d).

The number of time steps and the CPU times needed by the three solvers to obtain the solution for different mesh resolutions are given in Table 4.20 using the SG EOS. All solvers with this EOS need the same number of time steps to obtain the solution for this test problem. However, it can be observed that the cheapest solver is the HLL solver. The HLLC Riemann solver needs 29.47 % more CPU time than the HLL solver to obtain the results, whereas the VFRoe solver needs 92.67 % more CPU time than the HLL solver. The scaling order for the HLL, HLLC and VFRoe solvers for the water-air test are 1.0343, 0.9976 and 1.0106, respectively, as shown Figure 4.22

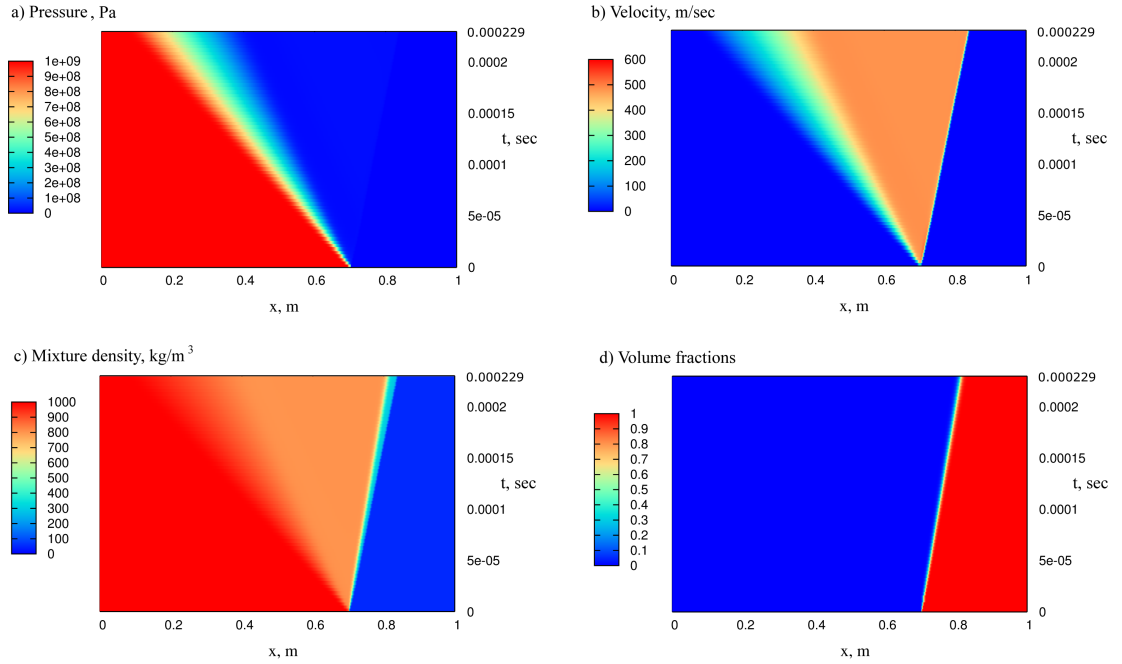


Figure 4.21: Water-air test example 4.6.3: Two-dimensional surface plot for time evolution for: (a) pressure, (b) velocity, (c) mixture density and (d) volume fraction.

The spatial convergence for the three solvers is demonstrated in Figure 4.23. As the mesh is refined, the L_2 error norm for the flow variables predicted by the three solvers is decreased as shown in Figure 4.23. A comparison between the three solvers is carried out in terms of pressure (a), velocity (b), mixture density (c) and volume fraction (d) for the water-air test. It is apparent that the VFRoe solver gave better results for pressure than the other solvers as shown in Figure 4.23(a). The results from the HLLC solver for pressure becomes closer to that obtained from the VFRoe solver at about 1000 cells. It can be seen from Figure 4.23(b), (c) and (d) that the HLLC solver produced results for the velocity, mixture density and volume fraction with lower L_2 norm than the other solvers. For resolutions more than 400 cells both the HLLC and VFRoe solvers have almost identical L_2 norms for the velocity,

Table 4.20: The number of time steps and CPU time for water-air test using SG EOS

Mesh cells	HLL		HLLC		VFRoe	
	Time step	CPU (s)	Time step	CPU (s)	Time step	CPU (s)
200	274	0.14	276	0.19	277	0.29
1000	1351	3.47	1354	4.74	1354	6.90
5000	6737	89.06	6739	126.35	6739	177.74
10000	13469	377.62	13471	507.94	13471	712.68
25000	33665	2309.82	33667	2632.61	33667	3959.52
50000	67325	9888.74	67327	11286.99	67327	18819.12

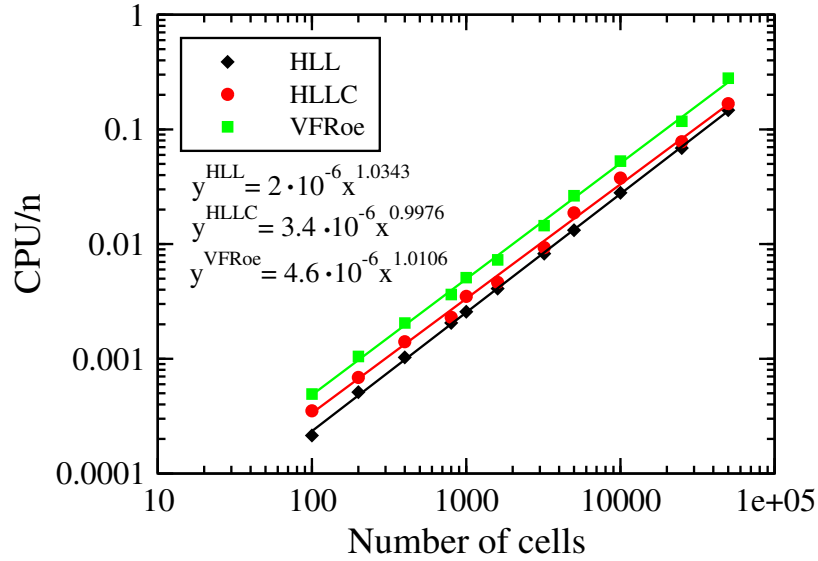


Figure 4.22: Water-air test example 4.6.3: Scaling order for the HLL, HLLC and VFRoe algorithms.

mixture density and volume fraction.

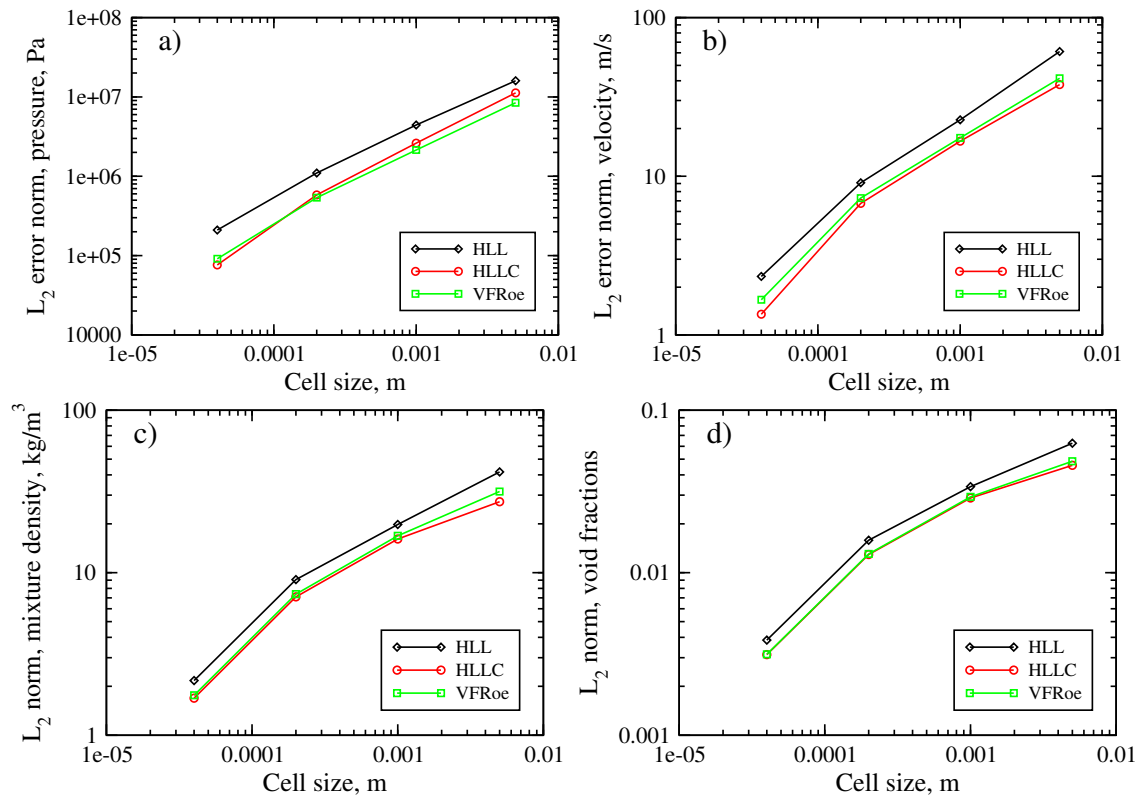


Figure 4.23: Water-air test example 4.6.3: L_2 error norm spatial convergence for: (a) pressure, (b) velocity, (c) mixture density and (d) volume fraction.

The order of accuracy of the HLL, HLLC and VFRoe algorithms for the results of the water-air test are given in Tables 4.21-4.23. It can also be observed that the order of accuracy is less than 2 due to the presence of the discontinuities in the solution as mentioned previously.

Table 4.21: Order of accuracy of the HLL for water-air test using SG EOS

Mesh cells	L_2		Order	
	p	α	p	α
200	15989621.1	0.06264		
1000	4429353.16	0.033874	0.79760	0.38197
5000	1100104.052	0.015855	0.86543	0.47169
25000	210110.271	0.003845	1.02863	0.88025

Table 4.22: Order of accuracy of the HLLC for water-air test using SG EOS

Mesh cells	L_2		Order	
	p	α	p	α
200	11234224.68	0.045806		
1000	2612823.108	0.02882	0.90624	0.28789
5000	582268.5232	0.012944	0.93278	0.49734
25000	76257.27703	0.00313	1.26306	0.88205

Table 4.23: Order of accuracy of the VFRoe for water-air test using SG EOS

Mesh cells	L_2		Order	
	p	α	p	α
200	8445342.897	0.048507		
1000	2143944.264	0.029296	0.85183	0.31331
5000	537371.1865	0.013049	0.85975	0.50250
25000	91124.781	0.003145	1.10253	0.88410

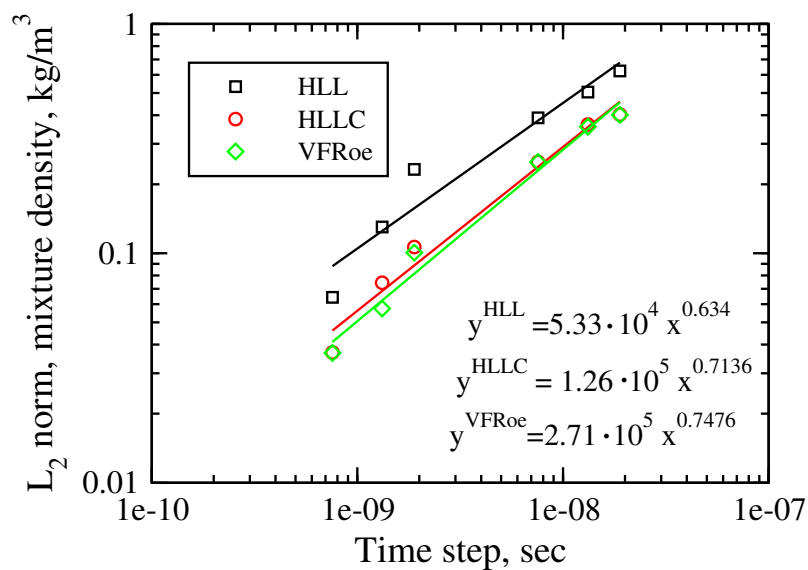


Figure 4.24: Water-air test example 4.6.3: Temporal convergence for the HLL, HLLC and VFRoe algorithms.

The temporal convergence is obtained using a fine mesh resolution of 10000 cells and various time steps. The order of temporal convergence for the HLL, HLLC and VFRoe solvers are 0.634, 0.7136 and 0.7476, respectively, as shown in Figure 4.24.

4.7 Numerical results - Comparison between EOSs

In this section comparisons between various EOSs are carried out using the three solvers. The first test is a single-phase liquid-liquid test which is used to compare the SG and Tait EOSs that are employed to govern water. The second test is a two-phase helium-air test which is used to compare the IG and vdW EOSs that are employed to govern air in case of gas-gas test. The third test is also a two-phase water-air test which is used to compare the IG and vdW EOSs that are employed to govern air in the case of the liquid-gas test. The last test is a water faucet test which is used to compare the SG and Tait EOSs that govern water and IG and vdW EOSs that govern air. The comparisons are done in terms of L_2 error norm, number of time steps and the CPU time required to obtain the solution.

4.7.1 Liquid-liquid test

The description of this test is given in subsection 4.6.1. The test is conducted here to compare the SG (4.21) and Tait (4.27) EOSs using the HLLC approximate Riemann solver. The initial conditions are given in Table 4.9. The parameters for the SG EOS are $\gamma = 4.4$ and $\pi = 6 \times 10^8$ Pa, whereas for the Tait EOS are given as $\gamma = 7.15$ and $B = 3.31 \times 10^8$ Pa.

Figure 4.25 shows a comparison between the SG and Tait EOSs for the liquid-liquid test. The comparison is carried out at instant $t = 80 \mu s$ using the HLLC approximate Riemann solver with 25000 cells to show the difference between these EOSs. The exact solution of the Riemann problem depends on the EOS governing the fluids under consideration. It can be observed that both EOSs gave the same behaviour. However, the SG EOS gave 4.65% and 0.075% more values than the Tait EOS for the pressure and velocity, respectively. Whereas the Tait EOS gave 0.36% more values than the SG EOS for the mixture density. Moreover, there is a slight difference in the position of the shock wave, i.e. shock positions predicted by the SG and Tait EOSs are 0.80492 m and 0.80018 m, respectively. In addition, a slight difference can be noticed in the expansion rarefaction wave. However, no difference can be observed in the position of the contact discontinuity, $x = 0.6703$ m, which can be identified in Figures 4.25(c) and 4.25(d) for the mixture density and volume fractions, respectively. These differences appear in the solution because the exact solution depends on the EOS used to govern the flow components.

The number of time steps and CPU times needed by the HLLC solver to obtain the solution for different mesh resolutions are given in Table 4.24 using the SG and

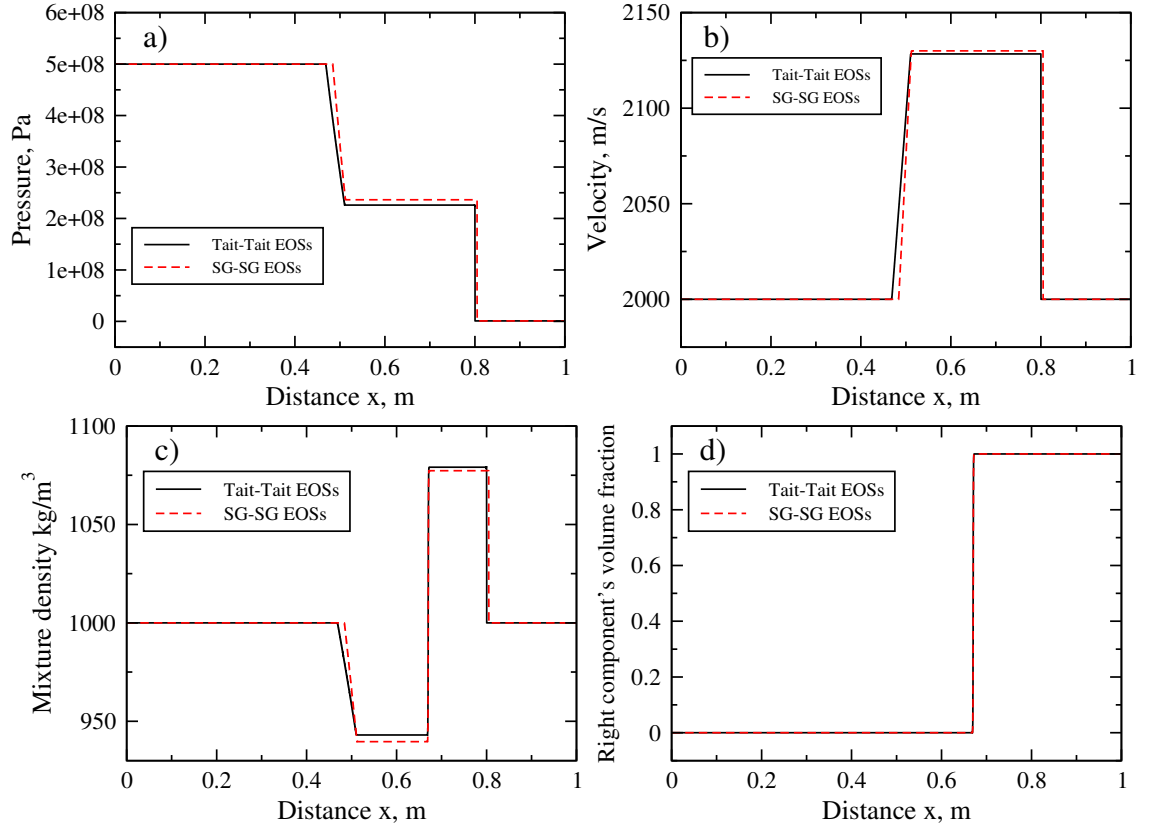


Figure 4.25: Liquid-liquid test example 4.7.1: Comparison between the SG and Tait EOSs using HLLC Riemann solver with 25000 cells at $t = 80 \mu\text{s}$ for: (a) pressure, (b) velocity, (c) mixture density and (d) volume fraction.

Table 4.24: The number of time steps and CPU time for liquid-liquid test using HLLC.

Mesh cells	SG EOS		Tait EOS	
	Time step	CPU (s)	Time step	CPU (s)
200	79	0.04	83	0.05
1000	378	1.10	395	1.15
5000	1871	27.41	1956	28.59
10000	3738	108.61	3908	113.48
25000	9338	719.24	9764	782.50
50000	18671	3172.63	19523	3252.63

Tait EOSs. There are slight differences between the two EOSs in the number of time steps and CPU times required by this solver to obtain the solution for this test problem, where the SG EOS needs 4.38 % number of time steps and 7.22 % CPU time less than the Tait EOS. The scaling order for the HLLC solver using the SG and Tait EOSs for the liquid-liquid test are 1.0403 and 1.0341, respectively, as shown Figure 4.26.

The spatial convergence for the HLLC solver when water is either governed by the Tait or SG EOSs is shown in Figure 4.27. The order of accuracy of the HLLC

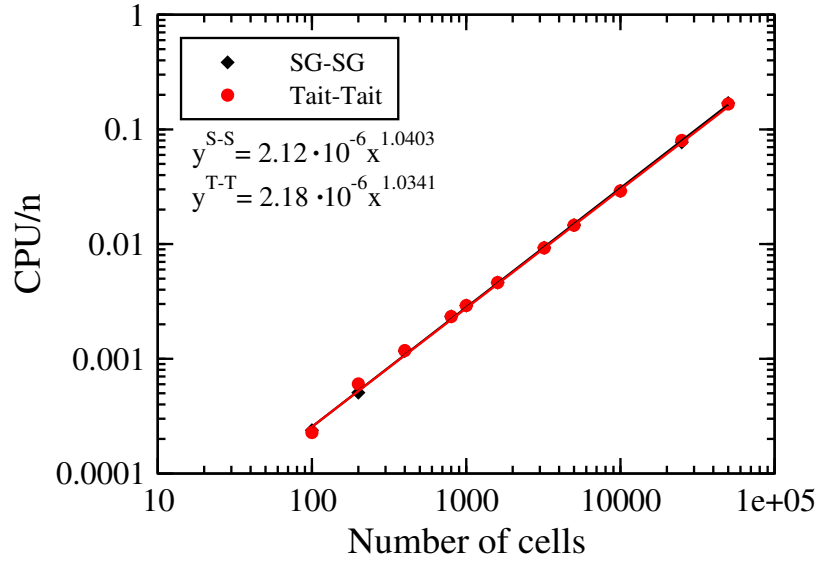


Figure 4.26: Liquid-liquid test example 4.7.1: Scaling order for the HLLC algorithm using the SG and Tait EOSs.

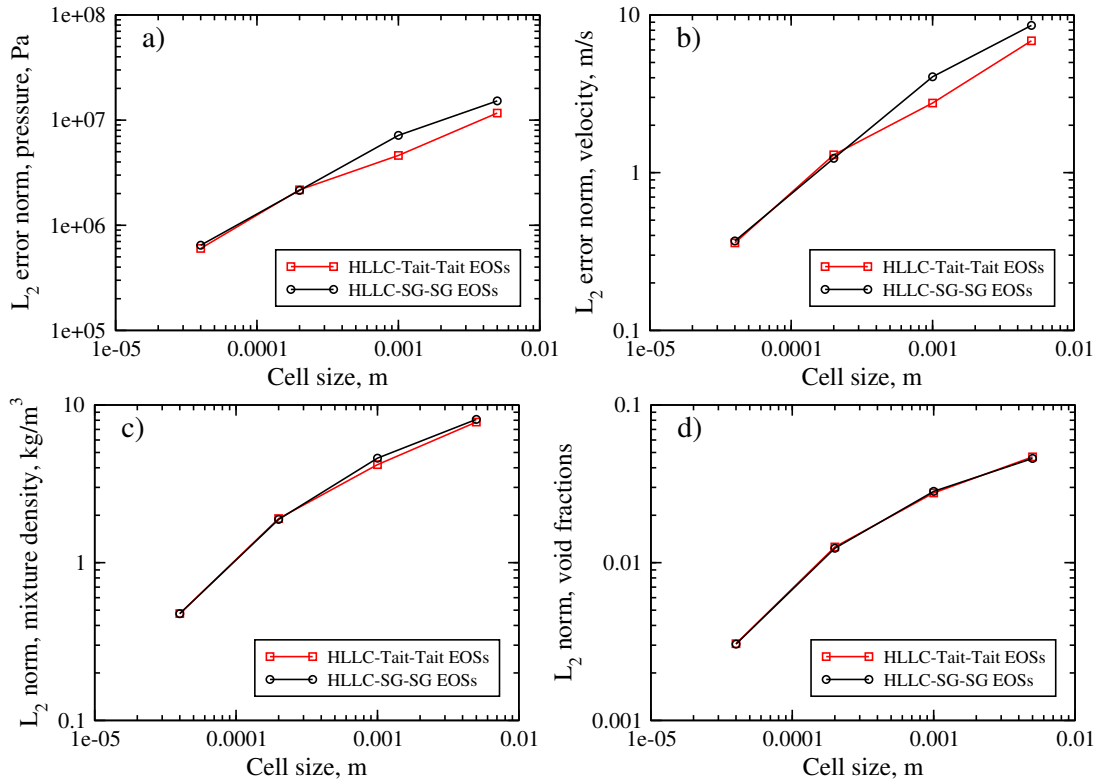


Figure 4.27: Liquid-liquid test example 4.7.1, L_2 error norm spatial convergence for: (a) pressure, (b) velocity, (c) mixture density and (d) volume fraction.

algorithm for the liquid-liquid test when water is either governed by the Tait or SG EOSs are given in Tables 4.25 and 4.26. It can also be observed that the order of accuracy is less than 2 due to the presence of the discontinuities in the solution as mentioned previously.

The temporal convergence is obtained using a fine mesh resolution of 10000 cells and various time steps. The order of temporal convergence for the HLLC solver when

water is either governed by the SG or Tait EOSs are 1.1783 and 1.157, respectively, as shown in Figure 4.28.

Table 4.25: Order of accuracy of the HLLC for liquid-liquid test using SG EOS

Mesh cells	L_2		Order	
	p	ρ	p	ρ
200	15222668.74	8.100902		
1000	7154702.837	4.600686	0.46912	0.35153
5000	2147424.75	1.88054	0.74778	0.55588
25000	646095.74	0.474834	0.74627	0.85517

Table 4.26: Order of accuracy of the HLLC for liquid-liquid test using Tait EOS

Mesh cells	L_2		Order	
	p	ρ	p	ρ
200	11655835.9	7.793681		
1000	4606985.564	4.186563	0.57674	0.38612
5000	2172355.456	1.903025	0.46710	0.48988
25000	601424.499	0.475616	0.79796	0.86154

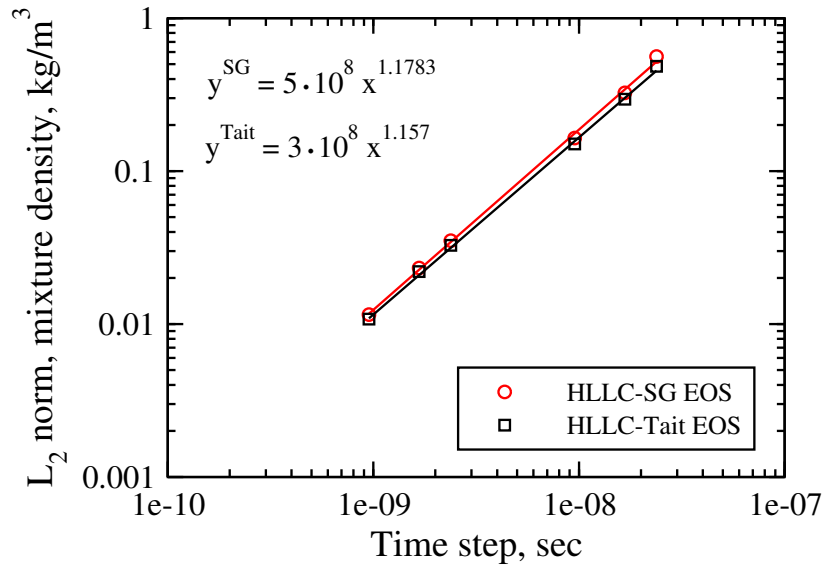


Figure 4.28: Liquid-liquid test example 4.7.1: Temporal convergence for the HLLC algorithms using the SG and Tait EOS.

4.7.2 Helium-air test

This test is described in subsection 4.6.2. Two simulations were conducted, in the first simulation air is governed by the IG EOS (4.14) and in the second simulation

air is governed by the vdW EOS (4.30). The vdW EOS constant parameters are $\gamma = 1.4$, $a = 5 \text{ Pa m}^6/\text{kg}$ and $b = 10^{-3} \text{ m}^3/\text{kg}$. The initial conditions are given in Table 4.14.

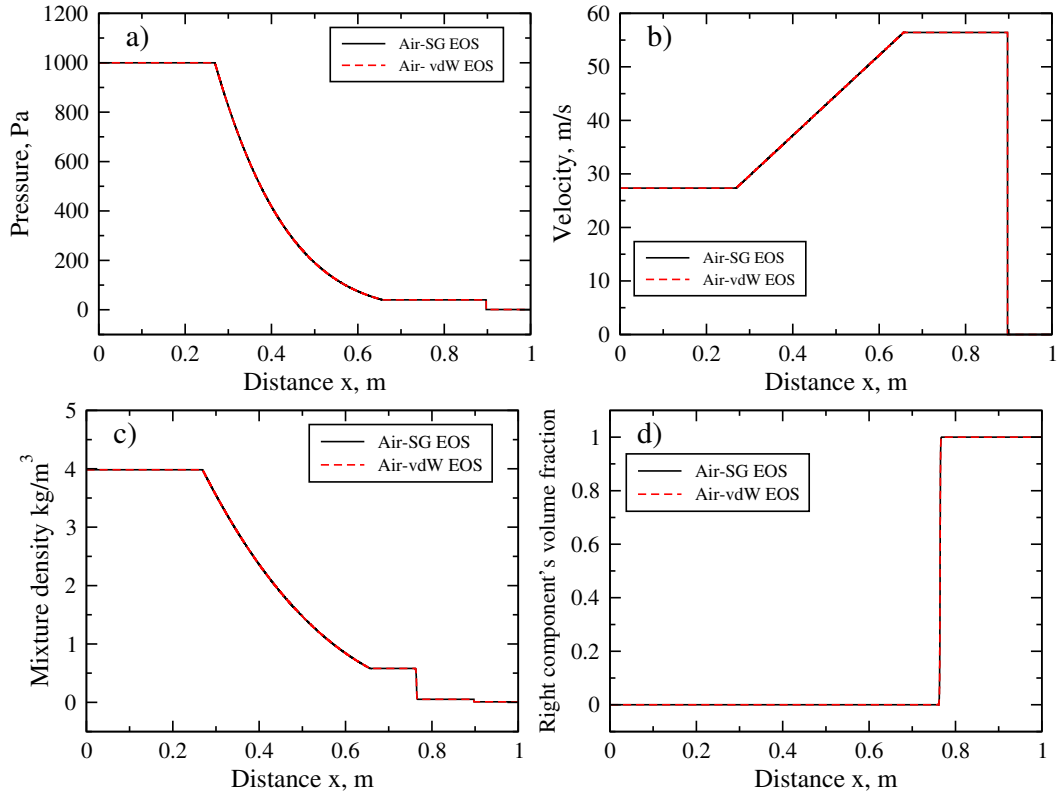


Figure 4.29: Helium-air test example 4.7.2: Comparison between IG and vdW EOSs at $t = 0.01 \text{ s}$ for: (a) pressure, (b) velocity, (c) mixture density and (d) volume fraction.

A comparison between the IG (4.14) and vdW (4.30) EOSs is shown in Figure 4.29 using the VFRoe solver for pressure (a), velocity (b), mixture density (c) and volume fraction (d). It is clear from this figure that both EOSs predict the same position of the shock, contact discontinuity and rarefaction waves.

The number of time steps and the CPU time needed by the VFRoe solver to obtain the solution for helium-air test using the IG (4.14) and vdW (4.30) EOSs with different mesh resolutions are given in Table 4.27. It can be seen that the IG EOS needs 2.58 % less CPU time than that required by the vdW EOS to obtain the solution. The required number of time steps for both EOSs are almost the same for all mesh resolutions. The scaling order for the VFRoe solver for the helium-air test when air is governed by either the IG or vdW EOS are 1.0106 and 1.0135, respectively, as shown Figure 4.30

A comparison of the L_2 error norm is carried out for the IG (4.14) and vdW (4.30) EOSs using the VFRoe solver. The results of spatial convergence are shown in Figure 4.31 for pressure (a), velocity (b), mixture density (c) and volume fraction (d). It can be seen that both EOSs have the same error L_2 for the pressure (a), velocity (b), mixture density (c) and volume fraction (d) for all mesh resolutions

Table 4.27: The number of time steps and the CPU time for helium-air test using VFRore

Mesh cells	IG EOS		vdW EOS	
	Time step	CPU (s)	Time step	CPU (s)
100	453	0.23	453	0.23
200	900	0.92	900	0.95
1000	4470	22.70	4470	23.41
5000	22315	586.82	22313	609.76
10000	44622	2410.92	44620	2459.60
25000	111542	15032.27	111540	15581.51

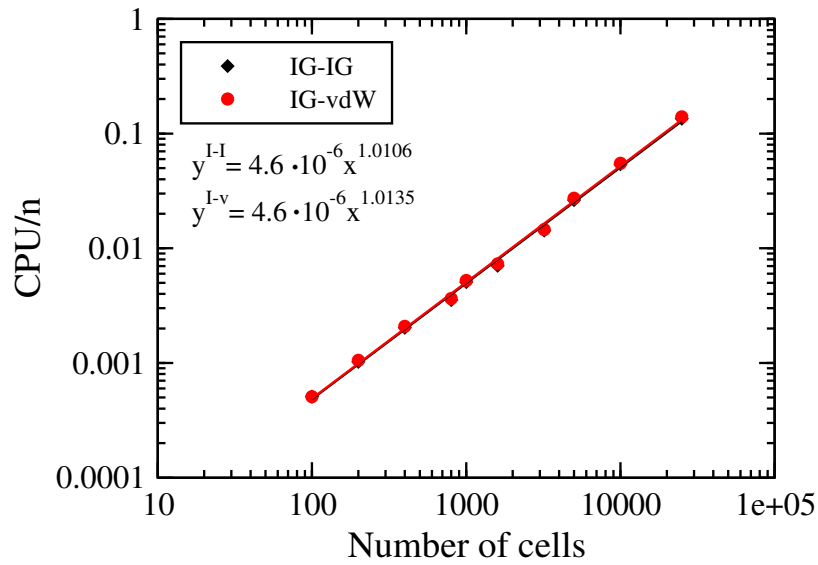


Figure 4.30: Helium-air test example 4.7.2: Scaling order for the VFRoe algorithm using the IG and vdW EOSs.

as shown in Figure 4.31. The order of accuracy of the VFRoe algorithm for the helium-air test when air is either governed by the IG or vdW EOSs are given in Tables 4.28 and 4.29. It can also be observed that the order of accuracy is less than 2 due to the presence of the discontinuities in the solution as mentioned previously.

Table 4.28: Order of accuracy of the VFRoe for helium-air test using IG EOS

Mesh cells	L_2		Order	
	u	α	u	α
200	5.503139	0.089501		
1000	2.292497	0.041263	0.54409	0.48109
5000	0.933792	0.018097	0.55805	0.51212
25000	0.281199	0.00424	0.74572	0.90167

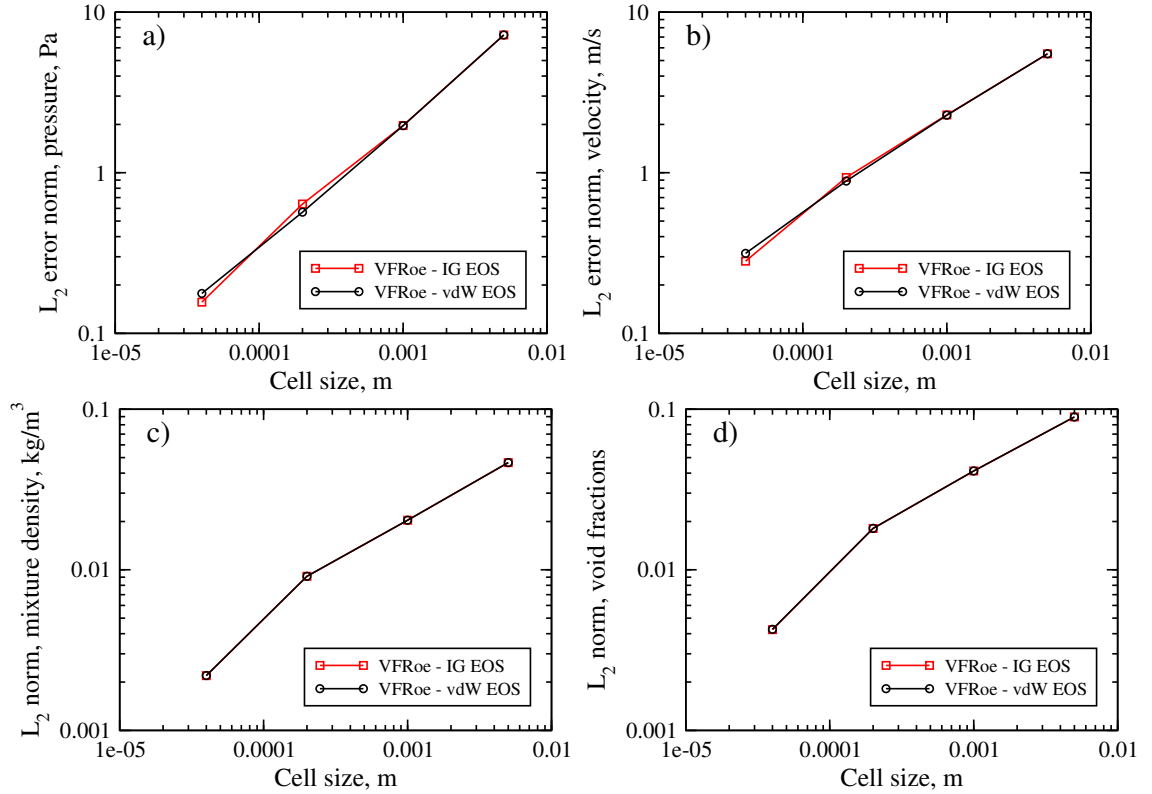


Figure 4.31: Helium-air test example 4.7.2: L_2 error norm spatial convergence for: (a) pressure, (b) velocity, (c) mixture density and (d) volume fraction.

Table 4.29: Order of accuracy of the VFRoe for helium-air test using vdW EOS

Mesh cells	L_2		Order	
	u	α	u	α
200	5.502491	0.08953		
1000	2.283164	0.041265	0.54655	0.48126
5000	0.886921	0.018111	0.58751	0.51167
25000	0.314617	0.004258	0.64395	0.89952

4.7.3 Water-air test

This test is described in subsection 4.6.3. Two different simulations were conducted by employing the IG and vdW EOSs using different mesh resolutions. Air is governed by the IG EOS (4.14) in the first simulation where $\gamma = 1.4$ and governed by the vdW EOS (4.30) in the second one where $\gamma = 1.4$, $a = 5 \text{ Pa m}^6/\text{kg}$ and $b = 10^{-3} \text{ m}^3/\text{kg}$. Water is governed by the SG EOS (4.21) in both simulation where $\gamma = 4.4$ and $\pi = 6 \times 10^8 \text{ Pa}$. Initial data are given in Table 4.19.

Figure 4.32 shows the results of the VFRoe solver for pressure, velocity, mixture density and volume fraction using a fine mesh resolution, in which the IG and vdW EOSs are employed. It can be seen that all values for pressure, velocity, mixture density and volume fraction obtained from both EOSs are the same. Moreover, the positions for the rarefaction and contact discontinuity are identical but the position

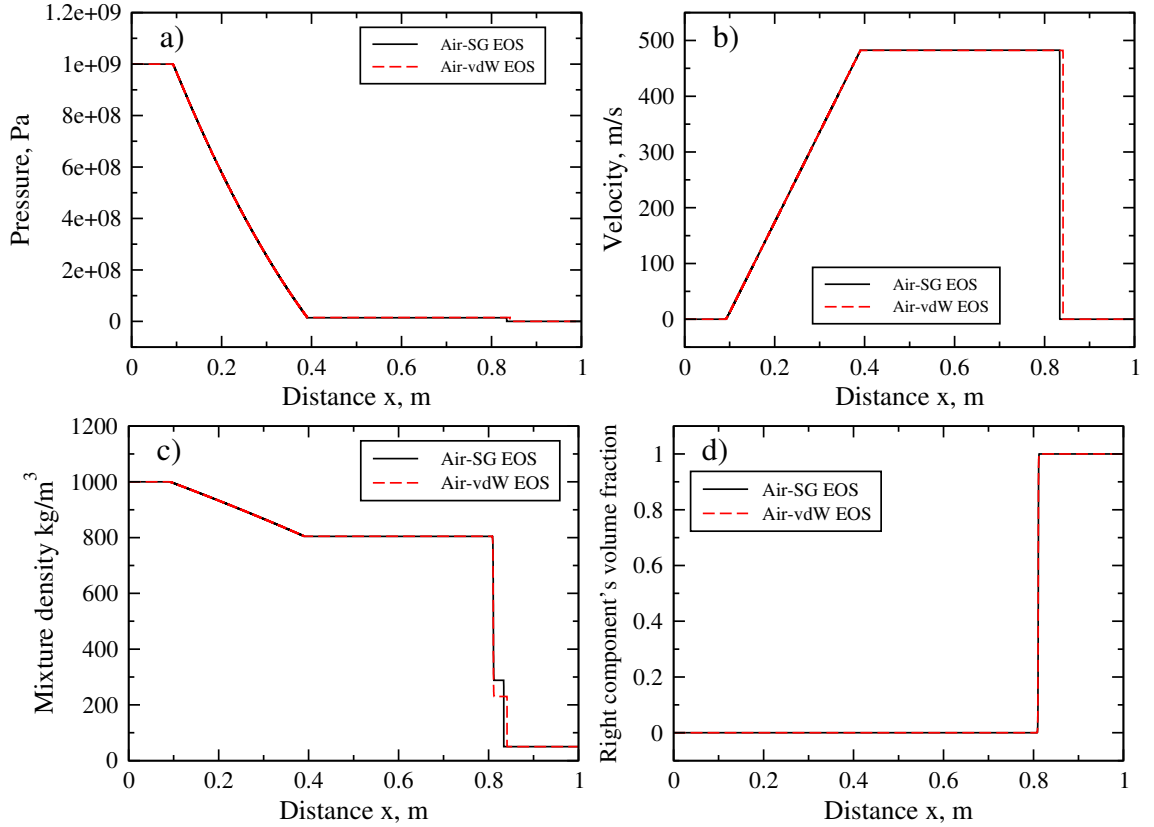


Figure 4.32: Water-air test example 4.7.3: Comparison between IG and vdW EOSs at $t = 229 \mu\text{s}$ for: (a) pressure, (b) velocity, (c) mixture density and (d) volume fraction.

of the shock wave was not identical, the positions predicted by the IG and vdW EOSs are $x = 0.83378 \text{ m}$ and $x = 0.84112 \text{ m}$, respectively.

The number of time steps and the CPU time required by the VFRoe solver to obtain the solution for the water-air test using different mesh resolutions for the IG and vdW EOSs are given in Table 4.30. It can be seen that the vdW EOS needs 2.51% more number of time steps than the IG EOS and 6.51% more CPU time than the IG EOS for this test problem. The scaling order for the VFRoe solver for the

Table 4.30: The number of time steps and the CPU time for water-air test using VFRoe.

Mesh cells	IG EOS		vdW EOS	
	Time step	CPU (s)	Time step	CPU (s)
200	277	0.29	144	0.30
1000	1354	6.90	1388	7.33
5000	6739	177.74	6913	187.63
10000	13471	712.68	13820	772.44
25000	33667	3959.52	34540	4879.39
50000	67327	18819.12	69075	17353.15

water-air test when air is governed by either the IG or vdW EOS are 1.0075 and 1.0117, respectively, as shown Figure 4.30

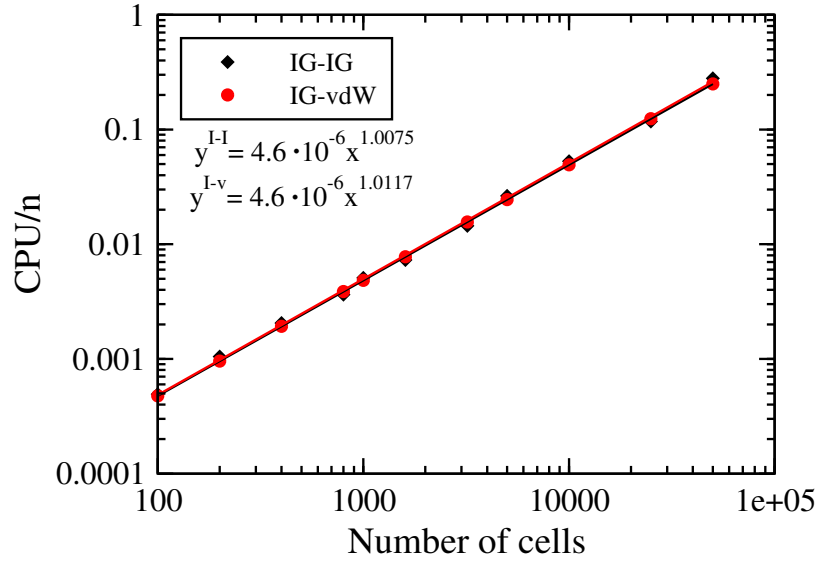


Figure 4.33: Water-air test example 4.7.3: Scaling order for the VFRoe algorithm using the IG and vdW EOSs.

Figure 4.34 shows the L_2 error norm for the water-air test, in which a comparison between both EOSs is carried out for the results of pressure (a), velocity (b), mixture density (c) and volume fraction (d). It can be observed that the solution converges

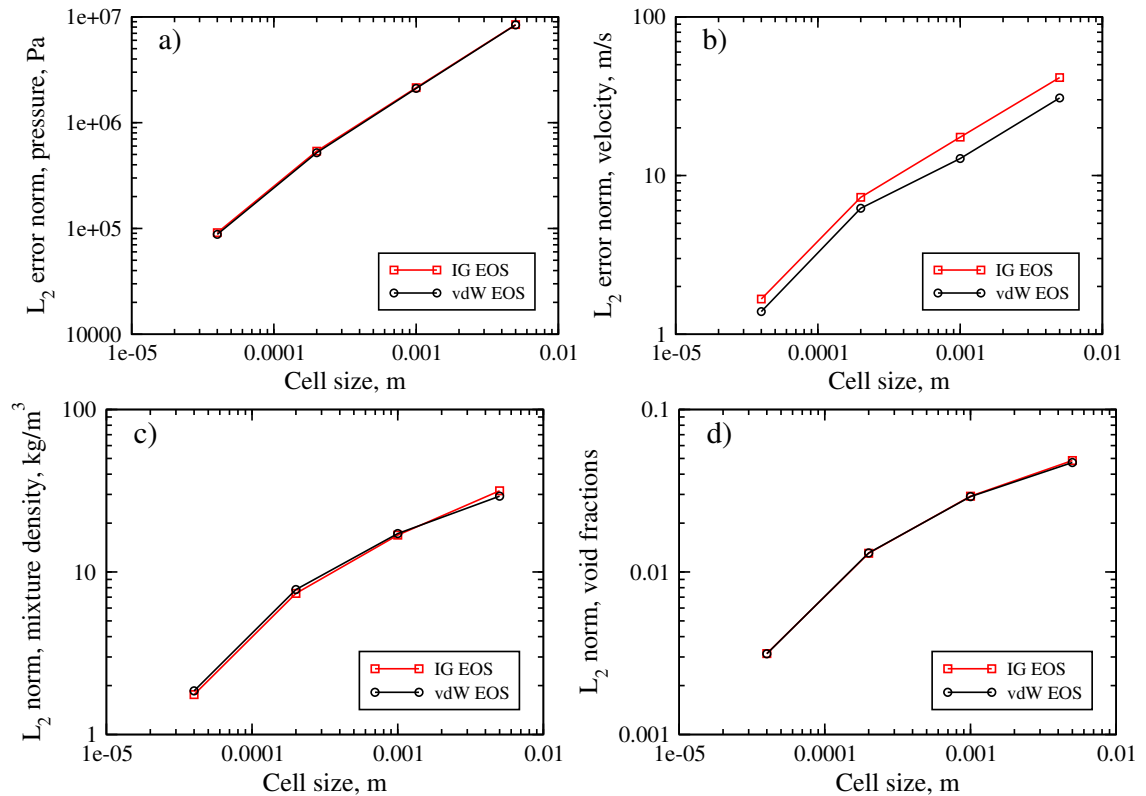


Figure 4.34: Water-air test example 4.7.3: L_2 error norm spatial convergence for: (a) pressure, (b) velocity, (c) mixture density and (d) volume fraction.

to the correct solution as the mesh is refined. The order of accuracy of the VFRoe algorithm for the water-air test when air is either governed by the IG or vdW EOSs are given in Tables 4.31 and 4.32. It can also be observed that the order of accuracy is less than 2 due to the presence of the discontinuities in the solution as mentioned previously.

Table 4.31: Order of accuracy of the VFRoe for water-air test using SG EOS

Mesh cells	L_2		Order	
	u	α	u	α
200	41.43568	0.048507		
1000	17.44702	0.029296	0.53744	0.31331
5000	7.286069	0.013049	0.54255	0.50250
25000	1.66605	0.003145	0.91679	0.8841

Table 4.32: Order of accuracy of the VFRoe for water-air test using vdW EOS

Mesh cells	L_2		Order	
	u	α	u	α
200	30.8431	0.047177		
1000	12.79782	0.029089	0.54655	0.30044
5000	6.223663	0.013092	0.44793	0.49605
25000	1.388419	0.003138	0.93212	0.88752

4.7.4 Water faucet test

This test is concerned with an incompressible two-phase flow. The test was proposed by Ransom (1987) where both phases behave as incompressible, but here they are treated with the current model (4.10) as fluids with a compressible behaviour. This test has been used to demonstrate the ability of the seven-equation compressible flow model (4.10) to solve incompressible flows. The test consists of a flow of water column surrounded by still air in a vertical tube with open ends. The water leaves the faucet and enters the tube, which is 12 m long, at a constant velocity $u_2^0 = 10$ m/s and volume fraction $\alpha_2^0 = 0.8$ and the air volume fraction is $\alpha_1^0 = 0.2$. The outflow boundary conditions set constant at atmospheric pressure. Due to the effect of gravity, the water accelerates and narrows as it moves down to maintain a constant flow rate as shown in Figure 4.35. The initial conditions are as given in Table 4.33. This test has become a benchmark test problem used to assess developed numerical codes. Moreover, the problem has an analytical solution that could be derived by assuming that the liquid is incompressible and neglecting the pressure variation in

Table 4.33: Initial data for water faucet test 4.7.4

State	ρ_1	u_1	p_1	α_1	ρ_2	u_2	p_2	α_2
	[kg/m ³]	[m/s]	[Pa]		[kg/m ³]	[m/s]	[Pa]	
	1	0	10 ⁵	0.2	1000	10	10 ⁵	0.8

liquid and interfacial drag between phases. The analytical solutions for the evolution of the air volume fraction and water velocity are as follows:

$$\alpha_1(x, t) = \begin{cases} 1 - \frac{\alpha_2^0 u_2^0}{\sqrt{2gx + (u_2^0)^2}} & \text{if } x \leq u_2^0 t + \frac{1}{2}gt^2, \\ \alpha_1^0 & \text{otherwise,} \end{cases} \quad (4.89a)$$

$$u_2(x, t) = \begin{cases} \sqrt{(u_2^0)^2 + 2gx} & \text{if } x \leq u_2^0 t + \frac{1}{2}gt^2, \\ u_2^0 + gt & \text{otherwise,} \end{cases} \quad (4.89b)$$

where, g is the gravity acceleration and t is the time.

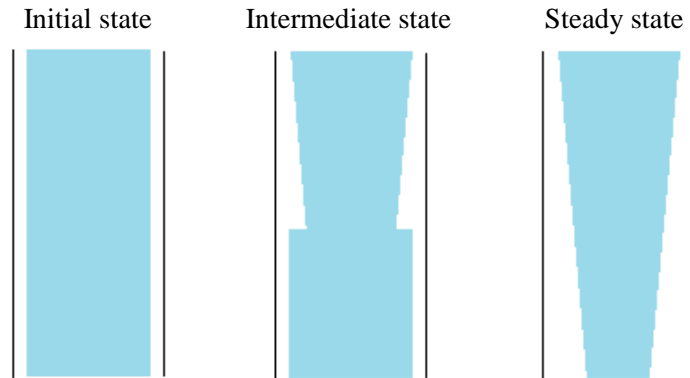


Figure 4.35: Water faucet test 4.7.4.

The constant parameters for water used for the Tait EOS (4.27) are $\gamma = 7.15$, $B = 3.31 \times 10^6$ Pa and for the SG EOSs are $\gamma = 4.4$, $\pi = 6 \times 10^6$ Pa as given in Andrianov (2003). The constant parameters for the air used for the IG (4.14) and vdW (4.30) EOSs are as given in the water-air test subsection 4.6.3. The gravitational effect is considered in the calculations for this test. However, the velocity relaxation process is suppressed during the solution of this problem because each fluid has a different velocity direction. Four different simulations are conducted for this test using various EOSs to govern water and air. EOSs used in these simulations are as given in Table 4.34. All results for this test are obtained at $t = 0.4$ s.

To show convergence of the results for this test, the same computations are performed using various mesh resolutions as shown in Figure 4.36. The results are shown for air volume fraction and water velocity for the first simulation, where the SG EOS (4.21) is employed to govern water and the IG EOS (4.14) to govern air.

Table 4.34: EOSs used to govern water and air for water faucet test 4.7.4.

Simulation	Water	Air
I	SG EOS	IG EOS
II	SG EOS	vdW EOS
III	Tait EOS	IG EOS
IV	Tait EOS	vdW EOS

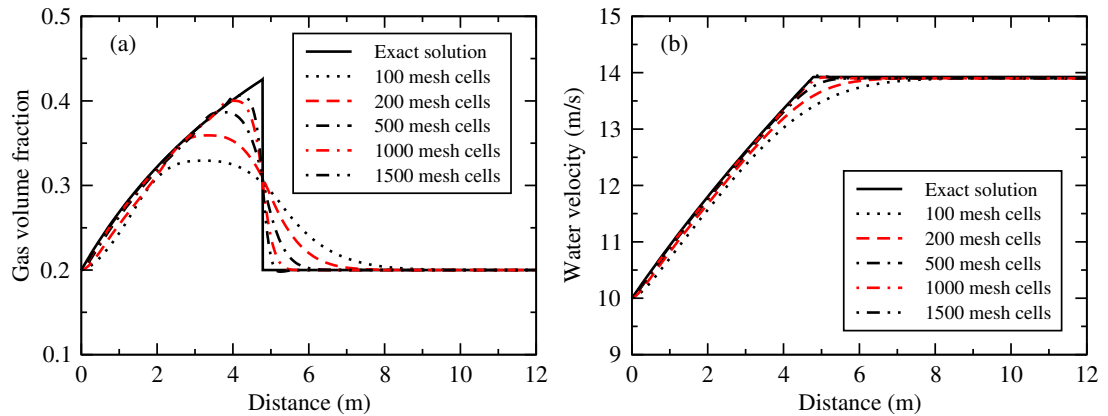


Figure 4.36: Water faucet test 4.7.4: Results using different mesh resolutions at $t = 0.4$ s. EOSs are for simulation (I) see Table 4.34: (a) air volume fraction and (b) water velocity.

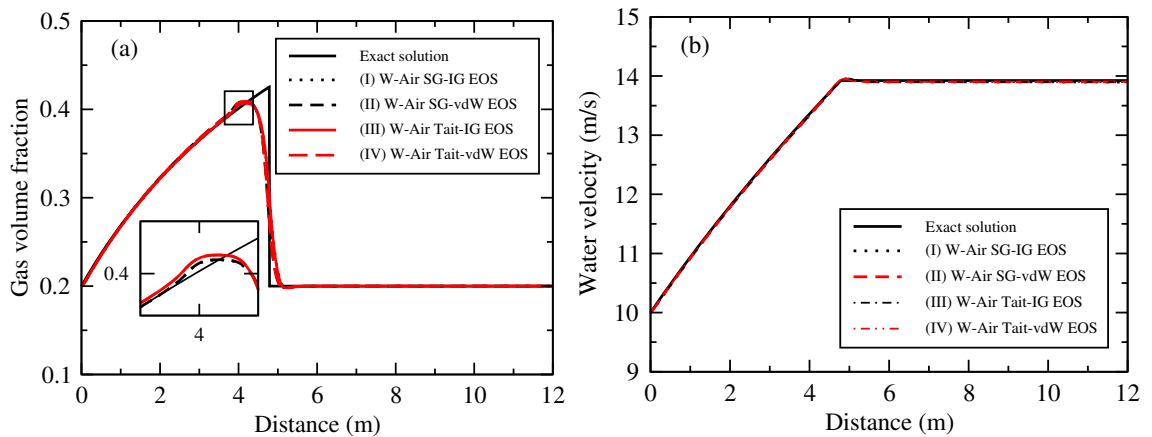


Figure 4.37: Water faucet test 4.7.4: Comparison between EOSs using 1500 cells for: (a) Air volume fraction (b) Water velocity. Curve (I) water is governed by SG EOS and air is governed by IG EOS. Curve (II) water is governed by SG EOS and air is governed by van der Waals EOS. Curve (III) water is governed by Tait's EOS and air is governed by IG EOS. Curve (IV) water is governed by Tait's EOS and air is governed by van der Waals EOS.

The results of the HLL approximate Riemann solver are compared to the exact solution. It can be noticed that a mesh of 100 cells gives a very diffusive solution, by increasing the number of cells the solution is improved.

Increasing the resolution more than 1500 cells would not improve much the results as an overshoot starts to grow as shown in Figure 4.37, which shows the

results for air volume fraction and water velocity for the four simulations using 1500 cells compared to the exact solution. The overshoot appears in the results of air volume fraction at 1500 cells, however, it does not appear in the results of the water velocity. An overshoot appears in the results of water velocity as the resolution is increased more than 1500 cells but with less amplitude than that in the results of the air volume fraction.

To compare the accuracy of the EOSs implemented in the four simulations, the error norm (L_2) is calculated using the equation (4.87). The results are shown in Figure 4.38 for the air volume fraction (a) and water velocity (b). It can be noticed that the error decreases as the number of cells increases. One can observe that the results of all EOSs are exactly the same for mesh resolutions of 1000 cells or less, however, when the number of cells is increased to 1500 cells the SG EOS governing water have less air volume fraction error norm (L_2) than that produced when water is governed by the Tait EOS as shown in Figure 4.38(a). Moreover, one can notice that the results obtained when air is governed by either the IG EOS or vdW EOS are identical in this test.

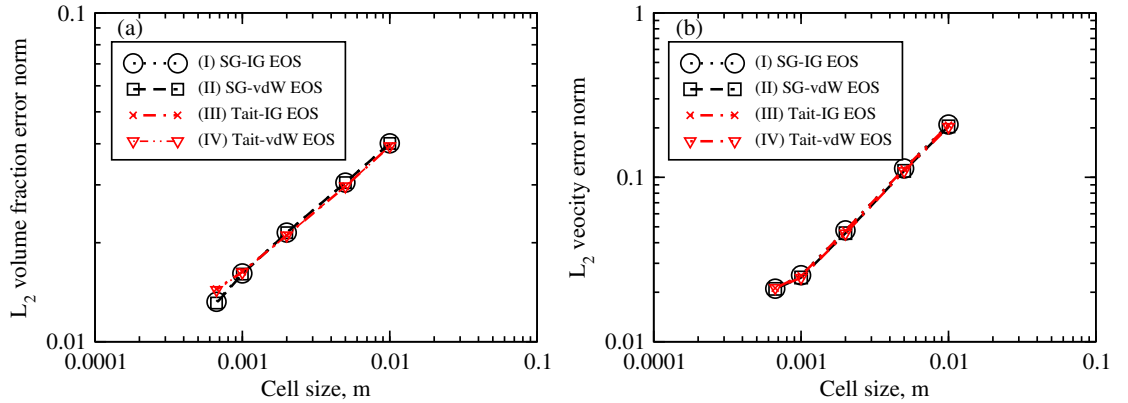


Figure 4.38: Water faucet test 4.7.4: L_2 error norm spatial convergence for: (a) Air volume fraction (b) Water velocity. Curve (I) water is governed by SG EOS and air is governed by IG EOS. Curve (II) water is governed by SG EOS and air is governed by van der Waals EOS. Curve (III) water is governed by Tait's EOS and air is governed by IG EOS. Curve (IV) water is governed by Tait's EOS and air is governed by van der Waals EOS.

The number of time steps and the CPU time for the first two simulations (I, II) are given in Table 4.35 where water is governed by the SG EOS and air is either governed by the IG EOS or the vdW EOS. It can be noticed that at relatively low mesh cells both the IG and vdW EOSs need almost the same number of time steps and CPU time to obtain the results. However, at higher mesh resolutions the vdW EOS needs more number of time steps and CPU time to obtain the results. The number of time steps and the CPU time for the last two simulations (III, IV) are given in Table 4.36 where water is governed by the Tait EOS and air is either governed by the IG EOS or the vdW EOS. One can observe the same notice for the

Table 4.35: The number of time steps and the CPU run time for water faucet: (I) water is governed by SG EOS and air is governed by IG EOS. (II) water is governed by SG EOS and air is governed by van der Waals EOS.

Mesh cells	I		II	
	Time step	CPU time (s)	Time step	CPU time (s)
100	2130	0.49	2133	0.55
200	4257	1.94	4263	2.19
400	8511	7.79	8637	8.82
800	17021	30.92	17589	35.98
1600	34042	123.78	35752	145.66

Table 4.36: The number of time steps and the CPU run time for water faucet: (III) water is governed by Tait's EOS and air is governed by IG EOS. (IV) water is governed by Tait's EOS and air is governed by van der Waals EOS.

Mesh cells	III		IV	
	Time step	CPU time (s)	Time step	CPU time (s)
100	2130	0.49	2133	0.55
200	4257	1.94	4263	2.19
400	8511	7.74	8641	8.83
800	17020	30.92	17600	35.90
1500	34039	123.84	35783	146.40

first two simulations that at relatively low mesh cells both the IG and vdW EOSs need almost the same number of time steps and CPU time to obtain the results. However, once again at higher mesh resolutions the vdW EOS needs more number of time steps and CPU time to obtain the results. Referring to the Tables 4.35 and 4.36, it can be observed that the SG and Tait's EOS for water with either the IG or vdW EOSs for air need the same number of time steps and CPU time to obtain the solution for the water faucet test problem. The scaling order for the HLL solver for the water faucet test when air is governed by either the IG or vdW EOS and water is governed by the SG or Tait EOS are 1.0007, 0.9927, 1.0005, and 0.9927, respectively, as shown Figure 4.39.

The order of accuracy of the HLL algorithm for the results of the water faucet test when air is governed by either the IG or vdW EOS and water is governed by the SG or Tait EOS are given in Tables 4.37-4.40. It can also be observed that the order of accuracy is less than 2 due to the presence of the discontinuities in the solution as mentioned previously.

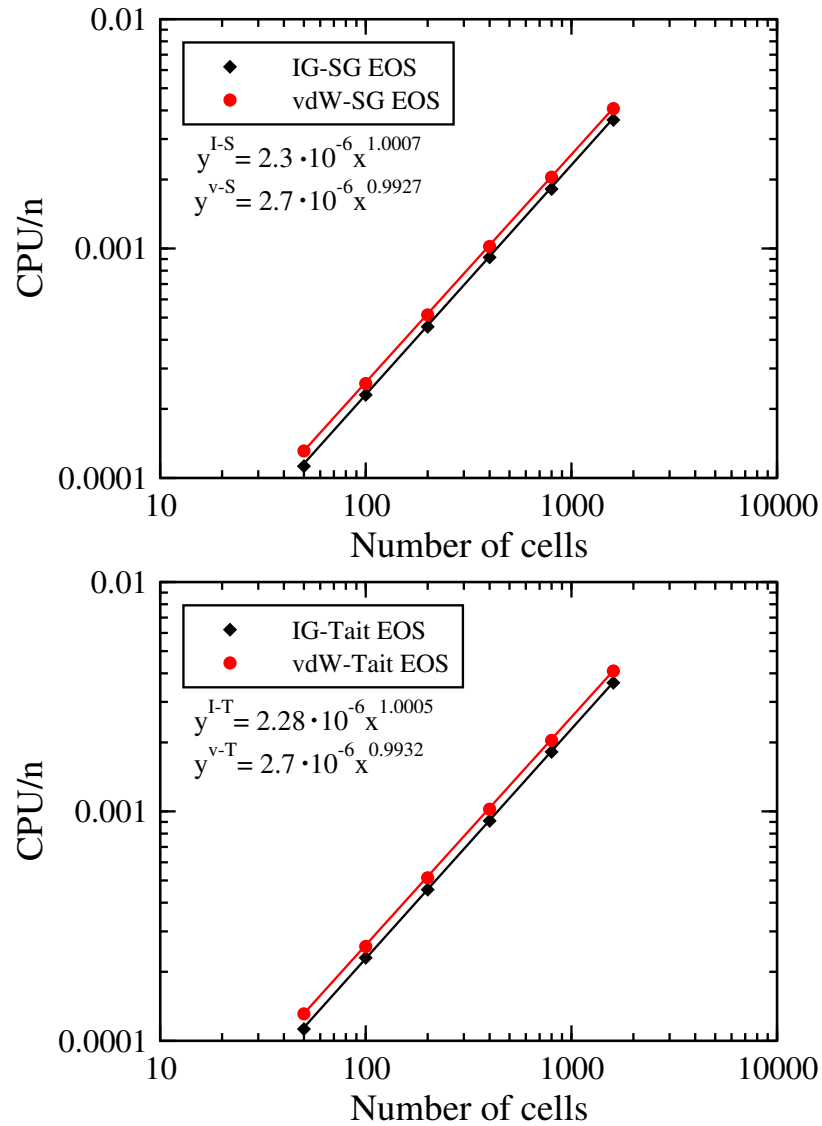


Figure 4.39: Water faucet test example 4.7.4: Scaling order for the HLL algorithm using the IG and vdW EOSs for air (up) and the SG and Tait EOSs for water (bottom).

Table 4.37: Order of accuracy of the HLL for water faucet test using IG-SG EOSs

Mesh cells	L_2		Order	
	u	α	u	α
100	0.208358	0.039915605		
200	0.112785	0.030388151	0.88549	0.39344
400	0.058858	0.023329027	0.93826	0.38138
800	0.030487	0.017742144	0.94904	0.39495
1600	0.020939	0.01264222	0.54200	0.48893

Table 4.38: Order of accuracy of the HLL for water faucet test using vdW-SG EOSs

Mesh cells	L_2		Order	
	u	α	u	α
100	0.206434	0.0398740		
200	0.112399	0.0303946	0.87705	0.39163
400	0.058666	0.0233271	0.93803	0.3818
800	0.030246	0.0176981	0.95578	0.39841
1600	0.021131	0.0125256	0.51738	0.49872

Table 4.39: Order of accuracy of the HLL for water faucet test using IG-Tait EOSs

Mesh cells	L_2		Order	
	u	α	u	α
00	0.20317553	0.039153354		
200	0.109149204	0.029597803	0.89643	0.40365
400	0.05661945	0.0227722	0.94693	0.37822
800	0.029263268	0.017589967	0.95221	0.37252
1600	0.020962643	0.013809866	0.48127	0.34905

Table 4.40: Order of accuracy of the HLL for water faucet test using vdW-Tait EOSs

Mesh cells	L_2		Order	
	u	α	u	α
100	0.201416325	0.039124334		
200	0.108803894	0.029613733	0.88845	0.4018
400	0.056409279	0.022777004	0.94773	0.37869
800	0.029175376	0.017547306	0.95118	0.37633
1600	0.021284288	0.013681942	0.45496	0.35898

Chapter 5

The six-equation compressible two-phase flow model

The two-phase flow model studied in the previous chapter, i.e. the seven-equation model, is a full non-equilibrium model. In this model each fluid has its own thermodynamic variables and is described by its own pressure and velocity. The proposed instantaneous relaxation methods for the pressure and velocity within the model have enabled a study of a wide range of applications (Saurel and Abgrall, 1999a). However, the large number of waves that exist in its solution are considered as a disadvantage (Zein, Hantke and Warnecke, 2010).

Many authors have studied a two-phase flow model which has less equations. This model is known as a *reduced model* or a *five-equation model* (Kapila, Menikoff and Stewart, 2001; Murrone and Guillard, 2005; Petitpas et al., 2007; Saurel, Petitpas and Abgrall, 2008). This model is derived by Kapila, Menikoff and Stewart (2001) from the seven-equation model of Baer and Nunziato (1986) by using an asymptotic limit of zero velocity and pressure relaxation times. The model consists of mass equation for each fluid, a mixture momentum equation and a mixture energy equation. These equations are written in conservative forms. The model is complemented with the non-conservative equation for the volume fraction evolution. This model has shown its ability to compute interface problems between compressible materials accurately as well as wave propagation in compressible two-phase mixtures for problems concerning strong shocks (Murrone and Guillard, 2005).

However, the existence of the non-conservative equation poses some significant numerical difficulties. These difficulties are related to shock computations due to the non-conservative model. Moreover, the non-monotonic behaviour of the mixture sound speed with respect to the volume fraction is shown in Figure 5.1 which results in inaccuracies in waves transmission across interfaces as shown in Figure 5.2. The five-equation model uses the Wood equation (5.1) to obtain the speed of sound for a mixture of two fluids:

$$\frac{1}{\rho c^2} = \frac{\alpha_1}{\rho_1 c_1^2} + \frac{\alpha_2}{\rho_2 c_2^2}. \quad (5.1)$$

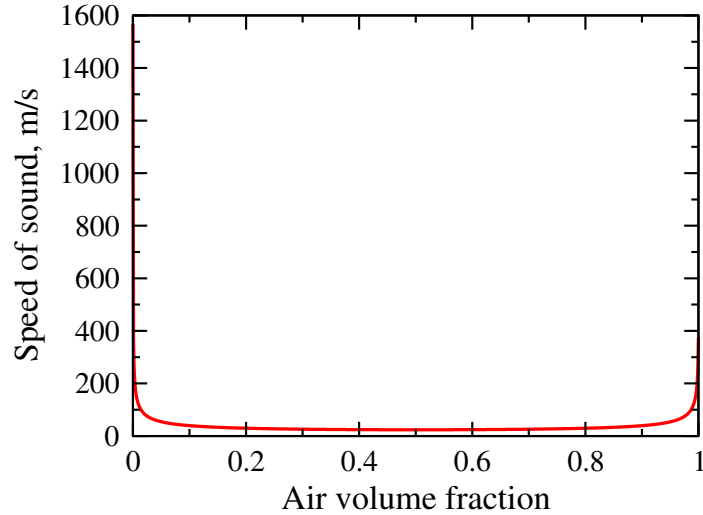


Figure 5.1: Speed of sound of the 5-equation model versus air volume fraction for water-air mixture. The densities and speeds of sound for water and air are: $\rho_{water} = 1000 \text{ kg/m}^3$, $c_{water} = 1568 \text{ m/s}$, $\rho_{air} = 1 \text{ kg/m}^3$ and $c_{air} = 374 \text{ m/s}$.

In addition, there are difficulties in maintaining positivity of the volume fraction due to the difficulties in the approximation of the velocity divergence term in the volume fraction equation. Furthermore, the assumption of pressure equilibrium causes the major difficulty in the numerical solution of the five-equation model of Kapila, Menikoff and Stewart (2001).

To overcome these difficulties is to use the other reduced model of Kapila, Menikoff and Stewart (2001) which was also derived from the generic seven-equation model of Baer and Nunziato (1986). This model was obtained in the asymptotic limit of zero velocity relaxation time. It consists of two mass balance equations, a mixture momentum equation, two energy equations and is complemented by the

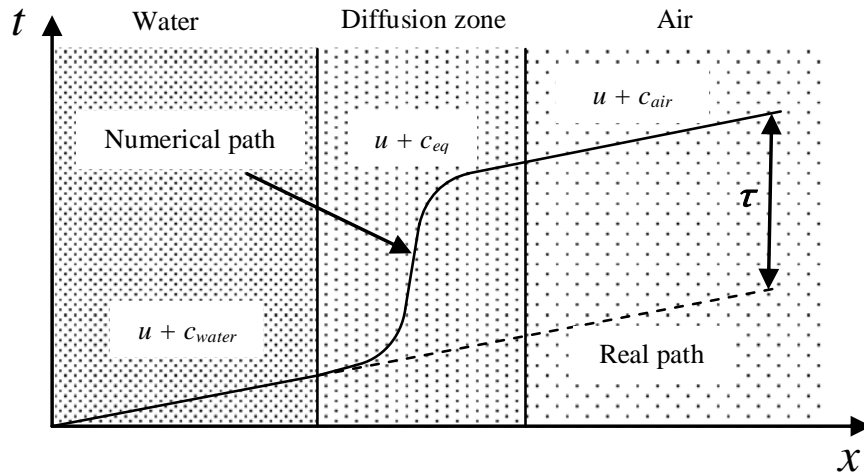


Figure 5.2: Wave transmission time delay τ through the numerical diffusion zone of an interface (Saurel, Petitpas and Berry, 2009).

volume fraction evolution equation of one of the phases. This model is called the *six-equation* model which differs from that used by Stewart and Wendroff (1984) and Toumi and Raymond (1995). This model was validated by Saurel, Petitpas and Berry (2009), who also showed that the main difficulties for the five-equation model can be circumvented. This is realised by restoring the effects of pressure non-equilibrium in the equation of the volume fraction evolution by using two pressures and associated pressure relaxation terms. The numerical simulations using the framework of the six-equation model were conducted in Saurel, Petitpas and Berry (2009) and Zein, Hantke and Warnecke (2010). It was shown in Saurel, Petitpas and Berry (2009) that the Abgrall's criterion (Abgrall, 1996) related to the uniformity of pressure and velocity is naturally satisfied and the applied numerical approximation preserves mechanical equilibrium conditions at the interface.

5.1 Partially equilibrium two-phase flow mathematical model

The six-equation compressible two-phase flow model is a partially equilibrium model. In this model, both fluids have the same velocity but each fluid has its own pressure. The model consists of the evolution equation for the volume fraction of one of the phases, the mass equations for each phase, a mixture momentum equation and the energy equations for each phase. The non-conservative hyperbolic model in one dimension without heat and mass transfer can be written in the following form:

$$\frac{\partial \alpha_1}{\partial t} + u \frac{\partial \alpha_1}{\partial x} = \mu(p_1 - p_2), \quad (5.2a)$$

$$\frac{\partial \alpha_1 \rho_1}{\partial t} + \frac{\partial \alpha_1 \rho_1 u}{\partial x} = 0, \quad (5.2b)$$

$$\frac{\partial \alpha_2 \rho_2}{\partial t} + \frac{\partial \alpha_2 \rho_2 u}{\partial x} = 0, \quad (5.2c)$$

$$\frac{\partial \rho u}{\partial t} + \frac{\partial (\rho u^2 + \alpha_1 p_1 + \alpha_2 p_2)}{\partial x} = 0, \quad (5.2d)$$

$$\frac{\partial \alpha_1 \rho_1 e_1}{\partial t} + \frac{\partial \alpha_1 \rho_1 e_1 u}{\partial x} + \alpha_1 p_1 \frac{\partial u}{\partial x} = -\mu p_{int}(p_1 - p_2), \quad (5.2e)$$

$$\frac{\partial \alpha_2 \rho_2 e_2}{\partial t} + \frac{\partial \alpha_2 \rho_2 e_2 u}{\partial x} + \alpha_2 p_2 \frac{\partial u}{\partial x} = \mu p_{int}(p_1 - p_2), \quad (5.2f)$$

where α_k , ρ_k , p_k and e_k are the volume fraction, the density, the pressure and the specific internal energy of phase k . The subscript k refers to the subscripts 1 and 2 that denote phases 1 and 2, respectively, p_{int} is the interfacial pressure, u is the x-component of the mixture velocity and ρ is the mixture density.

In the presence of shocks, inaccuracies in the thermodynamic state are expected because of the approximation of the two non-conservative internal energy equations. To correct these inaccuracies, an additional conservative total mixture energy equa-

tion was proposed in Saurel, Petitpas and Berry (2009). This equation is obtained by summing up the two internal energy equations with the mass and momentum equations:

$$\frac{\partial(\rho e + \frac{1}{2}\rho u^2)}{\partial t} + \frac{\partial u(\rho e + \frac{1}{2}\rho u^2 + \alpha_1 p_1 + \alpha_2 p_2)}{\partial x} = 0, \quad (5.3)$$

where ρe is the mixture internal energy which is defined as $\rho e = \alpha_1 \rho_1 e_1 + \alpha_2 \rho_2 e_2$.

5.1.1 Pressure relaxation terms

The term $\mu(p_1 - p_2)$ appearing on the right hand side of the volume fraction equation (5.2a) expresses the expansion rate of the volume fraction that drives the pressures of the two phases towards an equilibrium state. This is augmented by the pressure work done by the phases to achieve the pressure equilibrium expressed by the term $\mu p_{int}(p_1 - p_2)$ written on the right hand side of the energy equations (5.2e) and (5.2f), respectively. The parameter μ controls the rate at which the pressures of both fluids reach the equilibrium state. More details are given in Saurel and Abgrall (1999a). The existence of these terms, usually known as pressure relaxation terms, enables the model to deal with two different phases. These phases admit different pressures at every point in the flow domain. This has made it necessary to use some relaxation mechanism to drive the non-equilibrium pressure of the phases to an equilibrium state.

5.1.2 Closure relations

The six-equation two-phase flow model (5.2) can be obtained by an ensemble averaging the single phase conservation laws for each phase with the assumption that both phases have the same velocity. The averaging process results in additional terms in the energy equations that describe the interaction between the phases. In addition, the assumption of single velocity results in the reduction of the two momentum equations into one shared momentum equation (5.2d). Ishii (1975) proposed equation (5.2a) to link the phases together. The set of equations (5.2) remains incomplete as it contains more variables than equations. Consequently, one needs additional relations to close the model.

One of these relations is the volume fraction saturation constraint, which may be written as follows:

$$\alpha_1 + \alpha_2 = 1. \quad (5.4)$$

The other relations are the equation of state for each phase which are written in the general form of the Mie-Grüneisen EOS is as follows:

$$p(\rho, e) = \rho \Gamma_{\mathcal{H}}(\rho)[e - e_{\mathcal{H}}(\rho)] + p_{\mathcal{H}}(\rho), \quad (5.5)$$

where $\Gamma_{\mathcal{H}}(\rho)$, $e_{\mathcal{H}}(\rho)$ and $p_{\mathcal{H}}(\rho)$ are material dependent functions given in Table 4.2

for various types of EOSs as discussed in section 4.2.

The interfacial pressure is taken to be equal to the mixture pressure:

$$p_{int} = p = \alpha_1 p_1 + \alpha_2 p_2. \quad (5.6)$$

An alternative way of calculating the interfacial pressure is given in the subsection 4.1.1, point (c). Since each fluid has its own pressure, the pressure relaxation process is needed to achieve the equilibrium state at every grid point and time step.

The mixture velocity is calculated from the mass-weighted average of the constituent velocities, which can be written as follows:

$$u = \frac{\alpha_1 \rho_1 u_1 + \alpha_2 \rho_2 u_2}{\rho}, \quad (5.7)$$

where $\rho = \alpha_1 \rho_1 + \alpha_2 \rho_2$.

5.2 Mathematical structure of the six-equation model

Considering the left hand side of the equations of system (5.2) and writing them in a quasi-linear form in terms of primitive variables, we get:

$$\frac{\partial \mathbf{w}}{\partial t} + A(\mathbf{w}) \frac{\partial \mathbf{w}}{\partial x} = 0, \quad (5.8)$$

where \mathbf{w} is the primitive variables vector and is defined as:

$$\mathbf{w} = [\alpha_1 \quad \rho_1 \quad \rho_2 \quad u \quad p_1 \quad p_2]^T, \quad (5.9)$$

and $A(\mathbf{w})$ is the primitive variables Jacobian matrix and is defined as:

$$A(\mathbf{w}) = \begin{pmatrix} u & 0 & 0 & 0 & 0 & 0 \\ 0 & u & 0 & \rho_1 & 0 & 0 \\ 0 & 0 & u & \rho_2 & 0 & 0 \\ \frac{p_1 - p_2}{\rho} & 0 & 0 & u & \frac{\alpha_1}{\rho} & \frac{1 - \alpha_1}{\rho} \\ 0 & 0 & 0 & \rho_1 c_1^2 & u & 0 \\ 0 & 0 & 0 & \rho_2 c_2^2 & 0 & u \end{pmatrix}. \quad (5.10)$$

The phases speed of sound c_1 and c_2 are defined as:

$$c_k^2 = \frac{\frac{p_k}{\rho_k^2} - \left(\frac{\partial e_k}{\partial \rho_k} \right)_{p_k}}{\left(\frac{\partial e_k}{\partial p_k} \right)_{\rho_k}}, \quad k = 1, 2. \quad (5.11)$$

Using the definition of the speed of sound given by equation (5.11) and the EOSs governing the fluids, the speeds of sound can be obtained for various EOSs as given in the section 4.2.

The Jacobian matrix $A(\mathbf{w})$ has six real eigenvalues which are:

$$\begin{aligned}\lambda_1 &= \lambda_2 = \lambda_3 = \lambda_4 = u, \\ \lambda_5 &= u + c, \\ \lambda_6 &= u - c.\end{aligned}\tag{5.12}$$

These eigenvalues represent the waves speed that are shown in Figure 5.3 which illustrates the solution of the Riemann problem. The mixture speed of sound c is expressed as:

$$c^2 = \sum_{k=1}^2 Y_k c_k^2,\tag{5.13}$$

where Y_k is the mass fraction, defined as $Y_k = \frac{\alpha_k \rho_k}{\rho}$.

The eigenvalues of the system (5.2) are real but they are not distinct. Therefore, the model (5.2) is hyperbolic but non-strictly hyperbolic. The corresponding right eigenvectors are:

$$\mathbf{K}_1 = \begin{bmatrix} 0 \\ 0 \\ 0 \\ 0 \\ -\frac{\alpha_2}{\alpha_1} \\ 1 \end{bmatrix}, \mathbf{K}_2 = \begin{bmatrix} 0 \\ 0 \\ 1 \\ 0 \\ 0 \\ 0 \end{bmatrix}, \mathbf{K}_3 = \begin{bmatrix} 0 \\ 1 \\ 0 \\ 0 \\ 0 \\ 0 \end{bmatrix},\tag{5.14a}$$

$$\mathbf{K}_4 = \begin{bmatrix} 1 \\ 0 \\ 0 \\ 0 \\ \frac{p_2 - p_1}{\alpha_1} \\ 0 \end{bmatrix}, \mathbf{K}_5 = \begin{bmatrix} 0 \\ 1 \\ \frac{\rho_2}{\rho c} \\ \frac{\rho_1}{\rho c} \\ \frac{\alpha_1}{c_1^2} \\ \frac{c_2^2 \alpha_2}{\alpha_1} \end{bmatrix}, \mathbf{K}_6 = \begin{bmatrix} 0 \\ 1 \\ \frac{\rho_2}{\rho c} \\ -\frac{\rho_1}{\rho c} \\ \frac{\alpha_1}{c_1^2} \\ \frac{c_2^2 \alpha_2}{\alpha_1} \end{bmatrix}.\tag{5.14b}$$

5.3 Numerical method

Solutions to systems of partial differential equations may contain discontinuities which cannot be solved by classical finite difference methods. These solutions can be achieved accurately by finite volume methods based on the Godunov's method

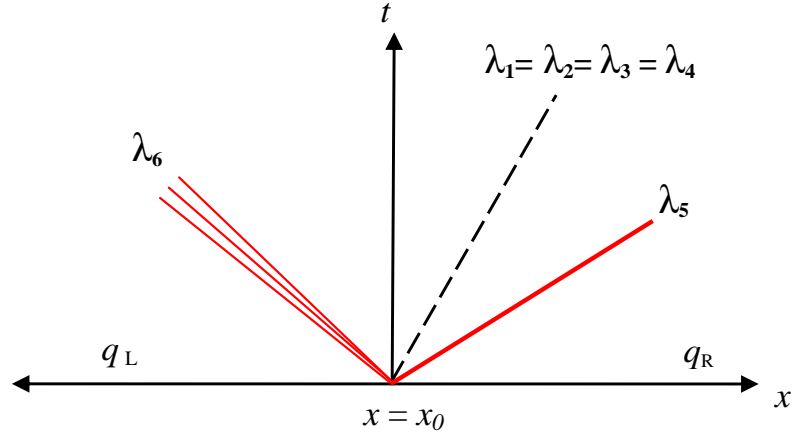


Figure 5.3: Solution of the Riemann problem for the six-equation model λ_m are given by (5.12).

(Godunov, 1959) which is used to solve a series of Riemann problems.

5.3.1 Numerical solution of the six-equation model

The numerical solution of the considered six-equation compressible multiphase flow model is complicated. This is due to the presence of the non-conservative equation of volume fraction evolution, the non-conservative terms and the relaxation and source terms in the model. Thus, the numerical solution of the model can be achieved by splitting the model into a hyperbolic part and a source and relaxation part. These different parts are solved in succession using the Strang splitting approach, which can symbolically be written in second order as follows:

$$Q_i^{n+1} = L_s^{\Delta t/2} L_h^{\Delta t} L_s^{\Delta t/2} Q_i^n. \quad (5.15)$$

The symbol $L_s^{\Delta t/2}$ represents the relaxation and source terms integration operator over a half of the time interval. $L_h^{\Delta t}$ is the numerical solution operator of the hyperbolic part. Q_i^n and Q_i^{n+1} are the conservative vectors at the time level n and $n + 1$, respectively. The components of the numerical method are presented in the next subsection.

5.3.2 The hyperbolic operator

In order to overcome the inaccuracies in the thermodynamic state predicted by the internal energy equations in the presence of shocks, the model (5.2) is extended to include the total mixture energy equation (5.3) proposed in Saurel, Petitpas and

Berry (2009). The hyperbolic part of the system (5.2) can be written as follows:

$$\frac{\partial \alpha_1}{\partial t} + u \frac{\partial \alpha_1}{\partial x} = 0, \quad (5.16a)$$

$$\frac{\partial \alpha_1 \rho_1 e_1}{\partial t} + \frac{\partial \alpha_1 \rho_1 e_1 u}{\partial x} + \alpha_1 p_1 \frac{\partial u}{\partial x} = 0, \quad (5.16b)$$

$$\frac{\partial \alpha_2 \rho_2 e_2}{\partial t} + \frac{\partial \alpha_2 \rho_2 e_2 u}{\partial x} + \alpha_2 p_2 \frac{\partial u}{\partial x} = 0, \quad (5.16c)$$

$$\frac{\partial Q}{\partial t} + \frac{\partial F(Q)}{\partial x} = 0, \quad (5.16d)$$

where Q is the conservative vector and $F(Q)$ is the numerical flux vector. These vectors are defined as:

$$Q = \begin{bmatrix} \alpha_1 \rho_1 \\ \alpha_2 \rho_2 \\ \rho u \\ \rho E \end{bmatrix}, \quad F(Q) = \begin{bmatrix} \alpha_1 \rho_1 u \\ \alpha_2 \rho_2 u \\ \rho u^2 + p \\ u(\rho E + p) \end{bmatrix}.$$

The last row in the above vectors corresponds to the additional equation of the total mixture energy (5.3), where E is the total specific energy and is defined as $E = e + \frac{1}{2}u^2$. The numerical solution of the system (5.16) represents the hyperbolic operator in equation (5.15).

Godunov-type scheme

The Godunov scheme is designed for conservation laws to capture shock waves correctly. This scheme enables solving Riemann problems to determine the local wave structure. It was extended to take into account the non-conservative terms to consider multiphase flow problems. In Saurel and Abgrall (1999a) the discretisations of the non-conservative terms were done based on the idea of Abgrall (1996), which considers the pressure and velocity to remain uniform during the time evolution. Based on the conventional Godunov first-order upwind scheme the discretisation of the conservative form (5.16d) of the hyperbolic part (5.16) can be written as:

$$Q_i^{n+1} = Q_i^n - \frac{\Delta t}{\Delta x} [F^*(Q_i^n, Q_{i+1}^n) - F^*(Q_{i-1}^n, Q_i^n)]. \quad (5.17)$$

where Δx is the space increment and Δt is the time step defined as:

$$\Delta t = \frac{\text{CFL} \Delta x}{S_{max}}. \quad (5.18)$$

where CFL is the Courant number and S_{max} is the maximum wave speed. The non-conservative equation for the volume fraction (5.16a) is discretised as follows:

$$\alpha_{1_i}^{n+1} = \alpha_{1_i}^n - \frac{\Delta t}{\Delta x} \left[(u\alpha_1)_{i+\frac{1}{2}}^* - (u\alpha_1)_{i-\frac{1}{2}}^* - \alpha_{1_i}^n (u_{i+\frac{1}{2}}^* - u_{i-\frac{1}{2}}^*) \right]. \quad (5.19)$$

This scheme guarantees the volume fraction positivity during the resolution of the hyperbolic operator. The non-conservative energy equations (5.16b) and (5.16c) cannot be approximated accurately in the presence of shocks. Therefore, the product $(\alpha p)_{k_i,j}^n$ is assumed to be constant during the time step by using the simplest approximation of the corresponding equations (Saurel, Petitpas and Berry, 2009) as follows:

$$(\alpha \rho e)_{k_i}^{n+1} = (\alpha \rho e)_{k_i}^n - \frac{\Delta t}{\Delta x} \left[(\alpha \rho e u)_{k_i+\frac{1}{2}}^* - (\alpha \rho e u)_{k_i-\frac{1}{2}}^* + (\alpha p)_{k_i}^n (u_{i+\frac{1}{2}}^* - u_{i-\frac{1}{2}}^*) \right], \quad (5.20)$$

where $k = 1, 2$. To achieve a second-order accuracy the MUSCL scheme is used which is detailed in Toro (2009) for a single phase.

The HLL approximate Riemann solver

This approach was introduced by Harten, Lax and van Leer (1983) to obtain the intercell numerical flux vector. Two waves left and right of speed S^- and S^+ are assumed to separate three constant states in the solution of the Riemann problem. The intercell flux for the left boundary is given according to the relations given below:

$$F_{i-\frac{1}{2}}^{hll} = \begin{cases} F_{i-1}^+ & \text{if } 0 \leq S_{i-\frac{1}{2}}^-, \\ \frac{S_{i-\frac{1}{2}}^+ F_{i-1}^+ - S_{i-\frac{1}{2}}^- F_i^- + S_{i-\frac{1}{2}}^- S_{i-\frac{1}{2}}^+ (Q_i^- - Q_{i-1}^+)}{S_{i-\frac{1}{2}}^+ - S_{i-\frac{1}{2}}^-} & \text{if } S_{i-\frac{1}{2}}^- \leq 0 \leq S_{i-\frac{1}{2}}^+, \\ F_i^- & \text{if } 0 \geq S_{i-\frac{1}{2}}^+. \end{cases} \quad (5.21)$$

The maximum and minimum wave speeds of the left and right waves for the left boundary can be computed according to the formulae introduced in Davis (1988) which are as follows:

$$\begin{aligned} S_{i-\frac{1}{2}}^+ &= \max(0, u_{i-\frac{1}{2}}^- + c_{i-\frac{1}{2}}^-, u_{i-\frac{1}{2}}^+ + c_{i-\frac{1}{2}}^+), \\ S_{i-\frac{1}{2}}^- &= \min(0, u_{i-\frac{1}{2}}^- - c_{i-\frac{1}{2}}^-, u_{i-\frac{1}{2}}^+ - c_{i-\frac{1}{2}}^+). \end{aligned} \quad (5.22)$$

The sound speed obeys relation (5.13), $u_{i-\frac{1}{2}}^\pm$ and $c_{i-\frac{1}{2}}^\pm$ represent the right and left velocities and sound speeds at the left boundary, respectively.

For the determination of the volume fraction (5.19), the conservative variables ρu , $\alpha_1 \rho_1$ and $\alpha_2 \rho_2$ of the mass and momentum equations, respectively, are calculated

through the following equation given in Toro (2009) for a single phase:

$$Q_{i-\frac{1}{2}}^{hll} = \begin{cases} Q_{i-1}^+ & \text{if } 0 \leq S_{i-\frac{1}{2}}^-, \\ \frac{S_{i-\frac{1}{2}}^+ Q_i^- - S_{i-\frac{1}{2}}^- Q_{i-1}^+ + (F_{i-1}^+ - F_i^-)}{S_{i-\frac{1}{2}}^+ - S_{i-\frac{1}{2}}^-} & \text{if } S_{i-\frac{1}{2}}^- \leq 0 \leq S_{i-\frac{1}{2}}^+, \\ Q_i^- & \text{if } 0 \geq S_{i-\frac{1}{2}}^+, \end{cases} \quad (5.23)$$

then the velocity at the left boundary $u_{i-\frac{1}{2}}^*$ is calculated as follows:

$$u_{i-\frac{1}{2}}^* = \begin{cases} u_{i-1}^+ & \text{if } 0 \leq S_{i-\frac{1}{2}}^-, \\ \frac{\rho u}{\alpha_1 \rho_1 + \alpha_2 \rho_2} & \text{if } S_{i-\frac{1}{2}}^- \leq 0 \leq S_{i-\frac{1}{2}}^+, \\ u_i^- & \text{if } 0 \geq S_{i-\frac{1}{2}}^+, \end{cases} \quad (5.24)$$

and the flux $(u\alpha_1)_{i-\frac{1}{2}}^*$ is calculated from (5.21).

The HLLC approximate Riemann solver

This solver basically is given in subsection 3.2.3 and more details are given in subsection 4.4.2 for the seven-equation model. The wave speed is computed as given in subsection 4.4.2. The conservative variables at the star region for the six-equation model are computed as follows:

$$Q_{*K} = \begin{bmatrix} \alpha_1^K \rho_1^K \left(\frac{S_K - u^K}{S_K - S^*} \right) \\ \alpha_2^K \rho_2^K \left(\frac{S_K - u^K}{S_K - S^*} \right) \\ \rho^K \left(\frac{S_K - u^K}{S_K - S^*} \right) S^* \\ \alpha_1^K \rho_1^K \left(\frac{S_K - u^K}{S_K - S^*} \right) \left(e_1 + (S^* - u^K) \left[S^* + \frac{p_1^K}{\rho_1^K (S_K - u^K)} \right] \right) \\ \alpha_2^K \rho_2^K \left(\frac{S_K - u^K}{S_K - S^*} \right) \left(e_2 + (S^* - u^K) \left[S^* + \frac{p_2^K}{\rho_2^K (S_K - u^K)} \right] \right) \\ \rho^K \left(\frac{S_K - u^K}{S_K - S^*} \right) \left(E^K + (S^* - u^K) \left[S^* + \frac{p^K}{\rho^K (S_K - u^K)} \right] \right) \end{bmatrix}, \quad (5.25)$$

where K represents left L and right R values.

The values of $\alpha^*(\alpha_{i\pm\frac{1}{2}}^-, \alpha_{i\pm\frac{1}{2}}^+)$ in the discretisation equation of the volume fraction in space and time (5.19) is computed as given in subsection 4.4.2.

The VFRoe approximate Riemann solver

This solver is given in Zein, Hantke and Warnecke (2010) for the six-equation model. It is described in subsection 3.2.4 and given in section 4.4.2 for the seven-equation model. After obtaining the average state using (3.32) with the primitive variables

given by (5.9), the intermediate state is determined as follows:

$$\mathbf{w}^* = \mathbf{w}_L + \sum_{\lambda_i < 0} a_i \mathbf{K}_i, \quad (5.26)$$

where the eigenvalues λ_i and the corresponding eigenvectors \mathbf{K}_i of the matrix $A(\bar{\mathbf{w}})$ are given by (5.12) and (5.14) and a_i are the coefficients of eigenvector decomposition of $\mathbf{w}_R - \mathbf{w}_L$ and are determined by:

$$\mathbf{w}_R - \mathbf{w}_L = \sum_{i=1}^6 a_i \mathbf{K}_i. \quad (5.27)$$

For the Jacobian matrix $A(\bar{\mathbf{w}})$ these coefficients are given by the following expressions:

$$\begin{aligned} a_4 &= \delta_1, \\ a_1 &= \frac{\delta_6 c_1^2 - \frac{\delta_5 \rho_2 c_2^2}{\rho_1} + \frac{\delta_1 \rho_2 c_2^2 (p_2 - p_1)}{\alpha_1 \rho_1}}{\frac{\alpha_2 \rho_2}{\alpha_1 \rho_1} c_2^2 + c_1^2}, \\ a_5 &= \frac{\delta_4 \rho_1 \rho_2 c_2 + \delta_6 \rho_1 c - \rho_1 c a_1}{2 \rho_2 c_2^2 c}, \\ a_6 &= a_5 - \frac{\delta_4 \rho_1}{c}, \\ a_2 &= \delta_3 - \frac{\rho_2}{\rho_1} (a_5 + a_6), \\ a_3 &= \delta_2 - a_5 - a_6, \end{aligned} \quad (5.28)$$

where δ_k is the k th component of:

$$\mathbf{w}_R - \mathbf{w}_L = [\delta_1, \dots, \delta_6]^T.$$

After solving the hyperbolic part of the model, following the Strang technique (5.15), the solution of the pressure relaxations is carried out to restore the pressures at the interface.

5.3.3 The pressure relaxation operator

The second step in the numerical solution of the model (5.2) is to solve the pressure relaxation operator according to the Strang splitting approach (5.15). The pressure relaxation process is a crucial step in the numerical solution as it is necessary for the boundary condition at the interface to be fulfilled. This is done by solving the following system of the ODE:

$$\frac{\partial Q}{\partial t} = D_P, \quad (5.29)$$

where Q and D_p are defined as follows:

$$Q = \begin{bmatrix} \alpha_1 \\ \alpha_1 \rho_1 \\ \alpha_2 \rho_2 \\ \rho u \\ \alpha_1 \rho_1 e_1 \\ \alpha_2 \rho_2 e_2 \\ \rho E \end{bmatrix}, \quad D_P = \begin{bmatrix} \mu(p_1 - p_2) \\ 0 \\ 0 \\ 0 \\ \mu p_I(p_2 - p_1) \\ -\mu p_I(p_2 - p_1) \\ 0 \end{bmatrix}.$$

Various methods are available for solving (5.29). The iterative procedure 4 that is proposed in Lallemand and Saurel (2000) has been implemented in this work. After computing the relaxed pressure, the gas volume fraction is calculated, which enables the determination of the gas density from the quantity $\alpha_1 \rho_1$, which remains constant during the relaxation process. Then the relaxed pressure is corrected to be consistent with the mixture EOS (5.30) which is written in terms of the Mie-Grüneisen EOS functions given for each EOS in Table 4.2 as follows:

$$p(\rho e, \alpha_1, \alpha_2) = \frac{\rho e - \sum_k^2 \left(\frac{\alpha_k(\rho_k \Gamma_k(\rho_k) e_k(\rho_k) - p_k(\rho_k))}{\Gamma_k(\rho_k)} \right)}{\sum_k^2 \left(\frac{\alpha_k}{\Gamma_k(\rho_k)} \right)}, \quad (5.30)$$

The value of ρe is calculated according to the correction criterion of Saurel, Petitpas and Berry (2009) from the conservative equation of total mixture energy (5.3). The mixture pressure for both fluids with two different types of EOSs is then calculated from the mixture EOS (5.30) with the help of the volume fractions. The obtained value of the mixture pressure is used to reset the values of the internal energies using the corresponding EOSs.

5.4 Numerical results - Verification of the methodology

To assess the numerical performance of the developed code to solve the six-equation model to simulate two-component problems, various compressible two-phase flow problems have been studied with either the same type of EOS or different type of EOS applied to each phase. In the examined test problems the ideal gas (IG) (4.14), shock wave (SW) (4.18), stiffened gas (SG) (4.21), Tait's (4.27), van der Waals (vdW) (4.30), Cochran-Chan (CC) (4.34) and Jones-Wilkins-Lee (JWL) (4.39) EOSs are employed in one dimension. All these types of EOSs are used in these problems to show the generality and the oscillation-free feature of the current method. A

comparison between the six and seven-equation models has been presented using single and two-phase test problems in section 5.6.

As mention in the previous chapter, in all test cases a common assumption is made, that is a presence of a negligible volume fraction $\epsilon = 10^{-8}$ of the other fluid in the fluid considered as a pure fluid, as shown in Figure 4.2. The numerical results have been obtained from various approximate Riemann solvers, i.e., HLL, HLLC and VFRoe, using the CFL = 0.9 unless otherwise mentioned. For the presented simulations the results were compared with either the exact solution or a fine grid solution, especially for those cases which don't have an exact solution. No spurious pressure oscillations are observed at the material interface for all conducted test problems.

5.4.1 TNT product gases interaction test

This is a single phase test studied by Rider (1999); Shyue (2001). The test considers a Riemann problem in a shock tube where the two chambers are filled with the product gases of the TNT explosive at different initial states. The diaphragm separating the two chambers is set at $x = 0.5$ m. The test is examined to show the ability of the developed code to deal with gases that are governed by the Jones-Wilkins-Lee (JWL) EOS (4.39). The initial states are given in Table 5.1.

Table 5.1: Initial data for TNT product gases interaction test 5.4.1

State	ρ_1 [kg/m ³]	u_1 [m/s]	p_1 [Pa]	α_1	ρ_2 [kg/m ³]	u_2 [m/s]	p_2 [Pa]	α_2
Left	1700	0	10^{12}	$1 - \epsilon$	1000	0	10^{12}	ϵ
Right	1700	0	5×10^{10}	ϵ	1000	0	5×10^{10}	$1 - \epsilon$

The detonation product gases constant parameters are taken as $\rho_o = 1840$ kg/m³, $A_1 = 8.545 \times 10^{11}$ Pa, $R_1 = 4.6$, $A_2 = 2.05 \times 10^{10}$ Pa, $R_2 = 1.35$, $C_v = 815$ J/(kg·K), $\gamma = 1.25$ and $C_{ek} = 0$ (Dobrtaz, 1972).

As the diaphragm is instantaneously removed at $t = 0$ s, three different waves, i.e. shock, contact and rarefaction, are formed due to the differences in pressure and density between the left and right states. These waves depict the solution of this Riemann problem. While the shock and contact waves propagate to the right the rarefaction wave propagates to the left. The three waves divide the flow domain into four different state regions as shown in Figure 5.4 at $t = 12$ μ s. These regions are as described in the gas-gas test, subsection 4.5.1.

The numerical results are obtained using the HLL approximate Riemann solver with a mesh of 200 cells and are compared with the fine grid solution using a mesh of 5000 cells. It can be observed that the resolution of the rarefaction wave agrees perfectly with that obtained from the fine grid and the method captures the shock

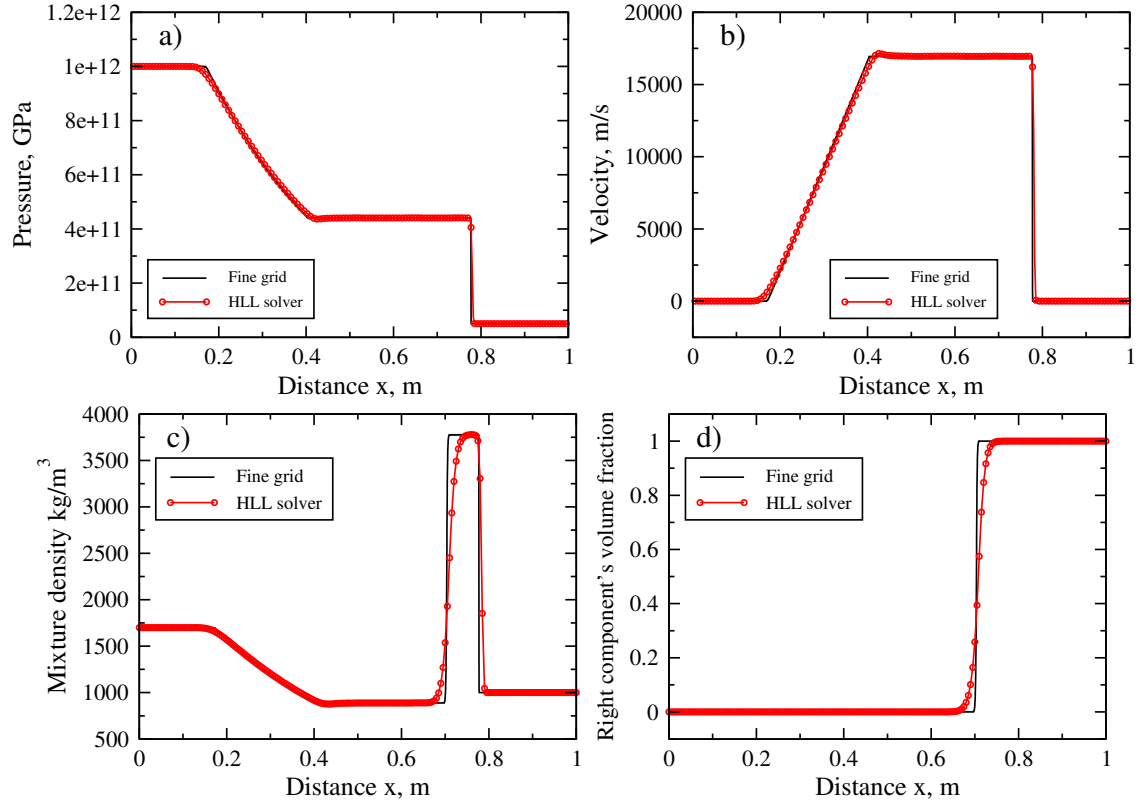


Figure 5.4: TNT product gases interaction test 5.4.1. Results for: (a) pressure, (b) velocity, (c) mixture density and (d) right component's volume fraction. Numerical solution from 6-eqn. model compared to the fine grid solution at $t = 12 \mu\text{s}$.

wave within a less number of cells, as shown in Figure 5.4(a, b, c), than it does for capturing the contact discontinuity as shown in Figure 5.4(c, d). In addition, the results are in good agreement with the results of Shyue (2001) which obtained from a different model and numerical method.

5.4.2 Interface advection test

This is a two-phase test problem presented in Allaire, Clerc and Kokh (2002). It is conducted to show the capability of the code to preserve a contact discontinuity moving in uniform velocity and pressure profiles and the ability to deal with various EOSs written in the general form of the Mie-Grüneisen EOS (4.12). The test is carried out in a computational domain of 1 m long, which is divided into two equal chambers, where the copper is considered on the left side and the explosive material on the right side. The two different materials are governed by the Cochran-Chan EOS (4.34) and their constant parameters are given in Table 4.6. The initial conditions are given in table 5.2.

Figure 5.5 displays the numerical results for the solution of this Riemann problem which consists of a single contact discontinuity only. The results for pressure (a), velocity (b), mixture density (c) and explosive volume fraction (d) are obtained from the six-equation model at time $t = 270 \mu\text{s}$ using the VFRoe approximate Riemann

Table 5.2: Initial data for interface advection test 5.4.2

State	ρ_1 [kg/m ³]	u_1 [m/s]	p_1 [Pa]	α_1	ρ_2 [kg/m ³]	u_2 [m/s]	p_2 [Pa]	α_2
Left	9000	1500	10^5	$1 - \epsilon$	2000	1500	10^5	ϵ
Right	9000	1500	10^5	ϵ	2000	1500	10^5	$1 - \epsilon$

solver with 1000 cells. The results show that the method preserves the contact discontinuity (interface) between two different gases, governed with the same EOS, as the flow evolves at a uniform velocity and pressure. A good agreement is observed comparing to the exact solution taken from Allaire, Clerc and Kokh (2002). The test is also examined by employing other EOSs and no pressure and velocity oscillations are noticed in the results of all EOSs.

5.4.3 Modified Sod test

This test is modified from the well known single phase Sod test problem (Fedkiw et al., 1999). The test which uses two different gases as a working fluid is conducted to verify that the developed code is able to simulate multi-component problems governed by the IG EOS (4.14). The shock tube is 1 m long, initially the diaphragm

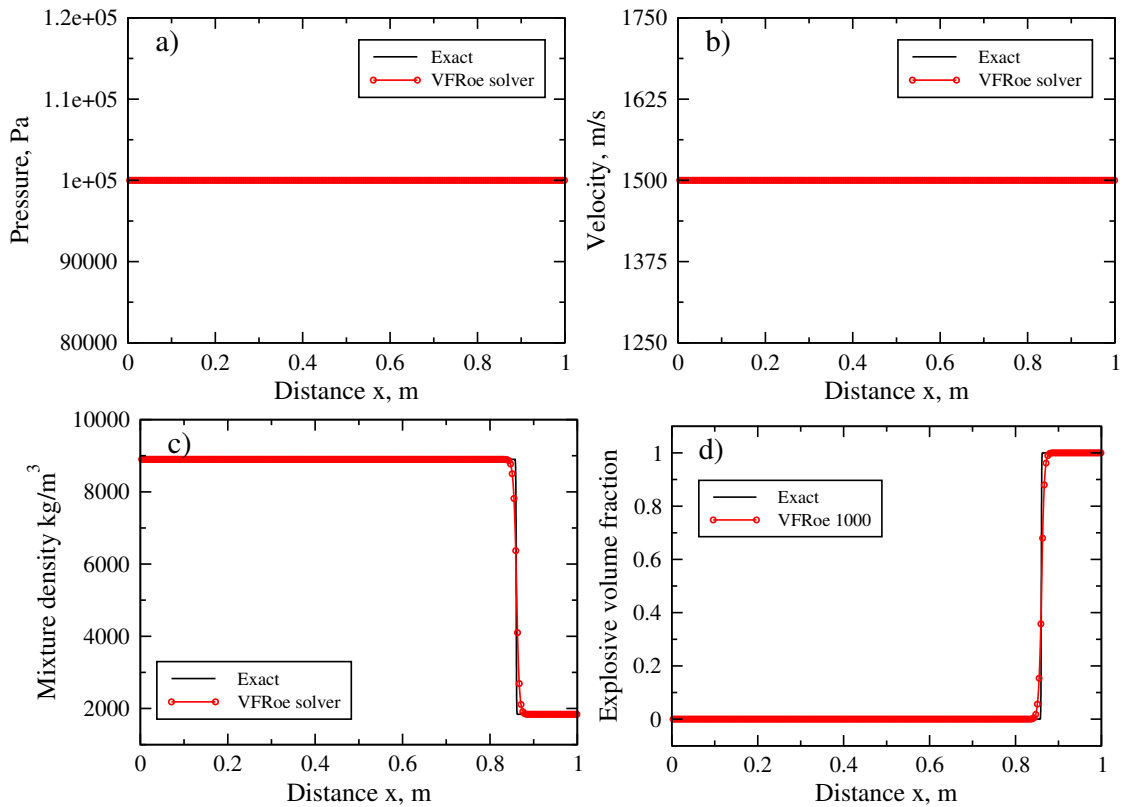


Figure 5.5: Interface advection test 5.4.2: Results for: (a) pressure, (b) velocity, (c) mixture density and (d) air volume fraction. Numerical solution (circles) and exact solution (line) Allaire, Clerc and Kokh (2002) at $t = 2.79$ ms.

Table 5.3: Initial data for modified Sod test 5.4.3

State	ρ_1	u_1	p_1	α_1	ρ_2	u_2	p_2	α_2
	[kg/m ³]	[m/s]	[Pa]		[kg/m ³]	[m/s]	[Pa]	
Left	1	0	10^5	$1 - \epsilon$	0.125	0	10^5	ϵ
Right	1	0	10^4	ϵ	0.125	0	10^4	$1 - \epsilon$

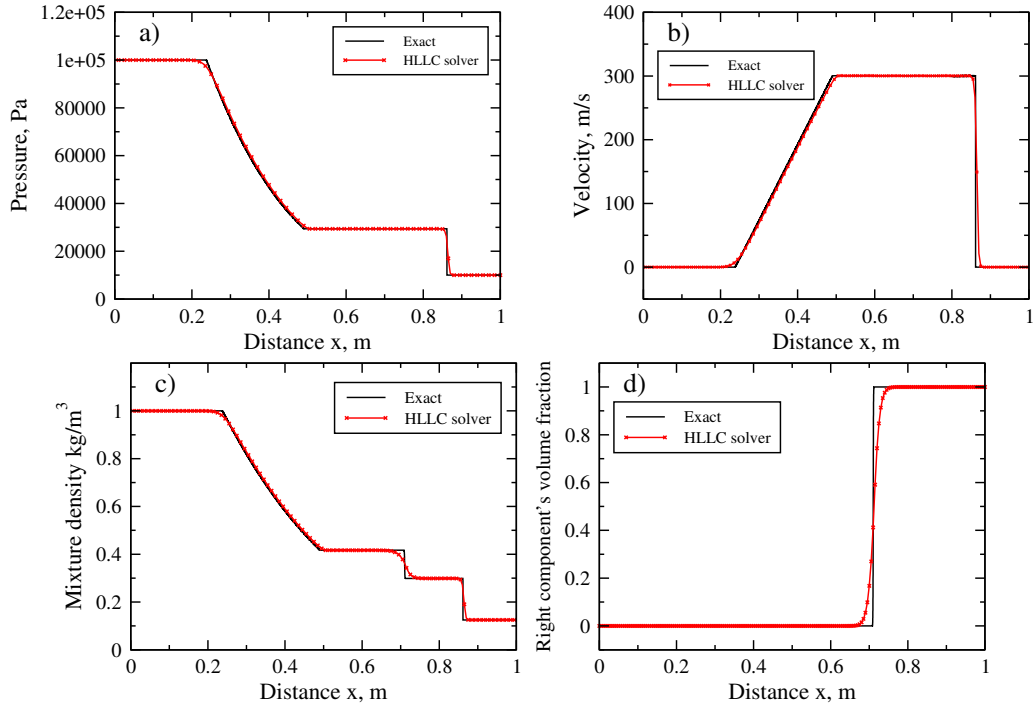


Figure 5.6: Modified Sod test 5.4.3: (a) Pressure. (b) Velocity. (c) Mixture density. (d) Air volume fraction. Numerical solution using the HLLC solver compared to the exact solution at $t = 0.0007$ s.

separating the left and right chambers is set at $x = 0.5$ m. The IG EOS parameters for the left and right gases are $\gamma_1 = 1.4$ and $\gamma_2 = 1.2$, respectively. The gas filled in the left chamber is at higher pressure and density, the initial states are given in Table 5.3.

As the diaphragm is instantaneously removed at $t = 0$ s. Three different waves are emerged and propagated in the same manner as explained in subsection 5.4.1. Moreover, they divide the flow domain into four regions as mentioned in the same subsection 5.4.1 as well. Figure 5.6 displays the numerical results for the modified Sod test obtained from the HLLC approximate Riemann solver with 200 cells. The results for pressure (a), velocity (b), mixture density (c) and volume fraction (d) are presented at time $t = 0.0007$ s. The results are in good agreement with the exact solution (Fedkiw et al., 1999) using a relatively low resolution of 200 cells.

5.4.4 Water-air test

This test is studied by Shyue (1999), it is similar to the second simulation of the standard water-air shock tube conducted using the seven-equation model and presented in the subsection 4.6.3, where the water is governed by the SG EOS (4.21) and air is governed by the van der Waals EOS (4.30). The constant parameters for water are $\gamma = 4.4$ and $\pi = 6 \times 10^8$ and for air are $\gamma = 1.4$, $a = 5 \text{ Pa m}^6/\text{kg}$ and $b = 10^{-3} \text{ m}^3/\text{kg}$. The initial conditions are given in Table 4.19

In this test a strong shock wave with a pressure ratio of 10,000 and density ratio of 20 propagates to the right from the high density fluid to the low density fluid and a rarefaction wave propagates to the left. Figure 5.7 shows the results for the pressure (a), velocity (b), mixture density (c) and air volume fraction (d). The results are obtained at time $t = 240 \mu\text{s}$ using the HLLC approximate Riemann solver with 500 cells. A good agreement is also achieved between the numerical solution (circles) and the exact solution (line) taken from Shyue (1999).

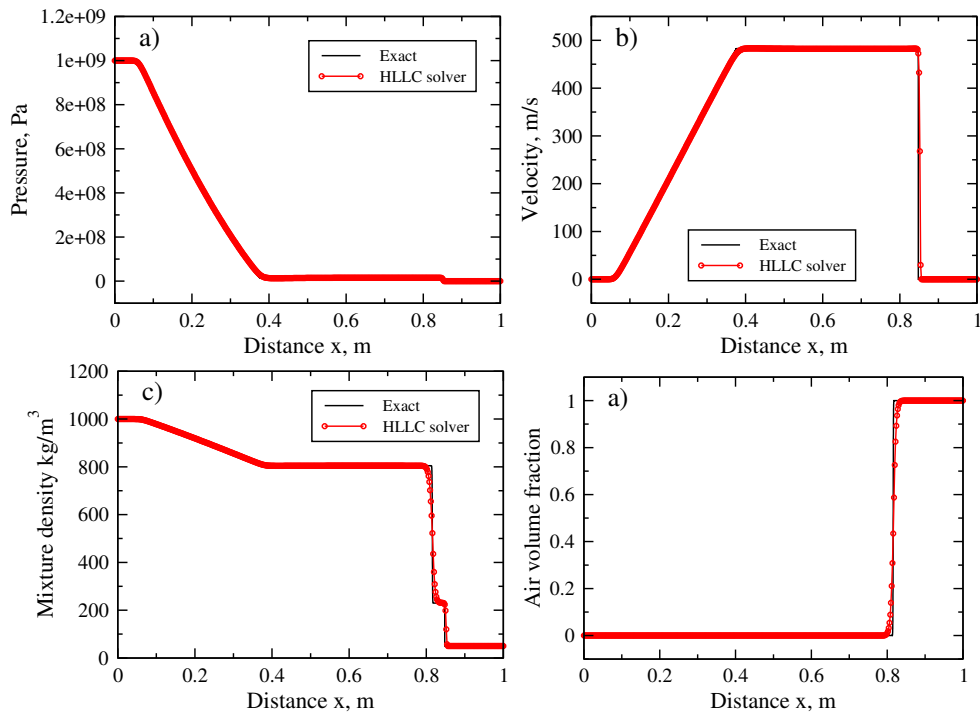


Figure 5.7: Water-air test 5.4.4: Results for: (a) pressure, (b) velocity, (c) mixture density and (d) air volume fraction. Numerical solution (circles) and exact solution (line) at $t = 229 \mu\text{s}$.

5.4.5 Water-air mixture test

This test considers a mixture of water-air (Murrone and Guillard, 2005), which is similar to the previous test and the standard water-air shock tube examined using the seven-equation model in the subsection 4.6.3. In this test the volume fraction is constant ($\alpha_1 = \alpha_2 = 0.5$) everywhere in the tube, the density of the air is 1 kg/m^3

and the initial discontinuity which separates liquid and gas is located at $x = 0.5$ m. The water is governed by the SG EOS (4.21) and its constant parameters are $\gamma = 4.4$ and $\pi = 6 \times 10^8$, whereas air is governed by the IG EOS (4.14) and its constant parameter is $\gamma = 1.4$. The initial conditions are given in Table 5.4:

Table 5.4: Initial data for water-air mixture test 5.4.5

State	ρ_1 [kg/m ³]	u_1 [m/s]	p_1 [Pa]	α_1	ρ_2 [kg/m ³]	u_2 [m/s]	p_2 [Pa]	α_2
Left	1000	0	10^9	0.5	1	0	10^9	0.5
Right	1000	0	10^5	0.5	1	0	10^5	0.5

In this test a strong shock wave with a pressure ratio of 10,000 and a density ratio of 1000 propagates to the right from the high density fluid to the low density fluid, a rarefaction wave also propagates to the left and a contact discontinuity also propagates to the right as described in the subsection 5.4. Figure 5.8 shows the results of the: pressure (a), velocity (b), mixture density (c), air volume fraction (d), water density (e) and air density (f). The results are obtained from the VFRoe approximate Riemann solver at time $t = 200\mu\text{s}$ using various resolutions to show the convergence of the solution as the mesh is refined. A good agreement is observed between the numerical solution and the exact solution taken from Murrone and Guillard (2005).

5.4.6 Molybdenum-MORB interaction test

This test problem involves the interaction of a shock wave in molybdenum and an encapsulated MORB (Mid-Ocean Ridge Basalt) liquid (Shyue, 2001). The setup and the initial conditions for the test are displayed in Figure 5.9. The initial interface separating the stationary molybdenum and the MORB liquid is located at $x = 0.6$ m, they are at atmospheric pressure $p = 10^5$ Pa. A right going shock wave travels in molybdenum is located at $x = 0.4$ m, the post-shock molybdenum is at a higher pressure $p = 3 \times 10^{10}$ Pa. Both components are modeled by the shock wave EOS (4.18). The shock wave EOS parameters for the molybdenum are $\rho_0 = 9961$ kg/m³, $c_0 = 4770$ m/s, $s = 1.43$, $\gamma = 3.56$, $\theta = 1$, $p_0 = 0$ and $e_0 = 0$ and for the MORB are $\rho_0 = 2660$ kg/m³, $c_0 = 2100$ m/s, $s = 1.68$, $\gamma = 2.18$, $\theta = 1$, $p_0 = 0$ and $e_0 = 0$

The right going shock wave coming from the higher pressure and density fluid to the lower pressure and density fluid accelerated the interface separating the molybdenum and the MORB. As time evolves, the resulting wave structure would consist of, an interface, a transmitted shock wave and a reflected rarefaction wave. Figure 5.18 shows the numerical results for the molybdenum-MORB interaction test problem at $t = 120$ s. It can be seen that the method captures the shock wave within a

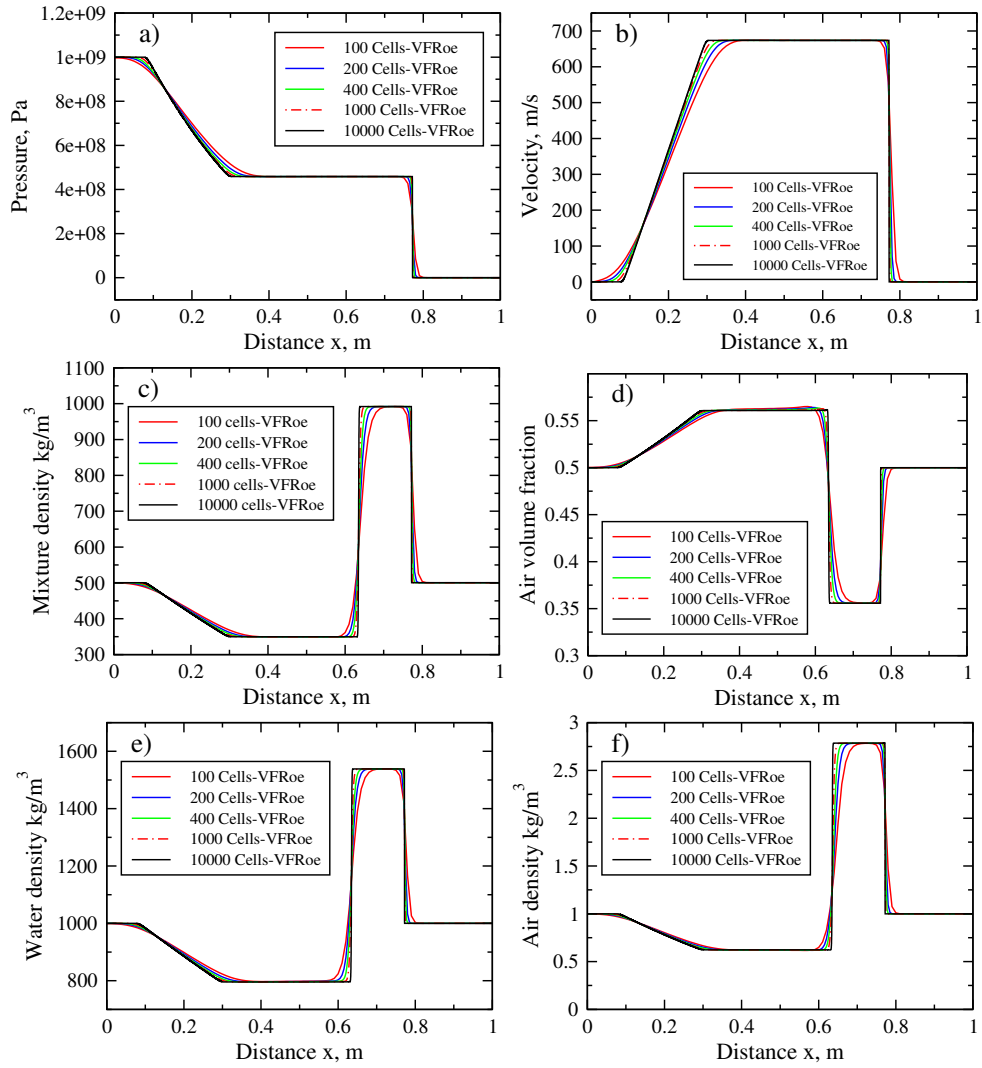


Figure 5.8: Water-air mixture test 5.4.5. Numerical solution at $t = 229 \mu\text{s}$ for: (a) pressure, (b) velocity, (c) mixture density, (d) air volume fraction, (e) water density and (f) air density.

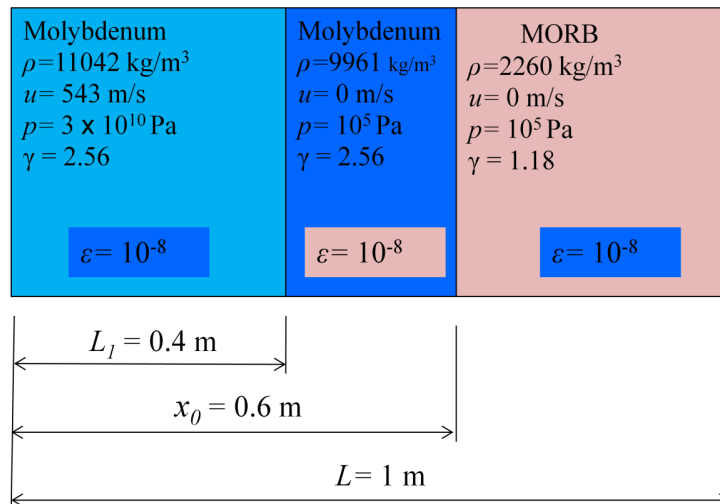


Figure 5.9: Setup and initial conditions for molybdenum-MORB interaction test 5.4.6

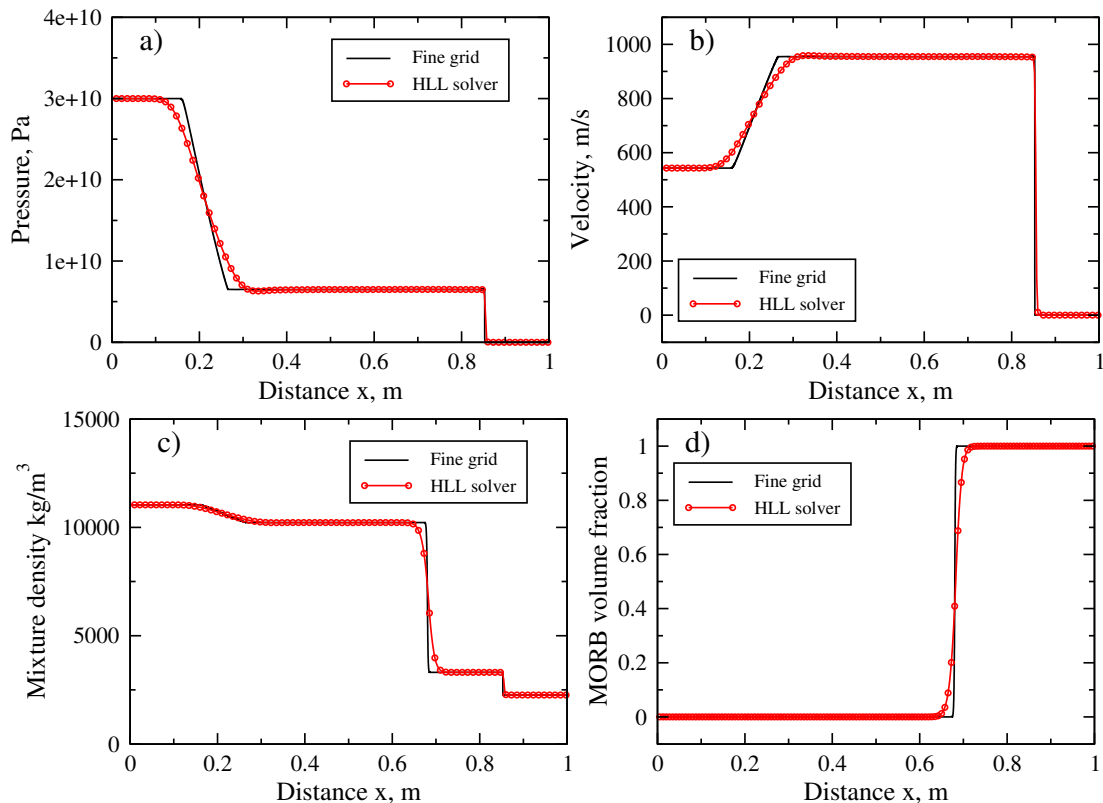


Figure 5.10: Molybdenum-MORB interaction test 5.4.6. Numerical solution at $t = 120 \mu\text{s}$ for: (a) pressure, (b) velocity, (c) mixture density and (d) MORB volume fraction.

less number of cells than it does to capture the contact discontinuity. The results for the pressure (a), velocity (b), mixture density (c) and MORB volume fraction (d) are obtained from the HLL approximate Riemann solver using 200 cells with the CFL = 0.6. They are in good agreement with the fine mesh solution.

5.5 Numerical results - Validation of the results

In this section validations of the results of the seven and six-equation models in one space dimension are demonstrated. It is concerned with computations involving strong shock waves in two-phase mixtures. The shock speed can be computed from the Rankine-Hugoniot conditions of the mixture Euler equations closed by the mixture equation of state as done in Saurel and Abgrall (1999a). The two-phase flow models do not admit the classical Rankine-Hugoniot conditions because of the presence of the non-conservative and relaxation terms in the equations. Therefore, the shock speed cannot be found analytically. The shock speed in various pure materials, i.e., liquids and solids, as well as mixtures have been determined experimentally (see for example, Marsh, 1980; Trunin et al., 1991). These results could be used as reference solutions. Indeed, for many materials the relation between the shock velocity and the impact velocity is determined experimentally and found to be linear:

$$U_s = c_0 + sU_p, \quad (5.31)$$

where U_s is the shock speed, c_0 is the speed of sound in the material under consideration at atmospheric conditions and initially at rest, s is a dimensionless constant and U_p is the impact velocity. This equation is called the shock wave equation of state (Shyue, 2001). It can be used to determine the SG EOS parameters γ and π using the relations (4.24) and (4.25) given in subsection 4.2.3. These experimental relations are known for many pure materials and alloys. Metal alloys under strong shock waves may be considered as two-component mixtures and can be treated as compressible materials.

5.5.1 Mixture Hugoniot test

In this test different alloys have been considered, i.e., iron-nickel, nickel-copper and stainless steel 304. The numerical results obtained from the six and seven-equation models have been compared to the experimental results of Marsh (1980) and Trunin et al. (1991). The test is conducted in a domain which was 1 m long, containing a mixture of two components at atmospheric pressure and initially at rest. The impact or particle velocity is set equals to the inlet flow velocity boundary condition. Several unsteady impact problems have been examined by varying the particle velocity which is kept in the same range of the experimental ones. Using 2000 cells and the CFL equals to 0.9, the three approximate Riemann solvers gave almost the same results. The shock speed is calculated from the ratio of the displacement of the biggest pressure gradient over the time interval. Consider the initial data for the iron-nickel and nickel-copper mixtures as given in Table 5.5 and for the stainless steel 304 alloy which is modelled as a single phase as given in Table 5.6.

Table 5.5: Initial data for iron-nickel and nickel-copper mixtures shock impact 5.6.2

State	ρ_1 [kg/m ³]	u_1 [m/s]	p_1 [Pa]	α_1	ρ_2 [kg/m ³]	u_2 [m/s]	p_2 [Pa]	α_2
Iron-nickel	7873	0	10 ⁵	0.821	8875	0	10 ⁵	0.179
Nickel-copper	8875	0	10 ⁵	0.5	8930	0	10 ⁵	0.5

Table 5.6: Initial data for stainless steel 304 alloy shock impact 5.6.2

State	ρ_1 [kg/m ³]	u_1 [m/s]	p_1 [Pa]	α_1	ρ_2 [kg/m ³]	u_2 [m/s]	p_2 [Pa]	α_2
S. steel 304	7890	0	10 ⁵	1 - ϵ	7890	0	10 ⁵	ϵ

The results for the iron-nickel and nickel-copper mixtures impact tests are compared to the experimental results of Marsh (1980) and Trunin et al. (1991). They

are displayed in Figures 5.11 and 5.12, respectively, for the particle velocity against shock velocity (a), pressure (b) and mixture density (c) and the relation between the specific volume and pressure (d). It can be seen that the numerical results obtained from the six and seven-equation models confirmingly agree with the experimental results.

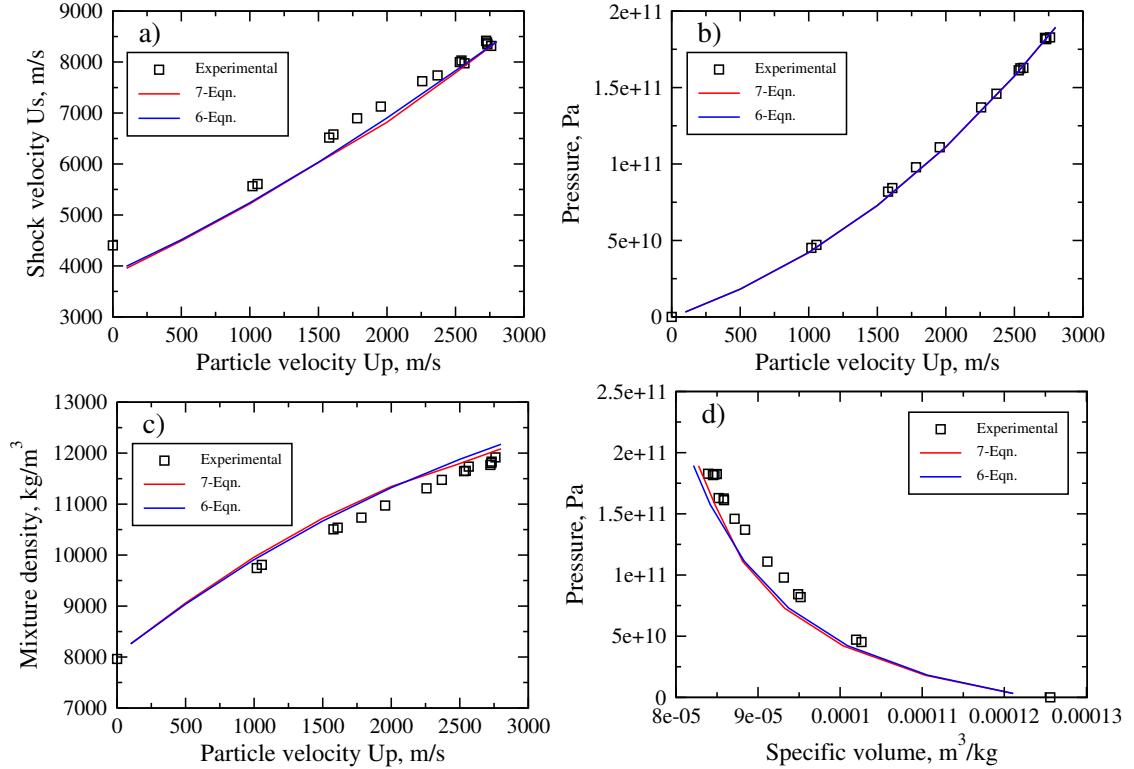


Figure 5.11: Mixture Hugoniot test 5.5.1: Iron-Nickel alloy experimental data (symbols) results from 6 and 7-Eqn. models (lines) obtained using 2000 cells.

Figure 5.13 shows the results of the shock wave propagation through the stainless steel alloy which is considered as a single phase by varying the particle velocity, shock velocity (a), pressure (b), mixture density (c) and the relation between the specific volume and pressure (d). It can also be seen that the numerical results obtained from the six and seven-equation models are in very good agreement with the experimental results of Marsh (1980).

5.6 Numerical results - Comparison between the six and seven-equation models

In this section a comparison between the six and seven-equation models is carried out using some test problems that both models could be used for their simulations. These test problems include single phase problems, i.e., Sod test, and two-phase problems, i.e., detonation products-copper interaction test. It is known that the seven-equation model is able to simulate some test problems that the six-equation

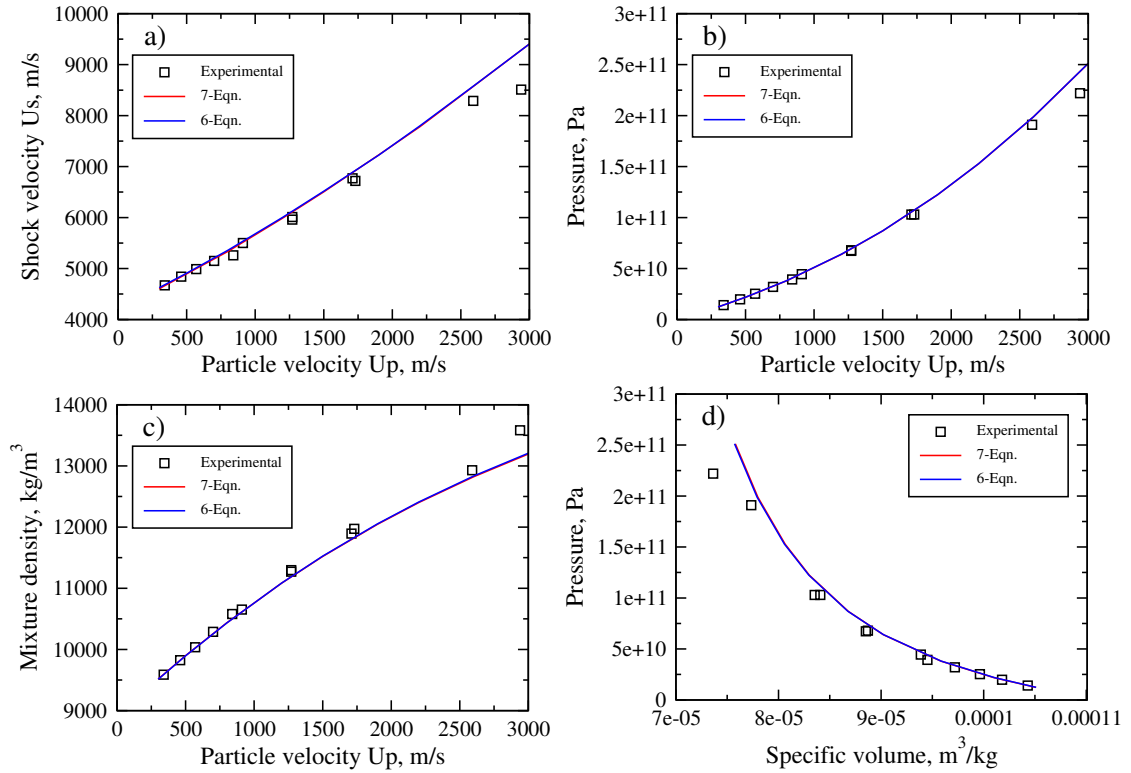


Figure 5.12: Mixture Hugoniot test 5.5.1: Nickel-Copper alloy experimental data (symbols) results from 6 and 7-Eqn. models (lines) obtained using 2000 cells.

model cannot solve, problems that consider two-phase flows with different phases

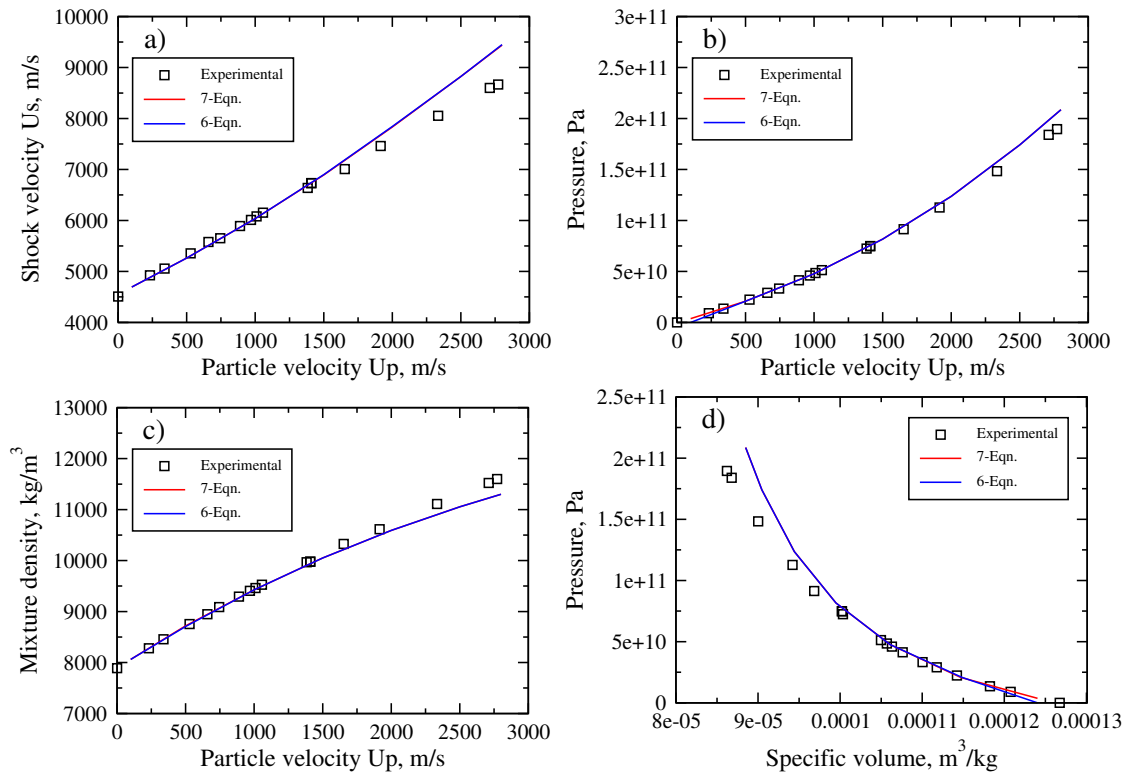


Figure 5.13: Mixture Hugoniot test 5.5.1: Stainless steel alloy experimental data (symbols) results from 6 and 7-Eqn. models (lines) obtained using 2000 cells.

velocity directions such as water faucet test 4.7.4 and sedimentation test (Abgrall and Saurel, 2003). The results are compared to the exact and fine grid solutions. The comparison is carried out in terms of L_2 error norm, the number of time steps and CPU time required to obtain the solution. Various mesh resolutions have been used to accomplish the comparison.

5.6.1 Sod test

This is a well known single phase shock tube test problem. The test which uses air as a working fluid is conducted to verify that the developed code is able to simulate single phase problems governed by the IG EOS (4.14), $\gamma = 1.4$. The test is examined also to compare between the six and seven-equation models. The shock tube is 1 m long, initially the diaphragm separating the left and right chambers is set at $x = 0.5$ m. The air at the left chambers is at higher pressure and density, the initial states are given in Table 5.7.

Table 5.7: Initial data for Sod test 5.6.1

State	ρ_1	u_1	p_1	α_1	ρ_2	u_2	p_2	α_2
	[kg/m ³]	[m/s]	[Pa]		[kg/m ³]	[m/s]	[Pa]	
Left	1	0	1	$1 - \epsilon$	0.125	0	1	ϵ
Right	1	0	0.1	ϵ	0.125	0	0.1	$1 - \epsilon$

As the diaphragm is instantaneously removed at $t = 0$ s. Three different waves are emerged and propagated in the same manner as explained previously, which divide the flow domain into four regions as mentioned earlier.

The results for this test are obtained using the HLLC approximate Riemann solver with a mesh of 200 cells. Figure 5.14 shows the results of the pressure (a), velocity (b), mixture density (c) and volume fraction (d) at instant $t = 0.25$ s using the six and seven-equation models compared with the exact solution (Toro, 2009). Both models gave almost the same results which are in good agreement with the exact solution using a relatively low resolution of 200 cells.

Figure 5.15 shows the error norm (L_2) spatial convergence comparison between the six and seven-equation models for the Sod test using the IG EOS. The results are shown for pressure (a), velocity (b), mixture density (c) and volume fraction (d) using different resolutions. It can be seen that as the number of cells increases the error norm decreases. Figure 5.15(a) shows that the pressure error norm for both models are almost identical except at 400 cells where the six-equation model has less value. Figure 5.15(b) shows that the six-equation model has more velocity error norm than the seven-equation model except at 400 cells and at relatively higher mesh resolutions. Figure 5.15(c, d) shows that the mixture density and volume fraction error norms are almost identical for both models for all mesh resolutions.

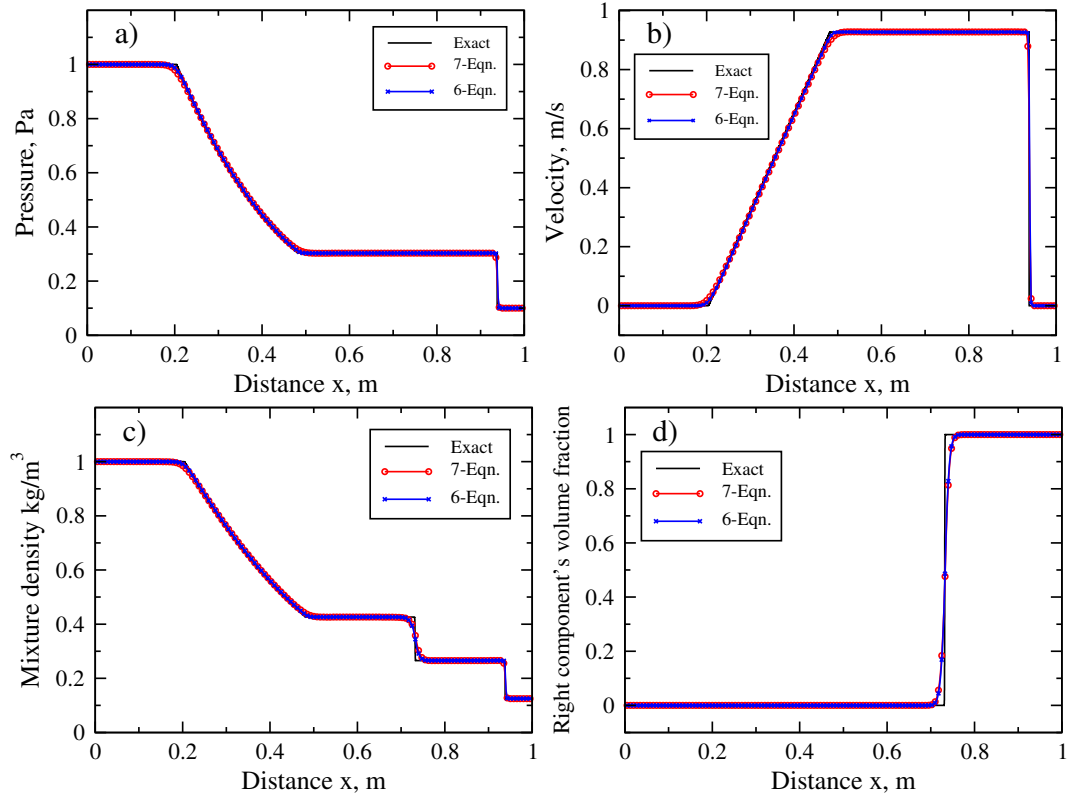


Figure 5.14: Sod test 5.6.1. Results for: (a) pressure, (b) velocity, (c) mixture density and (d) right component's volume fraction. Numerical solution from 6 and 7-eqn. models using the HLLC 200 cells compared to the exact solution at $t = 0.25$ s.

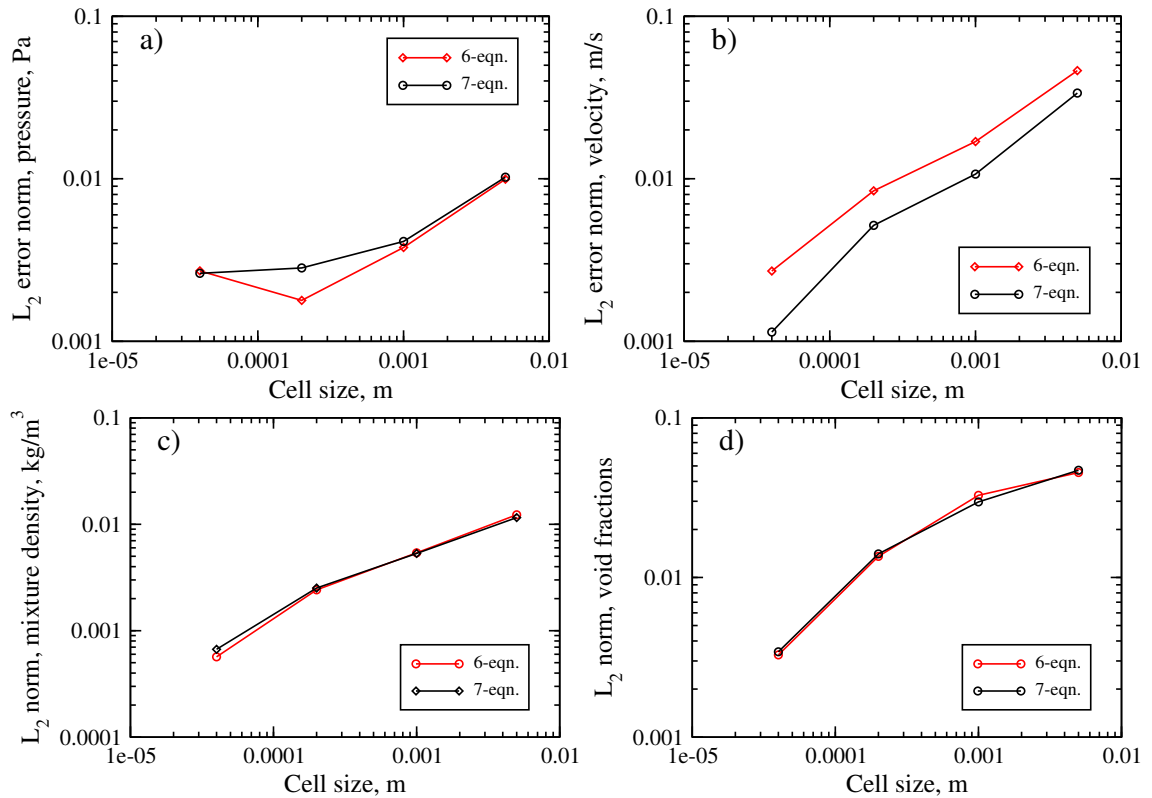


Figure 5.15: Sod test 5.6.1. L_2 error norm spatial convergence for: (a) pressure, (b) velocity, (c) mixture density and (d) volume fraction.

The order of accuracy of the HLLC algorithms for six and seven-equation models using the Sod test are given in Tables 5.8-5.9. It can also be observed that the order of accuracy is less than 2 due to the presence of the discontinuities in the solution as mentioned in subsection 4.6.1.

Table 5.8: Order of accuracy of the HLLC for the 6-Eqn. model for Sod test using IG EOS

Mesh cells	L_2		Order	
	u	ρ	u	ρ
200	0.0462983	0.011561		
1000	0.0169414	0.0053234	0.62466	0.48186
5000	0.0084255	0.0025156	0.434	0.46575
25000	0.002705	0.000669	0.70594	0.82295

Table 5.9: Order of accuracy of the HLLC for the 7-Eqn. model for Sod test using IG EOS

Mesh cells	L_2		Order	
	u	ρ	u	ρ
200	0.0337017	0.01228114		
1000	0.01068	0.005388	0.71402	0.51191
5000	0.005165	0.0024196	0.45138	0.49742
25000	0.0011387	0.0005672	0.93947	0.90134

Table 5.10: The number of time steps and CPU time for the Sod test

Mesh cells	Six-equation model		Seven-equation model	
	Time step	CPU (s)	Time step	CPU (s)
200	128	0.07	214	0.12
400	252	0.31	422	0.50
1000	625	1.93	1047	3.05
5000	3108	47.88	5213	77.68
10000	6211	190.31	10420	307.46
25000	15522	1229.16	26043	2119.18

The number of time steps and CPU time needed by the six and seven-equation models to obtain the solution using different mesh resolutions are given in Table 5.10. The average percentage of the number of time steps and CPU time required by the six-equation model are 40.32 % and 39.14 % less than that required by the seven-equation model to obtain the results for this test problem, respectively. The

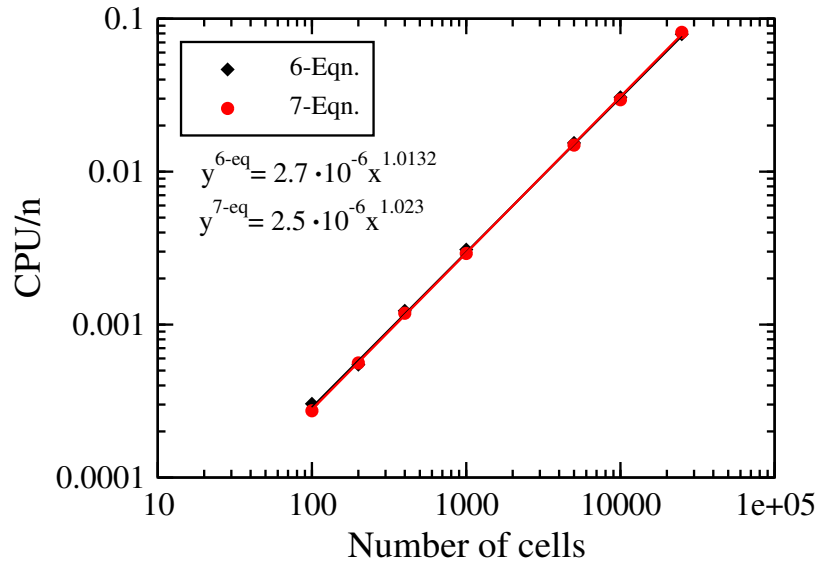


Figure 5.16: Sod test example 5.6.1: Scaling order for the HLLC algorithm for the 6-Eqn. and 7-Eqn. models.

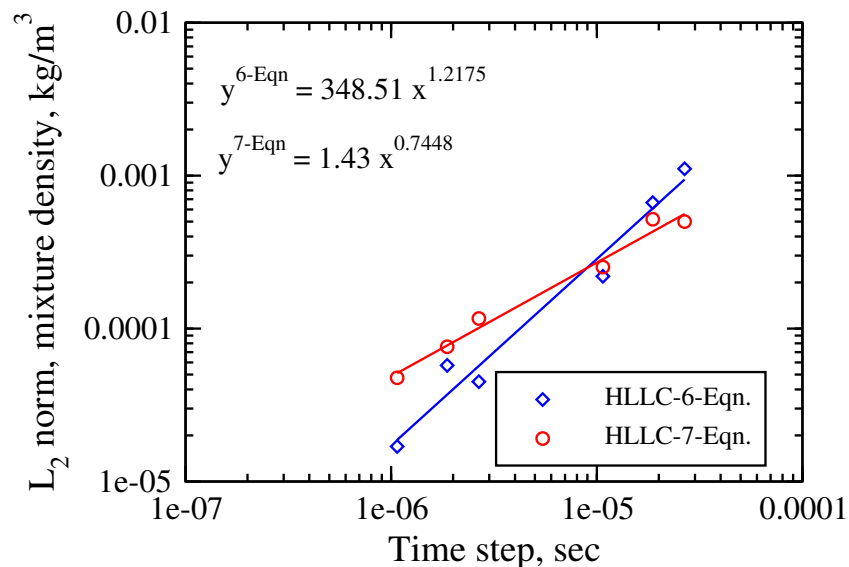


Figure 5.17: Sod test 5.6.1: Temporal convergence for the HLLC algorithm for the 6-Eqn. and 7-Eqn. models.

scaling order of the HLLC algorithm for the six and seven-equation models are 1.0132 and 1.023, respectively, as shown Figure 5.16 using the Sod test.

The temporal convergence is obtained using a fine mesh resolution of 10000 cells and various time steps. The order of temporal convergence for the HLLC solver for the six and seven-equation models are 0.7448 and 1.2175, respectively, as shown in Figure 5.17.

5.6.2 Detonation products-copper interaction test

This two-phase problem considers an interaction of detonation products with the solid copper. This test has been considered by many researchers (see for example,

Saurel and Abgrall, 1999a; Shyue, 2001; Zheng et al., 2011). Also it has been chosen here to show the ability of the developed code to deal with materials governed by a more complex EOS, i.e., the JWL EOS (4.39). This EOS is used to govern the detonation products and the Cochran-Chan (CC) EOS (4.34) is used to govern the copper. The computational domain used to model this problem is 1 m long. The interface separating the two materials is initially located at $x = 0.5$ m. While the detonation products of PBX-9404-3 explosive are put on the left hand side, the copper is put on the right hand side. The CC EOS parameters for copper are the same as those given in subsection 4.5.4, but those for the detonation products governed by the JWL EOS are $\rho_o = 1840$ kg/m³, $A_1 = 8.545 \times 10^{11}$ Pa, $R_1 = 4.6$, $A_2 = 2.05 \times 10^{10}$ Pa, $R_2 = 1.35$, $C_v = 815$ J/(kg·K), $\gamma = 1.25$ and $C_{ek} = 0$ (Dobrtaz, 1972). The initial conditions are given in Table 5.11:

Table 5.11: Initial data for detonation products-copper interaction test 5.6.2

State	ρ_1 [kg/m ³]	u_1 [m/s]	p_1 [Pa]	α_1	ρ_2 [kg/m ³]	u_2 [m/s]	p_2 [Pa]	α_2
Left	2485.37	0	3.7×10^{10}	$1 - \epsilon$	8900	0	3.7×10^{10}	ϵ
Right	2485.37	0	10^5	ϵ	8900	0	10^5	$1 - \epsilon$

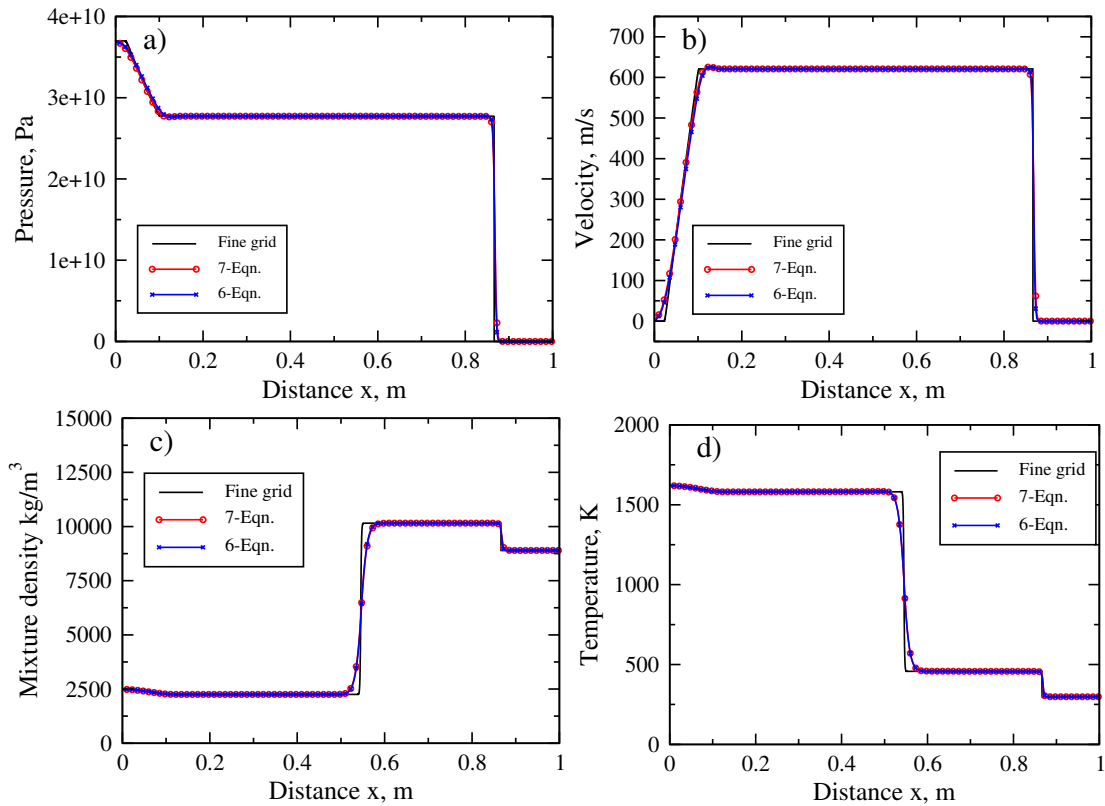


Figure 5.18: Detonation products-copper interaction test example 5.6.2. Results for: (a) pressure, (b) velocity, (c) mixture density and (d) temperature. Numerical solution compared to fine grid at $t = 73 \mu\text{s}$.

As in the previous example a comparison between the six and seven-equation models

is performed, but here the HLL solver is used. While the detonation products are governed by the JWL EOS, the copper plate is governed by the CC EOS. The solution of this test problem consists of three different waves. The first is a shock wave propagating to the right in the copper, the second is a rarefaction wave propagating to the left in the inert explosive and the third wave is a contact discontinuity moving to the right.

Figure 5.18 shows the results for pressure (a), velocity (b), mixture density (c) and temperature (d). The results are displayed using 200 cells at time $t = 73 \mu\text{s}$ and the CFL number equal to 0.6. As the test doesn't have an exact solution, the results are compared with a fine grid solution. It can be noticed that the shock wave is spread over a less number of cells than the contact discontinuity wave as shown in Figure 5.18(c). A good agreement was obtained compared with the reference data.

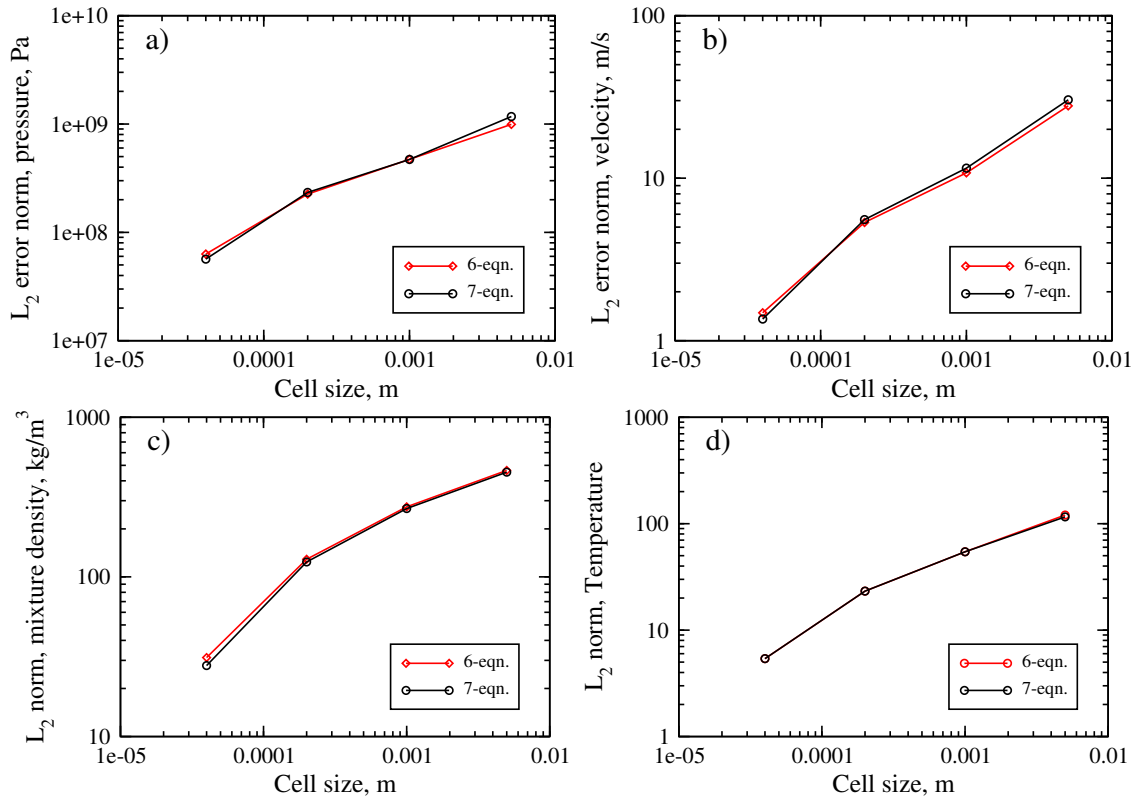


Figure 5.19: Detonation products-copper interaction test 5.6.2. L_2 error norm spatial convergence for: (a) pressure, (b) velocity, (c) mixture density and (d) temperature.

Figure 5.19 shows the error norm (L_2) spatial convergence comparison between the six and seven-equation models for the detonation products-copper interaction test. The results are shown for pressure (a), velocity (b), mixture density (c) and temperature (d) using different resolutions. It can be seen that as the number of cells increases the error norm decreases. The results are almost identical except for Figures 5.19(a) and (b) where the pressure and velocity error norms for the six-equation model at 200 cells has less value error norms but at 400 cells has more error norm. The order of accuracy of the HLL algorithms for six and seven-

equation models using the detonation products-copper interaction test are given in Tables 5.12-5.13. It can also be observed that the order of accuracy is less than 2 due to the presence of the discontinuities in the solution as mentioned in subsection 4.6.1.

Table 5.12: Order of accuracy of the HLLC for the 6-Eqn. model for Sod test using IG EOS

Mesh cells	L_2		Order	
	p	ρ	p	ρ
200	993223446.7	452.8293961		
1000	421601872	268.036043	0.53242	0.32582
5000	225439426.4	124.0956918	0.38896	0.47847
25000	63066098.1	27.81183584	0.7915	0.92926

Table 5.13: Order of accuracy of the HLLC for the 7-Eqn. model for Sod test using IG EOS

Mesh cells	L_2		Order	
	p	ρ	p	ρ
200	1172096546	464.344588		
1000	470875212	274.685549	0.56663	0.3262
5000	233545846.6	129.0332814	0.43569	0.46945
25000	56573185.8	31.2388661	0.88096	0.88131

Table 5.14: The number of time steps and CPU time for detonation products-copper test

Mesh cells	Six-equation model		Seven-equation model	
	Time step	CPU (s)	Time step	CPU (s)
200	176	0.73	183	1.30
400	348	2.87	362	5.09
1000	864	17.67	899	31.35
5000	4293	440.44	4482	770.72
10000	8581	1754.13	8960	3052.47
25000	21445	10983.49	22395	19326.11

The number of time steps and CPU time needed by the six and seven-equation models to obtain the solution using different mesh resolutions are given in Table 5.14. The average percentage of the number of time steps and CPU time required by the six-equation model are 4.05 % and 43.28 % less than that required by the seven-equation model to obtain the results for detonation products-copper interaction test

problem. The scaling order of the HLLC algorithm for the six and seven-equation models are 1.0011 and 0.993, respectively, as shown Figure 5.21 using the detonation products-copper interaction test.

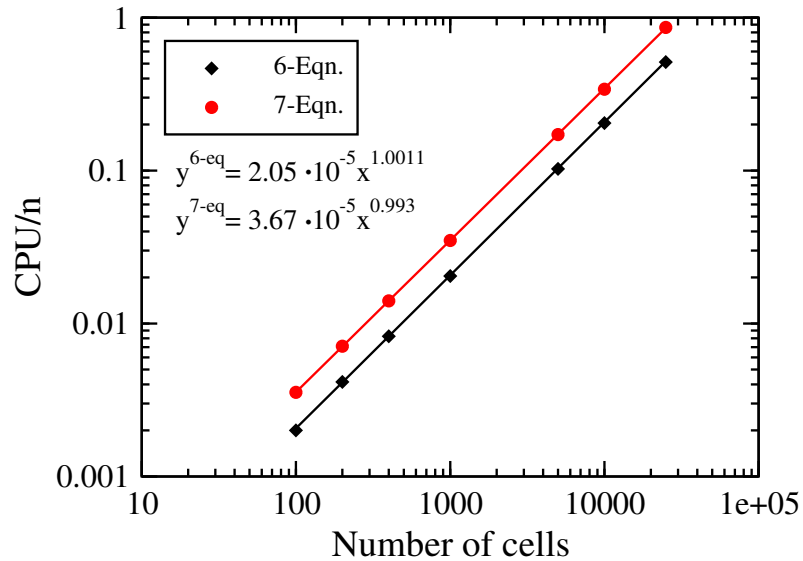


Figure 5.20: Detonation products-copper interaction test 5.6.2: Scaling order for the HLL algorithm for the 6-Eqn. and 7-Eqn. models for detonation products-copper interaction test.

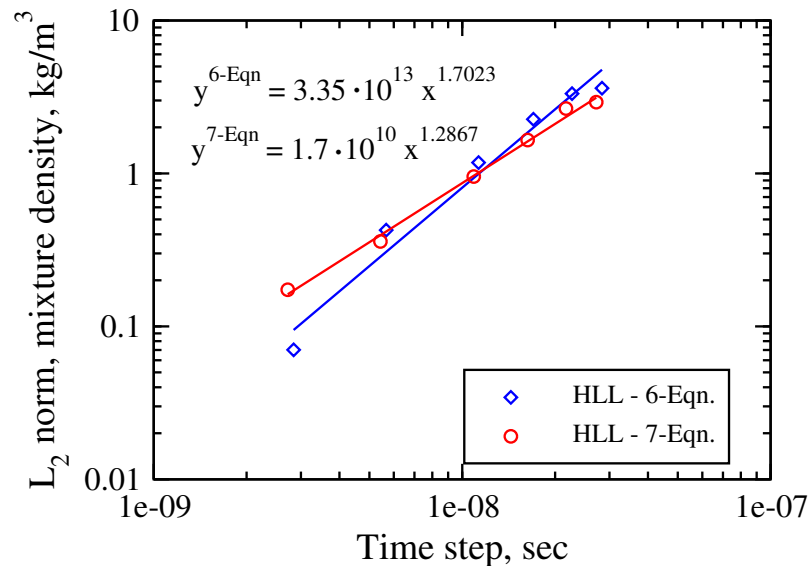


Figure 5.21: Detonation products-copper interaction test 5.6.2: Temporal convergence for the HLL algorithm for the 6-Eqn. and 7-Eqn. models.

The temporal convergence is obtained using a fine mesh resolution of 5000 cells and various time steps. The order of temporal convergence for the HLL solver for the six and seven-equation models are 1.7023 and 1.2867, respectively, as shown in Figure 5.21 using the detonation products-copper interaction test.

Chapter 6

Verification and validation of the two-phase flow models in two dimensions

The six and seven-equation models considered in the previous chapters are extended in this chapter to examine two-dimensional problems. The extended governing equations are discretised following finite volume approach, where the equations are solved numerically by the Godunov-type method in Cartesian coordinate. In this chapter both models have been written in two space dimensions and their mathematical structures and hyperbolicity are studied. The numerical method for solving the hyperbolic and relaxation parts of the models is presented and finally the numerical results are verified and validated using exact or available published results. The verification and validation of the results of the two-phase flow models in two dimensions are demonstrated using various test problems to include different equations of state. These EOSs are the IG (4.14), SG (4.21), vdW (4.30) and Tait's EOS (4.27). The obtained results illustrate that the results are in good agreement with reference data.

6.1 Extension of the seven-equation compressible multiphase flow model to two dimensions

The seven-equation compressible multiphase flow model in two-dimensional space consists of nine partial differential equations. Those are the volume fraction evolution equation for one of the phases, mass equation for each phase, two momentum equations for each phase and energy equation for each phase. The system with relaxation terms but without mass and heat transfer terms that may take place across the interface and without gravitational force terms can be written as follows:

$$\frac{\partial \alpha_1}{\partial t} + u_{int} \frac{\partial \alpha_1}{\partial x} + v_{int} \frac{\partial \alpha_1}{\partial y} = \mu(p_1 - p_2), \quad (6.1a)$$

$$\frac{\partial \alpha_1 \rho_1}{\partial t} + \frac{\partial \alpha_1 \rho_1 u_1}{\partial x} + \frac{\partial \alpha_1 \rho_1 v_1}{\partial y} = 0, \quad (6.1b)$$

$$\frac{\partial \alpha_1 \rho_1 u_1}{\partial t} + \frac{\partial(\alpha_1 \rho_1 u_1^2 + \alpha_1 p_1)}{\partial x} + \frac{\partial \alpha_1 \rho_1 u_1 v_1}{\partial y} = p_{int} \frac{\partial \alpha_1}{\partial x} + \lambda(u_2 - u_1), \quad (6.1c)$$

$$\frac{\partial \alpha_1 \rho_1 v_1}{\partial t} + \frac{\partial \alpha_1 \rho_1 u_1 v_1}{\partial x} + \frac{\partial(\alpha_1 \rho_1 v_1^2 + \alpha_1 p_1)}{\partial y} = p_{int} \frac{\partial \alpha_1}{\partial y} + \lambda(v_2 - v_1), \quad (6.1d)$$

$$\begin{aligned} & \frac{\partial \alpha_1 \rho_1 E_1}{\partial t} + \frac{\partial(\alpha_1 \rho_1 E_1 u_1 + \alpha_1 u_1 p_1)}{\partial x} + \frac{\partial(\alpha_1 \rho_1 E_1 v_1 + \alpha_1 v_1 p_1)}{\partial y} = \\ & p_{int} u_{int} \frac{\partial \alpha_1}{\partial x} + p_{int} v_{int} \frac{\partial \alpha_1}{\partial y} + u_{int} \lambda(u_2 - u_1) + v_{int} \lambda(v_2 - v_1) + p_{int} \mu(p_1 - p_2), \end{aligned} \quad (6.1e)$$

$$\frac{\partial \alpha_2 \rho_2}{\partial t} + \frac{\partial \alpha_2 \rho_2 u_2}{\partial x} + \frac{\partial \alpha_2 \rho_2 v_2}{\partial y} = 0, \quad (6.1f)$$

$$\frac{\partial \alpha_2 \rho_2 u_2}{\partial t} + \frac{\partial(\alpha_2 \rho_2 u_2^2 + \alpha_2 p_2)}{\partial x} + \frac{\partial \alpha_2 \rho_2 u_2 v_2}{\partial y} = -p_{int} \frac{\partial \alpha_1}{\partial x} - \lambda(u_2 - u_1), \quad (6.1g)$$

$$\frac{\partial \alpha_2 \rho_2 v_2}{\partial t} + \frac{\partial \alpha_2 \rho_2 u_2 v_2}{\partial x} + \frac{\partial(\alpha_2 \rho_2 v_2^2 + \alpha_2 p_2)}{\partial y} = -p_{int} \frac{\partial \alpha_1}{\partial y} - \lambda(v_2 - v_1), \quad (6.1h)$$

$$\begin{aligned} & \frac{\partial \alpha_2 \rho_2 E_2}{\partial t} + \frac{\partial(\alpha_2 \rho_2 E_2 u_2 + \alpha_2 u_2 p_2)}{\partial x} + \frac{\partial(\alpha_2 \rho_2 E_2 v_2 + \alpha_2 v_2 p_2)}{\partial y} = \\ & - p_{int} u_{int} \frac{\partial \alpha_1}{\partial x} - p_{int} v_{int} \frac{\partial \alpha_1}{\partial y} - u_{int} \lambda(u_2 - u_1) + v_{int} \lambda(v_2 - v_1) - p_{int} \mu(p_1 - p_2), \end{aligned} \quad (6.1i)$$

where E is the total specific energy, $E = e + \frac{1}{2}u^2 + \frac{1}{2}v^2$ and v_k is the velocity in y -direction for each phase v_{int} is the velocity in y -direction at the interface. The interfacial velocity in x -direction is as given in subsection 4.1.1 and in y -direction is given by:

$$v_{int} = \frac{\sum_k \alpha_k \rho_k v_k}{\sum_k \alpha_k \rho_k}. \quad (6.2)$$

The above relations (6.2) with the closure relations mentioned in subsection 4.1.1 are used to close the model in two dimensions.

6.1.1 Mathematical structure of the seven-equation model in two dimensions

The design of a numerical scheme to find the solution of the Riemann problem for the seven-equation two-dimensional flow model (6.1), requires the evaluation of the eigenvalues of the Jacobian matrices as well as their corresponding eigenvectors. In order to determine the eigenstructure of the model (6.1), the model is written in a quasilinear form without relaxation terms in terms of primitive variables as follows:

$$\frac{\partial \mathbf{w}}{\partial t} + A(\mathbf{w}) \frac{\partial \mathbf{w}}{\partial x} + B(\mathbf{w}) \frac{\partial \mathbf{w}}{\partial y} = 0, \quad (6.3)$$

where \mathbf{w} is the primitive variables vector, $A(\mathbf{w})$ and $B(\mathbf{w})$ are the Jacobian matrices in x and y directions. They are defined respectively as follows:

$$\mathbf{w} = [\alpha_1 \quad \rho_1 \quad u_1 \quad v_1 \quad p_1 \quad \rho_2 \quad u_2 \quad v_2 \quad p_2]^T, \quad (6.4)$$

$$A(\mathbf{w}) = \begin{pmatrix} u_{int} & 0 & 0 & 0 & 0 & 0 & 0 & 0 & 0 \\ \frac{\rho_g(u_1 - u_{int})}{\alpha_1} & u_1 & \rho_1 & 0 & 0 & 0 & 0 & 0 & 0 \\ \frac{(p_1 - p_{int})}{\alpha_1 \rho_1} & 0 & u_1 & \frac{1}{\rho_1} & 0 & 0 & 0 & 0 & 0 \\ 0 & 0 & 0 & u_1 & 0 & 0 & 0 & 0 & 0 \\ \frac{\rho_1 c_{1int}^2 (u_1 - u_{int})}{\alpha_1} & 0 & \rho_1 c_1^2 & 0 & u_1 & 0 & 0 & 0 & 0 \\ \frac{-\rho_2 (u_2 - u_{int})}{\alpha_2} & 0 & 0 & 0 & 0 & u_2 & \rho_2 & 0 & 0 \\ \frac{-(p_2 - p_{int})}{\alpha_2 \rho_2} & 0 & 0 & 0 & 0 & 0 & u_2 & 0 & \frac{1}{\rho_2} \\ 0 & 0 & 0 & 0 & 0 & 0 & 0 & u_2 & 0 \\ \frac{-\rho_2 c_{2int}^2 (u_2 - u_{int})}{\alpha_2} & 0 & 0 & 0 & 0 & 0 & \rho_2 c_2^2 & 0 & u_2 \end{pmatrix}, \quad (6.5)$$

$$B(\mathbf{w}) = \begin{pmatrix} v_{int} & 0 & 0 & 0 & 0 & 0 & 0 & 0 & 0 \\ \frac{\rho_1 (v_1 - v_{int})}{\alpha_1} & v_1 & 0 & \rho_1 & 0 & 0 & 0 & 0 & 0 \\ 0 & 0 & v_1 & 0 & 0 & 0 & 0 & 0 & 0 \\ \frac{(p_1 - p_{int})}{\alpha_1 \rho_1} & 0 & 0 & v_1 & \frac{1}{\rho_1} & 0 & 0 & 0 & 0 \\ \frac{\rho_1 c_{1int}^2 (v_1 - v_{int})}{\alpha_1} & 0 & 0 & \rho_1 c_1^2 & v_1 & 0 & 0 & 0 & 0 \\ \frac{-\rho_2 (v_2 - v_{int})}{\alpha_2} & 0 & 0 & 0 & 0 & v_2 & 0 & \rho_2 & 0 \\ 0 & 0 & 0 & 0 & 0 & 0 & v_2 & 0 & 0 \\ \frac{-(p_2 - p_{int})}{\alpha_2 \rho_2} & 0 & 0 & 0 & 0 & 0 & 0 & v_2 & \frac{1}{\rho_2} \\ \frac{-\rho_2 c_{2int}^2 (v_2 - v_{int})}{\alpha_2} & 0 & 0 & 0 & 0 & 0 & 0 & \rho_2 c_2^2 & v_2 \end{pmatrix}. \quad (6.6)$$

The eigenvalues of the Jacobian matrix $A(\mathbf{w})$ are as follows:

$$\begin{aligned}
 \lambda_{x1} &= u_{int}, & \lambda_{x2} &= \lambda_{x3} = \lambda_{x4} = \lambda_{x5} = u_1, \\
 \lambda_{x6} &= \lambda_{x7} = u_2, \\
 \lambda_{x8} &= u_2 + c_2, & \lambda_{x9} &= u_2 - c_2.
 \end{aligned} \tag{6.7}$$

The corresponding right eigenvectors for the Jacobian matrix $A(\mathbf{w})$ are:

$$\mathbf{K}_{x1} = \begin{bmatrix} \frac{(-u_1 + u_{int})\alpha_1\rho_1}{-(p_1 - p_{int})} \\ \frac{\rho_1[\rho_1(u_1 - u_{int})^2 + p_{int} - p_1]}{(p_1 - p_{int})(u_1 - u_{int})} \\ 1 \\ 0 \\ \frac{\rho_1[c_1^2(p_{int} - p_1) + \rho_1 c_{1int}^2(u_1 - u_{int})^2]}{(p_1 - p_{int})(u_1 - u_{int})} \\ \frac{-\alpha_1\rho_1(u_1 - u_{int})[\rho_2(c_{2int}^2 - \sigma_2) + p_{int} - p_2]}{-\alpha_2(p_1 - p_{int})\sigma_2} \\ \frac{\alpha_1\rho_1(u_1 - u_{int})(u_2 - u_{int})[p_{int} - p_2 + \rho_2 c_{2int}^2]}{-\alpha_2\rho_2(p_1 - p_{int})\sigma_2} \\ 0 \\ \frac{\alpha_1\rho_1(u_{int} - u_1)[c_2^2(p_{int} - p_2) + \rho_2 c_{2int}^2(u_2 - u_{int})^2]}{-\alpha_2(p_1 - p_{int})\sigma_2} \end{bmatrix},$$

$$\mathbf{K}_{x2} = \begin{bmatrix} 0 \\ 0 \\ 0 \\ 0 \\ 1 \\ 0 \\ 0 \\ 0 \\ 0 \end{bmatrix}, \quad \mathbf{K}_{x3} = \begin{bmatrix} 0 \\ 1 \\ 0 \\ 0 \\ 0 \\ 0 \\ 0 \\ 0 \\ 0 \end{bmatrix}, \quad \mathbf{K}_{x4} = \mathbf{K}_{x5} = \begin{bmatrix} 0 \\ 1 \\ 0 \\ 0 \\ 0 \\ 0 \\ 0 \\ 0 \\ 0 \end{bmatrix}, \quad \mathbf{K}_{x6} = \begin{bmatrix} 0 \\ 0 \\ 0 \\ 0 \\ 0 \\ 0 \\ 1 \\ 0 \end{bmatrix}, \tag{6.8}$$

$$\mathbf{K}_{x7} = \begin{bmatrix} 0 \\ 0 \\ 0 \\ 0 \\ 0 \\ 1 \\ 0 \\ 0 \\ 0 \end{bmatrix}, \quad \mathbf{K}_{x8} = \begin{bmatrix} 0 \\ 0 \\ 0 \\ 0 \\ 0 \\ 1 \\ \frac{c_2}{\rho_2} \\ 0 \\ c_2^2 \end{bmatrix}, \quad \mathbf{K}_{x9} = \begin{bmatrix} 0 \\ 0 \\ 0 \\ 0 \\ 0 \\ 1 \\ -\frac{c_2}{\rho_2} \\ 0 \\ c_2^2 \end{bmatrix},$$

where $\sigma_2 = c_2^2 - (u_2 - u_{int})^2$.

and the eigenvalues of the Jacobian matrix $B(\mathbf{w})$ are as follows:

$$\begin{aligned}\lambda_{y1} &= v_{int}, \\ \lambda_{y2} &= v_2 + c_2, \quad \lambda_{y3} = v_2 - c_2, \quad \lambda_{y4} = v_1 + c_1, \quad \lambda_{y5} = v_1 - c_1, \\ \lambda_{y6} &= \lambda_{y7} = v_1, \quad \lambda_{y8} = \lambda_{y9} = v_2.\end{aligned}\tag{6.9}$$

The corresponding right eigenvectors for the Jacobian matrix $B(\mathbf{w})$ are:

$$\begin{aligned}\mathbf{K}_{y1} &= \begin{bmatrix} 1 \\ -\frac{\rho_1[(v_1 - v_{int})^2 - (c_1^2 - c_{int}^2)] + (p_1 - p_{int})}{-\alpha_1 \zeta_1} \\ 0 \\ \frac{(-v_1 - v_{int})(\rho_1 c_{2int}^2 + p_{int} - p_1)}{-\alpha_1 \rho_1 \zeta_1} \\ \frac{c_1^2(p_{int} - p_1) - \rho_1 c_{1int}^2 (v_1 - v_{int})^2}{\rho_2[(v_1 - v_{int}) + (c_2^2 - c_{2int}^2)] + p_{int} - p_2} \\ -\alpha_2 \zeta_2 \\ 0 \\ \frac{(-v_2 - v_{int})(\rho_2 c_{2int}^2 + p_{int} - p_2)}{-\alpha_2 \rho_2 \zeta_2} \\ \frac{c_2^2(p_{int} - p_2) - \rho_2 c_{2int}^2 (v_2 - v_{int})^2}{-\alpha_2 \zeta_2} \end{bmatrix}, \\ \mathbf{K}_{y2} &= \begin{bmatrix} 0 \\ 0 \\ 0 \\ 0 \\ 0 \\ 1 \\ 0 \\ \frac{c_2}{\rho_2} \\ c_2^2 \end{bmatrix}, \mathbf{K}_{y3} = \begin{bmatrix} 0 \\ 0 \\ 0 \\ 0 \\ 0 \\ 1 \\ 0 \\ -\frac{c_2}{\rho_2} \\ c_2^2 \end{bmatrix}, \mathbf{K}_{y4} = \begin{bmatrix} 0 \\ 1 \\ 0 \\ \frac{c_1}{\rho_1} \\ c_1^2 \\ 0 \\ 0 \\ 0 \\ 0 \end{bmatrix}, \mathbf{K}_{y5} = \begin{bmatrix} 0 \\ 1 \\ 0 \\ -\frac{c_1}{\rho_1} \\ c_1^2 \\ 0 \\ 0 \\ 0 \\ 0 \end{bmatrix}, \\ \mathbf{K}_{y6} &= \begin{bmatrix} 0 \\ 0 \\ 1 \\ 0 \\ 0 \\ 0 \\ 0 \\ 0 \\ 0 \end{bmatrix}, \mathbf{K}_{y7} = \begin{bmatrix} 0 \\ 1 \\ 0 \\ 0 \\ 0 \\ 0 \\ 0 \\ 0 \\ 0 \end{bmatrix}, \mathbf{K}_{y8} = \begin{bmatrix} 0 \\ 0 \\ 0 \\ 0 \\ 0 \\ 0 \\ 1 \\ 0 \\ 0 \end{bmatrix}, \mathbf{K}_{y9} = \begin{bmatrix} 0 \\ 0 \\ 0 \\ 0 \\ 0 \\ 0 \\ 1 \\ 0 \\ 0 \end{bmatrix},\end{aligned}\tag{6.10}$$

where $\zeta_1 = c_1^2 - (v_1 - v_{int})^2$ and $\zeta_2 = c_2^2 - (v_2 - v_{int})^2$.

It can be observed that the eigenvalues (6.7) and (6.9) of the Jacobian matrices $A(\mathbf{w})$ and $B(\mathbf{w})$ are real but not distinct. Therefore, the model (6.23) is hyperbolic but non-strictly hyperbolic. The model may lose its hyperbolicity if any of the above eigenvectors (6.8) and (6.10) become linearly dependent. This occurs when any of the following conditions holds:

$$\sigma_2 = 0, \quad \zeta_1 = 0, \quad \zeta_2 = 0, \quad \alpha_1 = 0, \quad \alpha_2 = 0.$$

To avoid disappearance of both phases everywhere in the domain, it is necessary to assume that a small amount $\epsilon = 10^{-8}$ of the other phase exist in the main phase.

6.2 Extension of the six-equation compressible multiphase flow model to two dimensions

The six-equation compressible multiphase flow model is extended to two space dimensions. The system of governing equations including the derived conservative mixture energy equation takes the following form:

$$\frac{\partial \alpha_1}{\partial t} + u \frac{\partial \alpha_1}{\partial x} + v \frac{\partial \alpha_1}{\partial y} = \mu(p_1 - p_2), \quad (6.11a)$$

$$\frac{\partial \alpha_1 \rho_1}{\partial t} + \frac{\partial \alpha_1 \rho_1 u}{\partial x} + \frac{\partial \alpha_1 \rho_1 v}{\partial y} = 0, \quad (6.11b)$$

$$\frac{\partial \alpha_2 \rho_2}{\partial t} + \frac{\partial \alpha_2 \rho_2 u}{\partial x} + \frac{\partial \alpha_2 \rho_2 v}{\partial y} = 0, \quad (6.11c)$$

$$\frac{\partial \rho u}{\partial t} + \frac{\partial (\rho u^2 + p)}{\partial x} + \frac{\partial \rho u v}{\partial y} = 0, \quad (6.11d)$$

$$\frac{\partial \rho v}{\partial t} + \frac{\partial \rho u v}{\partial x} + \frac{\partial (\rho v^2 + p)}{\partial y} = 0, \quad (6.11e)$$

$$\frac{\partial \alpha_1 \rho_1 e_1}{\partial t} + \frac{\partial \alpha_1 \rho_1 e_1 u}{\partial x} + \alpha_1 p_1 \frac{\partial u}{\partial x} + \frac{\partial \alpha_1 \rho_1 e_1 v}{\partial y} + \alpha_1 p_1 \frac{\partial v}{\partial y} = \mu p_{int} (p_2 - p_1), \quad (6.11f)$$

$$\frac{\partial \alpha_2 \rho_2 e_2}{\partial t} + \frac{\partial \alpha_2 \rho_2 e_2 u}{\partial x} + \alpha_2 p_2 \frac{\partial u}{\partial x} + \frac{\partial \alpha_2 \rho_2 e_2 v}{\partial y} + \alpha_2 p_2 \frac{\partial v}{\partial y} = -\mu p_{int} (p_2 - p_1), \quad (6.11g)$$

$$\frac{\partial \rho E}{\partial t} + \frac{\partial u(\rho E + p)}{\partial x} + \frac{\partial v(\rho E + p)}{\partial y} = 0. \quad (6.11h)$$

where E is the total specific energy is defined as $E = e + \frac{1}{2}u^2 + \frac{1}{2}v^2$, v is the y -component of mixture velocity, p is the mixture pressure and p_{int} is the interfacial pressure. Both p and p_{int} are defined as $p = p_{int} = \alpha_1 p_1 + \alpha_2 p_2$.

In addition to the closure relations introduced in section 5.1.2, the mixture ve-

locity in y -direction v is given as follows:

$$v = \frac{\alpha_1 \rho_1 v_1 + \alpha_2 \rho_2 v_2}{\rho}. \quad (6.12)$$

6.2.1 Mathematical structure of the six-equation model in two dimensions

To explore the mathematical structure of the six-equation two-dimensional flow model (6.11), the eigenvalues and the corresponding eigenvectors are determined. Consider the model (6.11) without the additional relaxation terms written in a quasi-linear form in terms of primitive variables as follows:

$$\frac{\partial \mathbf{w}}{\partial t} + A(\mathbf{w}) \frac{\partial \mathbf{w}}{\partial x} + B(\mathbf{w}) \frac{\partial \mathbf{w}}{\partial y} = 0. \quad (6.13)$$

The vector of primitive variables \mathbf{w} is defined by:

$$\mathbf{w} = [\alpha_1 \quad \rho_1 \quad \rho_2 \quad u \quad v \quad p_1 \quad p_2]^T. \quad (6.14)$$

The primitive variables Jacobian matrices $A(\mathbf{w})$ and $B(\mathbf{w})$ are defined as follows:

$$A(\mathbf{w}) = \begin{pmatrix} u & 0 & 0 & 0 & 0 & 0 & 0 \\ 0 & u & 0 & \rho_1 & 0 & 0 & 0 \\ 0 & 0 & u & \rho_2 & 0 & 0 & 0 \\ \frac{p_1 - p_2}{\rho} & 0 & 0 & u & 0 & \frac{\alpha_1}{\rho} & \frac{1 - \alpha_1}{\rho} \\ 0 & 0 & 0 & 0 & u & 0 & 0 \\ 0 & 0 & 0 & \rho_1 c_1^2 & 0 & u & 0 \\ 0 & 0 & 0 & \rho_2 c_2^2 & 0 & 0 & u \end{pmatrix}, \quad (6.15)$$

$$B(\mathbf{w}) = \begin{pmatrix} v & 0 & 0 & 0 & 0 & 0 & 0 \\ 0 & v & 0 & 0 & \rho_1 & 0 & 0 \\ 0 & 0 & v & 0 & \rho_2 & 0 & 0 \\ 0 & 0 & 0 & v & 0 & 0 & 0 \\ \frac{p_1 - p_2}{\rho} & 0 & 0 & 0 & v & \frac{\alpha_1}{\rho} & \frac{1 - \alpha_1}{\rho} \\ \rho & 0 & 0 & 0 & \rho_1 c_1^2 & v & 0 \\ 0 & 0 & 0 & 0 & \rho_2 c_2^2 & 0 & v \end{pmatrix}. \quad (6.16)$$

The phases sound speeds c_1 and c_2 appearing in the above matrices are defined as:

$$c_k^2 = \frac{\frac{p_k}{\rho_k^2} - \left(\frac{\partial e_k}{\partial \rho_k} \right)_{p_k}}{\left(\frac{\partial e_k}{\partial p_k} \right)_{\rho_k}}, \quad k = 1, 2. \quad (6.17)$$

Using the definition of speed of sound given by equation (6.17) and any of the EOSs written in the form of the Mie-Grüneisen EOS (4.12), the phase sound speed can be derived for various EOSs as given in section 4.2.

The system of governing equations is said to be strictly hyperbolic if the eigenvalues of the Jacobian matrices $A(\mathbf{w})$ and $B(\mathbf{w})$ are real and distinct. The Jacobian matrix $A(\mathbf{w})$ has seven real eigenvalues which were determined to be:

$$\begin{aligned}\lambda_{x1} &= \lambda_{x2} = \lambda_{x3} = \lambda_{x4} = \lambda_{x5} = u, \\ \lambda_{x6} &= u + c, \\ \lambda_{x7} &= u - c.\end{aligned}\tag{6.18}$$

The mixture sound speed c is expressed as:

$$c^2 = \sum_{k=1}^2 Y_k c_k^2,\tag{6.19}$$

where $Y_k = \frac{\alpha_k \rho_k}{\rho}$. The right eigenvectors corresponding to the seven eigenvalues for the Jacobian matrix $A(\mathbf{w})$ were determined to be:

$$\begin{aligned}\mathbf{K}_{x1} &= \begin{bmatrix} 0 \\ 0 \\ 0 \\ 0 \\ 0 \\ \frac{\alpha_1 - 1}{\alpha_1} \\ 1 \end{bmatrix}, \quad \mathbf{K}_{x2} = \begin{bmatrix} 0 \\ 0 \\ 0 \\ 0 \\ 1 \\ 0 \\ 0 \end{bmatrix}, \quad \mathbf{K}_{x3} = \begin{bmatrix} 0 \\ 0 \\ 1 \\ 0 \\ 0 \\ 0 \\ 0 \end{bmatrix}, \quad \mathbf{K}_{x4} = \begin{bmatrix} 0 \\ 1 \\ 0 \\ 0 \\ 0 \\ 0 \\ 0 \end{bmatrix}, \\ \mathbf{K}_{x5} &= \begin{bmatrix} 1 \\ 0 \\ 0 \\ 0 \\ 0 \\ \frac{p_2 - p_1}{\alpha_1} \\ 0 \end{bmatrix}, \quad \mathbf{K}_{x6} = \begin{bmatrix} 0 \\ 1 \\ \frac{\rho_2}{\rho_1 c} \\ \frac{\rho_1}{\rho_1} \\ 0 \\ c_1^2 \\ \frac{\rho_2 c_2^2}{\rho_1} \end{bmatrix}, \quad \mathbf{K}_{x7} = \begin{bmatrix} 0 \\ 1 \\ \frac{\rho_2}{\rho_1} \\ -\frac{\rho_1}{\rho_1} \\ 0 \\ c_1^2 \\ \frac{\rho_2 c_2^2}{\rho_1} \end{bmatrix}.\end{aligned}\tag{6.20}$$

The Jacobian matrix $B(\mathbf{w})$ has seven real eigenvalues which were determined to be:

$$\begin{aligned}
 \lambda_{y1} &= \lambda_{y2} = \lambda_{y3} = \lambda_{y4} = \lambda_{y5} = v, \\
 \lambda_{y6} &= v + c, \\
 \lambda_{y7} &= v - c.
 \end{aligned} \tag{6.21}$$

Their corresponding right eigenvectors are as follows:

$$\begin{aligned}
 \mathbf{K}_{y1} &= \begin{bmatrix} 0 \\ 0 \\ 0 \\ 0 \\ 0 \\ \frac{\alpha_1 - 1}{\alpha_1} \\ 1 \end{bmatrix}, \quad \mathbf{K}_{y2} = \begin{bmatrix} 0 \\ 0 \\ 0 \\ 1 \\ 0 \\ 0 \\ 0 \end{bmatrix}, \quad \mathbf{K}_{y3} = \begin{bmatrix} 0 \\ 0 \\ 1 \\ 0 \\ 0 \\ 0 \\ 0 \end{bmatrix}, \quad \mathbf{K}_{y4} = \begin{bmatrix} 0 \\ 1 \\ 0 \\ 0 \\ 0 \\ 0 \\ 0 \end{bmatrix}, \\
 \mathbf{K}_{y5} &= \begin{bmatrix} 1 \\ 0 \\ 0 \\ 0 \\ 0 \\ \frac{p_2 - p_1}{\alpha_1} \\ 0 \end{bmatrix}, \quad \mathbf{K}_{y6} = \begin{bmatrix} 0 \\ 1 \\ \frac{\rho_2}{\rho_1} \\ 0 \\ c \\ \rho_1 \\ c_1^2 \\ \frac{\rho_2 c_2^2}{\rho_1} \end{bmatrix}, \quad \mathbf{K}_{y7} = \begin{bmatrix} 0 \\ 1 \\ \frac{\rho_2}{\rho_1} \\ 0 \\ -c \\ \rho_1 \\ c_1^2 \\ \frac{\rho_2 c_2^2}{\rho_1} \end{bmatrix}. \tag{6.22}
 \end{aligned}$$

One can observe that the eigenvalues (6.18) and (6.21) of the Jacobian matrices $A(\mathbf{w})$ and $B(\mathbf{w})$ are real but not distinct. Therefore, the model (6.11) is hyperbolic but non-strictly hyperbolic.

6.3 Numerical method for the two-dimensional seven-equation model

The seven-equation compressible multiphase flow model (6.1) mentioned in section 6.1 consists of a system of hyperbolic partial differential equations. The system cannot be written in the divergence form and hence the standard numerical methods developed for conservation laws are not applicable directly. In order to solve this system, a numerical scheme is constructed which decomposes this system of governing equations into hyperbolic and non-hyperbolic parts as mentioned previously in subsections 4.4.1 and 5.3.1.

6.3.1 The hyperbolic operator of the two-dimensional seven-equation model

Consider the hyperbolic part of the system (6.1) including the non-conservative equation (6.1a) and the non-conservative terms that exist in the momentum and energy equations. This part can be written without the additional relaxation terms in the following form:

$$\frac{\partial \alpha_1}{\partial t} + u_{int} \frac{\partial \alpha_1}{\partial x} + v_{int} \frac{\partial \alpha_1}{\partial y} = 0, \quad (6.23a)$$

$$\frac{\partial Q}{\partial t} + \frac{\partial F(Q)}{\partial x} + \frac{\partial G(Q)}{\partial y} = H_1(Q) \frac{\partial \alpha_1}{\partial x} + H_2(Q) \frac{\partial \alpha_1}{\partial y}, \quad (6.23b)$$

where Q , $F(Q)$, $G(Q)$, $H_1(Q)$ and $H_2(Q)$ are the vectors of conserved variables, fluxes in x -direction, fluxes in y -direction, non-conservative in x -direction and non-conservative in y -direction, respectively. These vectors are defined as follows:

$$Q = \begin{bmatrix} \alpha_1 \rho_1 \\ \alpha_1 \rho_1 u_1 \\ \alpha_1 \rho_1 v_1 \\ \alpha_1 \rho_1 E_1 \\ \alpha_2 \rho_2 \\ \alpha_2 \rho_2 u_2 \\ \alpha_2 \rho_2 v_2 \\ \alpha_2 \rho_2 E_2 \end{bmatrix}, F(Q) = \begin{bmatrix} \alpha_1 \rho_1 u_1 \\ \alpha_1 \rho_1 u_1^2 + \alpha_1 p_1 \\ \alpha_1 \rho_1 u_1 v_1 \\ u_1 (\alpha_1 \rho_1 E_1 + \alpha_1 p_1) \\ \alpha_2 \rho_2 u_2 \\ \alpha_2 \rho_2 u_2^2 + \alpha_2 p_2 \\ \alpha_2 \rho_2 u_2 v_2 \\ u_2 (\alpha_2 \rho_2 E_2 + \alpha_2 p_2) \end{bmatrix},$$

and

$$G(Q) = \begin{bmatrix} \alpha_1 \rho_1 v_1 \\ \alpha_1 \rho_1 u_1 v_1 \\ \alpha_1 \rho_1 v_1^2 + \alpha_1 p_1 \\ v_1 (\alpha_1 \rho_1 E_1 + \alpha_1 p_1) \\ \alpha_2 \rho_2 v_2 \\ \alpha_2 \rho_2 u_2 v_2 \\ \alpha_2 \rho_2 v_2^2 + \alpha_2 p_2 \\ v_2 (\alpha_2 \rho_2 E_2 + \alpha_2 p_2) \end{bmatrix}, H_1(Q) = \begin{bmatrix} 0 \\ p_{int} \\ 0 \\ p_{int} u_{int} \\ 0 \\ -p_{int} \\ 0 \\ -p_{int} u_{int} \end{bmatrix}, H_2(Q) = \begin{bmatrix} 0 \\ 0 \\ p_{int} \\ p_{int} v_{int} \\ 0 \\ 0 \\ -p_{int} \\ -p_{int} v_{int} \end{bmatrix}.$$

To solve the hyperbolic part (6.23), Godunov's method utilising exact or approximate Riemann solvers is used in implementing numerical schemes. These schemes,

which are developed for conservation laws, have the ability to capture shock discontinuities correctly whereas the non-conservative schemes are not able to capture the exact position of the discontinuity (LeVeque, 2004; Toro, 2009). According to the Godunov method the non-conservative equation for the volume fraction (6.23a) is discretised as follows:

$$\begin{aligned} \alpha_{i,j}^{n+1} = \alpha_{i,j}^n &- \frac{\Delta t}{\Delta x} [\alpha^*(\alpha_{i,j}^n, \alpha_{i+1,j}^n) - \alpha^*(\alpha_{i-1,j}^n, \alpha_{i,j}^n)] \\ &- \frac{\Delta t}{\Delta y} [\alpha^*(\alpha_{i,j}^n, \alpha_{i,j+1}^n) - \alpha^*(\alpha_{i,j-1}^n, \alpha_{i,j}^n)], \end{aligned} \quad (6.24)$$

and the equation (6.23b) is discretised as follows:

$$\begin{aligned} Q_{i,j}^{n+1} = Q_{i,j}^n &- \frac{\Delta t}{\Delta x} [F^*(Q_{i,j}^n, Q_{i+1,j}^n) - F^*(Q_{i-1,j}^n, Q_{i,j}^n)] \\ &- \frac{\Delta t}{\Delta y} [G^*(Q_{i,j}^n, Q_{i,j+1}^n) - G^*(Q_{i,j-1}^n, Q_{i,j}^n)] \\ &+ \Delta t H_1(Q_{i,j}^n) \Delta x + \Delta t H_2(Q_{i,j}^n) \Delta y, \end{aligned} \quad (6.25)$$

where Δx and Δy are space increments and Δt is the time step defined as:

$$\Delta t = \text{CFL} \min \left(\frac{\Delta x}{S_x}, \frac{\Delta y}{S_y} \right). \quad (6.26)$$

CFL is the Courant number, while S_x and S_y are the maximum wave speeds in x and y directions at time level n , respectively. To obtain a second order accuracy in both space and time for the solution of the hyperbolic operator, the MUSCL-Hancock high resolution scheme described in Toro (2009) is used.

6.3.2 The velocity and pressure relaxation operator

The second step in the numerical solution of the seven-equation model (6.1) is to solve the velocity and pressure relaxation operator following the Strang splitting method (??). The seven-equation model is a full non-equilibrium model which can deal with fluid and mixtures that have different velocity, pressure and so on. The velocity and pressure relaxation processes are assumed to take place instantaneously. To fulfill the boundary conditions at the interface that separates two fluids they are performed in the numerical solution at each time step. The complete solution is obtained by solving the following ordinary differential equations (ODE):

$$\frac{dQ}{dt} = D_V + D_P, \quad (6.27)$$

where Q is defined as:

$$Q = [\alpha_1, \alpha_1 \rho_1, \alpha_1 \rho_1 u_1, \alpha_1 \rho_1 v_1, \alpha_1 \rho_1 E_1, \alpha_2 \rho_2, \alpha_2 \rho_2 u_2, \alpha_2 \rho_2 v_2, \alpha_2 \rho_2 E_2]^T, \quad (6.28)$$

The velocity relaxation term is D_V and D_P is the pressure relaxation term. They are given by:

$$D_V = \begin{bmatrix} 0 \\ 0 \\ \lambda(u_2 - u_1) \\ \lambda(v_2 - v_1) \\ u_{int}\lambda(u_2 - u_1) + v_{int}\lambda(v_2 - v_1) \\ 0 \\ -\lambda(u_2 - u_1) \\ -\lambda(v_2 - v_1) \\ -u_{int}\lambda(u_2 - u_1) - v_{int}\lambda(v_2 - v_1) \end{bmatrix}, D_P = \begin{bmatrix} \mu(p_1 - p_2) \\ 0 \\ 0 \\ 0 \\ p_{int}\mu(p_1 - p_2) \\ 0 \\ 0 \\ 0 \\ -p_{int}\mu(p_1 - p_2) \end{bmatrix}. \quad (6.29)$$

Solution of the ODE (6.27) is obtained by solving the two integration operators associated with the corresponding vectors (6.29) in succession.

Velocity relaxation

In order to enable the velocity relaxation process to drive both phases to equilibrium in a very short time, the velocity relaxation parameter λ has to be infinite. Consider the ODE:

$$\frac{dQ}{dt} = D_V. \quad (6.30)$$

Combining the mass and momentum equations for each phase and integrating the resultant equation yields the following relation for the velocity relaxation in x direction:

$$u_1^* = u_2^* = u_{int}^* = \frac{\alpha_1^0 \rho_1^0 u_1^0 + \alpha_2^0 \rho_2^0 u_2^0}{\alpha_1^0 \rho_1^0 + \alpha_2^0 \rho_2^0}, \quad (6.31)$$

similarly for the velocity in y direction:

$$v_1^* = v_2^* = v_{int}^* = \frac{\alpha_1^0 \rho_1^0 v_1^0 + \alpha_2^0 \rho_2^0 v_2^0}{\alpha_1^0 \rho_1^0 + \alpha_2^0 \rho_2^0}, \quad (6.32)$$

where the variables with (*) and (0) represent the states after and before the relaxation process, respectively. Since velocity relaxation terms are present in the energy equation of the system (6.30), update of the internal energy for both phases is necessary after the velocity relaxation process using the following relations:

$$e_1^* = e_1^0 + \frac{1}{2} (u_1^* - u_1^0)^2 + \frac{1}{2} (v_1^* - v_1^0)^2, \quad (6.33a)$$

$$e_2^* = e_2^0 + \frac{1}{2} (u_2^* - u_2^0)^2 + \frac{1}{2} (v_2^* - v_2^0)^2. \quad (6.33b)$$

Pressure relaxation

Similar to the velocity relaxation process, the pressure relaxation process has to take place instantaneously to reach the state of equilibrium for both phases. To this end, the pressure relaxation parameter μ has to be infinite. Consider the following ODE:

$$\frac{dQ}{dt} = D_P. \quad (6.34)$$

Combining the mass, momentum and energy equations for phase 1. One obtains:

$$\frac{\partial e_1}{\partial t} = -\frac{p_{int}}{\alpha_1 \rho_1} \frac{\partial \alpha_1}{\partial t}. \quad (6.35)$$

Its integration yields:

$$e_1^* = e_1^0 - \frac{p_{int}}{\alpha_1 \rho_1} (\alpha_1^* - \alpha_1^0). \quad (6.36)$$

A similar equation for the second phase can be obtained. The pressures for both phases are obtained from their EOS and the iterative procedure (procedure 4) given in Lallemand and Saurel (2000) is used to achieve the equilibrium pressure.

6.3.3 The MUSCL-Hancock scheme

The second order accuracy in both space and time for the solution of the hyperbolic part (6.24) and (6.25) is achieved by the high resolution MUSCL-Hancock approach which consists of the following three steps:

(1) Extrapolation:

It is reported in Jenny, Müller and H. (1997) that it is important to implement this step using primitive variables instead of using conserved ones to avoid wrong values of pressure. The primitive variables $\mathbf{w}_{i,j}^n$ in the cell $I_{i,j}$ are used to obtain the extrapolated primitive variables at the boundaries of the cell $I_{i,j}$ in both directions x and y as follows:

$$\mathbf{w}_{i\pm\frac{1}{2},j}^\mp = \mathbf{w}_{i,j}^n \pm \frac{1}{2} \bar{\sigma}_i, \quad \mathbf{w}_{i,j\pm\frac{1}{2}}^\mp = \mathbf{w}_{i,j}^n \pm \frac{1}{2} \bar{\sigma}_j, \quad (6.37)$$

where $\bar{\sigma}_i$ and $\bar{\sigma}_j$ are the slope limiters which are used to eliminate numerical oscillations; they take the following values, respectively:

$$\bar{\sigma}_i = \begin{cases} \max[0, \min(\beta\Delta_{i-\frac{1}{2},j}, \Delta_{i+\frac{1}{2},j}), \min(\Delta_{i-\frac{1}{2},j}, \beta\Delta_{i+\frac{1}{2},j})] & \text{if } \Delta_{i+\frac{1}{2},j} > 0, \\ \min[0, \max(\beta\Delta_{i-\frac{1}{2},j}, \Delta_{i+\frac{1}{2},j}), \max(\Delta_{i-\frac{1}{2},j}, \beta\Delta_{i+\frac{1}{2},j})] & \text{if } \Delta_{i+\frac{1}{2},j} < 0, \end{cases}$$

where:

$$\Delta_{i-\frac{1}{2},j} = \mathbf{w}_{i,j}^n - \mathbf{w}_{i-1,j}^n, \quad \Delta_{i+\frac{1}{2},j} = \mathbf{w}_{i+1,j}^n - \mathbf{w}_{i,j}^n, \quad (6.38)$$

and:

$$\bar{\sigma}_j = \begin{cases} \max[0, \min(\beta\Delta_{i,j-\frac{1}{2}}, \Delta_{i,j+\frac{1}{2}}), \min(\Delta_{i,j-\frac{1}{2}}, \beta\Delta_{i,j+\frac{1}{2}})] & \text{if } \Delta_{i,j+\frac{1}{2}} > 0, \\ \min[0, \max(\beta\Delta_{i,j-\frac{1}{2}}, \Delta_{i,j+\frac{1}{2}}), \max(\Delta_{i,j-\frac{1}{2}}, \beta\Delta_{i,j+\frac{1}{2}})] & \text{if } \Delta_{i,j+\frac{1}{2}} < 0, \end{cases}$$

where

$$\Delta_{i,j-\frac{1}{2}} = \mathbf{w}_{i,j}^n - \mathbf{w}_{i,j-1}^n, \quad \Delta_{i,j+\frac{1}{2}} = \mathbf{w}_{i,j+1}^n - \mathbf{w}_{i,j}^n. \quad (6.39)$$

The parameter β equals 1 for minmod limiter and β equals 2 for superbee limiter.

(2) Evolution:

The extrapolated primitive variables are updated at time $n + \frac{1}{2}$ using the following equations:

$$\begin{aligned} \bar{\mathbf{w}}_{i\pm\frac{1}{2},j}^{\mp} &= \mathbf{w}_{i\pm\frac{1}{2},j}^{\mp} + \frac{\Delta t}{2\Delta x} A(\mathbf{w}_{i,j})(\mathbf{w}_{i-\frac{1}{2},j}^+ - \mathbf{w}_{i+\frac{1}{2},j}^-) \\ &\quad + \frac{\Delta t}{2\Delta y} B(\mathbf{w}_{i,j})(\mathbf{w}_{i,j-\frac{1}{2}}^+ - \mathbf{w}_{i,j+\frac{1}{2}}^-), \end{aligned} \quad (6.40a)$$

$$\begin{aligned} \bar{\mathbf{w}}_{i,j\pm\frac{1}{2}}^{\mp} &= \mathbf{w}_{i,j\pm\frac{1}{2}}^{\mp} + \frac{\Delta t}{2\Delta x} A(\mathbf{w}_{i,j})(\mathbf{w}_{i-\frac{1}{2},j}^+ - \mathbf{w}_{i+\frac{1}{2},j}^-) \\ &\quad + \frac{\Delta t}{2\Delta y} B(\mathbf{w}_{i,j})(\mathbf{w}_{i,j-\frac{1}{2}}^+ - \mathbf{w}_{i,j+\frac{1}{2}}^-). \end{aligned} \quad (6.40b)$$

Substituting (6.37) in (6.40), the equations reduce to the following equations:

$$\bar{\mathbf{w}}_{i\pm\frac{1}{2},j}^{\mp} = \mathbf{w}_{i\pm\frac{1}{2},j}^{\mp} - \frac{\Delta t}{2\Delta x} A(\mathbf{w}_{i,j})\sigma_i - \frac{\Delta t}{2\Delta y} B(\mathbf{w}_{i,j})\sigma_j, \quad (6.41a)$$

$$\bar{\mathbf{w}}_{i,j\pm\frac{1}{2}}^{\mp} = \mathbf{w}_{i,j\pm\frac{1}{2}}^{\mp} - \frac{\Delta t}{2\Delta x} A(\mathbf{w}_{i,j})\sigma_i - \frac{\Delta t}{2\Delta y} B(\mathbf{w}_{i,j})\sigma_j, \quad (6.41b)$$

where the matrices $A(\mathbf{w})$ and $B(\mathbf{w})$ are given by (6.15) and (6.16), respectively.

(3) Solution of the Riemann problem:

Solution of the Riemann problem can be obtained by utilising exact Riemann solver in the Godunov's method. However, using exact Riemann solvers tends to be very expensive and hence approximate Riemann solvers are used. The primitive variables obtained from the evolution step are used to compute the conservative variables and the intercell fluxes in the Godunov-type scheme. The discretised equations (6.24) and (6.25) can be written respectively according to the second-order discretisation as follows:

$$\begin{aligned} \alpha_{i,j}^{n+1} = \alpha_{i,j}^n &- \frac{\Delta t}{\Delta x} \left[\alpha^*(\bar{\alpha}_{i+\frac{1}{2},j}^-, \bar{\alpha}_{i+\frac{1}{2},j}^+) - \alpha^*(\bar{\alpha}_{i-\frac{1}{2},j}^-, \bar{\alpha}_{i-\frac{1}{2},j}^+) \right] \\ &- \frac{\Delta t}{\Delta y} \left[\alpha^*(\bar{\alpha}_{i,j+\frac{1}{2}}^-, \bar{\alpha}_{i,j+\frac{1}{2}}^+) - \alpha^*(\bar{\alpha}_{i,j-\frac{1}{2}}^-, \bar{\alpha}_{i,j-\frac{1}{2}}^+) \right], \end{aligned} \quad (6.42)$$

and:

$$\begin{aligned} Q_i^{n+1} = Q_i^n &- \frac{\Delta t}{\Delta x} \left[F \left(Q^*(\bar{Q}_{i+\frac{1}{2},j}^-, \bar{Q}_{i+\frac{1}{2},j}^+) \right) - F \left(Q^*(\bar{Q}_{i-\frac{1}{2},j}^-, \bar{Q}_{i-\frac{1}{2},j}^+) \right) \right] \\ &- \frac{\Delta t}{\Delta y} \left[G \left(Q^*(\bar{Q}_{i,j+\frac{1}{2}}^-, \bar{Q}_{i,j+\frac{1}{2}}^+) \right) - G \left(Q^*(\bar{Q}_{i,j-\frac{1}{2}}^-, \bar{Q}_{i,j-\frac{1}{2}}^+) \right) \right] \\ &+ \Delta t H_1(Q_{i,j}^n) \Delta x + \Delta t H_2(Q_{i,j}^n) \Delta y. \end{aligned} \quad (6.43)$$

The value of α^* in the equation (6.42) and the intercell numerical fluxes F and G in the equation (6.43) are computed using the HLL approximate Riemann solver as given below.

The HLL approximate Riemann solver:

This approach was presented by Harten, Lax and van Leer (1983) to obtain the intercell numerical flux vector. Two waves left and right of speed S^- and S^+ are assumed to separate three constant states in the solution of the Riemann problem. The intercell fluxes for the right boundary of the cell (i, j) are given as follows:

$$F_{i+\frac{1}{2},j}^{hll} = \begin{cases} F_{i,j}^+ & \text{if } 0 \leq S_{i+\frac{1}{2},j}^-, \\ F^{hll} & \text{if } S_{i+\frac{1}{2},j}^- \leq 0 \leq S_{i+\frac{1}{2},j}^+, \\ F_{i+1,j}^- & \text{if } 0 \geq S_{i+\frac{1}{2},j}^+, \end{cases} \quad (6.44)$$

where:

$$F^{hll} = \frac{S_{i+\frac{1}{2},j}^+ F_{i,j}^+ - S_{i+\frac{1}{2},j}^- F_{i+1,j}^- + S_{i+\frac{1}{2},j}^- S_{i+\frac{1}{2},j}^+ (Q_{i+1,j}^- - Q_{i,j}^+)}{S_{i+\frac{1}{2},j}^+ - S_{i+\frac{1}{2},j}^-}$$

and for the upper boundary of the cell (i, j) are given by:

$$G_{i,j+\frac{1}{2}}^{hll} = \begin{cases} G_{i,j}^+ & \text{if } 0 \leq S_{i,j+\frac{1}{2}}^-, \\ G^{hll} & \text{if } S_{i,j+\frac{1}{2}}^- \leq 0 \leq S_{i,j+\frac{1}{2}}^+, \\ G_{i,j+1}^- & \text{if } 0 \geq S_{i,j+\frac{1}{2}}^+. \end{cases} \quad (6.45)$$

where:

$$G^{hll} = \frac{S_{i,j+\frac{1}{2}}^+ G_{i,j}^+ - S_{i,j+\frac{1}{2}}^- G_{i,j+1}^- + S_{i,j+\frac{1}{2}}^- S_{i,j+\frac{1}{2}}^+ (Q_{i,j+1}^- - Q_{i,j}^+)}{S_{i,j+\frac{1}{2}}^+ - S_{i,j+\frac{1}{2}}^-}.$$

Similarly, the intercell fluxes for the left and lower boundaries can be obtained by applying (6.44) and (6.45), respectively, using their corresponding left and right or up and down data. The maximum and minimum wave speeds of the left and right waves can be computed according to the formulae introduced in Davis (1988). For the x -direction the wave speeds are:

$$\begin{aligned} S_{i\pm\frac{1}{2},j}^+ &= \max(u_{i\pm\frac{1}{2},j}^- + c_{i\pm\frac{1}{2},j}^-, u_{i\pm\frac{1}{2},j}^+ + c_{i\pm\frac{1}{2},j}^+), \\ S_{i\pm\frac{1}{2},j}^- &= \min(u_{i\pm\frac{1}{2},j}^- - c_{i\pm\frac{1}{2},j}^-, u_{i\pm\frac{1}{2},j}^+ - c_{i\pm\frac{1}{2},j}^+), \end{aligned} \quad (6.46)$$

and, for the y -direction the wave speeds are:

$$\begin{aligned} S_{i,j\pm\frac{1}{2}}^+ &= \max(v_{i,j\pm\frac{1}{2}}^- + c_{i,j\pm\frac{1}{2}}^-, v_{i,j\pm\frac{1}{2}}^+ + c_{i,j\pm\frac{1}{2}}^+), \\ S_{i,j\pm\frac{1}{2}}^- &= \min(v_{i,j\pm\frac{1}{2}}^- - c_{i,j\pm\frac{1}{2}}^-, v_{i,j\pm\frac{1}{2}}^+ - c_{i,j\pm\frac{1}{2}}^+), \end{aligned} \quad (6.47)$$

where the sound speed obeys relation (6.19), $u_{i\pm\frac{1}{2},j}^\pm, u_{i,j\pm\frac{1}{2}}^\pm, v_{i\pm\frac{1}{2},j}^\pm, v_{i,j\pm\frac{1}{2}}^\pm, c_{i\pm\frac{1}{2},j}^\pm$ and $c_{i,j\pm\frac{1}{2}}^\pm$ represent the velocities and wave speeds, respectively, at the right, left, upper and lower boundaries.

6.4 Numerical method for the two-dimensional six-equation model

The numerical solution to the six-equation multiphase flow model is similar to that explained in section 6.3 for solving the seven-equation model. The solution is obtained using the Strang method (??). However, the solution to the six-equation model comprises only the hyperbolic and pressure relaxation operators.

6.4.1 The hyperbolic operator of the two-dimensional six-equation model

Consider the hyperbolic equations of the two-dimensional six-equation model written as follows:

$$\frac{\partial \alpha_1}{\partial t} + u \frac{\partial \alpha_1}{\partial x} + v \frac{\partial \alpha_1}{\partial y} = 0, \quad (6.48a)$$

$$\frac{\partial \alpha_1 \rho_1 e_1}{\partial t} + \frac{\partial \alpha_1 \rho_1 e_1 u}{\partial x} + \alpha_1 p_1 \frac{\partial u}{\partial x} + \frac{\partial \alpha_1 \rho_1 e_1 v}{\partial y} + \alpha_1 p_1 \frac{\partial v}{\partial y} = 0, \quad (6.48b)$$

$$\frac{\partial \alpha_2 \rho_2 e_2}{\partial t} + \frac{\partial \alpha_2 \rho_2 e_2 u}{\partial x} + \alpha_2 p_2 \frac{\partial u}{\partial x} + \frac{\partial \alpha_2 \rho_2 e_2 v}{\partial y} + \alpha_2 p_2 \frac{\partial v}{\partial y} = 0, \quad (6.48c)$$

$$\frac{\partial Q}{\partial t} + \frac{\partial F(Q)}{\partial x} + \frac{\partial G(Q)}{\partial y} = 0, \quad (6.48d)$$

where Q is the conservative vector, $F(Q)$ and $G(Q)$ are the numerical flux vectors in x and y directions, respectively. These vectors are defined as:

$$Q = \begin{bmatrix} \alpha_1 \rho_1 \\ \alpha_2 \rho_2 \\ \rho u \\ \rho v \\ \rho E \end{bmatrix}, \quad F(Q) = \begin{bmatrix} \alpha_1 \rho_1 u \\ \alpha_2 \rho_2 u \\ \rho u^2 + p \\ \rho u v \\ u(\rho E + p) \end{bmatrix}, \quad G(Q) = \begin{bmatrix} \alpha_1 \rho_1 v \\ \alpha_2 \rho_2 v \\ \rho u v \\ \rho v^2 + p \\ v(\rho E + p) \end{bmatrix}.$$

Note that, the last row in the above vectors corresponds to the additional equation (6.11h). To obtain the numerical solution of the hyperbolic part (6.48) with the second order accuracy in both space and time, the high resolution MUSCL approach described in section 6.3.3 is used. Based on the Godunov second-order upwind scheme, the non-conservative equation for the volume fraction (6.48a) is discretised as follows:

$$\begin{aligned} \alpha_{1,i,j}^{n+1} = & \alpha_{1,i,j}^n - \frac{\Delta t}{\Delta x} \left[(u\alpha_1)^* \left((u\alpha_1)_{i+\frac{1}{2},j}^-, (u\alpha_1)_{i+\frac{1}{2},j}^+ \right) \right. \\ & - (u\alpha_1)^* \left((u\alpha_1)_{i-\frac{1}{2},j}^-, (u\alpha_1)_{i-\frac{1}{2},j}^+ \right) \\ & \left. - \alpha_{1,i,j}^n \left(u^*(u_{i+\frac{1}{2},j}^-, u_{i+\frac{1}{2},j}^+) - u^*(u_{i-\frac{1}{2},j}^-, u_{i-\frac{1}{2},j}^+) \right) \right] \\ & - \frac{\Delta t}{\Delta y} \left[(v\alpha_1)^* \left((v\alpha_1)_{i,j+\frac{1}{2}}^-, (v\alpha_1)_{i,j+\frac{1}{2}}^+ \right) \right. \\ & - (v\alpha_1)^* \left((v\alpha_1)_{i,j-\frac{1}{2}}^-, (v\alpha_1)_{i,j-\frac{1}{2}}^+ \right) \\ & \left. - \alpha_{1,i,j}^n \left(v^*(v_{i,j+\frac{1}{2}}^-, v_{i,j+\frac{1}{2}}^+) - v^*(v_{i,j-\frac{1}{2}}^-, v_{i,j-\frac{1}{2}}^+) \right) \right]. \quad (6.49) \end{aligned}$$

In the presence of shocks, the non-conservative energy equations (6.48b) and (6.48c) cannot be approximated accurately. Therefore, it is necessary to assume that the product $(\alpha p)_{k,i,j}^n$ is constant during the time step. This is done by using the simplest approximation of the corresponding equations (Saurel, Petitpas and Berry, 2009) as follows:

$$\begin{aligned}
 (\alpha \rho e)_{k,i,j}^{n+1} = & (\alpha \rho e)_{k,i,j}^n - \frac{\Delta t}{\Delta x} \left[(\alpha \rho e u)_k^* \left((\alpha \rho e u)_{i+\frac{1}{2},j}^-, (\alpha \rho e u)_{i+\frac{1}{2},j}^+ \right) \right. \\
 & - (\alpha \rho e u)_k^* \left((\alpha \rho e u)_{i-\frac{1}{2},j}^-, (\alpha \rho e u)_{i-\frac{1}{2},j}^+ \right) \\
 & \left. + (\alpha p)_{k,i,j}^n \left(u_k^*(u_{i+\frac{1}{2},j}^-, u_{i+\frac{1}{2},j}^+) - u_k^*(u_{i-\frac{1}{2},j}^-, u_{i-\frac{1}{2},j}^+) \right) \right] \\
 & - \frac{\Delta t}{\Delta y} \left[(\alpha \rho e v)_k^* \left((\alpha \rho e v)_{i,j+\frac{1}{2}}^-, (\alpha \rho e v)_{i,j+\frac{1}{2}}^+ \right) \right. \\
 & - (\alpha \rho e v)_k^* \left((\alpha \rho e v)_{i,j-\frac{1}{2}}^-, (\alpha \rho e v)_{i,j-\frac{1}{2}}^+ \right) \\
 & \left. + (\alpha p)_{k,i,j}^n \left(v_k^*(v_{i,j+\frac{1}{2}}^-, v_{i,j+\frac{1}{2}}^+) - v_k^*(v_{i,j-\frac{1}{2}}^-, v_{i,j-\frac{1}{2}}^+) \right) \right], k = 1, 2.
 \end{aligned} \tag{6.50}$$

The conservative equation (6.48d) can be written as the second-order accurate scheme as follows:

$$\begin{aligned}
 Q_i^{n+1} = Q_i^n - & \frac{\Delta t}{\Delta x} \left[F \left(Q^*(\overline{Q}_{i+\frac{1}{2},j}^-, \overline{Q}_{i+\frac{1}{2},j}^+) \right) - F \left(Q^*(\overline{Q}_{i-\frac{1}{2},j}^-, \overline{Q}_{i-\frac{1}{2},j}^+) \right) \right] \\
 & - \frac{\Delta t}{\Delta y} \left[G \left(Q^*(\overline{Q}_{i,j+\frac{1}{2}}^-, \overline{Q}_{i,j+\frac{1}{2}}^+) \right) - G \left(Q^*(\overline{Q}_{i,j-\frac{1}{2}}^-, \overline{Q}_{i,j-\frac{1}{2}}^+) \right) \right]
 \end{aligned} \tag{6.51}$$

6.4.2 The pressure relaxation operator

The solution procedure for the hyperbolic operator is presented in the previous sections without including the relaxation source term. The solution of the relaxation operator is crucial since it accounts for the boundary conditions at the interface. This is achieved by solving the ODE given by:

$$\frac{dQ}{dt} = D_P, \tag{6.52}$$

where Q is defined as:

$$Q = [\alpha_1, \alpha_1 \rho_1, \alpha_2 \rho_2, \alpha u, \alpha v, \alpha_1 \rho_1 e_1, \alpha_2 \rho_2 e_2, E]^T, \tag{6.53}$$

and D_P is the pressure relaxation term. It is given by:

$$D_P = \begin{bmatrix} \mu(p_1 - p_2) \\ 0 \\ 0 \\ 0 \\ 0 \\ p_{int}\mu(p_1 - p_2) \\ -p_{int}\mu(p_1 - p_2) \\ 0 \end{bmatrix}. \quad (6.54)$$

Lallemand and Saurel (2000) proposed the iterative procedure to solve the relaxation part for the seven-equation model of Saurel and Abgrall (1999a). This procedure was implemented to solve equations (6.52) together with the criterion of Saurel, Petitpas and Berry (2009) to correct the relaxed pressure in order to satisfy the mixture EOS at every time step. The value of ρe is calculated from the conservative equation of the total mixture energy (6.11h). Then the mixture pressure for fluids is calculated from the mixture EOS (6.55) with the help of the volume fraction. This mixture EOS is written in terms of the Mie-Grüneisen EOS functions given for each EOS in Table 4.2 as follows:

$$p(\rho e, \alpha_1, \alpha_2) = \frac{\rho e - \sum_k^2 \left(\frac{\alpha_k(\rho_k \Gamma_k(\rho_k) e_k(\rho_k) - p_k(\rho_k))}{\Gamma_k(\rho_k)} \right)}{\sum_k^2 \left(\frac{\alpha_k}{\Gamma_k(\rho_k)} \right)}, \quad (6.55)$$

Then the internal energies for both phases are updated using the corresponding EOSs. Such approach enables the interface conditions to be fulfilled at any time.

6.5 Numerical results - Verification test problems

In this section several test problems are conducted to verify the accuracy of the developed code to simulate two-dimensional test problems. These test problems include simulations of a single phase test problem and various two-phase test problems. Verifications of the six and seven-equation models have been demonstrated in two-dimensions using the ideal gas, van der Waals, stiffened gas and Tait EOSs. The usual assumption of presence of a negligible volume fraction $\epsilon = 10^{-8}$ of the other fluid in the fluid considered as a pure fluid is used in all test problems. The numerical results of all presented test problems are compared with either the exact solution or others published results. It can be seen that good results have been achieved for all examined test problems using various EOSs.

6.5.1 Air bubble explosion test

This is a single phase test problem where an air bubble with a higher density and pressure explodes in air. This test is usually used to verify the correctness of numerical solutions of implemented numerical methods in two dimensions (Toro, 2009). The test contains of a circular bubble with a radius of 0.4 m which is located at the centre of a square domain of 2 m \times 2 m. The fluid inside and outside the bubble is air and its initial states are given in Table 6.1. The ideal gas EOS (4.14) is used to govern the air inside and outside the bubble $\gamma = 1.4$. Periodic boundary conditions are imposed to all sides of the computational domain.

Table 6.1: Initial data for air bubble explosion test 6.5.1

Zone	[kg/m ³]	[m/s]	[m/s]	[Pa]	
Bubble	$\rho_1 = 1$	$u_1 = 0$	$v_1 = 0$	$p_1 = 1$	$\alpha_1 = 1 - \epsilon$
	$\rho_2 = 0.125$	$u_2 = 0$	$v_2 = 0$	$p_2 = 1$	$\alpha_2 = \epsilon$
Zone	[kg/m ³]	[m/s]	[m/s]	[Pa]	
Surrounding	$\rho_1 = 1$	$u_1 = 0$	$v_1 = 0$	$p_1 = 0.1$	$\alpha_1 = \epsilon$
	$\rho_2 = 0.125$	$u_2 = 0$	$v_2 = 0$	$p_2 = 0.1$	$\alpha_2 = 1 - \epsilon$

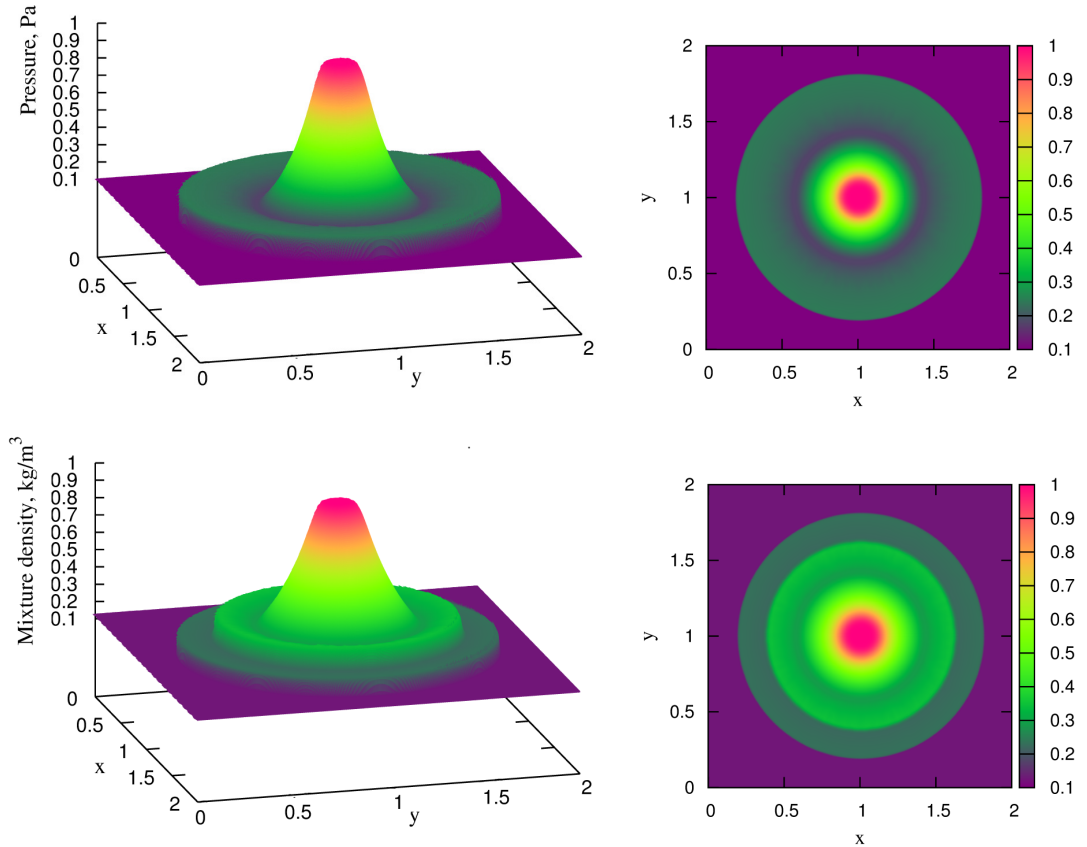


Figure 6.1: Air bubble explosion test 6.5.1: Surface and contour plots for pressure (top) and mixture density (bottom) at $t = 0.25$ s using the seven-equation model.

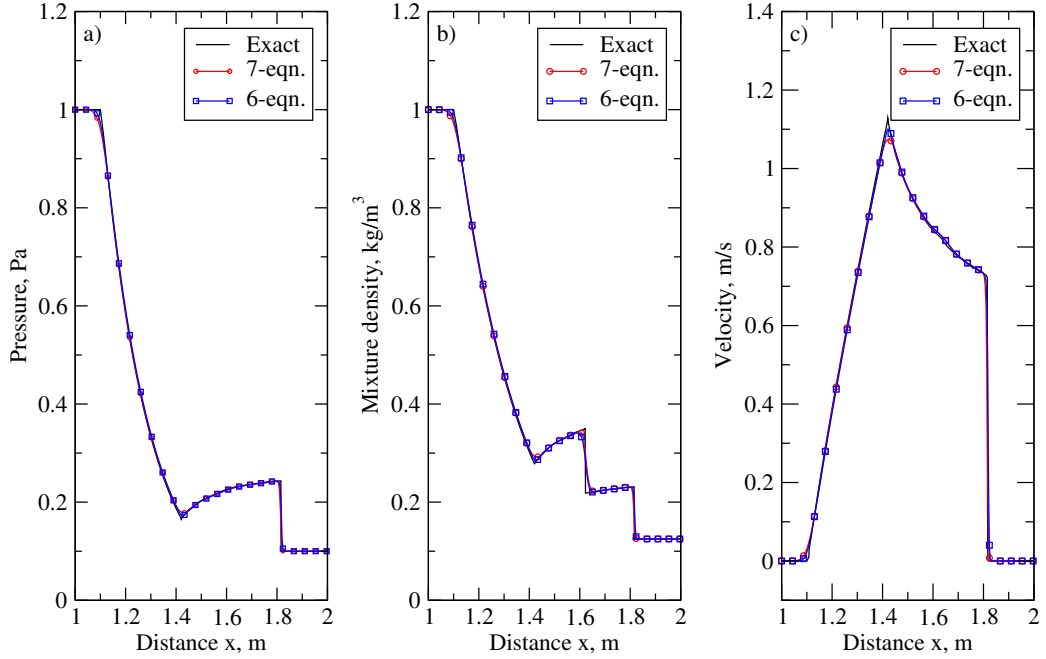


Figure 6.2: Air bubble explosion test 6.5.1: Cross-section plot at $y = 1$ m for the pressure (a), mixture density (b) and velocity (c) at $t = 0.25$ s. Comparison between six and seven-equation models with exact from Toro (2009).

The solution of this test problem comprises outward going shock and contact waves and an inward going rarefaction wave. The results for the air bubble explosion test are displayed in Figure 6.1. The figure shows surface and contour plots for pressure (top) and mixture density (bottom) at $t = 0.25$ s using the seven-equation model with 600×600 cells.

Since the results are symmetric about the vertical axis at the centre of the domain $(1 \text{ m}, 1 \text{ m})$, the results of the right half are shown in Figure 6.2. The figure shows cross-section plots for the results of pressure (a), mixture density (b) and velocity (c) at $y = 1$ m and $t = 0.25$ s. The results are obtained from the six and seven-equation models using a mesh of 600×600 cells with the $\text{CFL} = 0.6$. It can be observed that the method captures the shock more accurate than it does to capture the contact discontinuity. These results are compared with the exact solution taken from Toro (2009). It can be seen that these results are in good agreement with the exact solution.

The number of time steps (n) and CPU time needed by the six and seven-equation models to obtain the solution using different mesh resolutions are given in Table 6.2. The average percentage of the number of time steps and CPU time required by the six-equation model are 35.13 % and 46.41 % less than that required by the seven-equation model to obtain the results for the air bubble explosion test problem. The scaling order of the two-dimensional HLL algorithms for the six and seven-equation models are 1.1054 and 1.1331, respectively, as shown Figure 6.3.

Figure 6.4 shows the error norm (L_2) spatial convergence comparison between the six and seven-equation models for the air bubble explosion test. The results are

Table 6.2: The number of time steps and CPU time for air bubble explosion test

Mesh cells	Six-equation model		Seven-equation model	
	Time step	CPU (s)	Time step	CPU (s)
100×100	91	5.44	143	9.86
200×200	179	45.40	285	84.92
400×400	355	400.50	586	889.57
800×800	708	4293.74	1208	9581.70
1000×1000	884	9740.86	1520	21143.55

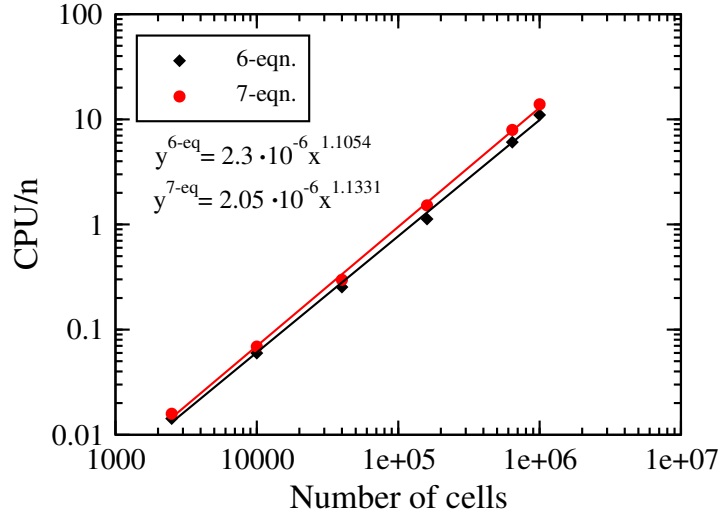


Figure 6.3: Air bubble explosion test 6.5.1: Scaling order for the HLL algorithm.

shown for pressure (a) and velocity (b) using different resolutions. It can be seen that as the number of cells increases the error norm decreases. The order of accuracy of the two-dimensional HLL algorithms for six and seven-equation models using the air bubble explosion test are given in Tables 6.3-6.4. It can also be observed that the order of accuracy is less than 2 due to the presence of the discontinuities in the solution as mentioned in subsection 4.6.1.

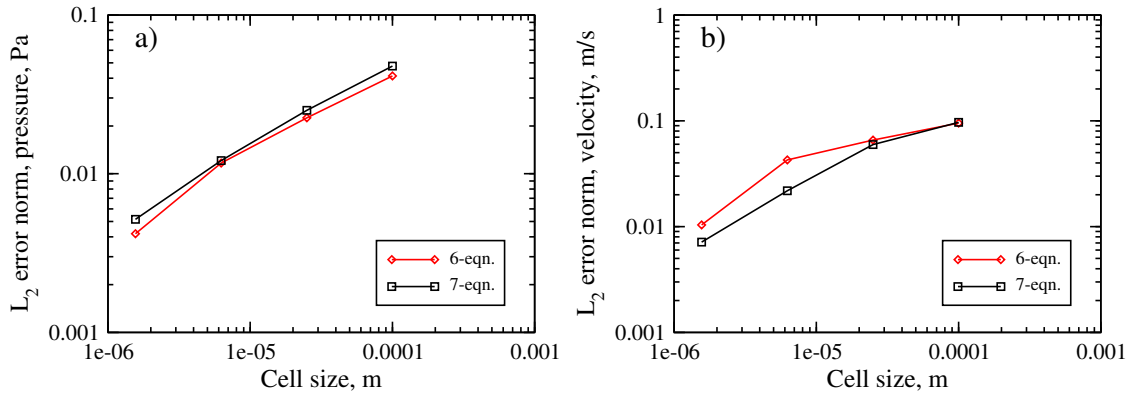


Figure 6.4: Air bubble explosion test example: L_2 error norm spatial convergence for: (a) pressure and (b) velocity.

Table 6.3: Order of accuracy of the HLL for 6-eqn. model for air bubble explosion test.

Mesh cells	L_2		Order	
	u	p	u	p
100×100	0.095270998	0.041331477		
200×200	0.065838611	0.022502692	0.26655	0.43857
400×400	0.042660716	0.011668186	0.31301	0.47376
800×800	0.010367620	0.004186070	1.02041	0.73946

Table 6.4: Order of accuracy of the HLL for 7-eqn. model for air bubble explosion test.

Mesh cells	L_2		Order	
	u	p	u	p
100×100	0.09668216	0.04766043		
200×200	0.05968657	0.0251008	0.34792	0.46253
400×400	0.02180695	0.01209312	0.72630	0.52677
800×800	0.00714383	0.00515438	0.80501	0.61516

6.5.2 Interface translation test

To verify the correctness of the numerical method developed for the two-dimensional two-phase flow problems. The code is subjected to the so called interface translation test which was demonstrated by Shyue (1998) and Zheng et al. (2011). They used different physical models and different numerical methods. The test comprises of two different gases, the first is filled in a circle and the second is surrounding this circle. The circle which has a radius of 0.16 m is located at (0.25 m, 0.25 m) in a square domain of 1 m \times 1 m as illustrated in Figure 6.5. Both gases inside and outside the circle are governed by the IG EOS. The constant parameters for the gases inside and outside the bubble are $\gamma = 1.4$ and $\gamma = 1.6$, respectively. The boundary conditions are set to be periodic for all sides of the computational domain. The initial conditions are given in Table 6.5.

Table 6.5: Initial data for interface translation test 6.5.2

Zone	[kg/m ³]	[m/s]	[m/s]	[Pa]
Bubble	$\rho_1 = 1$	$u_1 = 1$	$v_1 = 1$	$p_1 = 1$
	$\rho_2 = 0.1$	$u_2 = 1$	$v_2 = 1$	$p_2 = 1$
Surrounding	$\rho_1 = 1$	$u_1 = 1$	$v_1 = 1$	$p_1 = 1$
	$\rho_2 = 0.1$	$u_2 = 1$	$v_2 = 1$	$p_2 = 1$

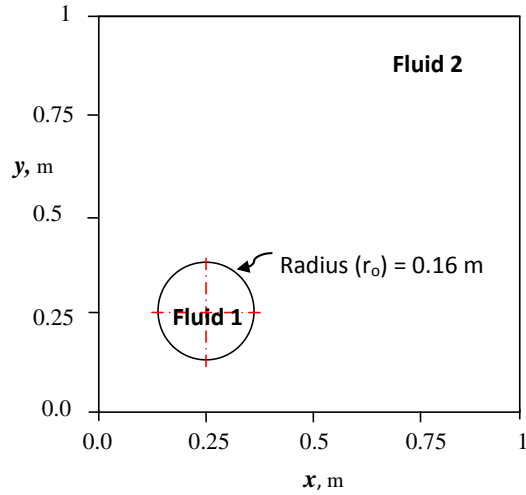


Figure 6.5: Interface translation test at $t = 0$ s.

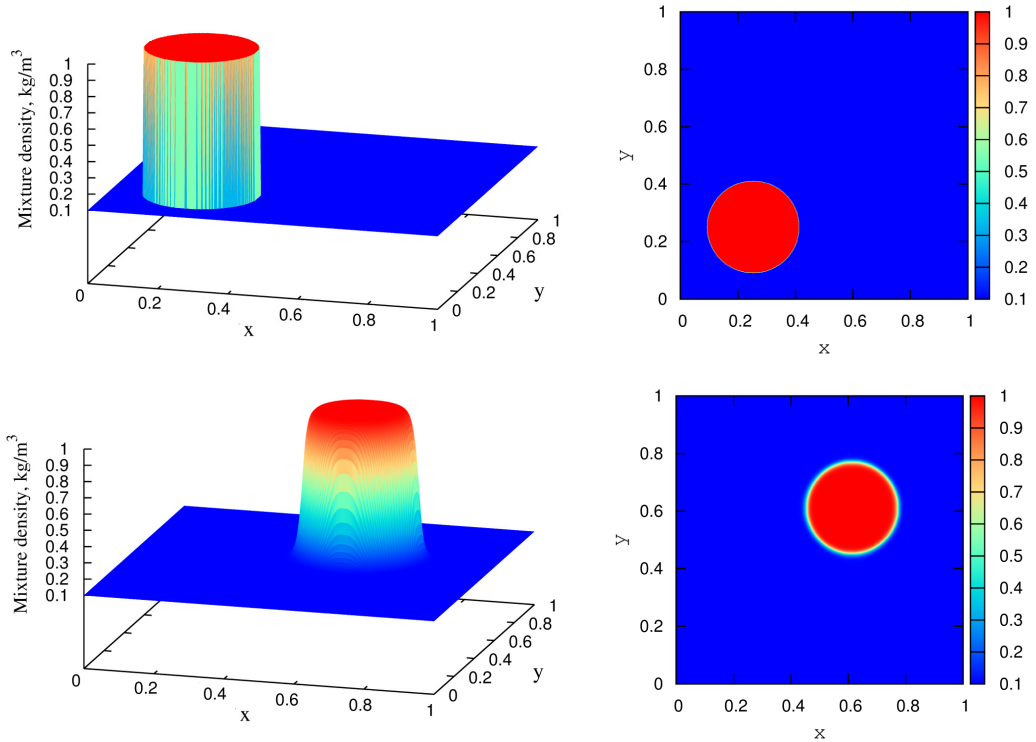


Figure 6.6: Interface translation test 6.5.2: Surface and contour plots for the mixture density distributions at $t = 0$ s (top) and $t = 0.36$ s (bottom) using the six-equation model.

These initial conditions will force the bubble to evolve with a constant velocity along the diagonal direction. The results are obtained using the six and seven-equation models with the CFL number being equal to 0.3. Figure 6.6 shows the surface and contour plots for the mixture density distributions at $t = 0$ s (top) and $t = 0.36$ s (bottom) with a mesh resolution of 300×300 cells. It can be seen that during the evolution of the two phases the method can preserve the sharpness of the contact discontinuity separating the two components with a relatively small

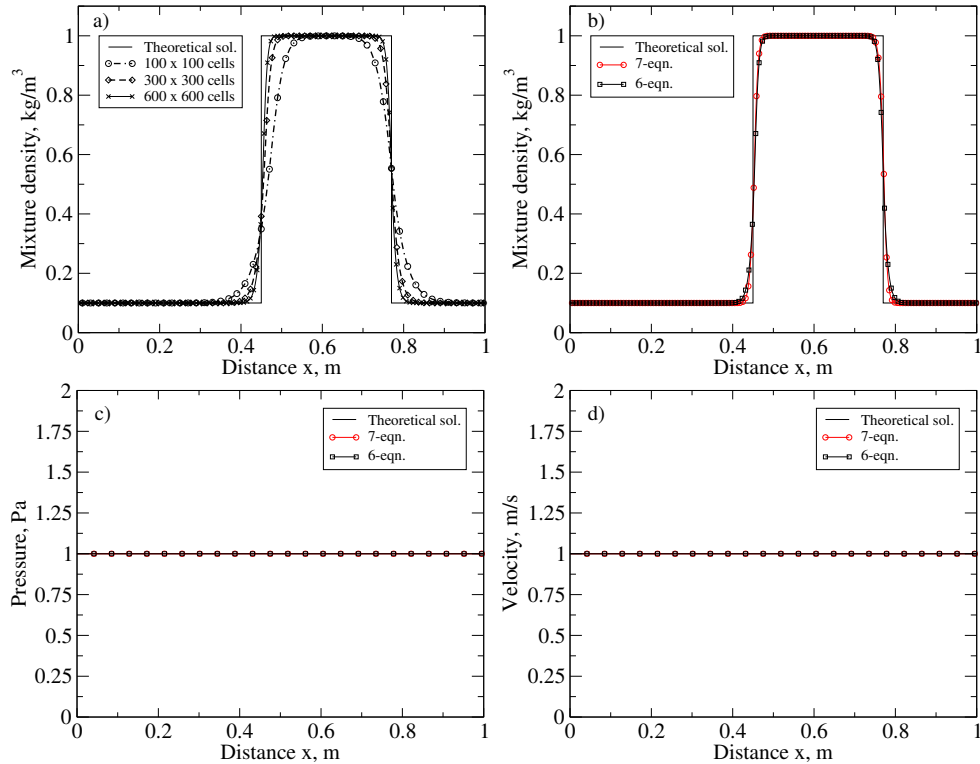


Figure 6.7: Interface translation test 6.5.2: Cross-section plot of the mixture density results at $y = 0.61$ m and $t = 0.36$ s: a) Different mesh resolutions using the six-equation model. b), c) and d) Comparisons between six and seven-equation models for mixture density, pressure and velocity.

numerical diffusion. The position of the bubble is verified at the given time as compared to the theoretical solution. Figure 6.7 shows cross-sectional plots of the mixture density (a, b), pressure (c) and velocity (d). Figure 6.7(a) shows cross-sectional plots of the mixture density with different resolutions obtained from the six-equation model to show the convergence of the numerical solution to the analytical solution. A comparison between the six and seven-equation models is shown in Figure 6.7(a) in terms of the mixture density (b), pressure (c) and velocity (d) using 600×600 cells. It can be seen that both models gave almost the same results. However, the six-equation model is cheaper than the seven-equation model by about 10% in this test problem.

A cross-section plot for the right half of the air bubble is drawn in Figure 6.8 at different instants. The figure shows the effect of the time evolution on the interface sharpness where a mesh of 600×600 cells is used. It can be seen that there is a very slight increase in the interface diffusion.

6.5.3 Gas bubble underwater explosion test

The gas bubble underwater explosion test is also a verification test examined by Shyue (1999). In this test an explosion of a circular gas bubble at a high pressure takes place under water in a square domain of $1 \text{ m} \times 1 \text{ m}$. The gas bubble which

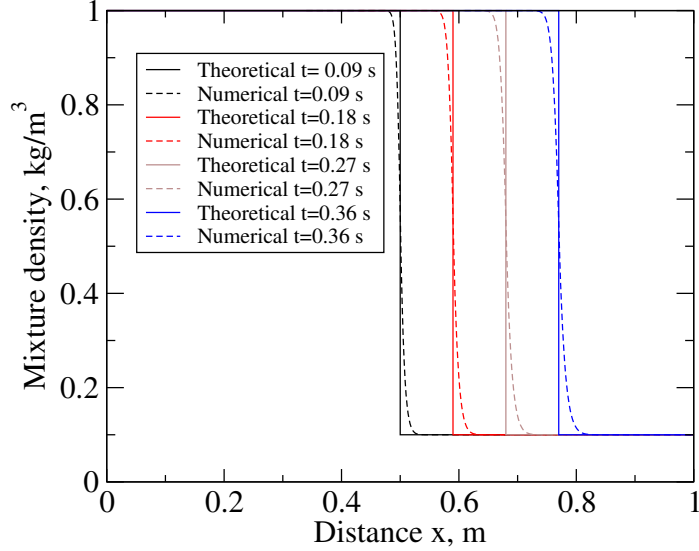


Figure 6.8: Interface translation test 6.5.2: Cross-section plot (right intrface of the bubble only) of the mixture density results at times 0.09, 0.18, 0.27 and 0.36 s.

has a radius of $r_o = 0.2$ m is located at the centre of the computational domain. While the top and bottom boundaries of the domain are set to be periodic boundary conditions, the left and right boundaries of the domain are set to be extrapolation boundary conditions. The water is governed by the SG EOS (4.21) and its constant parameters are $\gamma = 4.4, \pi = 6 \times 10^8$, whereas the gas is governed by the van der Waals EOS (4.30) and its constant parameters are $\gamma = 1.4, a = 1, b = 10^{-4}$. The initial conditions are as given in Table 6.6.

Table 6.6: Initial data for gas bubble underwater explosion test 6.5.2

Zone	[kg/m ³]	[m/s]	[m/s]	[Pa]	
Bubble	$\rho_1 = 1250$	$u_1 = 0$	$v_1 = 0$	$p_1 = 10^9$	$\alpha_1 = 1 - \epsilon$
	$\rho_2 = 1000$	$u_2 = 0$	$v_2 = 0$	$p_2 = 10^9$	$\alpha_2 = \epsilon$
Zone	[kg/m ³]	[m/s]	[m/s]	[Pa]	
Surrounding	$\rho_1 = 1250$	$u_1 = 0$	$v_1 = 0$	$p_1 = 10^5$	$\alpha_1 = \epsilon$
	$\rho_2 = 1000$	$u_2 = 0$	$v_2 = 0$	$p_2 = 10^5$	$\alpha_2 = 1 - \epsilon$

When the explosion of the gas bubble starts, an outward strong shock wave is transmitted to the surrounding water, an inward rarefaction wave propagates in the gas and a contact discontinuity continues to separate the gas and water. Figure 6.9 shows surface and contour plots for the pressure (top) and mixture density (bottom) at time $t = 120 \mu\text{s}$ using the six-equation model with a CFL number equals 0.3 with 600×600 cells. Figure 6.10 shows cross-section plots for the pressure (a), mixture density (b) and velocity (c) at the same instant $t = 120 \mu\text{s}$ using various resolutions to show the convergence of the numerical solution to the exact solution.

The number of time steps (n) and CPU time needed by the six-equation mode to obtain the solution using different mesh resolutions are given in Table 6.7. The

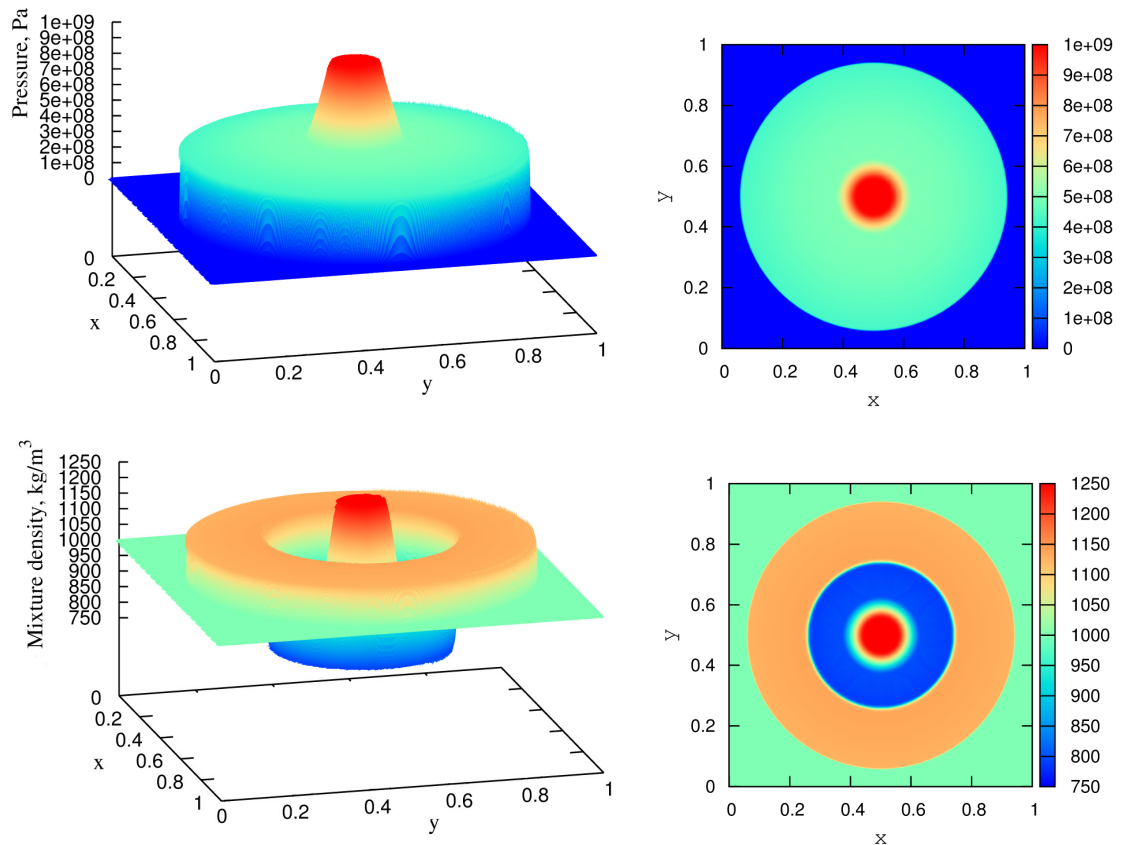


Figure 6.9: Gas bubble underwater explosion test 6.5.3: Surface and contour plots for pressure (top) and mixture density (bottom) at $t = 120 \mu\text{s}$.

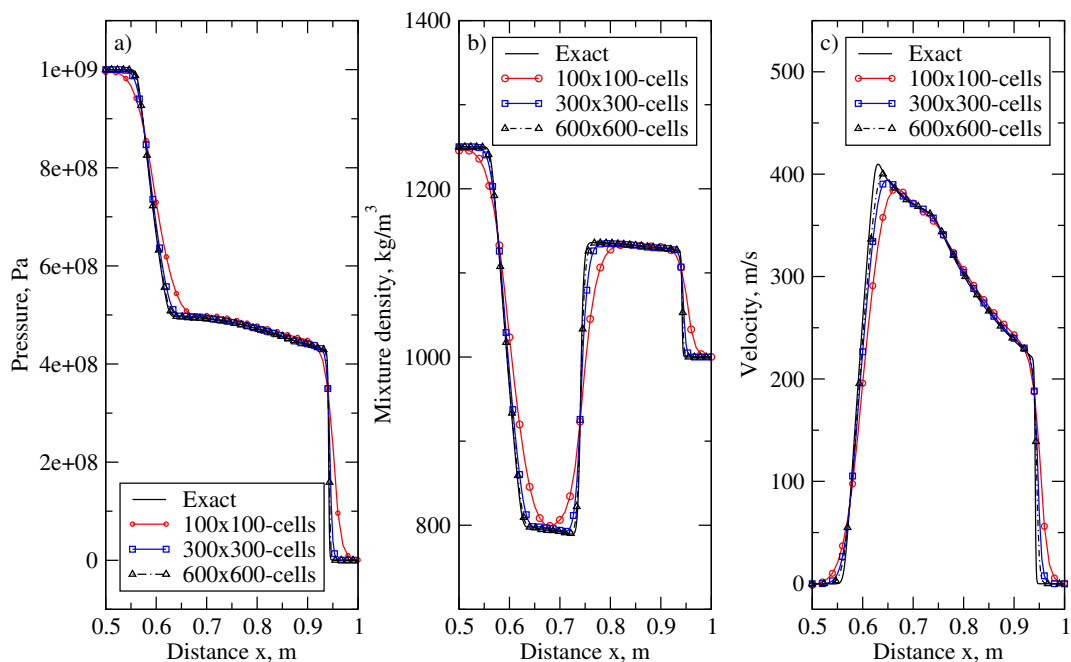


Figure 6.10: Gas bubble underwater explosion test 6.5.3: Cross-section plot at $y = 0.5 \text{ m}$ for the pressure (a), mixture density (b) and velocity (c) at $t = 120 \mu\text{s}$. Current results from the six-equation model with different resolutions, exact from Shyue (2001).

scaling order of the two-dimensional HLL algorithms for the six model is 1.1113 as shown Figure 6.11.

Table 6.7: The number of time steps and CPU time for gas bubble underwater explosion test.

Mesh cells	HLL	
	Time step	CPU (s)
100×100	99	6.50
200×200	195	54.81
400×400	390	465.61
800×800	778	4748.13
1000×1000	972	10986.95

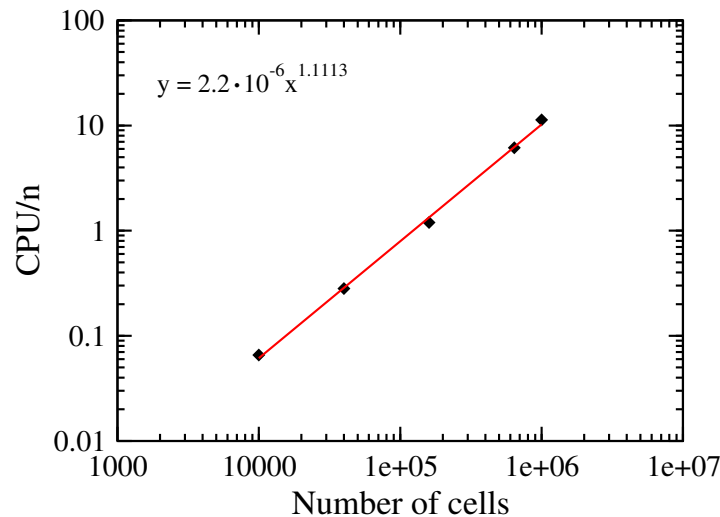


Figure 6.11: Gas bubble underwater explosion test 6.5.3: Scaling order for the HLL algorithm.

Table 6.8: Order of accuracy of the HLL for gas bubble underwater explosion test.

Mesh cells	L_2		Order	
	p	ρ	p	ρ
100×100	45261155.64	42.015082		
200×200	20873600.79	22.821439	0.55829	0.44026
400×400	7849182.45	10.007023	0.70553	0.59469
800×800	1228954.90	1.7750521	1.33756	1.24754

Figure 6.12 shows the error norm (L_2) spatial convergence for the six-equation model for the air bubble underwater explosion test. The results are shown for pressure (a) and mixture density (b) using different resolutions. The order of accuracy of the two-dimensional HLL algorithms for six-equation model using the air bubble

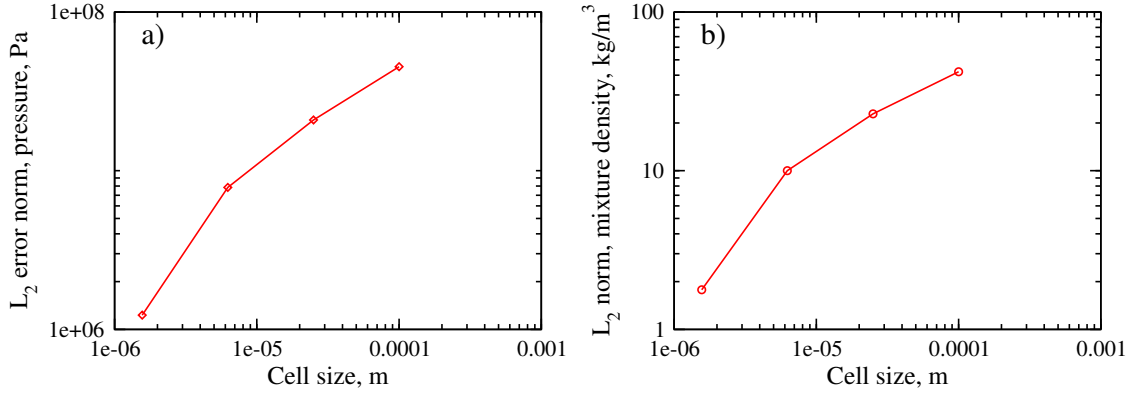


Figure 6.12: Gas bubble underwater explosion test 6.5.3: L_2 error norm spatial convergence for: (a) pressure and (b) mixture density.

underwater explosion test are given in Table 6.8. It can be seen that the order of accuracy is less than 2 because of the presence of the discontinuity in the solution.

6.5.4 Shock-bubble interaction

The shock-bubble interaction problem was examined to record the process of a planar shock wave interaction with an air bubble in water. The investigation of the shock-bubble interaction with a high density ratio (1000) and pressure ratio (10,000) between the water and air has been carried out by many researchers (see for example, Allaire, Clerc and Kokh, 2002; Zheng, Shu and Chew, 2008; Zheng et al., 2012). The geometry of this problem is schematically presented in Figure 6.13. The rectangular domain of size 1.2 m by 1.0 m contains the air bubble with a radius of 0.2 m which is initially located at the position (0.7 m, 0.5 m) in water. A shock wave initially at 0.95 m moves to the left with a Mach number of 1.422 and hits the bubble. While the reflective boundary conditions are imposed at the upper and lower boundaries, the extrapolation boundary conditions are imposed at the left and right boundaries. The initial conditions are given in Table 6.9 and the constant SG EOS parameters for air are $\gamma = 1.4$ and $\pi = 0$ Pa and for water are $\gamma = 4.4$ and $\pi = 6 \times 10^8$ Pa.

The simulation is performed on a mesh of 1440×1200 cells and a CFL equals 0.3. The results are obtained from the six-equation model and displayed using an idealised Schlieren function described in Quirk and Karni (1996) which may be written for mixture density ρ as follows:

$$\phi = \exp\left(-k(\psi) \frac{|\nabla\rho|}{|\nabla\rho|_{max}}\right) \quad (6.56)$$

where

$$k(\psi) = \begin{cases} 20 & \text{if } \psi \leq 0.25, \\ 100 & \text{if } \psi > 0.25, \end{cases} \quad (6.57)$$

Table 6.9: Initial data for shock-bubble interaction 6.5.4

Zone	[kg/m ³]	[m/s]	[m/s]	[Pa]	
Bubble	$\rho_1 = 1.2$	$u_1 = 0$	$v_1 = 0$	$p_1 = 10^5$	$\alpha_1 = 1 - \epsilon$
	$\rho_2 = 1000$	$u_2 = 0$	$v_2 = 0$	$p_2 = 10^5$	$\alpha_2 = \epsilon$
Zone	[kg/m ³]	[m/s]	[m/s]	[Pa]	
Pre-shock	$\rho_1 = 1.2$	$u_1 = 0$	$v_1 = 0$	$p_1 = 10^5$	$\alpha_1 = \epsilon$
	$\rho_2 = 1000$	$u_2 = 0$	$v_2 = 0$	$p_2 = 10^5$	$\alpha_2 = 1 - \epsilon$
Zone	[kg/m ³]	[m/s]	[m/s]	[Pa]	
Post-shock	$\rho_1 = 1230$	$u_1 = -432.69$	$v_1 = 0$	$p_1 = 10^9$	$\alpha_1 = 1 - \epsilon$
	$\rho_2 = 1000$	$u_2 = -432.69$	$v_2 = 0$	$p_2 = 10^9$	$\alpha_2 = \epsilon$

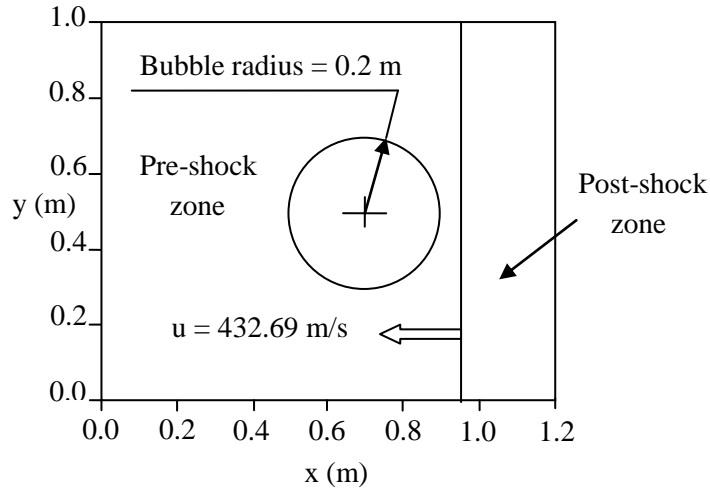


Figure 6.13: Setup for the shock bubble interaction test 6.5.4.

ψ is the mass fraction of air and

$$|\nabla\rho| = \left[\left(\frac{\partial\rho}{\partial x} \right)^2 + \left(\frac{\partial\rho}{\partial y} \right)^2 \right]^{1/2}$$

Figure 6.14 shows the current results of idealised schlieren mixture density (left column) compared to the results of Zheng, Shu and Chew (2008) which are obtained from the reduced model with the implementation of an adaptive mesh refinement technique (right column).

This figure illustrates the interaction of the planar shock wave with the air bubble as they evolve at different times $t = (1, 2, 3, 4) \times 10^{-4}$ s from top to bottom using the idealised schlieren mixture density. The shock wave propagates from right to left in water and hits the air bubble. The air bubble starts to deform due to the interaction with the shock wave as shown in Figure 6.14 at $t = 1 \times 10^{-4}$ s where a circular rarefaction wave is reflected to the right in water. It was observed that the shock

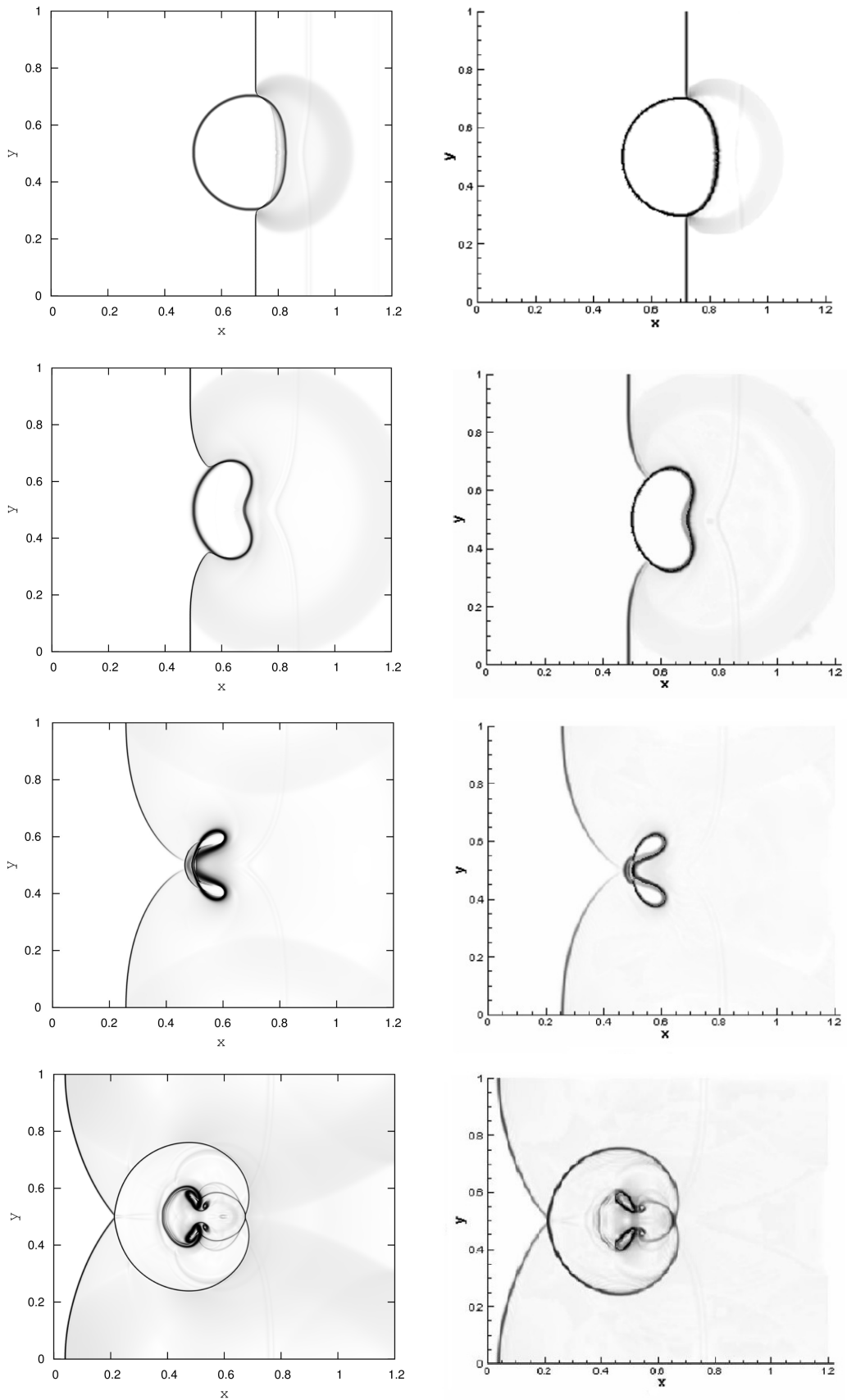


Figure 6.14: Shock-bubble interaction 6.5.4 results at $t = (1, 2, 3, 4) \times 10^{-4}$ s from top to bottom. Idealised schlieren mixture density current result using the six-equation model (left) and results from Zheng, Shu and Chew (2008) (right).

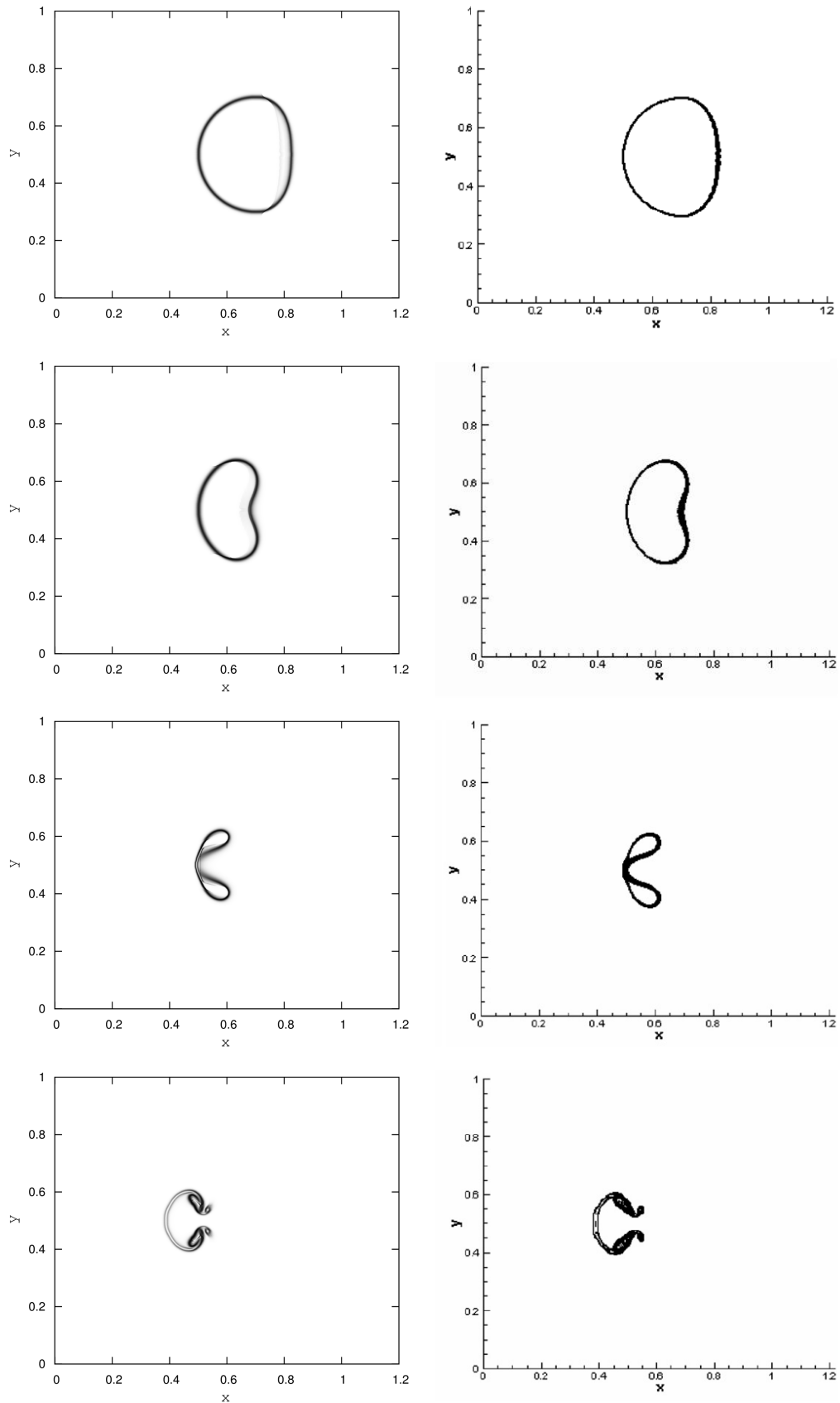


Figure 6.15: Shock-bubble interaction 6.5.4 results at $t = (1, 2, 3, 4) \times 10^{-4}$ s from top to bottom. Idealised schlieren volume fraction current result using the six-equation model (left) and results from Zheng, Shu and Chew (2008) (right).

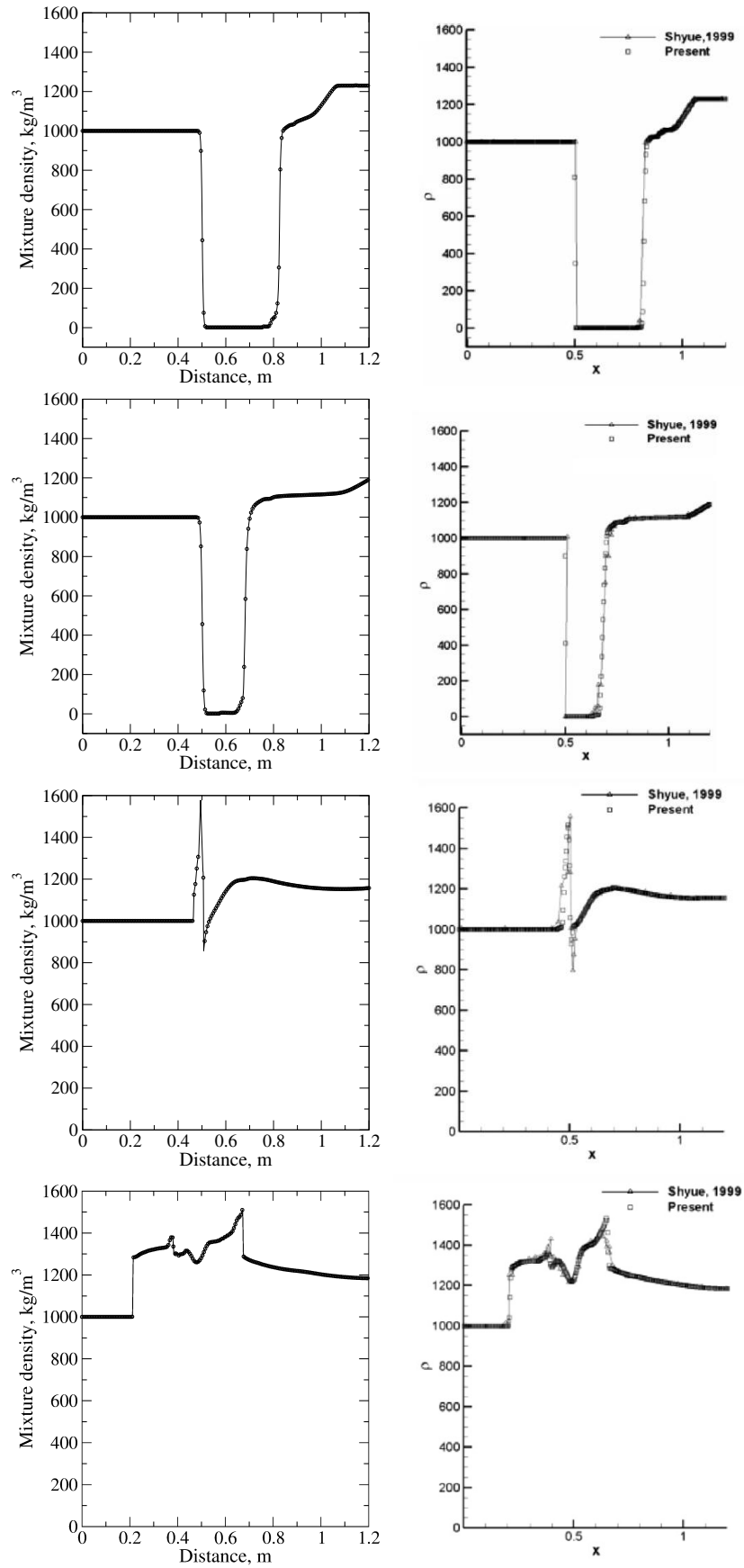


Figure 6.16: Shock-bubble interaction 6.5.4. Mixture density distribution across line of symmetry at $t = (1, 2, 3, 4) \times 10^{-4}$ s from top to bottom. Current results using the six-equation model (left) and results from Zheng, Shu and Chew (2008) (right).

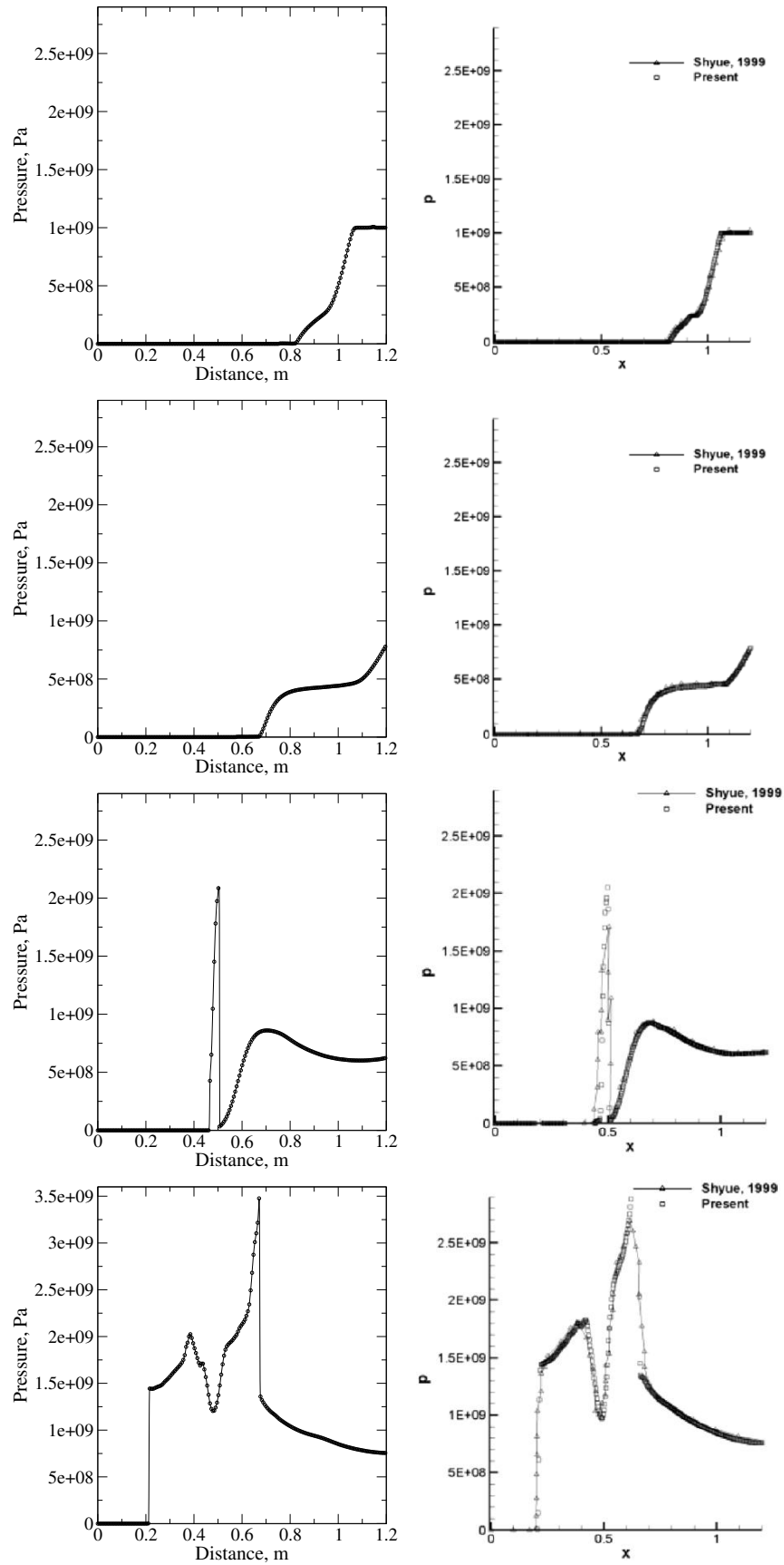


Figure 6.17: Shock-bubble interaction 6.5.4. Pressure distribution across line of symmetry at $t = (1, 2, 3, 4) \times 10^{-4}$ s from top to bottom. Current results using the six-equation model (left) and results from Zheng, Shu and Chew (2008) (right).

wave propagates in water faster than in the air bubble. Moreover, the unchanged interface of the bubble downstream is due to the fact that the air compressibility is larger than that of water. The deformation of the bubble takes a kidney shape at $t = 2 \times 10^{-4}$ s where the rarefaction wave reaches the upper and lower boundaries and starts to reflect away from these boundaries this is demonstrated in Figure 6.14 at $t = 3 \times 10^{-4}$ s. Then the bubble takes a crescent shape (not shown) and then a water jet is generated at the axis of symmetry. This jet continues to deform the bubble until it splits into two separate bubbles. The various stages of the deformation are shown in Figure 6.14 at times $t = (1, 2, 3) \times 10^{-4}$ s. Thereafter, the jet collides with the still water behind the bubble and generates a shock wave which propagates radially as can be seen in Figure 6.14 at times $t = (3, 4) \times 10^{-4}$ s. Figure 6.15 shows the current results of idealised schlieren volume fraction (left column) compared to the results of Zheng, Shu and Chew (2008) (right column) at the same instants. Mixture density distribution plots across the line of symmetry at times $t = (1, 2, 3, 4) \times 10^{-4}$ s are displayed in Figure 6.16 from top to bottom. The current results (left column) are compared to the results of Zheng, Shu and Chew (2008) (right column). Pressure distribution plots across the line of symmetry at times $t = (1, 2, 3, 4) \times 10^{-4}$ s are displayed in Figure 6.17 from top to bottom. The current results (left column) are compared to the results of Zheng, Shu and Chew (2008) (right column).

The results are in good agreement with those obtained by Allaire, Clerc and Kokh (2002) and Zheng, Shu and Chew (2008). This demonstrates the capability of the current code to capture the material interfaces as well as strong shock waves due to large pressure and density jump without the sophisticated refinement technique used in Zheng, Shu and Chew (2008).

6.5.5 Richtmyer-Meshkov instability

This test has been demonstrated by many researchers (see for example, Shyue, 1998; Nourgaliev, Dinh and Theofanous, 2006; Terashima and Tryggvason, 2009) to verify numerical methods. The test was chosen to verify the computed solutions for practical problems in two space dimensions converge to the correct weak solution. The Richtmyer-Meshkov instability considers a study of evolution of an unstable interface separating two fluids with different densities when a shock wave passes over this interface. In such cases the amplitude of the initially perturbed interface is growing as the time evolves regardless of the side of the heavy or light fluid that the shock is passing upon. This phenomenon differs from the Rayleigh-Taylor instability (RTI) in which the instability of the interface is induced by gravity only when a heavy fluid lies over a light fluid.

This test was carried out in a rectangular domain of $4 \text{ m} \times 1 \text{ m}$. The initial setup of this test is shown in Figure 6.18(top left), where a planar shock wave is located

at $x = 3.3$ m and the unperturbed edge of a perturbed interface separating two different gases is located at $x = 2.9$ m. This interface is governed by the following relation:

$$x = 2.9 - 0.1\sin(2\pi(y + 0.25)), \quad 0 < y < 1.$$

While the heavier gas which is sulphur-hexafluoride (SF_6) is put on the left side of the perturbed interface (bubble), the lighter gas (air) is put on the right side of the perturbed interface. The planar shock wave is moving left ward with a Mach of 1.24. Both gases are governed by the IG EOS 4.14 and the EOS parameters for the SF_6 and air are $\gamma = 1.093$ and $\gamma = 1.4$, respectively. Both gases which are left to the shock are initially at rest as given in Table 6.10 which provides the initial data for this test. While the extrapolation boundary conditions are imposed to the left and right boundaries, the periodic boundary conditions are imposed to the upper and lower boundaries of the computational domain.

Table 6.10: Initial data Richtmyer-Meshkov instability 6.5.5

Zone	[kg/m ³]	[km/s]	[km/s]	[bar]	
Bubble	$\rho_1 = 5.04$	$u_1 = 0$	$v_1 = 0$	$p_1 = 1$	$\alpha_1 = 1 - \epsilon$
	$\rho_2 = 1$	$u_2 = 0$	$v_2 = 0$	$p_2 = 1$	$\alpha_2 = \epsilon$
Pre-shock	$\rho_1 = 5.04$	$u_1 = 0$	$v_1 = 0$	$p_1 = 1$	$\alpha_1 = \epsilon$
	$\rho_2 = 1$	$u_2 = 0$	$v_2 = 0$	$p_2 = 1$	$\alpha_2 = 1 - \epsilon$
Post-shock	$\rho_1 = 1.411$	$u_1 = -0.39$	$v_1 = 0$	$p_1 = 1.628$	$\alpha_1 = 1 - \epsilon$
	$\rho_2 = 1$	$u_2 = -0.39$	$v_2 = 0$	$p_2 = 1.628$	$\alpha_2 = \epsilon$

The results of this test are obtained from the seven-equation model using 2000×500 cells and a CFL equals 0.3. These results are presented in Figures 6.18-6.19 at eight different instants. Figure 6.18 (top left column) shows the first instant at $t = 0$ s where the planar shock wave approaches a single mode perturbed interface. This figure shows the mixture density (a), idealised schlieren mixture density (b), idealised schlieren pressure (c), mixture density across line of symmetry (d) and pressure across line of symmetry (e). When the shock wave hits the perturbed interface, a transmitted shock wave propagates to the left through the SF_6 and a reflected shock wave propagates to the right through the air as illustrated in Figure 6.18 (bottom left column). One can notice that the interface is accelerated from the light fluid to heavy fluid and the amplitude grows as the time evolves. This acceleration is caused by the interaction of the shock wave, coming from the light fluid to the heavy fluid region, with the perturbed interface as illustrated in Figures 6.18 (bottom right column) and 6.19 (top columns). These figures also show the complicated interaction of the waves.

As the time evolves the instability grows to form a horn shape (roll-ups) as shown

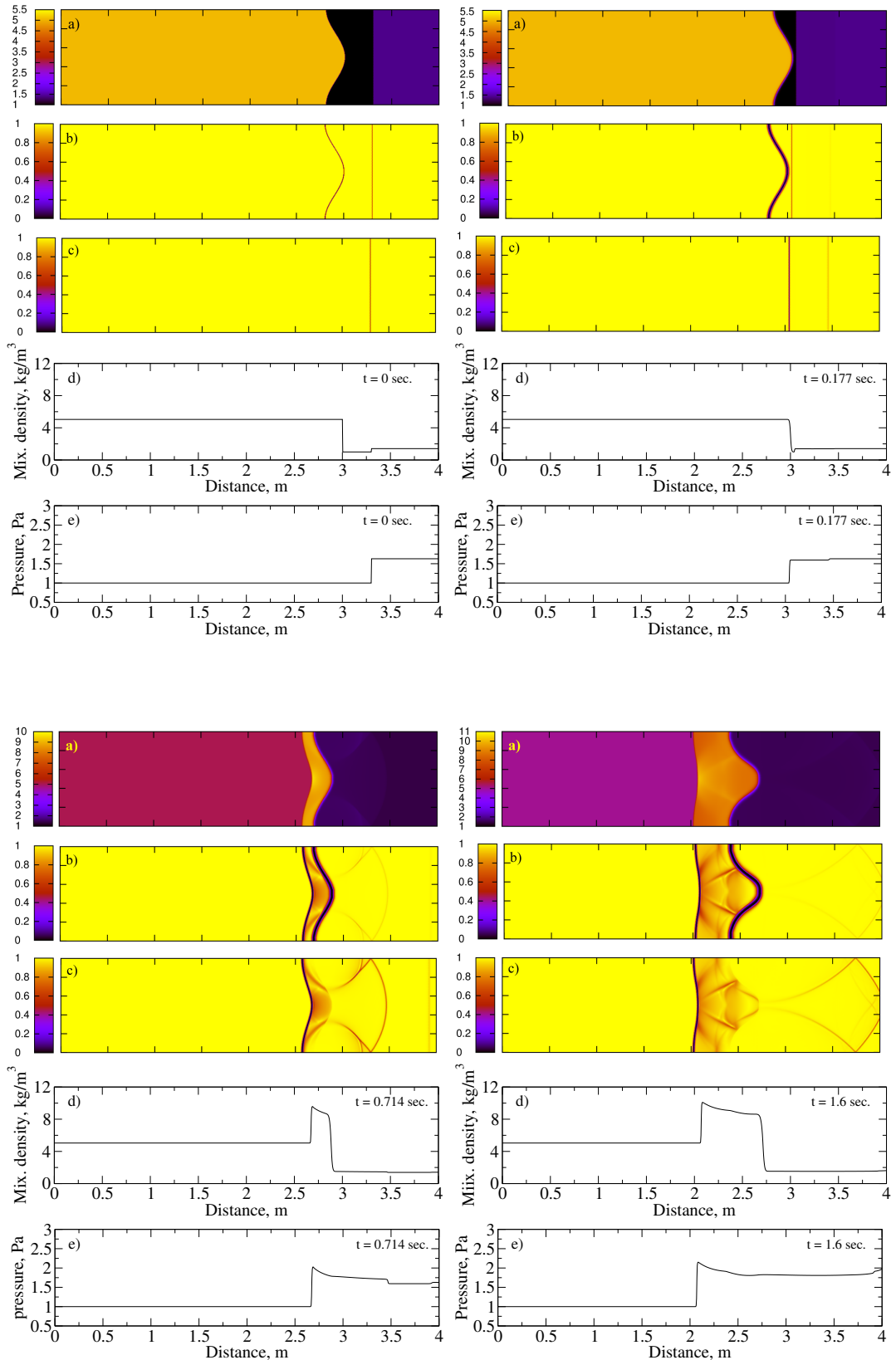


Figure 6.18: Richtmyer-Meshkov instability 6.5.5. Results from 7-equation model for (a) mixture density, (b) idealised schlieren mixture density, (c) idealised schlieren pressure, (d) mixture density plot across line of symmetry and (e) pressure plot across line of symmetry at $t = 0$ s (top left column), $t = 0.177$ (top right column), $t = 0.714$ s (bottom left column) and $t = 1.6$ s (bottom right column).

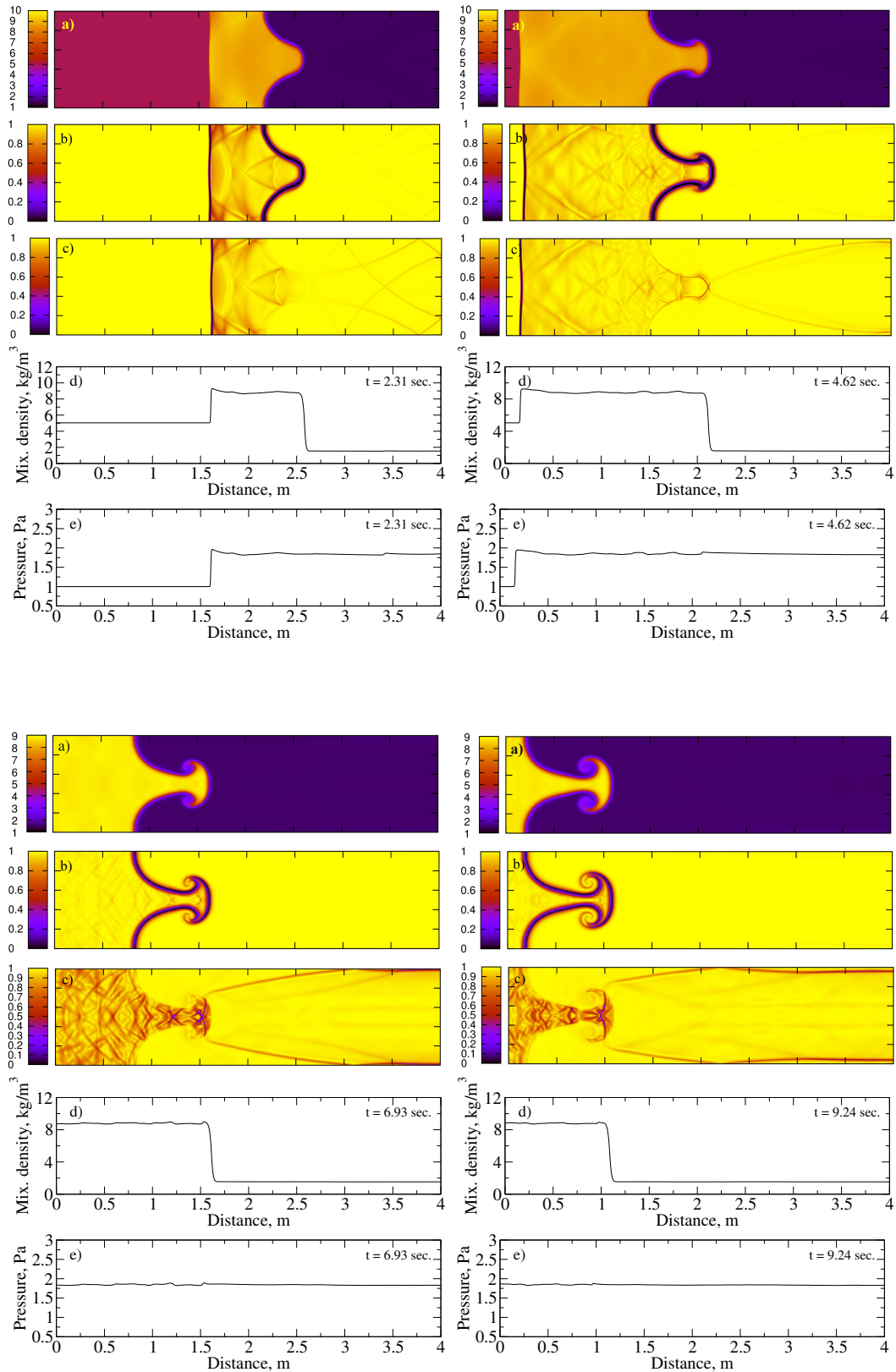


Figure 6.19: *Continued.* Richtmyer-Meshkov instability 6.5.5. Results from 7-equation model for (a) mixture density, (b) idealised schlieren mixture density, (c) idealised schlieren pressure, (d) mixture density plot across line of symmetry and (e) pressure plot across line of symmetry at $t = 2.31$ s (top left column), $t = 4.62$ s (top right column), $t = 6.93$ s (bottom left column) and $t = 9.24$ s (bottom right column).

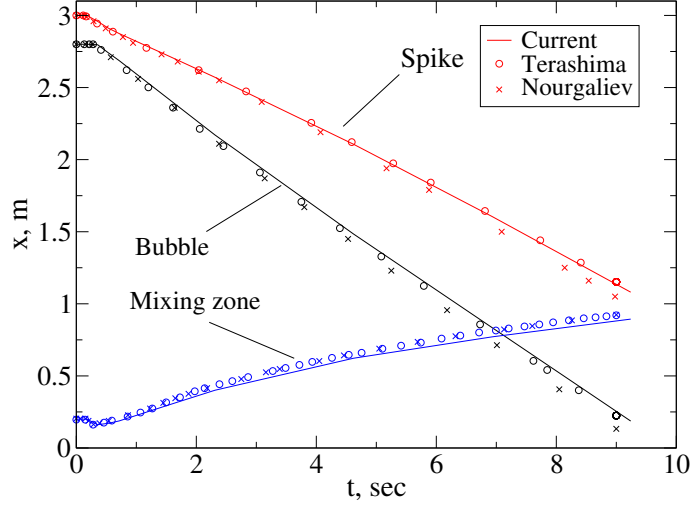


Figure 6.20: Richtmyer-Meshkov instability 6.5.5. Comparison of spike and bubble positions and mixing zone thickness as functions of time with results of Nourgaliev, Dinh and Theofanous (2006); Terashima and Tryggvason (2009).

in Figures 6.19 (bottom columns). These interface roll-ups are produced because of the vorticity generated by the passage of the shock wave. The misalignments of the pressure gradient of the shock and the local density gradient across the interface due to the curvature of the interface are the main sources of vorticity generation. The pressure and density gradients misalignments ($\nabla\rho \times \nabla p$) are known as the baroclinic effect, the vorticity is represented by the following equation:

$$\frac{D\omega}{Dt} = -\omega(\nabla \cdot V) + \frac{1}{\rho^2}(\nabla\rho \times \nabla p), \quad (6.58)$$

where ω is the vorticity and V is the velocity field. The first term on the right hand side of the above equation has no effect on vorticity generation at initial time (zero velocity at $t = 0$ s), the main source is the baroclinic effect which is represented by the second term on the right hand side of the above equation. The effect of the first term increases the vorticity generation as soon as the shock passes over the interface separating the flow components.

Figure 6.20 shows a comparison of the spike and bubble positions and mixing zone thickness as functions of time with results of Nourgaliev, Dinh and Theofanous (2006); Terashima and Tryggvason (2009). The current results are in good agreement with the results of Nourgaliev, Dinh and Theofanous (2006) who used an adaptive mesh refinement techniques in their computations, and with the results of Terashima and Tryggvason (2009) who used a front tracking-ghost fluid method in their studies.

6.6 Numerical results - Validation test problems

In this section, shock-R22 bubble, helium-bubble interactions and underwater explosion near free surface test problems are examined in two space dimensions to

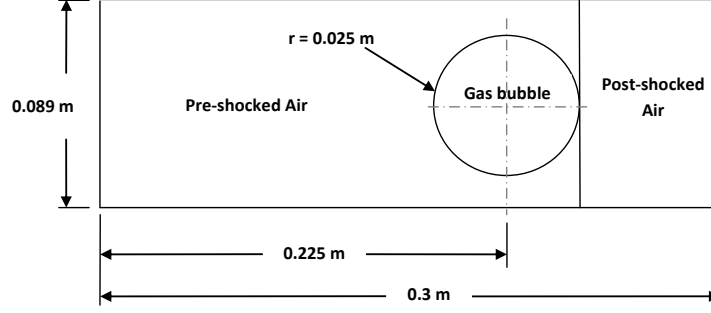


Figure 6.21: Initial configuration for air shock interactions with R22 and Helium bubbles.

validate the results obtained from the developed codes. Validations of the six and seven-equation models have been demonstrated in two-dimensions using the ideal gas, van der Waals, stiffened gas and Tait EOSs. The usual assumption of presence of a negligible volume fraction $\epsilon = 10^{-8}$ of the other fluid in the fluid considered as a pure fluid is used in all test problems. The numerical results of all presented test problems are compared with experimental results. It can be seen that good results have been achieved for these test problems using various EOSs.

In order to determine the flow field properties for shock bubble interaction test problems, the following subscripts 1, 2 and 3 have been used to represent pre-shocked zone, bubble and post-shocked zone, respectively. Assuming that the bubble is in thermal and mechanical equilibrium with the surrounding air, i.e. $p_1 = p_2$ and $T_1 = T_2$. The bubble density ρ_2 can then be calculated as follows:

$$\rho_2 = \rho_1 \frac{R_1}{R_2}. \quad (6.59)$$

The pressure, density and velocity of the post-shocked zone can be determined according to Toro (2009) as:

$$p_3 = p_1 \frac{2\gamma_1(M_1 - M_3)^2 - (\gamma_1 - 1)}{(\gamma_1 + 1)}. \quad (6.60)$$

$$\rho_3 = \rho_1 \frac{(\gamma_1 + 1)(M_1 - M_3)^2}{(\gamma_1 - 1)(M_1 - M_3)^2 + 2}. \quad (6.61)$$

The speed of sound in air according to the IG EOS is expressed by:

$$c = \sqrt{\frac{\gamma_1 p_1}{\rho_1}}. \quad (6.62)$$

Using the Mach number, the shock wave speed S can be determined as follows:

$$S = M_3 c. \quad (6.63)$$

The velocity of air in the post-shocked zone can be calculated as follows:

$$u_3 = \left(1 - \frac{\rho_1}{\rho_3}\right)S + u_1 \frac{\rho_1}{\rho_3}. \quad (6.64)$$

Properties of the gases which are used for the simulations conducted in the subsections 6.6.1 and 6.6.2 are given in Table 6.11.

6.6.1 R22 bubble-air shock interaction

The R22 bubble-air shock interaction is conducted to validate the numerical results obtained from the developed numerical application. This test was studied experimentally by Haas and Sturtevant (1987) and similar investigations using different gases were carried out by Layes and Le Métayer (2007). This test was also examined numerically by many authors (see for example, Quirk and Karni, 1996; Qamar and Warnecke, 2004) to assess the performance of numerical methods.

The test was carried out in a rectangular domain of 0.3 m \times 0.089 m. The initial setup of the computational domain is illustrated in Figure 6.21. While the extrapolation boundary conditions are imposed on the left and right boundaries, the reflective boundary conditions are imposed on the upper and lower boundaries. A left ward travelling planar shock wave is moving in air at $M = 1.22$. This shock is located on the right side of the R22 cylindrical bubble. The bubble and the surrounding air are assumed to be in thermal and mechanical equilibrium. The bubble and the surrounding air (pre-shock air) are also assumed to be at atmospheric pressure and temperature (101325 Pa and 25 °C). In this test the air is either governed by the IG or vdW EOSs. The IG EOS parameters for air and R22 are given in Table 6.11. The vdW EOS parameters for air are $\gamma = 1.4$, $a = 5 \text{ Pa}\cdot\text{m}^6/\text{kg}$ and $b = 10^{-3} \text{ m}^3/\text{kg}$. The initial conditions of the flow field are determined as detailed in section 6.6. They are given in Table 6.12.

The numerical results are obtained from the six-equation model using a mesh size of 2700 \times 801 cells and a CFL number equal to 0.3. The results for the R22 bubble-air shock interaction and the surrounding air using an idealised Schlieren function for mixture density are shown on the left column of the Figures 6.22-6.23. The results are compared to the experimental shadowgraph results of Haas and

Table 6.11: Gases properties used for the shock-bubble interactions.

Gas	γ	R J/kg·K	C_v J/kg·K
Air	1.4	0.287	0.72
R22	1.249	0.091	0.365
He + 28 % air	1.648	1.578	2.44

Table 6.12: Initial conditions for the R22 bubble test 6.6.1.

Physical property	Air pre-shock	R22 bubble	Air post-shock
Density, kg/m ³	1.1839	3.734	1.6295
velocity u, m/s	0	0	-115.478
velocity v, m/s	0	0	0
Pressure, Pa	101325	101325	159060

Sturtevant (1987) which are shown on the right column of the Figures 6.22-6.23 at times 55, 115, 135, 187, 247, 318, 342, 417 and 1020 μ s. A brief description of the interaction process of the planar shock wave with the R22 cylindrical bubble is given below, for detailed descriptions (see for example, Haas and Sturtevant, 1987; Quirk and Karni, 1996).

Table 6.13: A comparison of the computed velocities for the R22 bubble case with experimental results of (Haas and Sturtevant, 1987) and numerical results of (Quirk and Karni, 1996); for key, see Figure 6.24

Velocity	V_s	V_R	V_T	V_u	V_d
Experiment (Haas and Sturtevant, 1987)	415	240	540	73	78
Quirk and Karni (Quirk and Karni, 1996)	420	254	560	70	82
% Error	+1.2	+5.8	+3.7	-4.1	+5.1
Current	414.32	235.37	536.13	71.6	78.45
% Error	-0.16	-1.9	-0.7	-1.9	+0.57

Figure 6.22 (a) shows the R22 bubble at the instant $t = 55 \mu$ s after the bubble was hit by the incident shock wave coming from the right side. It can be seen that the bubble has undergone a slight deformation. Remaining portions of the incident shock wave are shown as two short vertical lines at the top and bottom of the bubble. These portions are joined by a curved refracted shock wave which appears inside the bubble. The figure also shows the reflected wave which propagates to the right. It can be observed that the refracted shock lags behind the incident shock wave due to the lower speed of sound inside the bubble than that outside the bubble.

As the time evolves, the lag of the refracted shock wave becomes more obvious and at the instant $t = 115 \mu$ s this wave has folded at its top and bottom. It can be observed that the two portions of the incident shock wave have started to diffract around the downstream half of the bubble. It can also be noticed that the reflected wave having hit the upper and lower boundaries of the domain (solid walls) reflected again and propagated towards the bubble and is hardly visible as shown at the bottom of Figure 6.22 (b).

At the instant $t = 135 \mu\text{s}$ each side of the folded refracted shock is nearly horizontal. The reflected waves that have hit the upper and lower walls of the tube are now more visible and are approaching the bubble as shown in Figure 6.22 (c). It can be noticed that the size of the bubble continues to decrease substantially due to the shock compression.

By $t = 187 \mu\text{s}$ the refracted shock is almost focused down to a point as shown

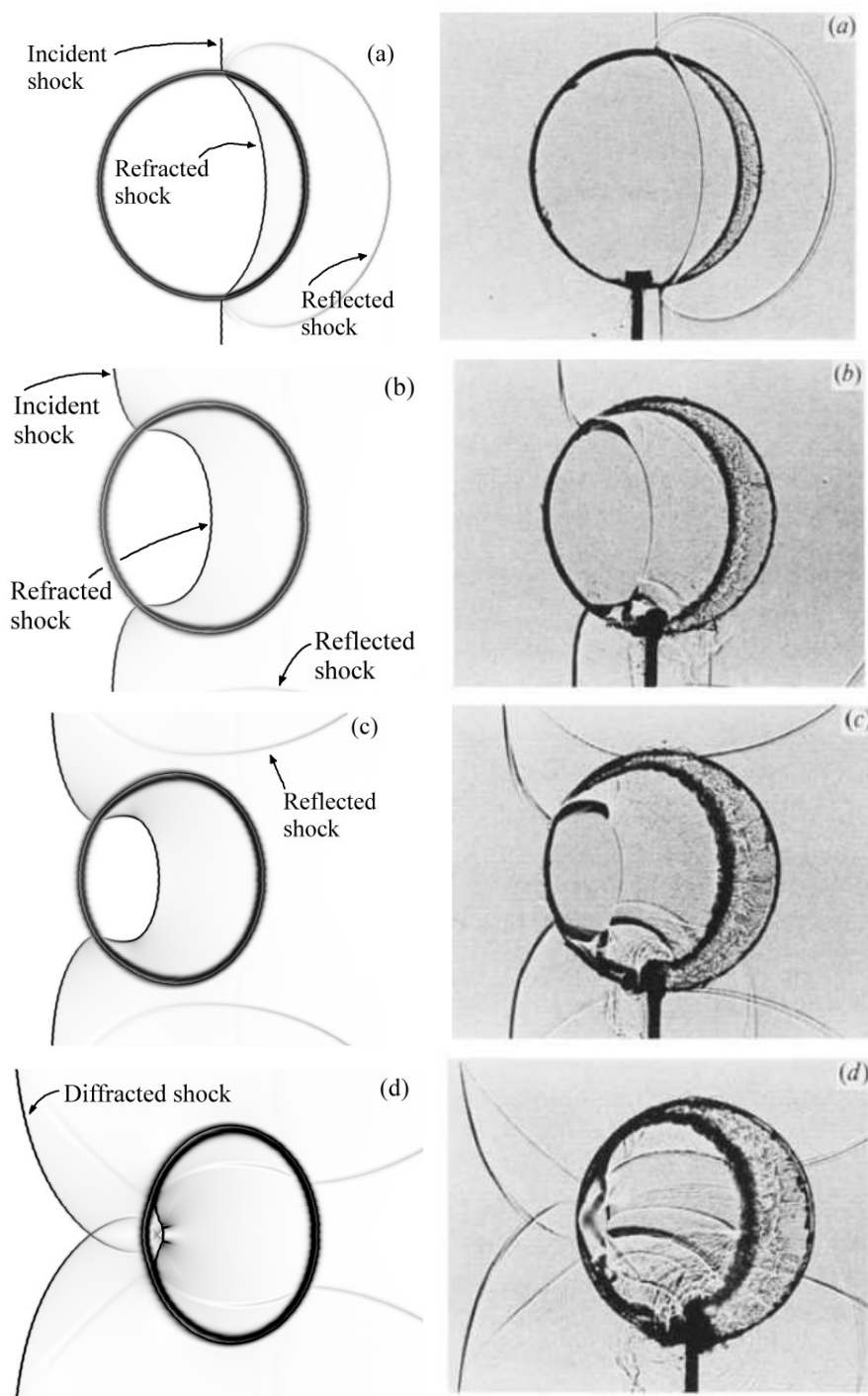


Figure 6.22: Mixture density idealised Schlieren images for R22 bubble-air shock interaction at times: (a) $55 \mu\text{s}$, (b) $115 \mu\text{s}$, (c) $135 \mu\text{s}$, (d) $187 \mu\text{s}$. Current results (left) and Haas and Sturtevant (1987) results (right).

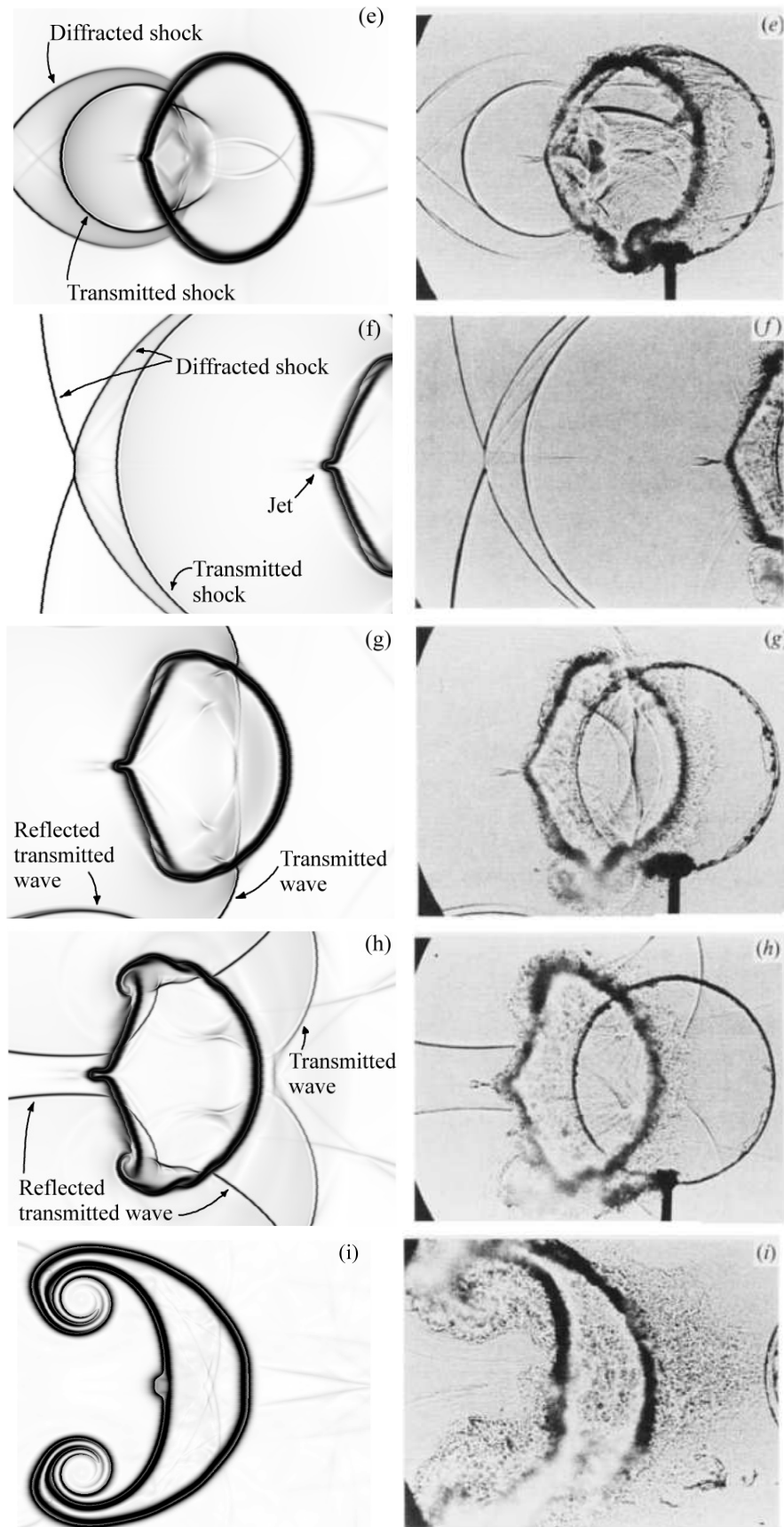


Figure 6.23: *Continued.* Mixture density idealised Schlieren images for R22 bubble-air shock interaction at times: (e) 247 μs , (f) 318 μs , (g) 342 μs , (h) 417 μs and (i) 1020 μs . Current results (left) and Haas and Sturtevant (1987) results (right).

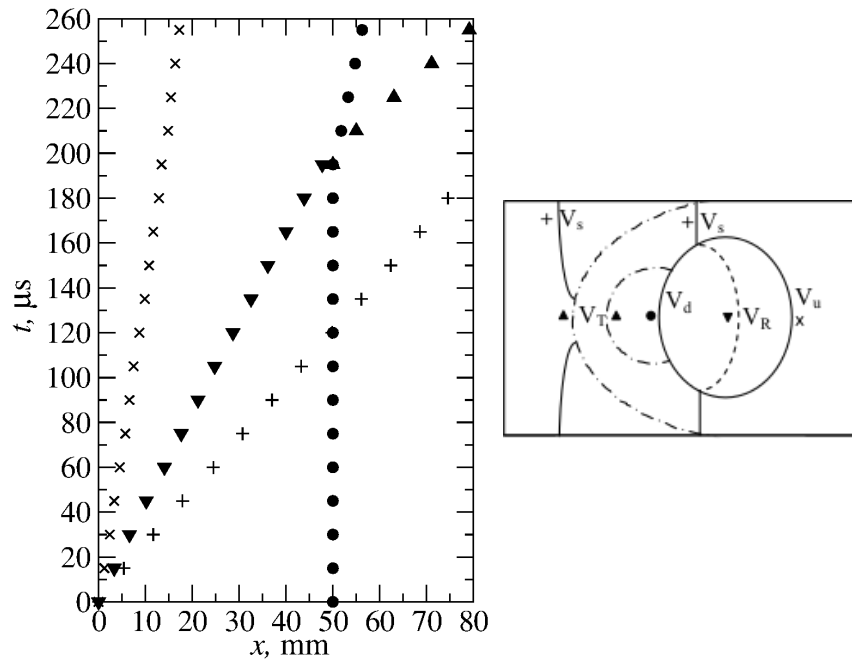


Figure 6.24: $x-t$ diagram for R22 bubbles (left), key points (right): V_s incident shock; V_R refracted shock; V_T transmitted shock; V_u upstream edge; V_d downstream edge;.

in Figure 6.22 (d). This causes the pressure increase as illustrated in the pressure plot shown in Figure 6.25 (d). At this moment, the diffracted incident shock wave portions intersect each other. The middle portions of the reflected waves from the top and bottom walls propagate through the bubble and are hardly discernible as shown in Figure 6.22 (d). Once again these shocks lag behind their counterparts outside the bubble because of the difference in the speeds of sound inside and outside the bubble.

When the refracted shock passed through the downstream interface of the bubble, it became a transmitted wave as shown in Figure 6.23 (e) which is more obvious at time $t = 247 \mu s$. The remaining portions of the reflected shocks from the walls continue to propagate inside the bubble and they intersect each other. A small jet is about to be formed at the downstream interface of the bubble, this jet is initiated by focusing of the refracted wave. The transmitted wave is trying to catch up the two portions of the diffracted incident shock wave in this stage as shown in Figure 6.23 (f).

A shock wave continues to propagate backward inside the bubble as shown in Figure 6.23 (g) at the instant $t = 342 \mu s$. This wave was initiated from the internal reflection of the refracted shock from the downstream interface. In the lower part of this image one can observe that the transmitted wave has reflected from the upper and lower walls of the shock tube. This causes a generation of vorticity along the interface due to the misalignment of the gradients in pressure and density (Haas and Sturtevant, 1987).

Figure 6.23 (h) shows the reflected waves from the walls which pass through the

bubble at the instant $t = 417 \mu\text{s}$ which results in a corrugated surface of the bubble. As the time moves on, the bubble takes a crescent shape and continues to elongate as shown in Figure 6.23 (i).

The $x-t$ diagram shown in Figure 6.24 depicts the position history of the upstream and downstream edges of the R22 bubble. Moreover, it presents the position history of the incident, refracted and transmitted shock waves. The schematic diagram on the right part of Figure 6.24 illustrates the points used to construct the $x-t$ diagram. All positions are considered at the axis of symmetry except for the incident shock wave which is considered either at the bottom or top boundaries of the domain. Since the used numerical method is diffusive the points were measured at mean thickness of the interface. The computed mean velocities compared to the experimental results of Haas and Sturtevant (1987) and Quirk and Karni (1996) are presented in Table 6.13. These results are in good agreement with the references results with a maximum estimated error of -1.9% compared to the experimental results.

The same test was carried out considering air as a real gas governed by the vdW EOS. To calculate the compressibility factor Z , the reduced temperature T_R and reduced pressure P_R are calculated for air as follows:

$$T_R = \frac{T}{T_c} \quad (6.65)$$

$$P_R = \frac{P}{P_c} \quad (6.66)$$

where T, P, T_c and P_c are the temperature and pressure at atmospheric and critical conditions, respectively. The atmospheric condition assumed to be $T = 293.15$ K and $P = 101325$ Pa and the critical condition for air is $T_c = 132.65$ K, $P_c = 37.71 \times 10^5$ Pa. The reduced temperature and pressure are calculated to be 2.2 and 0.2687, respectively.

Using the values of the reduced temperature, pressure and the compressibility char (see for example, Çengel and Boles, 2007) the value of Z is found to be very close to 1. Consequently, air could be considered as an ideal gas at this condition. The numerical results obtained from the van der Waals EOS are very close to that obtained from the ideal gas EOS. This can be realised from the results for mixture density and pressure obtained from both EOSs as shown in Figure 6.25.

6.6.2 Helium bubble-air shock interaction

The helium bubble-air shock interaction test is also conducted to validate the numerical results obtained from the six and seven-equation models. The test was investigated experimentally in Haas and Sturtevant (1987); Layes and Le Métayer (2007). This test was also examined numerically to check the accuracy and capa-

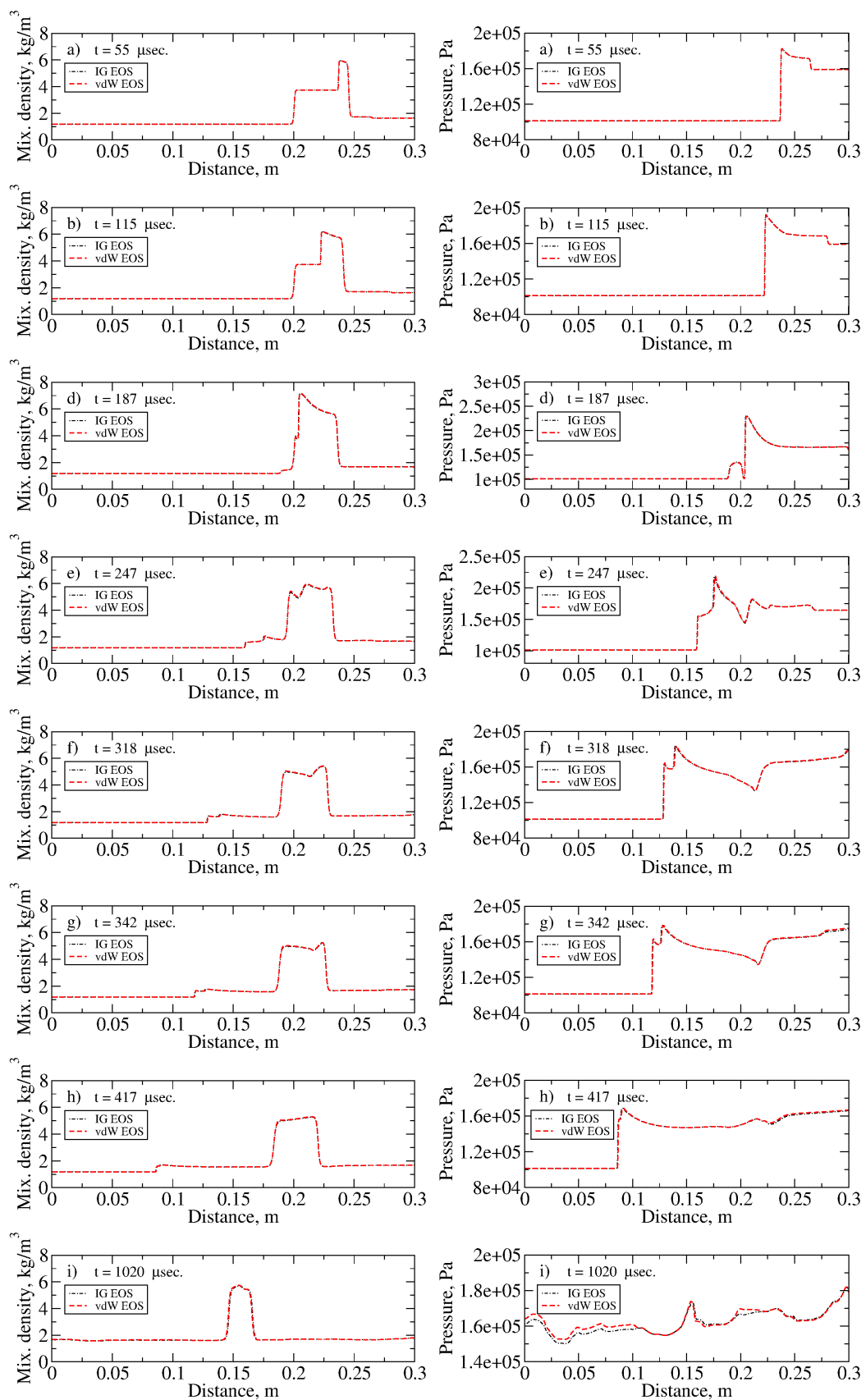


Figure 6.25: Comparison between results of the IG and vdW EOSs for mixture density (left) and pressure (right) plots at axis of symmetry for R22 bubble-air shock interaction at times: (a) $55 \mu\text{s}$, (b) $115 \mu\text{s}$, (d) $187 \mu\text{s}$ (e) $247 \mu\text{s}$, (f) $318 \mu\text{s}$, (g) $342 \mu\text{s}$, (h) $417 \mu\text{s}$ and (i) $1020 \mu\text{s}$.

bility of numerical methods (see for example, Quirk and Karni, 1996; Fedkiw et al., 1999; Marquina and Mulet, 2003; Giordano and Burtschell, 2006; Terashima and Tryggvason, 2009).

Table 6.14: Initial conditions for helium bubble-air shock test 6.6.2.

Physical property	Air pre-shock	He+28% air bubble	Air post-shock
Density, [kg/m ³]	1.1839	0.2153	1.6295
velocity u, [m/s]	0	0	-115.478
velocity v, [m/s]	0	0	0
Pressure, [Pa]	101325	101325	159060

The configuration of the computational domain and the boundary conditions are similar to the previous test as shown in Figure 6.21. The cylindrical helium bubble is contaminated with 28% of air to increase its density. Similar to the previous test initially the bubble and the surrounding air are assumed to be in thermal and mechanical equilibrium. In this test both gases are governed by the IG EOS and their EOS parameters are given in Table 6.11. The initial conditions for the bubble and post-shock zone were calculated as described in section 6.6 and are given in Table 6.14.

The numerical results for the idealised Schlieren mixture density for the helium bubble and the surrounding air are shown in Figures 6.26-6.27 at times 22, 44, 56, 72, 82, 102, 245, 427, 674 and 983 μ s. Note that only the first three times are different from that obtained from the experimental shadowgraph results of Haas and Sturtevant (1987). The reason behind that might be that only one shadowgraph shot could be taken during each run, and so the whole record was established by repeating the experiment with various delay times. The current results are obtained using a mesh size of 2700×801 cells and a CFL number is equal to 0.3. A brief description of the interaction process of the planar shock wave with the helium cylindrical bubble is given below (for more details see for example Haas and Sturtevant, 1987; Quirk and Karni, 1996).

Figure 6.26 (a) shows the helium bubble at the instant $t = 22 \mu$ s (in experiment was $t = 32 \mu$ s, the reason mentioned above) after the bubble was hit by the incident shock wave coming from the right side. The middle portion of the incident shock refracted inside the bubble and the remaining portions are seen as vertical lines at the top and bottom of the bubble. The refracted shock takes a curved shape which joins the two portions of the incident shock. It can be observed that the refracted shock propagates faster than the incident shock which propagates in air due to the fact that the sound speed in the helium bubble is higher than in the surrounding air. At this moment the bubble has undergone a slight deformation. A reflected wave is formed and propagated in a curved shape to the right in air.

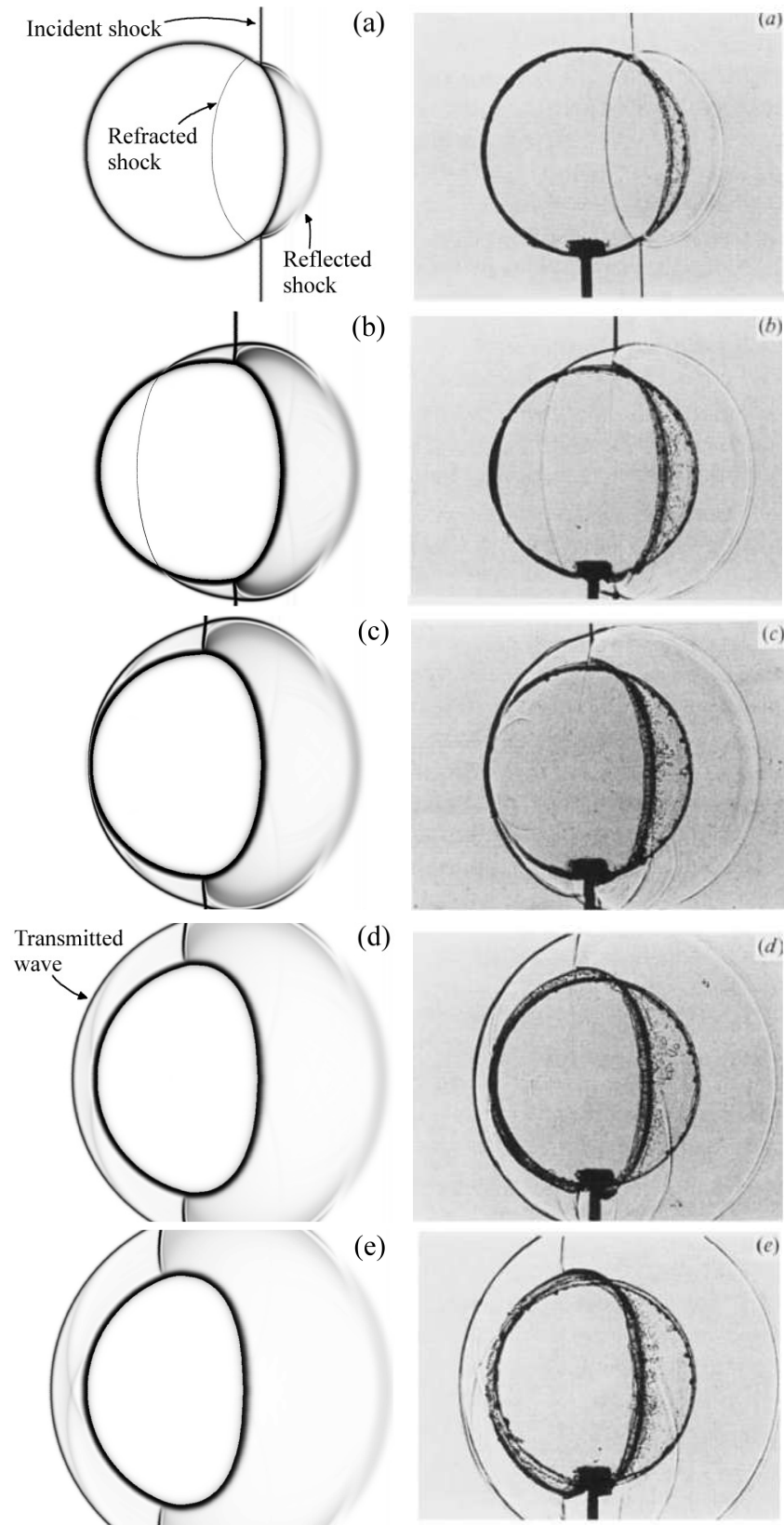


Figure 6.26: Mixture density: Current numerical Schlieren images (left) and experimental (Haas and Sturtevant, 1987) (right) for He + 28% air bubble-air shock interaction at times: (a) $22 \mu\text{s}$ ($32 \mu\text{s}$), (b) $44 \mu\text{s}$ ($52 \mu\text{s}$), (c) $56 \mu\text{s}$ ($62 \mu\text{s}$), (d) $72 \mu\text{s}$, (e) $82 \mu\text{s}$. Times between parentheses are corresponding times in the experiments which are different from numerical times.

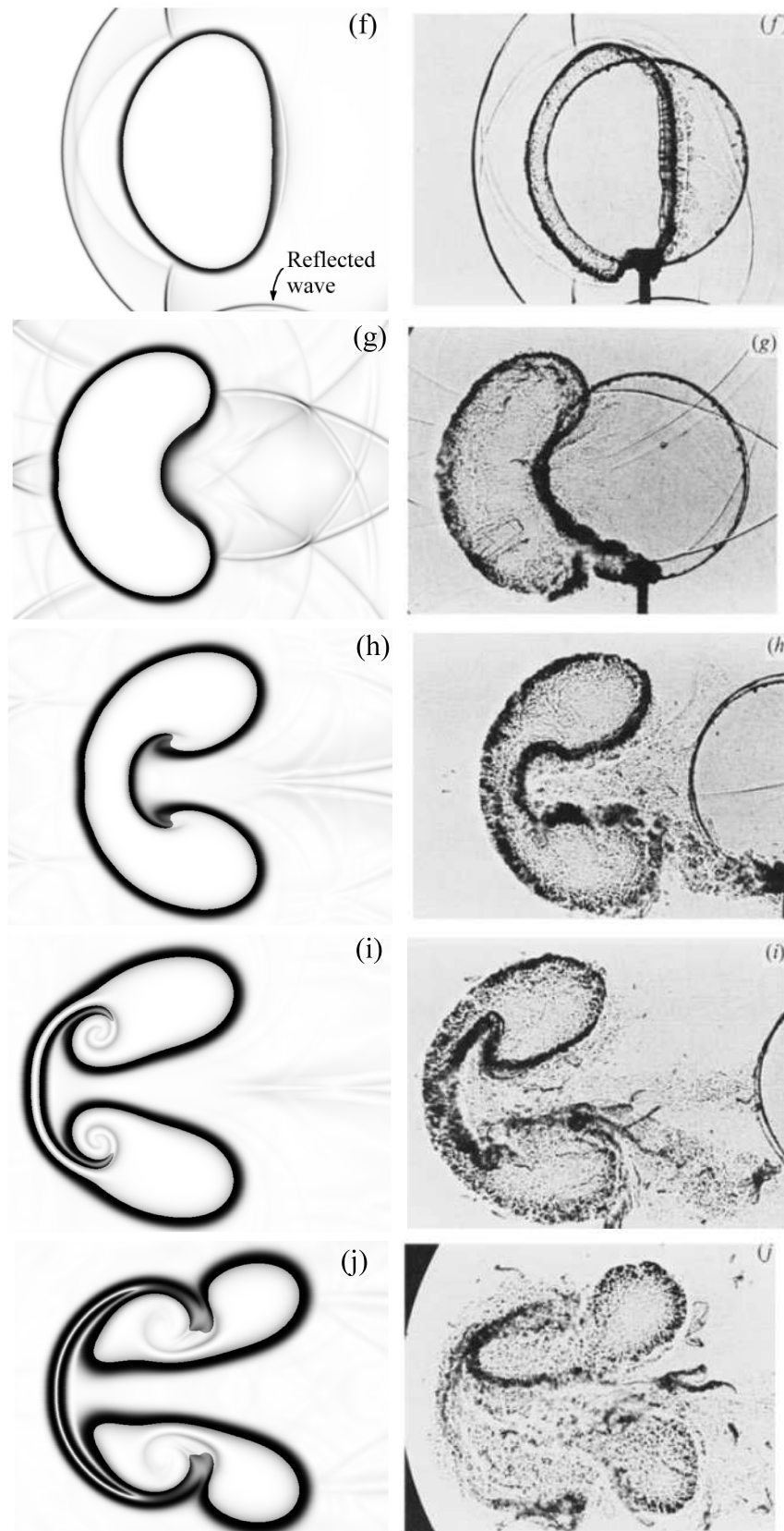


Figure 6.27: *Continued*: Mixture density: Current numerical Schlieren images (left) and experimental (Haas and Sturtevant, 1987) (right) for He + %28 air bubble-air shock interaction at times: (f) $102 \mu\text{s}$, (g) $245 \mu\text{s}$, (h) $427 \mu\text{s}$ (i) $674 \mu\text{s}$ and (j) $983 \mu\text{s}$.

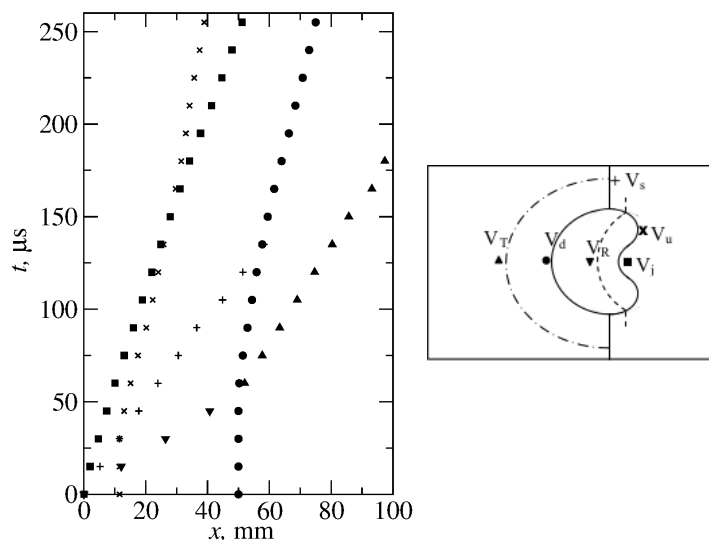


Figure 6.28: $x-t$ diagram for He + 28% air bubbles (left), key points (right): V_s incident shock; V_R refracted shock; V_T transmitted shock; V_u upstream edge; V_d downstream edge and V_j air jet head.

Indeed, the cross-section plots 6.29 (a - f) for the pressure and mixture density field confirm that the reflected wave is an expectation wave as pointed out in Quirk and Karni (1996). Figure 6.26 (b) shows that the difference in speeds of sound between the gases inside and outside the bubble becomes more obvious by $t = 44 \mu s$ (in experiment was $t = 52 \mu s$) where the refracted shock has advanced well ahead of the incident wave.

At the instant $t = 56 \mu s$ (in experiment was $t = 62 \mu s$) the refracted shock coincides with the downstream interface of the bubble as shown in Figure 6.26 (c). Then this wave emerges from this interface to become a transmitted wave as shown in Figure 6.26 (d) at time $t = 72 \mu s$. At this instant internally reflected waves are hardly visible which intersect each other at the axis of symmetry by $t = 82 \mu s$ as shown in Figure 6.26 (e). The bubble size continues to decrease due to the shock compression as shown in Figure 6.26 (f) at $t = 102 \mu s$. The original reflected wave which propagated to the right has hit the walls of the tube and reflected again as shown at this instant at the bottom of Figure 6.26 (f).

As time moves on, the bubble continues to deform which takes a kidney shape at $t = 245 \mu s$ as shown in Figure 6.26 (g). The figure also shows a complex view of intersected waves produced by the original reflected and transmitted waves reflected from the walls which passed through the bubble. These waves have the major role in the bubble deformation which is induced by vorticity produced at the edge of the bubble due to the passage of the shock. As the time evolves, a jet of air is induced along the axis of symmetry as shown in Figure 6.26 (h) at $t = 427 \mu s$. This jet tries to split the bubble as shown in Figure 6.26 (i) at $t = 674 \mu s$ and elongates the bubble laterally as shown in Figure 6.26 (j) at $t = 983 \mu s$.

These results are in good agreement with these experimental results and the other

Table 6.15: A comparison of the computed velocities for the He+28% air bubble case with experimental results of Haas and Sturtevant (1987), and numerical results of Quirk and Karni (1996) (Numerical (A)) and of Marquina and Mulet (2003) (Numerical (B)); for key, see Figure 6.28

Velocity	V_s	V_R	V_T	V_u	V_d	V_j
Experimental	410	900	393	170	145	230
Numerical (A)	422	943	377	178	146	227
% Error	+2.9	+4.8	+4.1	+4.7	+0.7	-1.3
Numerical (B)	414	943	373	176	153	229
% Error	+1	+4.8	-5.4	+3.4	+5.2	-0.4
Current	407.4	904.64	377.68	166.23	144	223.58
% Error	+0.63	+0.52	-3.9	-2.2	-0.69	-2.8

numerical results of Quirk and Karni (1996); Fedkiw et al. (1999); Marquina and Mulet (2003); Giordano and Burtschell (2006); Terashima and Tryggvason (2009).

The $x-t$ diagram which illustrates the position history of the interaction between the Helium bubble and the incident shock is shown in Figure 6.28. The figure indicates the x positions of the upstream and downstream edges of the cylindrical helium bubble as well as the incident, refracted and transmitted shock waves. The schematic diagram on the right part of the Figure 6.28 illustrates the points used to construct the $x-t$ diagram. All positions are measured at the axis of symmetry except for the upstream edge and the incident shock wave, i.e. the upstream edge is measured at 0.0214 above the axis of symmetry and the incident shock wave is measured either at the top or bottom boundaries of the domain. Since our numerical method is diffusive, the points were measured at mean thickness of the interface. The computed mean velocities compared to the experimental results of Haas and Sturtevant (1987) and numerical results of Quirk and Karni (1996); Marquina and Mulet (2003) are given in Table 6.15. It can be observed that these results are in very good agreement with the experimental results with a maximum estimated error of -3.9%.

The numerical results obtained from the six-equation model are compared to that obtained from the seven-equation model in terms of the mixture density and pressure distributions across the line of symmetry as depicted in Figure 6.29. These results are obtained when both gases were governed by the IG EOS. One can observe that both models gave almost the same results using a mesh size of 1500×445 cells.

6.6.3 Underwater explosion near a free surface test

While the previous validation test problems focused on the interaction of a planar shock wave with a curved interface, the present test investigates the interaction of

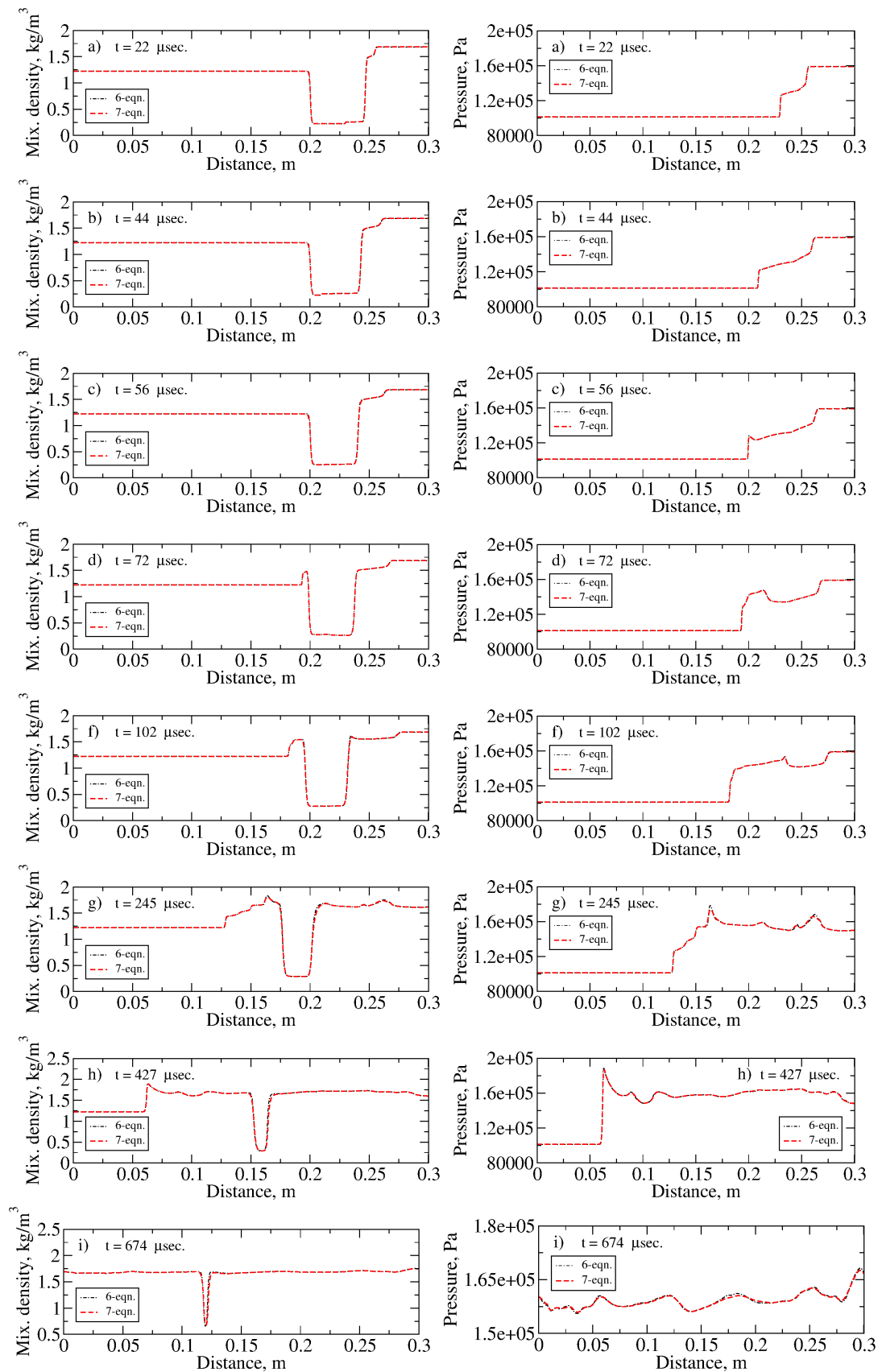


Figure 6.29: Comparison between results of the six and seven-equation models for mixture density (left) and pressure (right) plots at axis of symmetry for helium bubble-air shock interaction at times: (a) $28 \mu s$, (b) $44 \mu s$, (c) $56 \mu s$, (d) $72 \mu s$, (f) $102 \mu s$, (g) $245 \mu s$, (h) $427 \mu s$ and (i) $674 \mu s$ (j) $983 \mu s$.

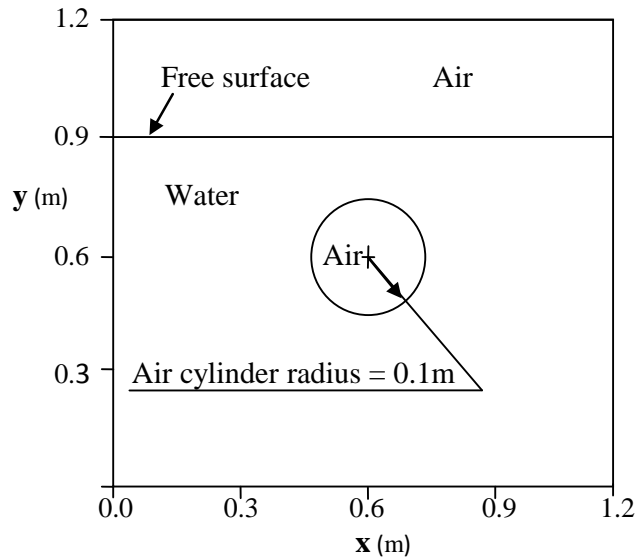


Figure 6.30: Underwater explosion test 6.6.3.

a curved shock wave with a planar interface. The test was conducted numerically by many researchers (see for example, Liu, Khoo and Yeo, 2001; Zheng et al., 2011) and investigated experimentally by Kleine et al. (2009).

The test is carried out in a square computational domain of size $1.2 \text{ m} \times 1.2 \text{ m}$. A highly pressurised air cylinder is initially located at the centre of the computational domain $(0.6 \text{ m}, 0.6 \text{ m})$ as shown in Figure 6.30. The air cylinder which is surrounded by water has a radius of 0.1 m . A free surface which separates atmospheric air and water is located at a height of 0.9 m as shown in Figure 6.30. The zero extrapolation boundary conditions are imposed to the top, left and right boundaries of the domain. Two different situations were studied for dealing with the bottom boundary. The first situation at which the bottom boundary is treated as a solid wall where the reflective boundary conditions are imposed. The second situation at which the bottom boundary is treated as an open far field where the zero extrapolation boundary conditions are imposed. Also two scenarios were examined where two different EOSs are used to govern the water, i.e. the SG and Tait EOSs. For water, the SG EOS parameters are $\gamma = 4.4, \pi = 6 \times 10^8 \text{ Pa}$ and Tait EOS parameters are $\gamma = 7.15, B = 3.31 \times 10^8 \text{ Pa}$. The air is governed by the IG EOS $\gamma = 1.4$. The initial conditions are given in Table 6.16:

The numerical results for the underwater explosion near a free surface test are obtained from the six-equation model by employing the SG and Tait EOSs. The results for the mixture density using the idealised Schlieren function, mixture density and pressure are shown in the Figures 6.31 and 6.32. These results are compared at times $0.0175, 0.035, 0.07, 0.147, 0.225$ and 0.3 ms . The same results are obtained from the seven-equation model and are compared to those obtained from the six-equation

Table 6.16: Initial conditions for the underwater explosion near a free surface test 6.6.3.

Physical property	Air cylinder	Water	Air above free surface
Density, [kg/m ³]	1270	1000	1.0
velocity u, [m/s]	0	0	0
velocity v, [m/s]	0	0	0
Pressure, [Pa]	9.21×10^8	1.1×10^5	1.1×10^5

model at the same instants as illustrated in Figures 6.33 and 6.34.

As the explosion is initiated at the pressurised air cylinder, a strong shock wave propagates radially outward through the surrounding water and a strong rarefaction wave propagates inward through the air cylinder as illustrated in Figure 6.31 (a). While these waves are represented respectively by the outer and inner circles, the material interface is represented by the middle circle. It can be observed that the shock wave moves faster than the rarefaction wave as shown in Figure 6.31 (b) due to the fact that the speed of sound in water is higher than that in air. One can notice from Figure 6.31 (b) that there is a difference between the position of the shock wave predicted by the SG EOS than that predicted by the Tait EOS. This agrees with what has been observed by Nourgaliev, Dinh and Theofanous (2006) when they obtained different results using the SG EOS from those obtained by Ball et al. (2000) using the Tait EOS for a strong shock interactions with an air bubble in water simulation. This difference becomes clearer as the time evolves as shown in Figures 6.31 (c) - 6.31 (f). This difference is not clear in the position of the rarefaction due to the previous reason. One can also notice that the positions of the material interfaces predicted by both EOSs are the same.

As the time evolves, the shock wave continues to propagate outward till it hits the free surface which causes the free surface to move upward. A small part of the shock wave is transmitted into the air and the rest is reflected downward into the water as shown in Figure 6.31 (d). Indeed, the reflected wave into water is a strong rarefaction wave which can be observed in the plots of mixture density and pressure Figure 6.31 (d). Once again, one can notice that there is a difference in the position of this strong rarefaction wave predicted by both EOSs. This rarefaction wave continues to propagate downward until it reaches the top of the expanding cylinder. The interaction of the rarefaction wave with the expanding air cylinder generates a compression wave which moves upward as shown in Figure 6.31 (e). This causes the upper interface of the air cylinder to be accelerated upward. Therefore, the air cylinder starts to take an oval shape.

At the centre of the air cylinder, a second shock wave is generated which propagates outward as shown in Figure 6.31 (e) and its related plots for mixture density

and pressure. From this figure one can notice that the first outgoing shock is about to reach the left, right and bottom boundaries of the domain.

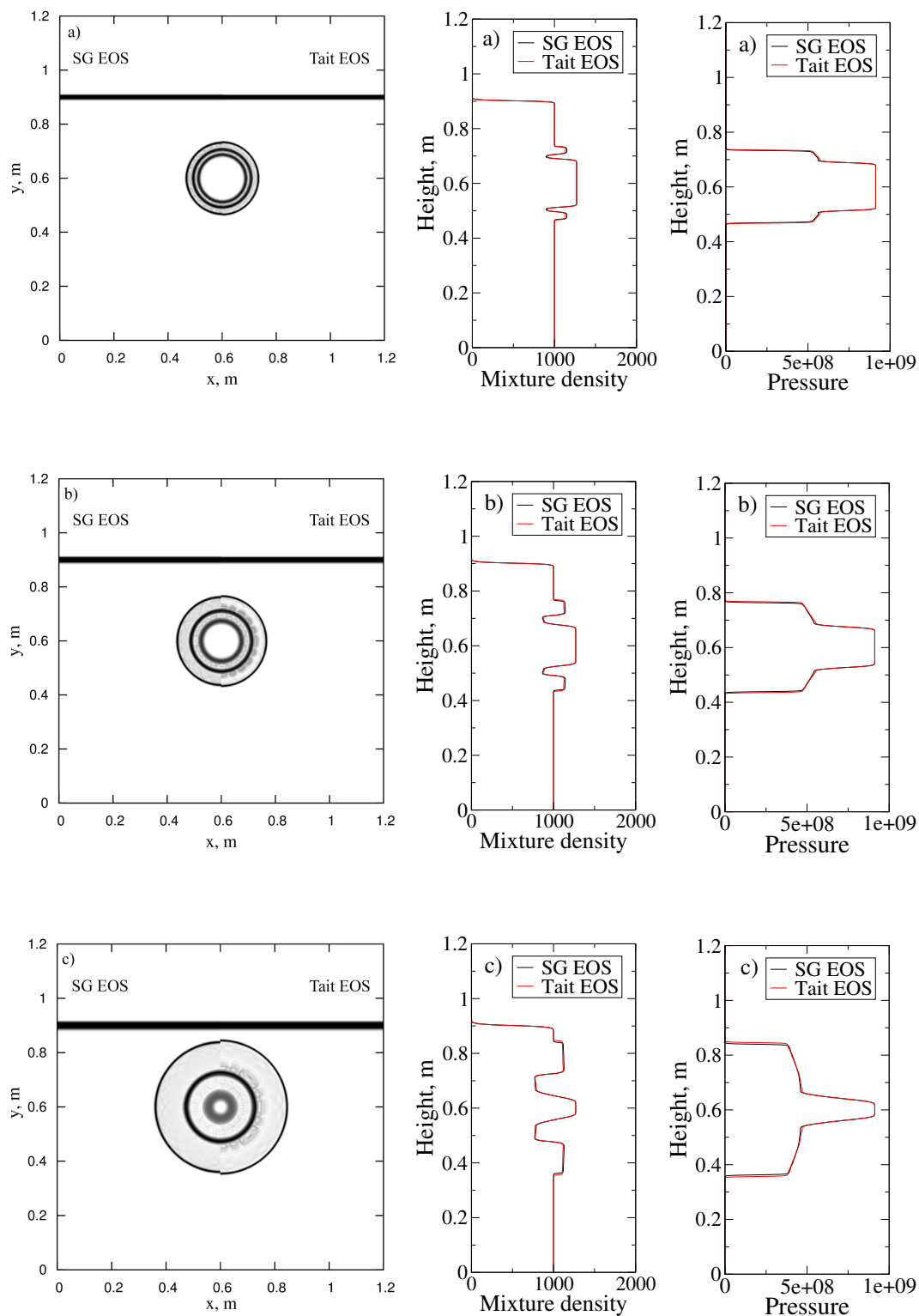


Figure 6.31: Underwater explosion near a free surface test 6.6.3. Comparison between the SG and Tait EOSs: Idealised Schlieren images of mixture density (left) and plots of mixture density (kg/m^3) (middle) and pressure (Pa) (right) at line of symmetry at times: (a) 0.0175 ms, (b) 0.035 ms, (c) 0.07 ms.

While the first outgoing shock has disappeared when it reached the left and right boundaries, it has reflected when it reached the bottom boundary as shown

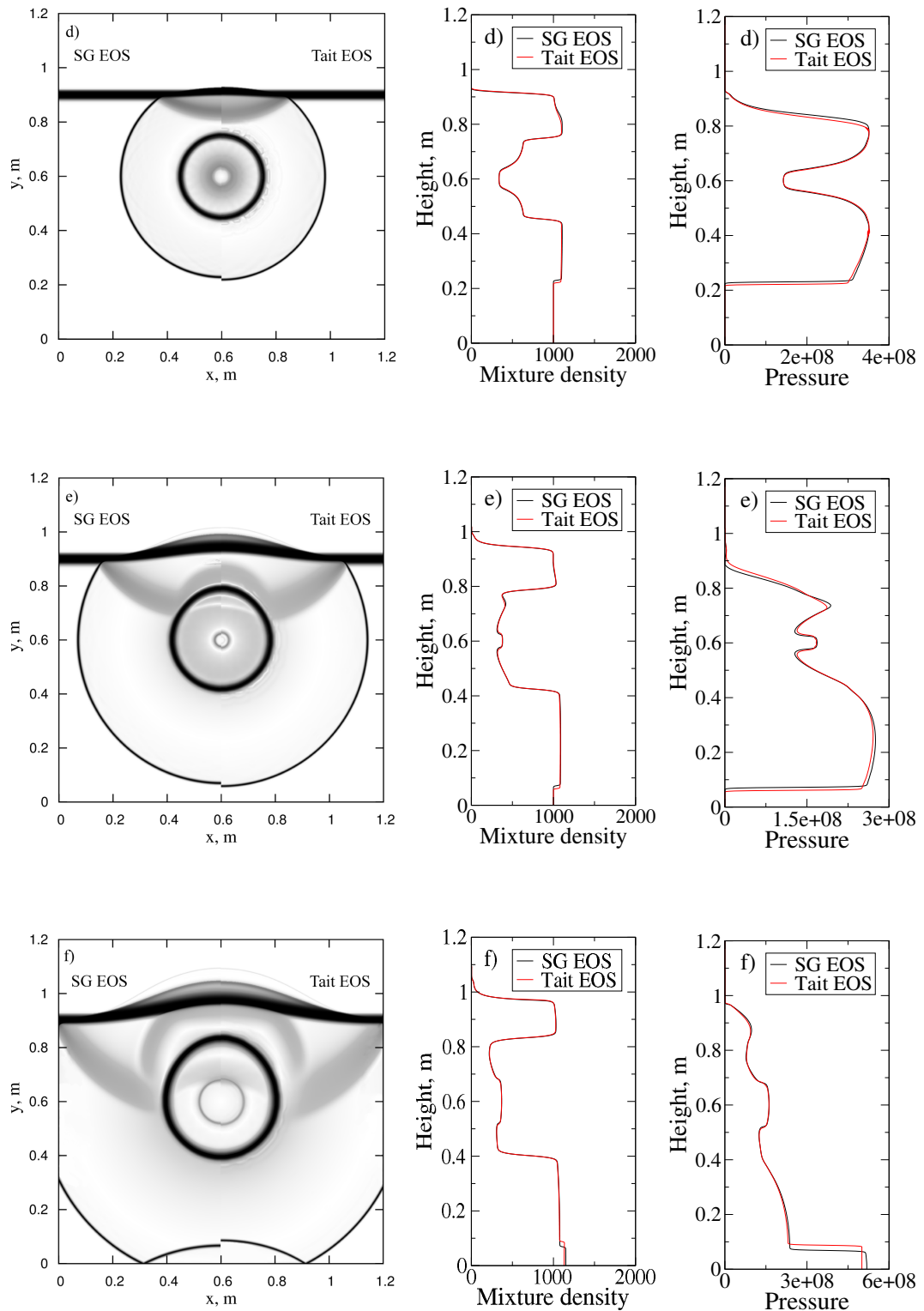


Figure 6.32: *Continued.* Underwater explosion near a free surface test 6.6.3. Comparison between the SG and Tait EOS: Idealised Schlieren images of mixture density (left) and plots of mixture density (kg/m^3) (middle) and pressure (Pa) (right) at line of symmetry at times: (d) 0.147 ms, (e) 0.225 ms, (f) 0.3 ms.

in Figure 6.31 (f). This is due to the extrapolation boundary conditions imposed on the left and right boundaries which represent the far field and the reflective

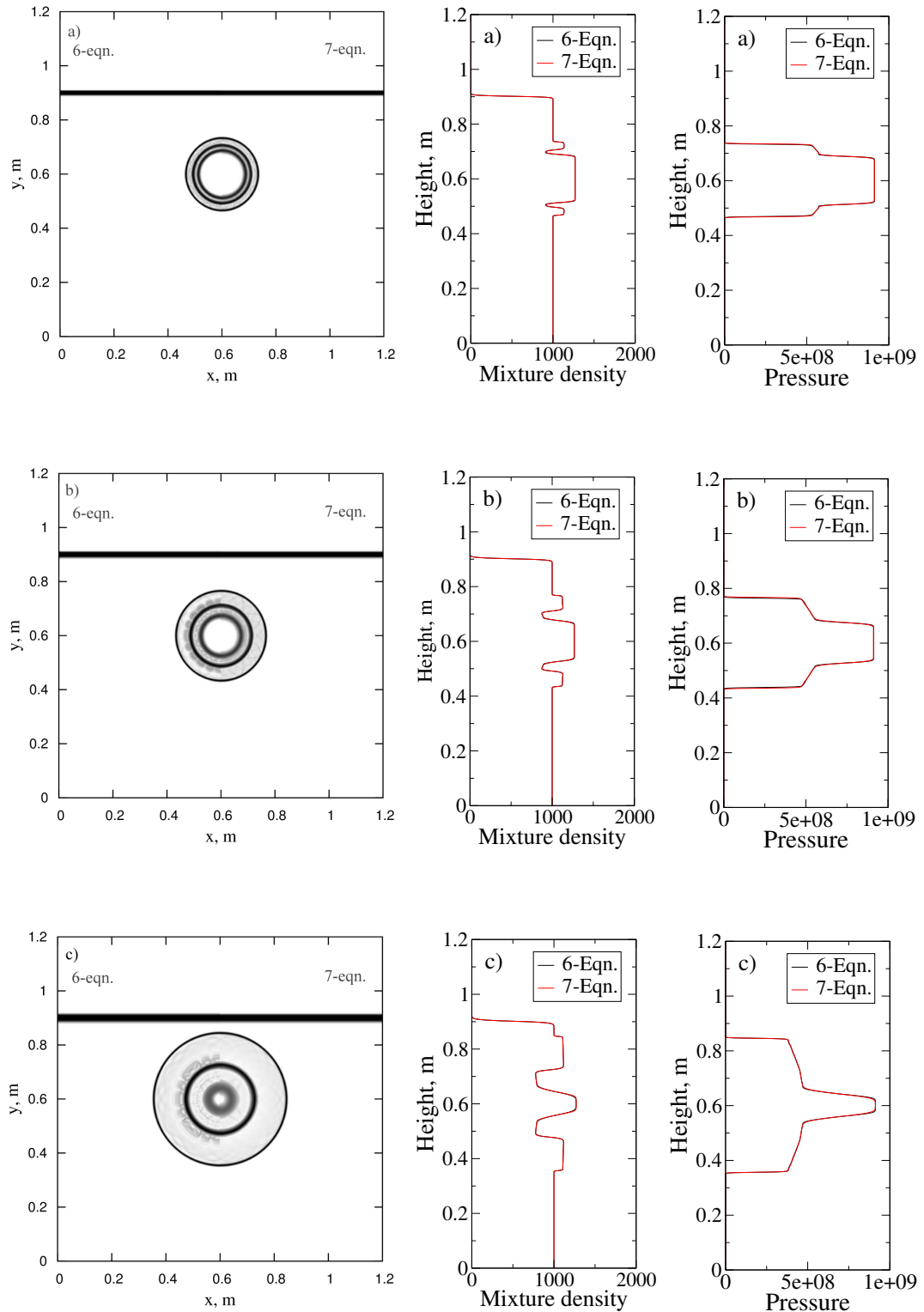


Figure 6.33: Underwater explosion near a free surface test 6.6.3. Comparison between the six and seven-equation models: Idealised Schlieren images of mixture density (left) and plots of mixture density (kg/m^3) (middle) and pressure (Pa) (right) at line of symmetry at times: (a) 0.0175 ms, (b) 0.035 ms, (c) 0.07 ms.

boundary conditions imposed on the bottom boundary which represents the solid wall. In the meantime the inner shock wave continues to expand outward inside

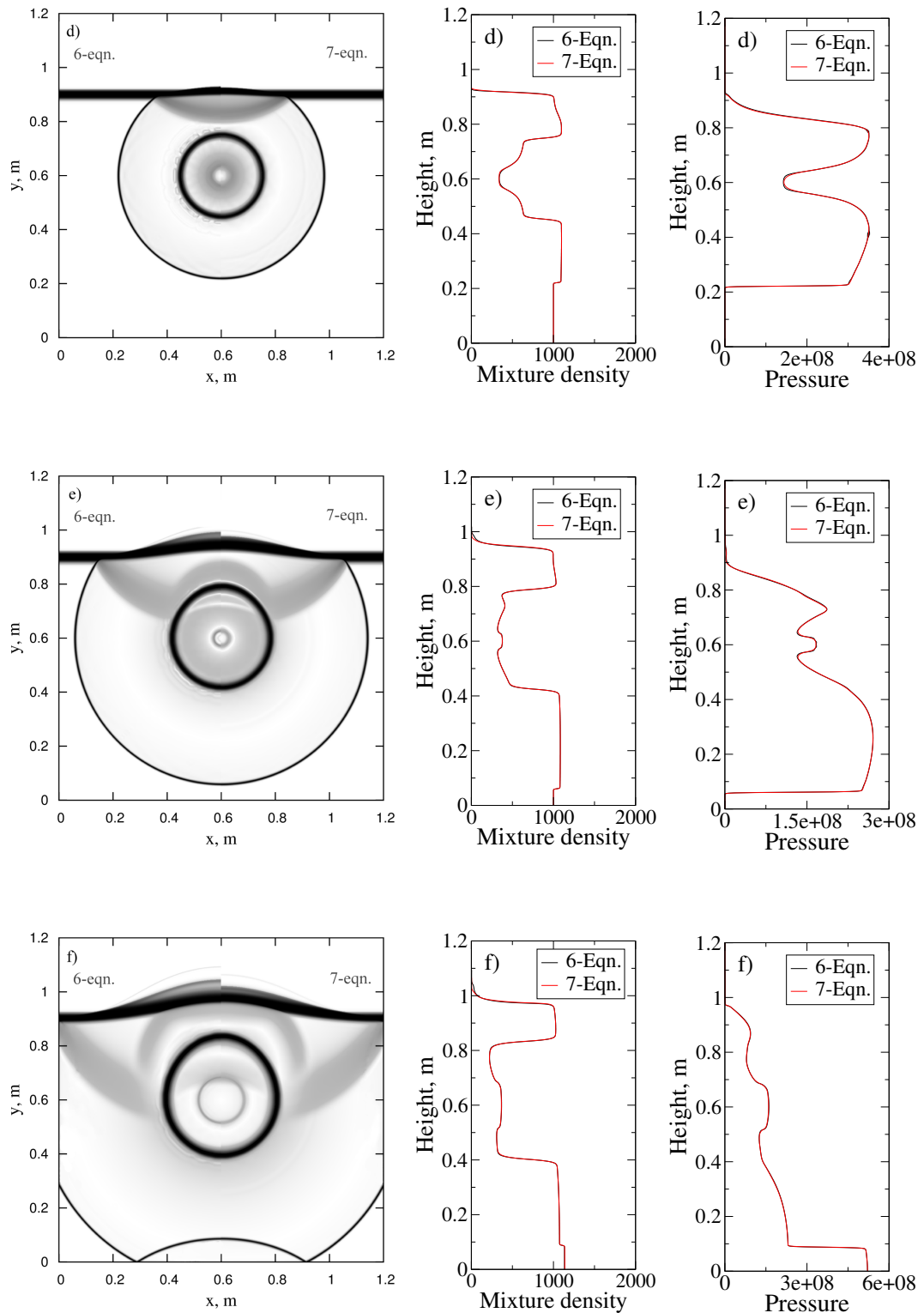


Figure 6.34: *Continued.* Underwater explosion near a free surface test 6.6.3. Comparison between the six and seven-equation models: Idealised Schlieren images of mixture density (left) and plots of mixture density (kg/m^3) (middle) and pressure (Pa) (right) at line of symmetry at times: (d) 0.147 ms, (e) 0.225 ms, (f) 0.3 ms.

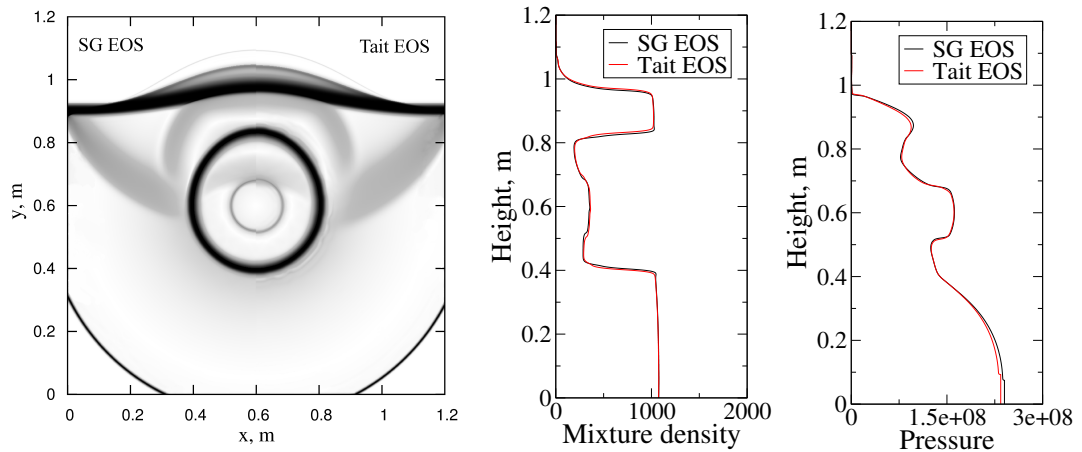


Figure 6.35: Underwater explosion near a free surface test 6.6.3. Comparison between the SG and Tait EOSs, bottom wall with extrapolation BCs: Idealised Schlieren images of mixture density (left) and plots of mixture density (kg/m^3) (middle) and pressure (Pa) (right) at line of symmetry at time 0.3 ms.

the air cylinder and the compression wave continues to propagate upward, until it has hit the free surface separating water and air. When the bottom boundary of the computational domain is a far field, the extrapolation boundary conditions are imposed and the results are shown in Figure 6.35 for the idealised schlieren mixture density (left), mixture density plot at line of symmetry (middle) and pressure plot at line of symmetry (right) at time $t = 0.3$ ms.

The conducted simulations are performed using the HLL Riemann solver with a CFL number equal to 0.4 and the resolution of 1000×1000 cells. The same features were also observed in the experimental results of Kleine et al. (2009) and in the numerical results reported by Liu, Khoo and Yeo (2001) and Zheng et al. (2011) who used different mathematical models and numerical methods.

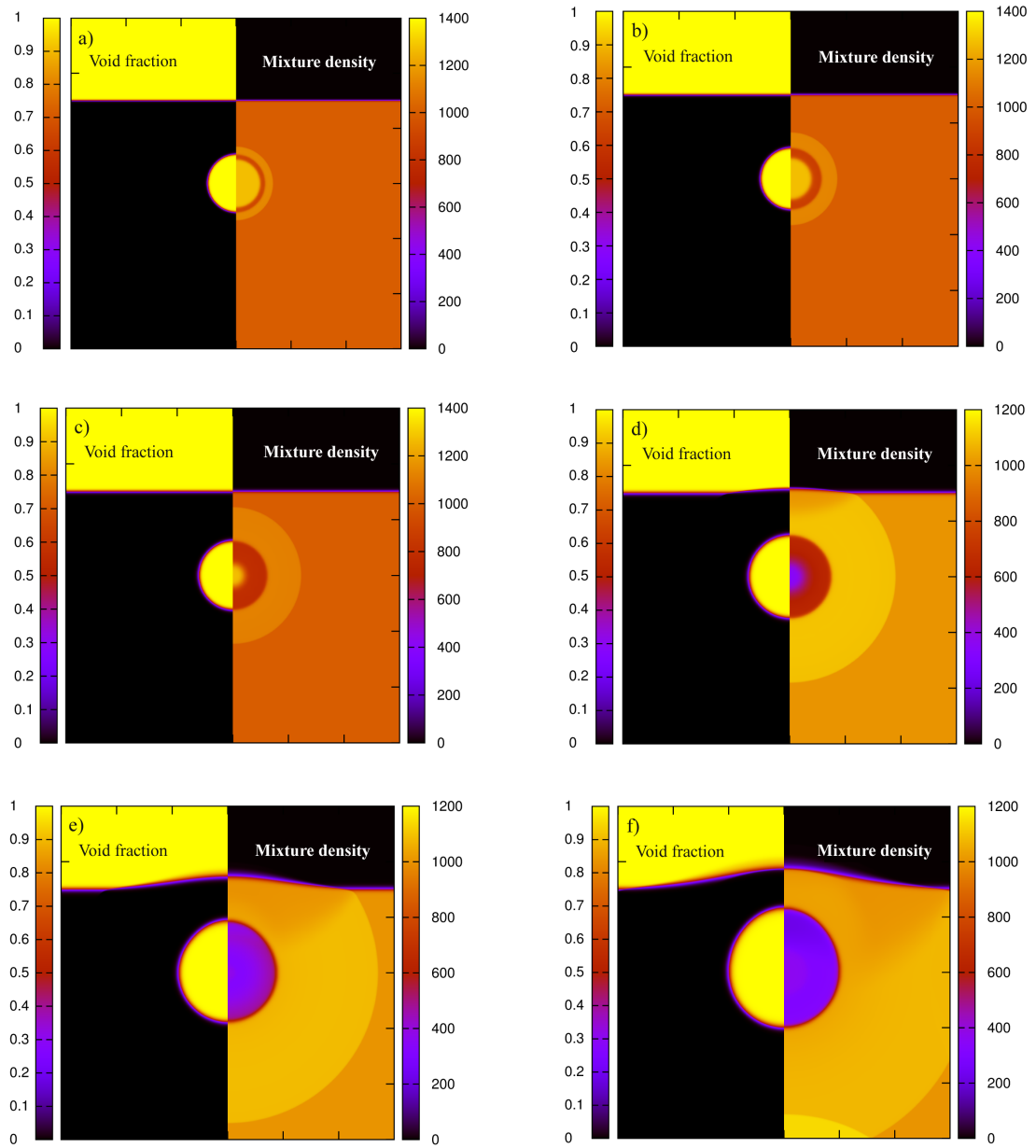


Figure 6.36: Underwater explosion near a free surface test 6.6.3. Volume fraction and mixture density at times: (a) 0.0175 ms, (b) 0.035 ms, (c) 0.07 ms, (d) 0.147 ms, (e) 0.225 ms, (f) 0.3 ms.

Chapter 7

Conclusions and future work

7.1 Conclusions

The work accomplished in this PhD study successfully addressed the specified objectives listed in the thesis introduction (section 1.2). A computer application has been developed to conduct numerical flow simulations based on the fully non-equilibrium (seven-equation) and partially equilibrium (six-equation) compressible multiphase flow models. These models are able to resolve interfaces separating fluids. The product of this work is a C-code equipped with a general formulation to enable easy switching between different EOSs. Meanwhile, some researchers need to add advection equations to their models depending on EOS parameters and others need to change their code in order to use different EOS. Such approach was proposed for the first time in this thesis. Each phase or component is either governed by the same EOS (e.g. helium and air are governed by the IG EOS) or different EOSs (e.g. explosive material is governed by the CC EOS and detonation products are governed by the JWL EOS). The interface which separates flow components is treated as a diffused zone. The formulations of the equations have been written and implemented with the second order accuracy in both space and time. This was possible by using the MUSCL scheme. The numerical results were obtained using the HLL, HLLC and VFRoe Riemann solvers. These results were verified or validated where possible in one and two space dimensions against available reference data. This chapter summarises the concluding remarks and provides possible suggestions for future work.

1. No pressure oscillations at the interface were observed in all results of the six and seven-equation models.
2. The numerical approach revealed that complicated flow patterns containing interfaces could be simulated with fixed grid mesh without using additional reconstruction or adaptive mesh refinement techniques.

3. The seven-equation model needs more CPU time than the six-equation model to obtain the solution. This is because the developed code for solving the seven-equation model uses an additional step, i.e. velocity relaxation process. The results show that both models gave almost the same results, however the six-equation model is cheaper than the seven-equation model in the examined tests by about 38 - 40 %.
4. Although the velocity relaxation process used in the solution of the seven-equation model slows down the simulation it allows to simulate a wider range of two-phase flow problems than the six-equation model, see for example water-faucet test problem 4.7.4.
5. The following tests proved that the model and its numerical representation could be used for the pseudo two-dimensional (axisymmetric) problems with area variation. Such an extension requires only a source term to be added to the governing equations, which makes this approach attractive for engineering applications. The specific conclusions from the test problems confirming area variation applicability are:
 - (a) The single phase flow through a convergent-divergent nozzle test performed in subsection 4.5.5 in which the IG EOS is used to govern air. The obtained results from the VFRoe solver for pressure and Mach number distributions through the C-D nozzle are qualitatively and quantitatively in good agreement with the theoretical reference results as shown in Figure 4.9. It can be observed that the position of the shock moves downstream as the back pressure is reduced.
 - (b) The two-phase flows through the C-D nozzle test investigated in subsection 4.5.6 in which the flow components are governed by the IG and SG EOSs and flows of mixtures of various air-water ratios are investigated at a fixed exit pressure of 8.5×10^8 Pa. The results show that the distributions of the flow parameters are again qualitatively similar to that of single phase flow for all investigated air-water ratios. However, quantitative variations can be observed in the values of the flow parameters as shown in Figure 4.11. Moreover, the location of the sonic flow moved downstream of the throat as the liquid content is increased.
6. The two multiphase flow models automatically reduce to the classical Euler equations for the single-phase flow. This is manifested in the following test problems:
 - (a) The gas-gas test examined in subsection 4.5.1 in which the IG EOS is used to govern air. The obtained results from the HLLC solver are in good

agreement with the exact solutions and the results of Kurganov and Tadmor (2000) who used different mathematical and numerical techniques for the single-phase.

- (b) The solid-solid test conducted in subsection 4.5.2 in which the shock wave EOS is used to govern aluminium. The obtained results from the HLL solver are in good agreement with the fine grid solution and the results of Shyue (2001) who used the Euler equations as a mathematical model.
- (c) The liquid-liquid test demonstrated in subsections 4.6.1 and 4.7.1 in which the SG or Tait EOSs are employed. The obtained results agree very well with the exact solution.

7. Two-phase test problems which are conducted by employing the same or different EOS to govern the flow components. These tests are as follows:

- (a) The interface advection test demonstrated in subsection 4.5.3 in which the flow components are governed by the SG and JWL EOSs. The obtained results show that no pressure or velocity oscillations can be observed at the interface as illustrated in Figure 5.4.2. The obtained results from the VFRoe solver are in good agreement with the exact solutions and the results of Petitpas et al. (2007).
- (b) The copper-explosive impact interaction test performed in subsection 4.5.4 in which the flow components are governed by the CC EOS. The results obtained from the HLL solver are in good agreement with the exact solutions and the results of Shyue (2001).

8. Comparisons between the HLL, HLLC and VFRoe approximate Riemann solvers are conducted in section 4.6. It can be observed from Tables 4.10, 4.15 and 4.20 that the three solvers need almost the same number of time steps to obtain the solution. However, the HLL and VFRoe solvers need the least and the most CPU run time to obtain the solutions, respectively. The CPU run time required by the solvers depends on the stiffness of the problem. For example for the conducted tests the HLLC and VFRoe need 14.74 %-29.47 % and 71.21 %-92.67 % more than the HLL solver, respectively.

9. It can be observed that the order of accuracy, spatial convergence and temporal convergence of the solvers are less than expected due to the presence of discontinuities in the solutions of the conducted test problems.

10. Comparisons between the SG and Tait EOSs which are used to govern water and between the IG and vdW EOSs which are used to govern air revealed that the results are qualitatively the same but quantitatively may have slight differences in the position of shocks or the values of flow parameters which can

be observed from the results of the conducted one and two-dimensional test problems.

7.2 Future work

The possible topics that could be addressed for further work are listed as follows:

1. Extension of the HLLC and VFRoe approximate Riemann solvers used in this thesis to simulate two and three-dimensional problems.
2. Using adaptive mesh strategy to reduce the computational time.
3. Application of the area variation source term to the other two-fluid models.
4. Study of the Rayleigh-Taylor instabilities resulting from gravity effect on the interface separating two fluids with different densities.

Bibliography

- Abgrall, R. 1988. “Generalisation of the ROE scheme for the computation of mixture of perfect gases.” *Rech. Aérop.* 6.
- Abgrall, R. 1996. “How to prevent pressure oscillations in multicomponent flow calculations: A quasi conservative approach.” *J. Comput. Phys.* 125(1):150–60.
- Abgrall, R. and R. Saurel. 2003. “Discrete equations for physical and numerical compressible multiphase mixtures.” *J. Comput. Phys.* 186(2):361–396.
- Abgrall, R. and S. Karni. 2001. “Computations of Compressible Multifluids.” *J. Comput. Phys.* 169:594–623.
- Abgrall, R. and V. Perrier. 2006. “A symptotic expansion of a multiscale numerical scheme for compressible multiphase ows.” *SIAM J. Multiscale and Modeling and Simulation* 186(2):84–115.
- Allaire, G., S. Clerc and S. Kokh. 2000. “A five-equation model for the numerical simulation of interfaces in two-phase flows.” *C. R. Acad. des Sci. Paris - Séries I: Mathematics* 331(12):1017–1022.
- Allaire, G., S. Clerc and S. Kokh. 2002. “A five-equation model for the simulation of interfaces between compressible fluids.” *J. Comput. Phys.* 181(2):577–616.
- Anderson, J. 1990. *MODERN COMPRESSIBLE FLOW With Historical Perspective*. McGraw-Hill Publishing Company, Singapore.
- Andrianov, N. 2003. Analytical and numerical investigation of two-phase flows PhD thesis Otto-von-Guericke University.
- Andrianov, N., R. Saurel and G. Warnecke. 2003. “A simple method for compressible multiphase mixtures and interfaces.” *Int. J. Numer. Methods in Fluids* 41:109–131.
- Baer, M. R. and J.W. Nunziato. 1986. “A Two-Phase Mixture Theory for the Deflagration to Detonation Transition DDT in Reactive Granular Materials.” *Int. J. Multiphase Flow* 12:861–889.

- Ball, G.J., B.P. Howell, T.G. Leighton and M.J. Schofield. 2000. "Shock-Induced Collapse of a Cylindrical Air Cavity in Water: a Free-Lagrange Simulation." *Shock Waves* 10:265–276.
- Banks, J. W. 2010. "On Exact Conservation for the Euler Equations with Complex Equations of State." *Commun. Comput. Phys.* 8(5):995–1015.
- Banks, J. W., D. W. Schwendeman, A. K. Kapila and W. D. Henshaw. 2007. "A high-resolution Godunov method for compressible multi-material flow on overlapping grids." *J. Comput. Phys.* (223):262–297.
- Benson, D. J. 1992. "Computational methods in Lagrangian and Eulerian hydrocodes." *Comput. Meth. App. Mech. Engng* 99(2-3):235–394.
- Bo, W., X. Liu, J. Glimm and X. Li. 2011. "A robust front tracking method: Verification and application to simulation of the primary breakup of a liquid jet." *SIAM J. Sci. Comput.* 33(4):1505–1524.
- Brennen, C.E. 2005. *Fundamentals of multiphase flow*. Cambridge University Press.
- Çengel, Y. A. and M. A. Boles. 2007. *THERMODYNAMICS an engineering approach*. Vol. 24.
- Chalmers, N. and E. Lorin. 2010. "Approximation of non-conservative hyperbolic systems based on different shock curve definitions." *Canadian Applied Mathematics Quarterly* 4.
- Cocchi, J. P. and R. Saurel. 1997. "A Riemann problem based method for compressible multifluid flows." *J. Comput. Phys.* 137:265–298.
- Cocchi, J.P., R. Saurel and J.C. Loraud. 1996. "Treatment of interface problems with Godunov-type schemes." *Shock Waves* 5:347–357.
- Cortes, J., A. Debussche and I. Toumi. 1998. "A density perturbation method to study the eigenstructure of two-phase flow equation systems." *J. Comput. Phys.* 147:463–484.
- Dafermos, C. M. 1973. "The entropy rate admissible criterion for solutions of hyperbolic conservation laws." *J. Diff. Equations* 14:202–212.
- Dal Maso, G., P. LeFloch and F. Murat. 1995. "Definition and weak stability of non-conservative products." *J. Math. Pures Appl.* 74:483–548.
- Davis, S. 1988. "Simplified second-order Godunov-type methods." *SIAM J. Sci. Comput.* 9(3):445–473.

- de Vahl Davis, G. 1983. “Natural Convection of Air in a Square Cavity: A Benchmark Numerical Solution.” *Int. J. Numer. Methods in Fluids* 3(3):249–264.
- Dobrtaz, B. M. 1972. Explosive handbook of properties of chemical explosives and explosive, Lawrence Livermore Laboratory, UCRL-51319, December 15. Technical report.
- Drew, D. A. 1983. “Mathematical Modeling of two-phase flow.” *Ann. Rev. Fluid Mech.* 15:261–291.
- Drew, D. and S. L Passman. 1998. *Theory of Multicomponent Fluids*. Springer.
- Dumbser, Michael and Eleuterio F. Toro. 2011. “A Simple Extension of the Osher Riemann Solver to Non-conservative Hyperbolic Systems.” *J. Sci. Comput.* 48:70–88.
- Farhat, C. and F. X. Roux. 1991. “A method of finite element tearing and inter-connecting and its parallel solution algorithm.” *Int. J. Numer. Meths. Engng.* 32:1205–1227.
- Fedkiw, R.P., T. Aslam, B. Merriman and S. Osher. 1999. “A Non-oscillatory Eulerian Approach to Interfaces in Multimaterial Flows (the Ghost Fluid Method).” *J. Comput. Phys.* 152(2):457–492.
- Fedkiw, R.P., T. Aslam, B. Merriman and S. Osher. 2002. “Coupling an Eulerian Fluid Calculation to a Lagrangian Solid Calculation with the Ghost Fluid Method.” *J. Comput. Phys.* 175:200–224.
- Fletcher, C. A. J. 1991. *Computational Techniques for Fluid Dynamics 1: Fundamental and General Techniques*. Springer-Verlag.
- Fortov, V.E. and I.V. Lomonosov. 2010. “Equations of State of Matter at High Energy Densities.” *The Open Plasma Physics Journal* 3:122–130.
- Gallouët, T., J. M. Hérard and Seguin. 2002. “Some recent finite volume schemes to compute Euler equations using real gas EOS.” *Int. J. Numer. Meth. Fluids* 39:1073–1138.
- Gallouët, T. and J. M. Masella. 1996. “Un schéma de Godunov approché.” *Comptes Rendus de l’Academie des Sciences Paris, Séries I: Mathematics* 323:77–84.
- Ghangir, F. and A. Nowakowski. 2012. Computing the evolution of interfaces using multi-component flow equations. In *New Approaches in Modeling Multiphase Flows and Dispersion in Turbulence, Fractal Methods and Synthetic Turbulence*, ed. F.C.G.A. Nicolleau, C. Cambon, J.-M. Redondo, J.C. Vassilicos, M. Reeks and A.F. Nowakowski. Vol. 18 of *ERCOfTAC Series* Springer Netherlands pp. 103–117.

- Ghangir, F., A. Nowakowski, F.C.G.A. Nicolleau and T. M. Michelitsch. 2008. "The application of HLLC numerical solver to the reduced multiphase model." *Proceedings of World Academy of Science, Engineering and Technology* .
- Giordano, J. and Y. Burtschell. 2006. "Richtmyer-Meshkov instability induced by shock-bubble interaction: Numerical and analytical studies with experimental validation." *Phys. Fluids* 18:036102.
- Glimm, J., C. Klingenberg, O. McBryan, B. Plohr, D. Sharp and S. Yaniv. 1985. "Three dimensional front tracking." *Adv. Appl. Math.* 6:259–290.
- Glimm, James, John W. Grove, Xiao Lin Li, Keh-Ming Shyue, Yanni Zeng and Qiang Zhang. 1998. "Three Dimensional Front Tracking." *SIAM J. Sci. Comp* 19:703–727.
- Godunov, S. K. 1959. "A Finite Difference Method for the Computation of Discontinuous Solutions of the Equations of Fluid Dynamics." *Mat. Sb* 47:357–393.
- Gonthier, K. and J. Powers. 2000. "A high-resolution numerical method for a two-phase model of Deflagration-to-Detonation transition." *J. Comput. Phys.* 163(2):376–433.
- Gray, W. G. 1975. "A derivation of the equations for multi-phase transport." *Chem. Engng Sci.* 30:229–233.
- Gray, W., G. and S. M. Hassanizadeh. 1989. "Averaging Theorems and Averaged Equations for Transport of Interface Properties in Multiphase Systems." *Int. J. Multiphase Flow* 15:81–95.
- Grove, J. W. 1994. "Applications of front tracking to the simulation of shock refractions and unstable mixing." *J. Appl. Num. Math.* 14:213–237.
- Haas, J. F. and B. Sturtevant. 1987. "Interaction of weak shock waves with cylindrical and spherical gas inhomogeneities." *J. Fluid Mech.* 181:41–76.
- Harten, A. and M. J. Hyman. 1983. "Self adjusting grid methods for one-dimensional hyperbolic conservation laws." *J. Comput. Phys.* 50:235–269.
- Harten, A., P. Lax and B. van Leer. 1983. "On upstream differencing and Godunov-type schemes for hyperbolic conservation laws." *SIAM Review* 25(1):35–61.
- Hirt, C. and B. Nichols. 1981. "Volume of fluid (VOF) method for the dynamics of free boundaries." *J. Comput. Phys.* 39(1):201–225.
- Hirt, C.W., A.A. Amsden and J.L. Cook. 1974. "An arbitrary Lagrangian-Eulerian computing method for all flow speeds." *J. Comput. Phys.* 14(3):227–253.

- Hu, X. Y. and B. C. Khoo. 2004. “An interface interaction method for compressible mult fluids.” *J. Comput. Phys.* 198:35–64.
- Ishii, M. 1975. *Thermo-fluid dynamic theory of two-phase flow*. Vol. 22 Paris: Eyrolles.
- Ishii, M. and T. Hibiki. 2006. *Thermo-fluid dynamics of two-phase flow*. Springer.
- Ivings, M. J., D. M. Causon and E. F. Toro. 1998. “On Riemann solvers for compressible liquids.” *Int. J. Numer. Methods in Fluids* 28:395–418.
- Jenny, P., B. Müller and Thomann H. 1997. “Correction of Conservative Euler Solvers for Gas Mixtures.” *J. Comput. Phys.* 132:91–107.
- Jolgam, S.A., A.R. Ballil, A.F. Nowakowski and F.C.G.A. Nicolleau. 2012a. “On Equations of State for Simulations of Multiphase Flows.” *Proceedings of the World Congress on Engineering* .
- Jolgam, S.A., A.R. Ballil, A.F. Nowakowski and F.C.G.A. Nicolleau. 2012b. “Simulations of compressible multiphase flows through a tube of varying cross-section.” *Proceedings of ASME 2012 11th Biennial Conference on Engineering Systems Design and Analysis* .
- Kadioglu, Samet Y. and Mark Sussman. 2008. “Adaptive solution techniques for simulating underwater explosions and implosions.” *J. Comput. Phys.* 227(3):2083–2104.
- Kapila, A. K., R. Menikoff and D. Stewart. 2001. “Two-phase modeling of deflagration-to-detonation transition in granular materials: Reduced equations.” *Phys. Fluids* 13(10):3002–3024.
- Karni, S. 1994. “Multicomponent Flow Calculations by a Consistent Primitive Algorithm.” *J. Comput. Phys.* 112(1):31–43.
- Karni, S. 1996. “Hybrid mult fluid algorithms.” *J. Sci. Comput.* 17(5):1019–1039.
- Kleine, H., S. Tepper, K. Takehara, TG. Etoh and K. Hiraki. 2009. “Cavitation induced by low speed underwater impact.” *26th Int. Symp. Shock Waves, Proceedings* 2:895–900.
- Kurganov, Alexander and Eitan Tadmor. 2000. “New High-Resolution Central Schemes for Nonlinear Conservation Laws and ConvectionDiffusion Equations.” *J. Comput. Phys.* 160:241–282.
- Lallemand, M. H., A. Chinnayya and O. Le Métayer. 2005. “Pressure relaxation procedures for multiphase compressible flows.” *Int. J. Numer. Methods in Fluids* 49(1):1–56.

- Lallemand, M-H. and R. Saurel. 2000. "Pressure relaxation procedures for multi-phase compressible flows." *INRIA Research Report No. 4038*.
- Larreteguy, A. E. 2002. "Modeling and simulation of multicomponent flows." *Mecanica Computacional XXI*:40–54.
- Larrouturou, B. 1991. "How to preserve the mass fractions positivity when computing compressible multi-component flows." *J. Comput. Phys.* 95(1):59–84.
- Lax, P. D. 1954. "Weak solutions of nonlinear hyperbolic equations and their numerical computation." *Comm. Pure Appl. Math.* 159(7).
- Lax, P. D. 1972. *Hyperbolic systems of conservation laws and mathematical theory of shock waves*. Number number 11 SIAM Regional Conf. Ser. Appl. Math.
- Layes, G. and O. Le Métayer. 2007. "Quantitative numerical and experimental studies of the shock accelerated heterogeneous bubbles motion." *Phys. Fluids* 19:042105.
- Lee, B. J., E. F. Toro, C. E. Castro and N. Nikiforakis. 2013. "Adaptive Osher-type scheme for the Euler equations with highly nonlinear equations of state." *J. Comput. Phys.* 246:165–183.
- LeFloch, P. 1989. "Shock waves for nonlinear hyperbolic systems in nonconservative form." *Institute for Math. and its Appl., Minneapolis*, Preprint No. 593.
- LeVeque, R. J. 1992. *Numerical Methods for Conservation Laws*. Birkhauser Verlag, Basel.
- LeVeque, R. J. 2004. *Finite Volume Methods for Hyperbolic Problems*. Cambridge University Press.
- LeVeque, R. J. and K. M. Shyue. 1996. "Two-dimensional front tracking based on high resolution wave propagation methods." *J. Comput. Phys.* 123:354–368.
- Liu, T. 1976. "The entropy condition and the admissibility of shocks." *J. Math. Anal. Appl.* 53:78–88.
- Liu, T.G., B.C. Khoo and K.S. Yeo. 2001. "The simulation of compressible multi-medium flow. Part II: Applications to 2D underwater shock refraction." *Comput. Fluids* 30:315–337.
- Losasso, R., T. Shinar and A. Selle. 2006. "Multiple interacting fluids." *ACM Transaction on Graphics* 25(3):812–819.
- Mao, D. K. 1993. "A treatment of discontinuities for finite difference methods in two dimensional case." *J. Comput. Phys.* 104:235–269.

- Margolin, L.G. 1997. “Introduction to An Arbitrary Lagrangian-Eulerian Computing Method for All Flow.” *J. Comput. Phys.* 135(1):198–202.
- Marquina, Antonio and Pep Mulet. 2003. “A flux-split algorithm applied to conservative models for multicomponent compressible flows.” *J. Comput. Phys.* 185(1):120–138.
- Marsh, S. P. 1980. *LASL shock Hugoniot data*. Univ. of California Press, Berkeley.
- Menikoff, R. and B. Plohr. 1989. “The Riemann problem for fluid flow of real materials.” *Rev. Mod. Phys.* 61(75).
- Mulder, W, S Osher and James A Sethian. 1992. “Computing interface motion in compressible gas dynamics.” *J. Comput. Phys.* 100(2):209 – 228.
- Murrone, A. and H. Guillard. 2005. “A five equation reduced model for compressible two phase flow problems.” *J. Comput. Phys.* 202:664–698.
- Niu, Y. 2005. “Towards a simple and robust two-phase flow algorithm.” *Zhongguo Hangkong Taikong Xuehui Huikan/Transactions of the Aeronautical and Astronautical Society of the Republic of China* 37(3):275–280.
- Nourgaliev, R.R., T.N. Dinh and T.G. Theofanous. 2006. “Adaptive characteristics-based matching for compressible multifluid dynamics.” *J. Comput. Phys.* 213(2):500–529.
- Nowakowski, A., B. Librovich and L. Lue. 2004. “Reactor safety analysis based on a developed two-phase compressible flow simulation.” in *Proceedings of the 7th Biennial Conference on Engineering Systems Design and Analysis* 1:929–936.
- Nowakowski, A.F. Ballil, A.R., , S.A. Jolgam and F.C.G.A. Nicolleau. 2012. “CAPTURING OF INTERFACE EVOLUTION USING DIFFUSE INTERFACE METHOD.” *XX Polish Fluid Mechanics Conference* .
- Nowakowski, A.F. Ballil, A.R., , S.A. Jolgam and F.C.G.A. Nicolleau. 2013. “The application of a multi-component Eulerian model for the resolution of interfaces interacting with shock waves in two-phase flows.” *8th International Conference on Multiphase Flow* .
- Nowakowski, A.F., S.A. Jolgam, A.R. Ballil and F.C.G.A. Nicolleau. 2011. “Simulation of Multiphase Flows with Strong Shocks and Density Variations.” *Proceedings in Applied Mathematics and Mechanics* .
- Osher, S. and F. Solomon. 1982. “Upwind difference schemes for hyperbolic conservation laws.” *Math. Comput.* 38:339–374.

- Perigaud, G. and R. Saurel. 2005. “A compressible flow model with capillary effects.” *J. Comput. Phys.* 209(1):139–178.
- Petitpas, Fabien, Erwin Franquet, Richard Saurel and Olivier Le Métayer. 2007. “A relaxation-projection method for compressible flows. Part II: Artificial heat exchanges for multiphase shocks.” *J. Comput. Phys.* 225(2):2214–2248.
- Qamar, Shamsul and Gerald Warnecke. 2004. “Simulation of multicomponent flows using high order central schemes.” *App. Numer. Math.* 50(2):183–201.
- Quirk, J. 1994. “An alternative to unstructured grids for computing gas dynamic flow around arbitrarily complex two dimensional bodies.” *Comput. Fluids* 23:125–142.
- Quirk, James J. and S. Karni. 1996. “On the dynamics of a shock-bubble interaction.” *J. Fluid Mech.* 318:129–163.
- Ransom, V. H. 1987. *Numerical benchmark tests, In Multiphase Science and Technology*. Vol. 3 Hemisphere, Washington.
- Rider, W. J. 1999. “An adaptive Riemann solver using a two-shock approximation.” *Comput. Fluids* 741(28).
- Roe, P. L. 1982. Fluctuations and signals-A framework for numerical evolution problems. In *Numerical Methods for Fluid Dynamics*, ed. K. W. Morton and M. J. Baines. ERCOFTAC Series Academic Press, New York pp. 219–257.
- Saurel, R., F. Petitpas and R. Abgrall. 2008. “Modelling phase transition in metastable liquids: application to cavitating and flashing flows.” *J. Fluid Mech.* 607:313–350.
- Saurel, R., F. Petitpas and R. Berry. 2009. “Simple and efficient relaxation methods for interfaces separating compressible fluids, cavitating flows and shocks in multiphase mixtures.” *J. Comput. Phys.* 228(5):1678–1712.
- Saurel, R. and O. Le Métayer. 2001. “A multiphase model for compressible flows with interfaces, shocks, detonation waves and cavitation.” *J. Fluid Mech.* 431:239–271.
- Saurel, R. and R. Abgrall. 1999a. “A multiphase Godunov method for compressible multifluid and multiphase flows.” *J. Comput. Phys.* 150(2):425–467.
- Saurel, Richard, E. Franquet, E. Daniel and Olivier Le Métayer. 2007. “A relaxation-projection method for compressible flows. Part I: The numerical equation of state for the Euler equations.” *J. Comput. Phys.* 223:822–845.

- Saurel, Richard and Jacques Massoni. 1998. “On Riemann-problem-based methods for detonations in solid energetic materials.” *Int. J. for Numer. Methods in Fluids* 26(1):101–121.
- Saurel, Richard and Rémi Abgrall. 1999b. “A Simple Method for Compressible Multifluid Flows.” *SIAM J. Sci. Comput.* 21(3):1115–1145.
- Saurel, Richard, S. Gavrilyuk and F. Renaud. 2003. “A multiphase model with internal degrees of freedom: application to shockbubble interaction.” *J. Fluid Mech.* 495:83–321.
- Schwendeman, D. W., C. W. Wahle and A. K. Kapila. 2006. “The Riemann problem and a high-resolution Godunov method for a model of compressible two-phase flow.” *J. Comput. Phys.* 212:490–526.
- Shyue, Keh-Ming. 1998. “An efficient shock-capturing algorithm for compressible multi-component problems.” *J. Comput. Phys.* 142(1):208–242.
- Shyue, Keh-Ming. 1999. “A fluid-mixture type algorithm for compressible multicomponent flow with van der Waals equation of state.” *J. Comput. Phys.* 156(1):43–88.
- Shyue, Keh-Ming. 2001. “A Fluid-Mixture Type Algorithm for Compressible Multicomponent Flow with Mie-Grüneisen Equation of State.” *J. Comput. Phys.* 171(2):678–707.
- Smoller, J. 1983. *Shock waves and reaction-diffusion equations*. Springer, New York.
- Sousa, F.S., N. Mangiavacchi, L.G. Nonato, A. Castelo, M.F. Tomé, V.G. Ferreira, J.A. Cuminato and S. McKee. 2004. “A front-tracking/front-capturing method for the simulation of 3D multi-fluid flows with free surfaces.” *J. Comput. Phys.* 198(2):469–499.
- Stewart, H. B. and B. Wendroff. 1984. “Two phase flow: Models and methods.” *J. Comput. Phys.* 56:363–409.
- Strang, G. 1968. “On the construction and comparison of difference schemes.” *SIAM J. Numer. Anal.* 5:506–517.
- Terashima, Hiroshi and Grtar Tryggvason. 2009. “A front-tracking/ghost-fluid method for fluid interfaces in compressible flows.” *J. Comput. Phys.* 228(11):4012–4037.
- Tiselj, Iztok and Stojan Petelin. 1997. “Modelling of Two-Phase Flow with Second-Order Accurate Scheme.” *Journal of Computational Physics* 136(2):503–521.
- Toro, E. 2009. *Riemann Solvers and Numerical Methods for Fluid Dynamics: A Practical Introduction*. Springer.

- Toro, E. F., M. Spruce and W. Speares. 1994. “Restoration of the Contact Surface in the HLLRiemann Solver.” *Shock Waves* 4:25–34.
- Toumi, I. and P. Raymond. 1995. Upwind numerical scheme for a two-fluid two-phase flow model. In *Fourteenth International Conference on Numerical Methods in Fluid Dynamics*, ed. SureshM. Deshpande, ShivarajS. Desai and Roddam Narasimha. Vol. 453 of *Lecture Notes in Physics* Springer Berlin Heidelberg pp. 299–306.
- Trunin, R. F., M. Yu. Belyakova, M. V. Zhernokletov and Yu. N. Sutulov. 1991. “Shock compression of metallic alloys.” *Izv. Akad. Nauk SSSR. Fiz. Zemli* 2:99–106.
- Whitaker, S. 1973. “Pressure relaxation procedures for multiphase compressible flows.” *Int. J. for Numer. Methods in Fluids* 28(1):139–147.
- Youngs, D.L. 1982. “Time-dependent multi-material flow with large fluid distortion.” *Academic Press, New York* .
- Zein, A., M. Hantke and G. Warnecke. 2010. “Modeling phase transition for compressible two-phase flows applied to metastable liquids.” *J. Comput. Phys.* 229:2964–2998.
- Zheng, H. W., C. Shu and Y. T. Chew. 2008. “An object-oriented and quadrilateral-mesh based solution adaptive algorithm for compressible multi-fluid flows.” *J. Comput. Phys.* 227(14):6895–6921.
- Zheng, H. W., C. Shu, Y. T. Chew and N. Qin. 2011. “A solution adaptive simulation of compressible multi-fluid flows with general equation of state.” *Int. J. for Numer. Methods in Fluids* 67(5):616–637.
- Zheng, H. W., C. Shu, Y. T. Chew and N. Qin. 2012. Oscillation-Free Adaptive Simulation of Compressible Two-Fluid Flows with Different Types of Equation of State. In *New Approaches in Modeling Multiphase Flows and Dispersion in Turbulence, Fractal Methods and Synthetic Turbulence*, ed. F.C.G.A. Nicolleau, C. Cambon, J.-M. Redondo, J.C. Vassilicos, M. Reeks and A.F. Nowakowski. Vol. 18 of *ERCOfTAC Series* Springer Netherlands pp. 103–117.

Appendix A

Derivations of speed of sound for various EOSs

Derivation of the speed of sound at the pure fluid and at the interface for the shock wave, van der Waals, Cochran-Chan (CC), and Jones-Wilkins-Lee (JWL) EOSs are as given in the following sections. The local speed of sound is defined as:

$$c^2 = \frac{\frac{p}{\rho^2} - \frac{\partial e}{\partial \rho} \Big|_p}{\frac{\partial e}{\partial p} \Big|_\rho}. \quad (\text{A-1})$$

The speed of sound at the interface is given by:

$$c_{int}^2 = \frac{\frac{p_{int}}{\rho^2} - \frac{\partial e}{\partial \rho} \Big|_p}{\frac{\partial e}{\partial p} \Big|_\rho}. \quad (\text{A-2})$$

A.1 Speed of sound for the shock wave EOS

The Mie-Grüneisen EOS (4.12) may be rewritten as follows:

$$e = \frac{p - p_{\mathcal{H}}(\rho)}{\rho \Gamma_{\mathcal{H}}(\rho)} + e_{\mathcal{H}}(\rho). \quad (\text{A-3})$$

where $p_{\mathcal{H}}(\rho)$, $e_{\mathcal{H}}(\rho)$ and $\Gamma_{\mathcal{H}}(\rho)$ for the shock wave EOS are given as follows:

$$p_{\mathcal{H}}(\rho) = \frac{\rho_o C_o^2 \left(1 - \frac{\rho_o}{\rho}\right)}{\left[1 - s \left(1 - \frac{\rho_o}{\rho}\right)\right]^2}, \quad e_{\mathcal{H}}(\rho) = \frac{C_o^2 \left(1 - \frac{\rho_o}{\rho}\right)^2}{2 \left[1 - s \left(1 - \frac{\rho_o}{\rho}\right)\right]^2} \quad \text{and} \quad \Gamma_{\mathcal{H}}(\rho) = \Gamma \left(\frac{\rho_o}{\rho}\right)^\theta$$

where Γ is defined as $\Gamma = \gamma - 1$. Differentiating the above equation (A-3) with

respect to the density and setting $\eta = 1 - s\psi$, $\psi = 1 - \frac{\rho_o}{\rho}$ and $\zeta = \rho\Gamma\left(\frac{\rho_o}{\rho}\right)^\theta$ yields:

$$\left.\frac{\partial e}{\partial \rho}\right|_p = \frac{-\frac{\rho_o^2 c_o^2}{\rho^2 \eta^2} - \frac{2\rho_o^2 c_o^2 s\psi}{\rho^2 \eta^3}}{\zeta} + \frac{(p - \frac{\rho_o c_o^2 \psi}{\eta^2})\theta}{\zeta \rho} - \frac{p - \frac{\rho_o c_o^2 \psi}{\eta^2}}{\zeta \rho} + \frac{\rho_o c_o^2 \psi}{\eta^2 \rho^2} + \frac{\rho_o c_o^2 s\psi^2}{\eta^3 \rho^2}, \quad (\text{A-4})$$

and with respect to the pressure yields:

$$\left.\frac{\partial e}{\partial p}\right|_\rho = \frac{1}{\zeta}. \quad (\text{A-5})$$

The equations (A-4) and (A-5) are substituted into equation (A-1). The resulting form is simplified and finally the speed of sound for the shock wave EOS materials can be written as:

$$c^2 = \left(\frac{p}{\rho^2} - \frac{-\frac{\rho_o^2 c_o^2}{\rho^2 \eta^2} - \frac{2\rho_o^2 c_o^2 s\psi}{\rho^2 \eta^3}}{\zeta} - \frac{(p - \frac{\rho_o c_o^2 \psi}{\eta^2})\theta}{\zeta \rho} + \frac{p - \frac{\rho_o c_o^2 \psi}{\eta^2}}{\zeta \rho} - \frac{\rho_o c_o^2 \psi}{\eta^2 \rho^2} - \frac{\rho_o c_o^2 s\psi^2}{\eta^3 \rho^2} \right) \zeta \quad (\text{A-6})$$

Similarly, the speed of sound at the interface can be obtained by substituting the equations (A-4) and (A-5) into equation (A-2) and the simplified form can be written as follows:

$$c_{int}^2 = \left(\frac{p_{int}}{\rho^2} - \frac{-\frac{\rho_o^2 c_o^2}{\rho^2 \eta^2} - \frac{2\rho_o^2 c_o^2 s\psi}{\rho^2 \eta^3}}{\zeta} - \frac{(p - \frac{\rho_o c_o^2 \psi}{\eta^2})\theta}{\zeta \rho} + \frac{p - \frac{\rho_o c_o^2 \psi}{\eta^2}}{\zeta \rho} - \frac{\rho_o c_o^2 \psi}{\eta^2 \rho^2} - \frac{\rho_o c_o^2 s\psi^2}{\eta^3 \rho^2} \right) \zeta \quad (\text{A-7})$$

A.2 Speed of sound for the van der Waals EOS

The van der Waals EOS (4.30) may be rewritten as follows:

$$e = \left(\frac{p}{\rho} + a\rho \right) \left(\frac{1 - b\rho}{\gamma - 1} \right) - a\rho. \quad (\text{A-8})$$

Differentiating the above equation (A-8) with respect to the density yields:

$$\left.\frac{\partial e}{\partial \rho}\right|_p = -\frac{p}{\rho^2(\gamma - 1)} + \frac{a}{\gamma - 1} - \frac{2ab\rho}{\gamma - 1} - a, \quad (\text{A-9})$$

and with respect to the pressure yields:

$$\left. \frac{\partial e}{\partial p} \right|_{\rho} = -\frac{1 - b\rho}{\rho(\gamma - 1)}. \quad (\text{A-10})$$

The equations (A-9) and (A-10) are substituted into equation (A-1). The resulting form is simplified and finally the speed of sound can be written as:

$$c = \sqrt{\frac{\gamma(p + a\rho^2)}{\rho(1 - b\rho)} - 2a\rho}. \quad (\text{A-11})$$

Similarly, the speed of sound at the interface can be obtained by substituting the equations (A-9) and (A-10) into equation (A-2) and the simplified form can be written as follows:

$$c_{int}^2 = \frac{p_{int}(\gamma - 1) + p + a\rho^2\gamma}{\rho(1 - b\rho)} - 2a\rho. \quad (\text{A-12})$$

A.3 Speed of sound for the Cochran-Chan EOS

The Cochran-Chan EOS (4.34) may be rewritten as follows:

$$e = \frac{p - \left[A_1 \left(\frac{\rho_o}{\rho} \right)^{1-E_1} - A_2 \left(\frac{\rho_o}{\rho} \right)^{1-E_2} \right]}{\rho(\gamma - 1)} - \frac{A_1}{\rho_o(1 - E_1)} \left[\left(\frac{\rho_o}{\rho} \right)^{1-E_1} - 1 \right] + \frac{A_2}{\rho_o(1 - E_2)} \left[\left(\frac{\rho_o}{\rho} \right)^{1-E_2} - 1 \right] - C_v T. \quad (\text{A-13})$$

Differentiating the above equation with respect to the density yields:

$$\left. \frac{\partial e}{\partial \rho} \right|_p = \frac{-\frac{A_1 \left(\frac{\rho_o}{\rho} \right)^{-E_1} E_1}{\rho} + \frac{A_2 \left(\frac{\rho_o}{\rho} \right)^{-E_2} E_2}{\rho}}{\rho(\gamma - 1)} - \frac{p - A_1 \left(\frac{\rho_o}{\rho} \right)^{-E_1} + A_2 \left(\frac{\rho_o}{\rho} \right)^{-E_2}}{\rho^2(\gamma - 1)} + \frac{A_1 \left(\frac{\rho_o}{\rho} \right)^{1-E_1} - A_2 \left(\frac{\rho_o}{\rho} \right)^{1-E_2}}{\rho_o \rho}, \quad (\text{A-14})$$

and with respect to the pressure yields:

$$\left. \frac{\partial e}{\partial p} \right|_{\rho} = \frac{1}{\rho(\gamma - 1)}. \quad (\text{A-15})$$

The equations (A-14) and (A-15) are substituted into equation (A-1). The resulting form of sound speed for the Cochran-Chan EOS materials is simplified and it can

be written as follows:

$$c^2 = \frac{p\gamma}{\rho} + \frac{A_1}{\rho} \left(\frac{\rho_o}{\rho} \right)^{-E_1} \left[E_1 - \gamma \right] - \frac{A_2}{\rho} \left(\frac{\rho_o}{\rho} \right)^{-E_2} \left[E_2 - \gamma \right]. \quad (\text{A-16})$$

Similarly, the speed of sound at the interface can be obtained by substituting the equations (A-14) and (A-15) into equation (A-2) and the simplified form can be written as follows:

$$c_{int}^2 = \frac{p_{int}}{\rho} (\gamma - 1) + \frac{p}{\rho} + \frac{A_1}{\rho} \left(\frac{\rho_o}{\rho} \right)^{-E_1} \left[E_1 - \gamma \right] - \frac{A_2}{\rho} \left(\frac{\rho_o}{\rho} \right)^{-E_2} \left[E_2 - \gamma \right]. \quad (\text{A-17})$$

A.4 Speed of sound for the Jones-Wilkins-Lee (JWL) EOS

The Jones-Wilkins-Lee (JWL) EOS (4.39) may be rewritten as follows:

$$e = \frac{p - A_1 e^{(-R_1 \frac{\rho_o}{\rho})} - A_2 e^{(-R_2 \frac{\rho_o}{\rho})}}{(\gamma - 1)\rho} + \frac{A_1 e^{(-R_1 \frac{\rho_o}{\rho})}}{\rho_o R_1} + \frac{A_2 e^{(-R_2 \frac{\rho_o}{\rho})}}{\rho_o R_2} - C_{ek}. \quad (\text{A-18})$$

Differentiating the above equation (A-18) with respect to the density yields:

$$\left. \frac{\partial e}{\partial \rho} \right|_p = \frac{-\frac{A_1 R_1 \rho_o e^{(-R_1 \frac{\rho_o}{\rho})}}{\rho^2} - \frac{A_2 R_2 \rho_o e^{(-R_2 \frac{\rho_o}{\rho})}}{\rho^2}}{(\gamma - 1)\rho} - \frac{p - A_1 e^{(-R_1 \frac{\rho_o}{\rho})} - A_2 e^{(-R_2 \frac{\rho_o}{\rho})}}{(\gamma - 1)\rho^2} + \frac{A_1 e^{(-R_1 \frac{\rho_o}{\rho})} + A_2 e^{(-R_2 \frac{\rho_o}{\rho})}}{\rho^2}, \quad (\text{A-19})$$

and with respect to the pressure yields:

$$\left. \frac{\partial e}{\partial p} \right|_\rho = \frac{1}{\rho(\gamma - 1)}. \quad (\text{A-20})$$

The equations (A-19) and (A-20) are substituted into equation (A-1). The resulting form of sound speed for the Jones-Wilkins-Lee (JWL) EOS materials is simplified and finally it can be written as follows:

$$c^2 = \frac{p\gamma}{\rho} + \frac{A_1}{\rho} e^{(-R_1 \frac{\rho_o}{\rho})} \left(\frac{R_1 \rho_o}{\rho} - \gamma \right) + \frac{A_2}{\rho} e^{(-R_2 \frac{\rho_o}{\rho})} \left(\frac{R_2 \rho_o}{\rho} - \gamma \right). \quad (\text{A-21})$$

Similarly, the speed of sound at the interface can be obtained by substituting the equations (A-19) and (A-20) into equation (A-2) and the simplified form can be written as follows:

$$c_{int}^2 = \frac{p_{int}}{\rho}(\gamma - 1) + \frac{p}{\rho} + \frac{A_1}{\rho} e^{(-R_1 \frac{\rho_o}{\rho})} \left(\frac{R_1 \rho_o}{\rho} - \gamma \right) + \frac{A_2}{\rho} e^{(-R_2 \frac{\rho_o}{\rho})} \left(\frac{R_2 \rho_o}{\rho} - \gamma \right). \quad (\text{A-22})$$

Appendix B

Publications

B.1 On Equations of State for Simulations of Multiphase Flows

Proceedings of the World Congress on Engineering 2012 Vol III WCE 2012, July 4 - 6, 2012, London, U.K.

Jolgam et al. (2012*a*)

Abstract

An efficient Eulerian numerical method is considered for simulating multiphase flows governed by general equation of state (EOS). The method allows interfaces between phases to diffuse in a transitional region over a small number of computational cells. The seven-equation model of Saurel and Abgrall [Saurel, R. and Abgrall, R., A multiphase Godunov method for compressible multifluid and multiphase flows, *J. Comput. Phys.* 150 (1999), 425 - 467] is employed to describe the compressible multiphase flows. For one dimensional flow the model which is strictly hyperbolic consists of seven equations. These equations are the volume fraction evolution equation and the conservation equations (mass, momentum and energy) for each phase. The solution of the hyperbolic equations is obtained using HLL Riemann solver. In the present work various equations of state (EOSs) have been discussed. Error analysis, number of time steps and CPU time comparisons between EOSs have been presented. Well known test cases are examined to simulate compressible as well as incompressible multiphase flows.

Keywords: Compressible multiphase flow, hyperbolic PDEs, Riemann problem, Godunov methods, shock waves, HLL Riemann solver.

B.2 Simulations of Compressible Multiphase Flows Through a Tube of Varying Cross-section

Proceedings of ASME 2012 11th Biennial Conference on Engineering Systems Design and Analysis, ESDA 2012, July 2 - 4, 2012, Nantes, France

Jolgam et al. (2012*b*)

Abstract

The simulation of multiphase compressible flows through high pressure nozzles is presented. The study uses the developed numerical approach. There are many important engineering applications which are concerned with multiphase flows and convergent-divergent nozzles. This work presents the developed extension of the model and numerical algorithm based on the so called parent model earlier introduced by Saurel and Abgrall [Saurel, R. and Abgrall, R., A Multiphase Godunov Method for Compressible Multifluid and Multiphase Flows, *J. Comput. Phys.* 150 (1999), 425 - 467]. This model which consists of conservation laws for each phase complemented with the volume fraction evolution equation is modified by adding a source term to simulate area variation. The model is strictly hyperbolic and non-conservative due to the existence of non-conservative terms. The model is able to deal with compressible and incompressible flows. Moreover, it can deal with mixtures and pure fluids, where each fluid has its own pressure and velocity. The presence of velocity and pressure relaxation terms in the governing equations has made the velocity and pressure relaxation processes essential to tackle the boundary conditions at the interface. The interface separating phases is considered as a numerical diffusion zone in this method. The model is solved using an efficient Eulerian numerical method. A second order Godunov-type scheme with approximate Riemann solver is used to enable capturing of a physical interface by the resolution of the Riemann problem. The solution is obtained by splitting the hyperbolic part and source terms parts in the numerical algorithm. The source terms, including relaxation parts of the model, are tackled in succession using Strang splitting technique. The governing equations are solved at each computational cell using the same numerical algorithm for the whole domain including the interface. The main aim of this work has been to study different flow regimes with respect to pressure boundary conditions through the numerical solutions of single and multiphase flows. The performance of the programme has been verified via well established benchmark test problems for multiphase flows.

B.3 Simulation of Multiphase Flows with Strong Shocks and Density Variations

Proceedings in Applied Mathematics and Mechanics, 20 June 2011

Nowakowski et al. (2011)

Abstract

The system of extended Euler type hyperbolic equations is considered to describe a two-phase compressible flow. A numerical scheme for computing multi-component flows is then examined. The numerical approach is based on the mathematical model that considers interfaces between fluids as numerically diffused zones. The hyperbolic problem is tackled using a high resolution HLLC scheme on a fixed Eulerian mesh. The global set of conservative equations (mass, momentum and energy) for each phase is closed with a general two parameters equation of state for each constituent. The performance of various variants of a diffuse interface method is carefully verified against a comprehensive suite of numerical benchmark test cases in one and two space dimensions. The studied benchmark cases are divided into two categories: idealized tests for which exact solutions can be generated and tests for which the equivalent numerical results could be obtained using different approaches. The ability to simulate the Richtmyer-Meshkov instabilities, which are generated when a shock wave impacts an interface between two different fluids, is considered as a major challenge for the present numerical techniques. The study presents the effect of density ratio of constituent fluids on the resolution of an interface and the ability to simulate Richtmyer-Meshkov instabilities by various variants of diffuse interface methods.

B.4 Capturing of Interface Evolution Using Diffuse Interface Method

XX Polish Fluid Mechanics Conference, Gliwice, 17 - 20 September 2012

Nowakowski et al. (2012)

Abstract

In the present contribution the diffuse interface method is used to track the interface evolution in multi-component flow systems. A numerical framework is developed to solve a hyperbolic Eulerian type model with a general stiffened gas equation of state. The model consists of six equations with two pressures and single velocity. The extended finite volume method is developed using a second order Godunov approach which is implemented with HLL and HLLC Riemann solvers in one and two space dimensions. The numerical scheme considers both the non-conservative equations and non-conservative terms that exist in the model to fulfill the interface condition. A verification procedure starts with a successful computation of a selection of numerical benchmark problems. Further, a numerically challenging shock bubble interaction problem is conducted and compared with published experimental data.

B.5 The Application of a Multi-component Eulerian Model for the Resolution of Interfaces Interacting with Shock Waves in Two-phase Flows

8th International Conference on Multiphase Flow, ICMF 2013, Jeju, Korea, May 26 - 31, 2013

Nowakowski et al. (2013)

Abstract

The numerical method which considers interfaces represented by contact discontinuities as numerically diffused zones, has been applied to simulate compressible two-phase flows. The approach takes advantage of the inherent numerical diffusion which is usually present in numerical solutions of compressible flows with shock waves. The mathematical formulation of the presented method was obtained after an averaging process of the single phase Navier-Stokes equations. The resulting equations are encapsulated into the six equation or seven equation Eulerian frameworks for the case of 1D compressible two-phase flow problems. The Euler-type equations representing the computational model were discretized and solved using a high-resolution Godunov method which was developed and implemented with HLL, HLLC and Roe type Riemann solvers in one and two space dimensions. The numerical scheme considers both the non-conservative equations and non-conservative terms that exist in the model to fulfill the interface condition. A verification procedure starts with a successful computation of a selection of numerical benchmark problems. Further, a numerically challenging shock bubble interaction problem is conducted and compared with published experimental data.

Keywords: Numerical simulations, compressible multi-component flow, interface evolution, shock waves, Riemann solver